DESIGN AND DEVELOPMENT OF A BIOLOGICALLY INSPIRED HYPER-REDUNDANT ROBOT JOINT MECHANISM

By

AFOLAYAN, Matthew Olatunde
PhD/Eng/39544/2004-05
Mechanical Engineering Department
Ahmadu Bello University
Zaria

A DISSERTATION SUBMITTED TO THE SCHOOL OF POST GRADUATE STUDIES, AHMADU BELLO UNIVERSITY, ZARIA.

IN FULFILLMENT OF THE REQUIREMENT FOR THE AWARD OF DOCTOR OF PHILOSOPHY DEGREE (PhD) IN MECHANICAL ENGINEERING

FEBRUARY 2013

DECLARATION

I hereby declare that this project work was written by me, and that it is a record of my own research study. It has not been presented in any other institution of higher learning for award of any degree.

All quotations and sources of information are to the best of my knowledge duly referenced.

_____ _____

AFOLAYAN MATTHEW OLATUNDE DATE

CERTIFICATION

This project entitled "**DESIGN AND DEVELOPMENT OF A BIOLOGICALLY INSPIRED HYPER-REDUNDANT ROBOT JOINT MECHANISM**" by AFOLAYAN MATTHEW OLATUNDE meets the regulations governing the award of Doctor of Philosophy in Mechanical Engineering of Ahmadu Bello University Zaria and is approved for its contribution to scientific knowledge and literary presentation.

_____ _____

Dr. D.S. Yawas Date
Chairman, Supervisory committee

_____ _____

Prof C.O. Folayan Date
Member, Supervisory committee

_____ _____

Prof S.Y. Aku Date
Member, Supervisory committee

_____ _____

Dr. M. Dauda Date
Head of Department

_____ _____

Prof A.A. Joshua Date
Dean, School of Postgraduate Studies

DEDICATION

This project is dedicated to God, the creator of heaven and the earth who saw me through, who heard my cries when nature refused to corporate with me; who consoled me and bailed me out when I had to bear the pain and memory of my late son, David and had to still keep moving. Lord all my life will be for your glory in Jesus name. Amen.

ACKNOWLEDGEMENT

I want to say thank you to all my supervisory committee: Dr. D.S. Yawas, Prof C.O. Folayan and Prof S.Y. Aku. I want to also thank the **MacArthur Foundation, Ahmadu Bello University Board of Research** and **STEP B** for their financial support of this work. I cannot forget the former Vice Chancellor, Professor S.U. Abdullahi for the special money he approved for me to buy some of the equipment I needed for this work.

I want to thank Dr. D.S. Yawas (chairman, supervisory committee) who has shown me the way even before he joined the supervisory committee. May the Lord of heaven remember you always and shine his light in your paths daily. Amen

I want to thank Prof C.O. Folayan for all his efforts at ensuring that I get the equipment for this work – volumes of letters were written and he took it upon himself to help me get the funding, may you always have and remain to give to all. Thanks for all your pastoral prayer too, especially when my BP was abnormal at the peak of my simulation, I will not forget those things you have done.

Prof S.Y. Aku has been someone who for a wonderful reason waded in to bail me out of supervisory quagmire I was in. He is the Nigerian equivalent of Japanese JIT – just in time. I and my colleagues have been wondering how he gets to package so much into so little and finite daily time. My write ups are out JIT, comments, JIT etc. I will always remember all the help rendered to me and my wife also while we sought for extra family funds in the name of employment, sincerely sorry for all you received while pursuing a cause not yours. It still touches my heart up till tomorrow.

I want to say thank you to late Prof Madakson whom I started this work with, your contributions to my life cannot be shoveled under the carpet; you really gave me the encouragement to start research in such an area many are shying away from. Thanks for the computer, personal counsel, concern about my progress, my family, health etc.

Prof Obi, Dr Pam, Dr Dauda, Dr Kulla, Dr (Mrs) Suleiman, Dr Anafi, Engr Malachi, Engr Laminu, Engr Alabi Abdulmumin, Engr Itonya and virtually all my other colleagues have shown practical interest in my progress, you are all wonderful to relate with. I shall not forget Tayo Ogunwede and Otopa Zubairu,

I greatly appreciate the following for their contributions; Dr Idris Abubakar of Civil engineering for helping me with ANSYS Multiphysis software, Dr Oricha for the Oscilloscope, Mr Matthew of Electrical Engineering laboratory for all his suggestions, Prof D.D. Yusuf for the journal material, suggestions, counsels, visitation etc to me. Bro Samuel Ohimakhare (UK) for sourcing the equipment for me from USA, Dr Akerejola for sourcing CoreChart software from Australia, Prof Ogundipe for all his practical counsel, Dr Azi Joseph (Industrial design) for sourcing my servo motors and parallax ping))) sensors and his counsels, Dr Henry Igbadun, Mr Owolabi and Mr Femi of Agric Engineering for all their counsel, prayer and encouragements. Big thanks go to a friend and counselor, Dr Akinsanmi (Electrical Engineering), he gave me the equipment I used for the rubber testing, it is nice to have you around at such a difficult time (academic, spiritual etc).

I want to express my gratitude to Dr Ati (Geography) for all his pastoral care and counsels, Pastor S.I.A Odeme (Deeper Life) for all his pastoral prayer for me and counsels also. I want to thank Pastor Elachi for his prayers and counsel, Bro Philemon and Dr Stephen of Civil engineering for their counsel, encouragements and prayers too. The Lord will surely not forget all your labour of love in Jesus name. Amen. I want to thank the brethren of Deeper Life Bible Church and other ministries too, who have made a mark upon my life by their godly concern for me.

My acknowledgment will be like a broken bridge without thanking Dr Z.O. Oyedokun (Namibia) and family for laying the foundation in my life and enabling me to

learn all I need to learn and experiment with digital equipment when he was in Nigeria - he was my mentor. He gave me practically all the knowledge, social re-orientation, spiritual re-acclimatization I needed in an academic world.

My parents are such a wonderful pair you will be amused to live with. They never see me as an independent individual but as a child that must receive counsel all the time, almost pampering me. I am grateful to God for always having them around. I will not forget my junior ones (Yinka, Bola, Tayo and Ayo) for all their concerns, counsel and especially their prayers, the good Lord heard it all, he will surely crown each of your concerns with a testimony in Jesus name, Amen. What shall I say of Jumoke (my sister in law) she did contribute her quota of concern to the work. I pray God will always remember you for all this too. I remember the likes of Kemi (a cousin), always proud that her cousin is into robotics, I am equally proud of you too as you make much progress in your works too.

I am at a loss on use of words on how to thank my precious wife (Moji) and my kids (Benjamin, Favour and Hannah) for all their patience with me, for bearing my frustrations, joy, ups, downs, exhilaration, tenebrous and disconsolate attitudes. My special thanks to Moji for all those sessions of prayers and fasting. And for the kids, each was practically helping me to press the computer keyboard while sitting on my laps (which is their favourite chair) when they were all very young and research had to proceed even while taking naps also on my laps. I didn't really have time to take them out as the work got hotter except to entertain them while working. Thank you for all the patience and understanding with daddy. My son designed and constructed his own snake robot ahead of my own to prove he understood the work daddy was doing!

Finally, I want to acknowledge those who are so mendacious in mind as to take it upon themselves to frustrate this work for whatever reasons that is best known to

them and of cause to God who created all too. May the Lord give you all another heart and open up your obscured reasoning. Amen.

ABSTRACT

This work presents a design and development of biomorphic hyper-redundant joint mechanism for robotic applications using carbon filled natural rubber. A *teleost* species of fish (a 394.1 mm Mackerel) was modeled using the biomorphic hyper-redundant joint developed. The control algorithm uses built in motion patterns and the path planning algorithm is sensor based; both were hosted within a single PIC18F4520 microcontroller. Three Futaba 3003 servomotors drive the joints under the control of the microcontroller control algorithm. Frequency softening test on the rubber used for the joints yielded a critical value of 25Hz at a temperature range of 33.8^{o} to 34.9^{o}. The joints were able to oscillate at a maximum of 4.3Hz in open air test and down to 1.7Hz when the robot was tested inside water. A test of the robot inside a body of water showed that the relationship between tail frequency and speed is not linear. Furthermore, the robot was able to attain a maximum linear speed of 0.985 m/s in the water. This speed is about 1/3 of that of a live mackerel and is attributed to the use of rubber in the tail design when compared to similar robots (Essex G9 and Japanese PFU series fish robots) by other researchers. The computer simulations predicted the maximum stress that the rubber for the joint will experience are $4.64kN/m^2$ and $9.24\ kN/m^2$ for the plywood material. Also, the design did not warp as predicted in the computer simulation especially as the oscillation did not reach the critical speed of 25Hz where the Payne effect will occur and cause frequency induced softening. The servo motors rating (0.29Nm) was adequate to handle the torque of 0.0000237Nm(at 0.5Hz) to 0.00088804Nm(at 1.7Hz) and at peduncle displacement of 90^{o} actually experienced by the robot while being tested. Furthermore, stability analysis indicates that the controller design is unstable when hydro dynamic drag is considered and marginally stable without it. The controller is also very sensitive to perturbation as implemented.

TABLE OF CONTENTS

		Page
TITLE PAGE		i
DECLARATION		ii
CERTIFICATION		iii
DEDICATION		iv
ACKNOWLEDGEMENT		v
ABSTRACT		viii
TABLE OF CONTENTS		ix
LIST OF FIGURES		xxi
LIST OF TABLES		xxx
LIST OF APPENDICES		xxxi
CHAPTER ONE	**INTRODUCTION**	
1.1	BACKGROUND	1
1.2	ROBOTICS	3
1.3	USES OF ROBOTS	5
1.4	ROBOTIC TRENDS	5
1.5	HYPER-REDUNDANT ROBOTS	8
1.6	ADVANTAGES AND DISADVANTAGES OF AN HYPER-REDUNDANT ROBOTS	9
1.7	EXAMPLES OF BIOLOGICAL HYPER-REDUNDANT BODIES	10
1.8	SCENARIOS WHERE HYPER-REDUNDANT ROBOT CAN PERFORM	11
1.9	STATEMENT OF THE PROBLEM	11
1.1 0	AIM AND OBJECTIVES	13
1.11	JUSTIFICATION	13
1.12	SCOPE OF THE RESEARCH	15

CHAPTER TWO LITERATURE REVIEW 16

2.1 JOINT DESIGNS 16

2.1.1 Robotic Joint Designs 16

2.1.1.1 Hyper-redundant robot joint implementations 16

2.1.2 Joint Types Found in Biological Models 19

2.1.2.1 Bony joints 19

2.1.2.2 Hydrostatic joints 19

2.2 ISOCHORIC NATURE OF HYDROSTATIC JOINTS 21

2.2.1 Sectional Isochoric Hydrostatic Joints/Support 21

2.2.2 Whole Body Isochoric Hydrostatic Joints/Support 22

2.3 BIOMECHANISM AND HYDROSTATIC JOINTS/SUPPORT 22

2.4 REVIEW OF SELECTED HYDROSTATIC SKELETONS MODELS 24

2.4.1 Leech - Hirudo Medicinalis 24

2.4.2 Tobacco Hornworm Caterpillar 26

2.4.3 Octopus Vulgaris 28

2.4.4 Tongues 31

2.4.5 Mammalian Penis 34

2.5 HYPER–ELASTICITY AND BIOLOGICAL MATERIALS 35

2.5.1 The Nature of Hyper – Elastic Materials 35

2.5.2 Hyper – Elastic Materials Mathematical Models (Constitutive Equations) 35

2.5.2.1 Neo–Hookean model 36

2.5.2.2 Mooney – Rivling model 37

2.5.2.3 Ogden model 37

2.5.2.4 Yeoh model 38

2.5.2.5 Polynomial model 39

2.5.3 Extensions To The Constitutive Equations and Modifying Factors 39

2.5.3.1 Temperature 40

2.5.3.2 Homogeneity of material 40

2.5.3.3 Compressibility 41

2.5.3.4 Mullin effect 41

2.5.3.5 Reinforcement 41

2.5.3.6 Cavitation 42

2.5.3.7 Payne effect 42

2.6 ADVANTAGES OF TRANSFORMING HYDROSTATIC JOINT AND SUPPORTS INTO ROBOTIC JOINTS 43

2.7 HYPER REDUNDANT ROBOTS 45

2.7.1 Mobile Hyper-Redundant Robots Such as Snake Robots and Serpentine Robots 45

2.7.2 Fixed Base Robots 45

2.8 SOME EXAMPLES OF HYPER REDUNDANT ROBOTS AND THEIR APPLICATION AREAS 45

2.8.1 Active Cord Mechanism (ACM) 45

2.8.2 GMD Robot 47

2.8.3 Carnegie Mellon University Elephant Trunk Robot. 47

2.8.4 Germany Sewer and Pipe Inspection Robot 48

2.8.5 Pneu-Worm Robot or Wormbot 49

2.8.6 NASA Snakebot 50

2.8.7 OBLIX and MOGURA 52

2.8.8 OmniTread 52

2.9 OTHER APPLICATIONS OF HYPER-REDUNDANT ROBOTS 55

2.9.1 Military Purposes 55

2.9.2 Medical Purposes (Minimally Invasive Surgery) 56

2.10 STRATEGIES USED FOR CONTROLLING HYPER-REDUNDANT ROBOT JOINTS 58
2.10.1 The Serpenoid Curve 60
2.10.2 Follow the Leader Approach 60
2.10.3 Built In Motion Pattern 61
2.11 PATH PLANNING 62
2.11.1 Roadmap 62
2.11.2 Tunnels 62
2.11.3 Local Sensor Based Planning. 62
2.11.4 Generalized Voronoi Graph (GVG) 63
2.11.5 Classical Planning 64
2.11.6 Motion Planning for Fixed Base Hyper-Redundant Robots 65
2.12 A REVIEW OF ACTUATORS FOR ROBOTIC JOINTS 65
2.12.1 Brief Description of Actuators 66
2.12.2 Tested Method of Actuating Hyper-Redundant Robots 68
2.13 REVIEW OF PAST WORK ON ROBOTIC FISH AS AN EXAMPLE OF HYPER-REDUNDANT ROBOTS 69
2.13.1 Robotuna 70
2.13.2 Robopike 71
2.13.3 Japanese PF-300, PF-600, PF-700,UPF-2001 Robotic Fishes 72
2.13.4 Essex G9 Robotic Fish 73

CHAPTER THREE DESIGN CONSIDERATIONS, THEORIES AND CALCULATION 75

3.1 DESIGN CONSIDERATIONS 75
3.1.1 Biomimicry 75
3.1.2 Simplified Control Scheme Of The Hyper-Redundant Joints 75
3.1.3 Simplified And Functional Joint Design 76

3.1.4 Material Selection 76

3.1.5 Capturing The Model Geometry/Design 76

3.2 FRAMEWORK FOR THE HYDROSTATIC JOINTS 76

3.2.1 Description Of The Rubber Based Artificial Hydrostatic Joint 77

3.2.2 Kinematics Of The Model 78

3.2.3 Comparison Of The Two Diamond Design 79

3.2.4 Strength And Weakness of the Evolved Artificial Hydrostatic Joint 80

3.3 ADAPTATION OF THE ARTIFICIAL HYDROSTATIC JOINTS TO A FISH MODEL 81

3.3.1 Selection Of A Biological Hyper-Redundant Body Model 81

3.3.2 Selection Of A Fish Model 81

3.3.3 The Active Joint Area Of The Fish Model 82

3.3.4 Description Of The Hydrostatic Joint Mechanism As Adapted for the Fish Model 82

3.4 MATERIALS SELECTION 90

3.4.1 List Of Materials 90

3.4.2 Description Of The Materials 90

3.5 COMPONENT DESIGN 91

3.5.1 Finite Element Analysis (FEA) for General Simulation 92

3.5.2 Stress Within An Elastomer (Rubber) 93

3.5.3 Stress Within The Plywood Material 93

3.5.4 Forces Experienced By A Moving Foil (Or Plate) Inside Water 94

3.5.5 Forces On Rings 95

3.5.6 Bending Stress Within A Cantilevered Object 95

3.5.7 Stress in a Cable 96

3.5.8 Tensile Stress Within a Glue 96

3.5.9 Large-Amplitude Elongated-Body Motion Theory 97

3.5.10 Mullins Effect – Preconditioning 98

3.5.11 Payne Effect – Frequency Induced Softening 99

3.5.12 Power Requirements of an Electric Motor 100

3.6 CALCULATIONS OF FORCES AND LOADS EXPERIENCED BY THE COMPONENTS 101

3.6.1 Component: Rings. 101

3.6.2 Component: Quarter Pulleys 102

3.6.3 Component: Nylon Cable 103

3.6.4 The Wooden Supports, Rubber Stripes and the Fin for the Peduncle 104

3.6.4.1 Parameters that were simulated 104

3.6.4.2 Setup of the finite element tool and the constraints used for the simulation 105

3.6.5 The Servo Motor 112

3.6.6 The Battery Size Required 114

3.6.7 The Rubber Joints; Estimating the Mullins Effect 115

3.6.8 The Rubber Joints; Estimating the Payne Effect 115

3.7 STABILITY AND SENSITIVITY ANALYSIS OF THE ROBOTIC FISH DEVELOPED 117

3.7.1 The Hydrodynamic Drag 118

3.7.2 Teleost Fish Swimming Equation 118

3.7.3 Derivation Of The Mathematical Model And Transfer Function Of The Fish Model 119

3.7.3.1 The servo motor 119

3.7.3.2 The hydrodynamic drag 119

3.7.3.3 The rubber joint resistance to bending 120

3.7.3.4 The tail fin resistance to paddling 120

3.7.4 Mathematical Model Of The Robotic Fish 120

3.7.5 Stability Response Of The Robotic Fish Control 122

3.8 RESULTS OF THE CALCULATIONS AND SIMULATIONS 125

3.8.1 Forces On Rings 125

3.8.2 Bending Stress Experienced By The Haul 126

3.8.3 Stress The Cables Will Experience 126

3.8.4 The Forces Acting On The Quarter Pulleys 126

3.8.5 Tensile Stress Within The Glue 127

3.8.6 Stress Within The Rubber Joints 128

3.8.7 Stress Within The Plywood Material 132

3.8.8 Maximum Stress Within The Fin 132

3.8.9 Test For Warping/ Bending Result 133

3.8.10 Frequency Induced Softening 133

3.8.11 Result Of Dynamic Torque / Motor Loads For Various Mode (Frequency, Angle Of Oscillation) Of The Peduncle 139

3.8.12 The Battery Requirement To Drive The Servo Motor 141

3.8.13 Stability Response Of The Robotic Fish Control 141

3.8.14 Sensitivity Of The Robotic Fish Control 142

CHAPTER FOUR CONSTRUCTION PROCESSES AND PERFORMANCE EVALUATION OF THE FISH ROBOT 143

4.1 CONSTRUCTION SEQUENCE 143

4.2 CONSTRUCTION PROCESS OF THE HARDWARE 143

4.3 FIRMWARE (SOFTWARE) CODE ASSEMBLY 162

4.3.1 Development Environment 162

4.3.1.1 Integrated development environment (Microchip MPLAB v8.56.00 IDE) 162

4.3.1.2 Assembler (MPASM Assembler v5.37) 162

4.3.1.3 Linker (MPLINK Object Linker v4.37) 162

4.3.1.4 Library (MPLIB v4.37) 162

4.3.1.5 Debugger (MPLAB SIM and PICkit 2) 162

4.3.1.6 Programmer (PICkit 2) 163

4.3.1.7 Clock (8MIP or 32Mhz) 163

4.3.1.8 Operating system (OS) - Windows 7 Home Basic, 6.1.7601.2 SP1 163

4.3.1.9 Oscilloscope (TFD Scope v2.0 http://www.adrosoft.com) 163

4.3.1.10 Logic analyzer (MPLAB SIM Simulator logic analyzer) 163

4.3.2 Capabilities Built Into The Robot Firmware 164

4.3.3 Description Of The Robot Firmware 164

4.3.3.1 The firmware generalize flowchart 164

4.3.3.2 Bump switch based obstacle detection subroutine flowchart 165

4.3.3.3 Ultrasonic based obstacle detection subroutine flowchart 165

4.3.3.4 Human override subroutine flowchart 167

4.3.3.5 The tail oscillation amplitude control subroutine flowchart 169

4.3.3.6 The speed of oscillation control subroutine flowchart 171

4.3.3.7 The turning subroutine flow chart 172

4.3.3.8 Pulse width modulator (PWM) protocol generator 174

4.4 THE LABORATORY TESTS 177

4.4.1 Test On The Pulse Width Modulation (PWM) Code Generation 177

4.4.1.1 Equipment used 178

4.4.1.2 Test procedure 178

4.4.2 Test For The Microcontroller Concurrent Pulse Width Modulation (PWM) Code Generation 178

4.4.2.1 Equipment used 179

4.4.2.2 Test procedure carried out 179

4.4.3 Test For Establishing Correct Angular Displacement (Swing) Of The Motor 179

4.4.3.1 Equipment used 179

4.4.3.2 Test procedure 180

4.4.4 Test Of The Sonar Sensor. 181

4.4.4.1 Equipment used 181

4.4.4.2 Test procedure 182

4.4.5 Test Of The Bump Sensor Routine And Performance 183

4.4.5.1 Equipment used 183

4.4.5.2 Test procedure 183

4.4.5.3 Equipment used 184

4.4.5.4 Test procedure 184

4.4.6 Test of the Human Override Control i.e. the Remote Control 185

4.4.6.1 Equipment used 186

4.4.6.2 Test procedure 187

4.4.7 Test For Motion Pattern 187

4.4.7.1 Equipment used 189

4.4.7.2 Test procedure 189

4.4.8 Test For Water Leakages 189

4.4.8.1 Equipment used 189

4.4.8.2 Test procedure 189

4.5 FIELD TESTS 190

4.5.1 Experimental Conditions – Water Tank 190

4.5.1.1 Equipment required for the experiment in the water tank 190

4.5.1.2 Test procedure 191

4.5.2 Experimental Conditions – Shallow Pond 192

4.5.2.1 Equipment used 192

4.5.2.2 Test procedure 192

CHAPTER FIVE RESULTS AND DISCUSSIONS 196

5.1 LABORATORY TEST RESULTS 196

5.1.1 Result Of Test On The Pulse Width Modulation (PWM) Code Generation 196

5.1.2 Result Of Concurrency PWM (Pulse Width Modulation) Code Generation 196

5.1.3 Result Of The Test For Correct Angular Displacement (Swing) Of The Motor 197

5.1.4 The Result Of The Test On The Sonar Sensor 197

5.1.4.1 The result of the test on the sonar sensor in the air 197

5.1.4.2 The result of the test on the sonar sensor in the water 198

5.1.5 Result Of The Test Of The Bump Sensor Routine And Performance 198

5.1.5.1 The switch debounce test result 198

5.1.5.2 Activation load test result 200

5.1.5.3 Foam compression test result 200

5.1.6 Result Of The Test Of The Human Override Control 201

5.1.7 Test For Motion Pattern 201

5.2 RESULT OF THE FIELD TESTS 203

5.2.1 Tail Oscillation Speed 203

5.2.2 Dynamic Turning (Turning While Swimming) 203

5.2.3 Amplitude Of Oscillation Of The Tail 204

5.2.4 Sharp Turning 204

5.2.5 Swimming Speed At Different Peduncle Amplitude And Different Tail Frequencies 204

5.2.6 Maximum Linear Speed 205

5.2.7 Other Field Test Result 205

5.3 DISCUSSION OF THE LABORATORY TESTS RESULTS 205

5.3.1 Pulse Width Modulation (PWM) Code Generation 205

5.3.2 Concurrent Pulse Width Modulation (PWM) Code Generation 206
5.3.3 Angular Displacement (Swing) Of The Motor 206
5.3.4 The Sonar Sensor 206
5.3.4.1 The test of the sonar sensor in the air 206
5.3.4.2 The test of the sonar sensor in the water 206
5.3.5 The Bump Sensor Routine And Performance 206
5.3.5.1 The switch debounce test 206
5.3.5.2 Activation load test 207
5.3.6 The Human Override Control 209
5.3.7 Discussion On The Test For Motion Pattern 209
5.4 DISCUSSION OF THE FIELD TESTS RESULTS 210
5.4.1 Tail Oscillation Speed 210
5.4.2 Dynamic Turning (Turning While Swimming) 210
5.4.3 Amplitude Of Oscillation Of The Tail 210
5.4.4 Sharp Turning 211
5.4.5 Swimming Speed At Different Peduncle Amplitude And Different Tail Frequencies 211
5.4.6 Maximum Linear Speed 212

CHAPTER SIX CONCLUSIONS AND RECOMMENDATIONS 213
6.1 CONCLUSIONS 213
6.2 RECOMMENDATIONS 214

REFERENCES 215
APPENDICES 234

LIST OF FIGURES

		Page
Figure 1.1	Examples of Biomimetic robots	6
Figure 1.2	The meaning of 1, 2 and 3 degree of freedom (DOF) mechanism	9
Figure 1.3	An hyper-redundant bodies have large possible configurations without any constraints.	9
Figure 1.4	Examples of biological hyper-redundant bodies	11
Figure 2.1	Hyper-redundant robot joint type and their implementation	17
Figure 2.2.	Generalized oblique mechanism	19
Figure 2.3	Examples of joints found in vertebrates	20
Figure 2.4	Segementally isochoric Leech body.	21
Figure 2.5	Manduca sexta Caterpillar.	22
Figure 2.6	Manduca sexta Caterpillar body have internally connected chambers	22
Figure 2.7	Muscle layouts in Muscular Hydrostat	24
Figure 2.8	Picture of a leech	24
Figure 2.9	Compartmentalized cylindrical model of a leech.	25
Figure 2.10	The ventral interior longitudinal (VIL) muscle of M. Sexta.	27
Figure 2.11	Similarity in the pseudo-elastic behaviour of the VIL of Manduca Muscle (A) and Carbon-black-reinforced natural rubber (B) during loading and unloading	28
Figure 2.12	A multi-segment model of an octopus arm	30
Figure 2.13	The torus model used in modeling Aplysia Californica	32
Figure 2.14	A chameleon hyoid. Source	32
Figure 2.15	Dorso-Ventral model of Python molurus – packed and extended	33
Figure 2.16	Dynamic sinusoidal loading superimposed on a large mean strain in an elastomer	40
Figure 2.17	Stress-softening effects in the transverse vibrational frequency of a bio-material membrane. (f = frequency of vibration, α = preconditioning extent, γ=a dimensionless constant, λ=stretch.	43

Figure 2.18	Some Hirose's Active Cord Mechanism (ACM).	46
Figure 2.19	Paap's GMD Snake crossing an obstacle.	47
Figure 2.20	Urban Search and Rescue elephant trunk robot with camera on its end	48
Figure 2.21	MAKRO an autonomous robot for sewer inspection	49
Figure 2.22	Pneu-Worm Robot	50
Figure 2.23	NASA Snakebot A) closer view of the robot. B) Field test of the robot	51
Figure 2.24	Yim's Polybot Robot as used by NASA.	51
Figure 2.25	OBLIX and MOGURA in different configurations	53
Figure 2.26	Conditions for the waterwheel grinding operations, men have to enter to grind with hand	53
Figure 2.27	Configuration of the MOGURA system when used for grinding operations	54
Figure 2.28	OmniTread 8"	54
Figure 2.29	OmniTread 4" with the segment internals on the left.	55
Figure 2.30	An endoscope (A) The endoscope device (B) The endoscope is being inserted behind a pig heart	57
Figure 2.31	Nereis diversicolor: A) Slow and B) Fast crawling.	58
Figure 2.32	A snake equipped with EMG and normal force detectors	59
Figure 2.33	Snake motion (A) Sinus Lifting to reduce friction (B) Sketch of normal force distribution about the sinus	59
Figure 2.34	Serpenoid curves showing pattern as the snake take turns to left, right and forward motion	60
Figure 2.35	The ticked line segments are the planar GVG for the bounded environment	64
Figure 2.36	Laser crosshair projector	65
Figure 2.37	Robotuna	70
Figure 2.38	Robotuna tail construction	71
Figure 2.39	Robopike	71

Figure 2.40	Robopike spiral spring exoskeleton of the tail section.	72
Figure 2.41	PF-300 robot	73
Figure 2.42	PF-2001 robot	73
Figure 2.43	Essex G9 robotic fish	74
Figure 2.44	Mechanical Configuration of the Essex Robot Fish	74
Figure 3.1	Diamond design of the evolved joint – short and long elastomer designs	77
Figure 3.2	The diamond design - cross-section of the model	78
Figure 3.3	Kinematics of the diamond designs	78
Figure 3.4	The minimum radius of curvature of the joints	79
Figure 3.5	3-Dimensional motions capabilities about other axis	80
Figure 3.6	Cantilever of multiple links	80
Figure 3.7	A lateral view of the Mackerel used for this project.	84
Figure 3.8	The CAD model of the Mackerel shown in figure 4.6. – not to scale	84
Figure 3.9	Isometric CAD view of the haul (front rigid part) – not to scale	84
Figure 3.10	Isometric CAD view of the tail section (flexible part) – not to scale	84
Figure 3.11	The critical dimensions (in mm) of the model	85
Figure 3.12	CAD model of the hydrostatic joints showing cables connected to the first segment only.	87
Figure 3.13	How the tail fin will respond as the servomotor pull on the cables	88
Figure 3.14	The detail design of the cable showing one side only	89
Figure 3.15	The ring geometry	90
Figure 3.16	Instantaneous force and velocity component of an active tail fin	98
Figure 3.17	Experimental elastomer membrane subjected to stress induced softening	99
Figure 3.18	A fish peduncle	105
Figure 3.19	Uniaxial tensile test data plotted using ANSYS multiphysis 10	106

Figure 3.20	Biaxial tensile test data plotted using ANSYS multiphysis 10	107
Figure 3.21	Mooney-Rivling parameter constitutive equation used within the ANSYS 10 shows very close prediction of the rubber sample behavior. It means that Mooney-Rivling parameter can be safely used for the Finite element analysis of the rubber sample.	108
Figure 3.22	Optimized ANSYS 10 generated mesh pattern used for the finite element analysis.	109
Figure 3.23	The simulation inputs: 0.001N on the fin, 0.00141421N (vector sum of 0.001N –z axis and 0.001 N - x axis) on the plywood support.	111
Figure 3.24	Simulated input loads – plan and side views. The finite element tool determines the centroid of the area.	111
Figure 3.25	The precision frequency induced machine assembled for the frequency induced softening test	116
Figure 3.26	The geometrical parameter used in modeling the robotic fish	117
Figure 3.27	The SIMULINK block diagram of the robotic fish model	120
Figure 3.28	Step response of the robotic fish control system	122
Figure 3.29	Nyquist Diagram for the robotic fish control system	123
Figure 3.30	Pole-Zero Map Diagram for the robotic fish control system	123
Figure 3.31	Bode diagram for the robotic fish control system	124
Figure 3.32	Nyquist Diagram for the robotic fish motor control system (equivalent to behaviour outside water – no hydrodynamic drag)	124
Figure 3.33	Impulse response of the robotic fish control system	125
Figure 3.34	The contact analysis of the composite material. All the glued contacts show a complete sticking which implies that the weight and loads will be spread/absorbed properly.	127
Figure 3.35	Simulation Result – von Mises stress acting within the peduncle using the simulated loads	128
Figure 3.36	The maximum and minimum stress within the rubber used for the joints	129
Figure 3.37	von Mises stress within the peduncle under its own static weight.	130
Figure 3.38	The load distributions on the tail due to the components weights	131
Figure 3.39	The maximum and minimum stress within the plywood support	133

Figure 3.40	Simulation Result – Directional deformation – It shows vertical straight patterns. The top view further shows the evidence of rigid non warping bending. The implication of this is that a rigid support is guaranteed for the Hydrostatic skeleton.	134
Figure 3.41	Lag at 0.5Hz frequency of oscillation.	135
Figure 3.42	Lag at 1Hz frequency of oscillation.	135
Figure 3.43	Lag at 5Hz frequency of oscillation.	136
Figure 3.44	Lag at 10Hz frequency of oscillation.	136
Figure 3.45	Lag at 15Hz frequency of oscillation.	137
Figure 3.46	Lag at 20Hz frequency of oscillation.	137
Figure 3.47	Lag at 25Hz frequency of oscillation.	138
Figure 3.48	Lag at 30Hz frequency of oscillation.	138
Figure 3.49	Different room temperature at which test was carried out.	139
Figure 3.50	Progressive drops in response time with increasing frequency	139
Figure 3.51	Torque developed at different peduncle oscillation frequency and swing angle	141
Figure 4.1	The assembled fish robot	150
Figure 4.2	The rings (**A**) for building the robot haul which are then glued together to form the front part of the robot fish (**B**).	151
Figure 4.3	Assembling the bump detector on the haul	152
Figure 4.4	The cone holds the ultrasonic sensors – the receiver is at the tip and the transmitter is at the top.	152
Figure 4.5	The haul with foundation coating of TOP BOND® wood glue	153
Figure 4.6	The haul with wood glue soaked fine sawdust ~3mm	153
Figure 4.7	Microwave oven being used for preliminary drying at 5 min at 100watt.	154
Figure 4.8	The bump switch was waterproofed with the haul using silicone rubber.	154
Figure 4.9	The slabs used for building the robot tail support structures according to drawing nos 6 to 11	155
Figure 4.10	Kings tire rubber tube used (size=165/175-13)	155

Figure 4.11	The rubber is cut according to the dimensions taken from drawing nos 12 to 16. The first 2 stripes from the tail fin (left on this picture are 20mm wide and the remaining ones are 25mm wide).	155
Figure 4.12	The quarter pulleys and unplasticized PVC tubings glued in place	156
Figure 4.13	The fin, made from plywood board.	156
Figure 4.14	The rings – half ring pairs used for the tail contour	157
Figure 4.15	The head board	157
Figure 4.16	Water proofing the servomotor.	158
Figure 4.17	The battery before (A) and after (B) it was covered with epoxy glue.	158
Figure 4.18	The Li-Po battery were glued to the side of the motors, 2 per side, viewed from the side	159
Figure 4.19	The Li-Po battery were glued to the side of the motors, 2 per side, viewed from above	159
Figure 4.20	The half rings glued to the supporting board with epoxy glue	160
Figure 4.21	The three servomotors are connected serially and then glued to the head board	160
Figure 4.22	The final tail assembly	160
Figure 4.23	The assembled electronic and controller parts showing the remote control receiver (A), the microcontroller board (B), the inputs diode board (C), the programmer/debugger connectors (D)	161
Figure 4.24	The electronic and controller after covering with silicone.	161
Figure 4.25	The finished electronic and controller assembly is placed externally to the haul, just at the middle of the robot	161
Figure 4.26	The generalized flow chart of the firmware controlling the robot.	165
Figure 4.27	Bump switch based obstacle detection subroutine	166
Figure 4.28	Ultrasonic based obstacle detection subroutine	167
Figure 4.29	Human override control subroutine	168
Figure 4.30	Tail oscillation amplitude control routine	170
Figure 4.31	Tail oscillation speed control routine	171
Figure 4.32	Turning routine	172

Figure 4.33	Concurrent Pulse Width Modulator (PWM) generation routine	174
Figure 4.34	An exaggerated illustration of lag present in the concurrent PWM generator.	176
Figure 4.35	PWM control protocol for Futaba remote control servomotors.	178
Figure 4.36	Angular displacement measurement setup using protractor	180
Figure 4.37	The setups (A and B) used to test the ultrasonic sender and receiver fidelity.	182
Figure 4.38	The micro switch used for the bump sensor	184
Figure 4.39	Measuring the force required to activate the bump switch	185
Figure 4.40	The modified remote control transmitter and receiver	186
Figure 4.41	Teleost fish swimming pattern – tail amplitude increases toward the tail fin	188
Figure 4.42	Sharp turning behavior	188
Figure 4.43	The tail and servomotors are placed inside a bucket of water for test against water leakages and soaking of wood.	190
Figure 4.44	The robot inside the wooden water tank	191
Figure 4.45	Static picture of the robotic fish swimming in the shallow pond of Ahmadu Bello University Faculty of Engineering quadrangle pond.	193
Figure 5.1	Oscilloscope output of the microcontroller generating the PWM	196
Figure 5.2	Logic analyzer output of the microcontroller generating 3 concurrent pulse width modulated signal	197
Figure 5.3	Oscilloscope displaying the undebounced micro switch signal output. Signals from 0-20ms and 30-100ms are artifact due to the 50Hz power line	198
Figure 5.4	Spectrum analyzer display of the undebounced micro switch signal output	199
Figure 5.5	A plot of force to activate the left and right bump switch	200
Figure 5.6	A plot of force to activate the left and right bump switch	201
Figure 5.7	Result of the motion pattern	202
Figure 5.8	Pause/coasting mode – in this mode, the robot is straighten up, the servomotors are receiving commands to turn their horns to 90^{o} and	203

	remains at it.	
Figure 5.9	Speed of robot against peduncle (last segment) oscillation at different peduncle amplitude	205
Figure 5.10	Relationship between swim speed and tail flapping speed.	212
Figure A1	a) Ball-Socket-Tendon Design b) Closer View c) Another Closer view d) Cross-section of the model	234
Figure A2	Spinal-Chord / Bead Model a) Top View b) Perspective view b) Cross-section of the model	234
Figure A3	Ball-Socket-Tendon Design Kinematics	235
Figure A4	Spinal-Chord/Bead Model Kinematics	236
Figure A5	Tree climbing robot	237
Figure A6	Underwater devices in form of fish	238
Figure A7	Snake/serpentine robot can be assembled from the artificial hydrostatic joint	238
Figure A8	A rod shape endoscope with section bearing different payload (equipment). It can be self propelling if actuators are attached.	239
Figure A9	A short and sturdy design can be used as manufacturing arm	240
Figure B1	The Lateral and dorsal view of the life Mackerel used in the modeling	241
Figure B2a	Projecting the mackerel image on a board and tracing it out (scale 1:1)	242
Figure B2b	Projecting the mackerel image on a board and tracing it out (scale 1:1) - continuation	242
Figure B2c	Projecting the mackerel image on a board and tracing it out (scale 1:1) – continuation	243
Figure B3	CAD model of the live fish after copying it – here the tail has not being covered. The life fish lateral view is displayed again as a show of the precision of the translation process	243
Figure B4	The dimensions of the rings used for the haul.	243
Figure C1	The frequency loss determination equipment	244
Figure C2	Closer view of the test board	245
Figure C3	The DAQ signal accessories (Left) showing its interfacing to a	246

	computer (Right)	
Figure C4	Signal pattern showing presence and absence of sample rubber.	246
Figure C5	Linear motor design and its component	247
Figure C6	Linear motor components dimensions.	247
Figure C7	Expanded view for header inertia at 0.5Hz	248
Figure C8	Expanded view for header inertia at 1Hz	249
Figure C9	Expanded view for header inertia at 10Hz	249
Figure C10	Expanded view for header inertia at 15Hz	250
Figure C11	Expanded view for header inertia at 25Hz	250
Figure C12	Circuit diagram of the motor driver	251
Figure C13	Internal design of the displacement sensor	253
Figure C14	The Spectral Plus 5.0 Signal Generator software interface showing the dialog boxes for the signal frequency and type setting. Inset is the timing for the selected setting.	255
Figure C15	National Instrument VI Logger interface – showing result at 25Hz input frequency	255
Figure C16	Signal pattern showing presence and absence of sample rubber	257
Figure E1	Parallax ping))) exemplifies commercial piezo sensor	269
Figure E2	The signal response of matched piezo crystal transmitter and receiver	270
Figure E3	Watch Buzzer crystal plates	271
Figure E4	The response of watch buzzer plates to various input frequencies.	271
Figure E5	Watch buzzer plate radiation is in all direction	272
Figure E6	Radiation pattern of Parallax ping)))	272
Figure E7	Transmitter-receiver pair using buzzer plate piezo crystals	273

LIST OF TABLES

		Page
Table 3.1	Some common family member of teleost species of fish with their peak speed, average body length, speed to length ratio (V/L)	83
Table 3.2	Forces within the rings for building the hauls	101
Table 3.3	Forces acting on the quarter pulleys	102
Table 3.4	Stress within the Nylon cable	103
Table 3.5	Simulated inputs loads for the finite element analysis and how they were derived	110
Table 3.6	Estimating the motor requirements	112
Table 3.7	Calculating the dynamic torque for 1Hz oscillation speed	113
Table 3.8	Other parameters used in simulating the control action of the robotic fish.	117
Table 3.9	The maximum and minimum stress within the rubber joints	129
Table 3.10	The weights and centroid of action of the rubber joints and the supports	131
Table 3.11	The maximum and minimum stress within the plywood support	132
Table 3.12	Summary of dynamic torque developed as a function of angle of oscillation and its frequency (medium is water of density=990kg/m3)	140
Table 4.1	Step by step construction process of the hardware	143
Table 4.2	The 16 possible combinations a 4 bit can generate. The counting start from 0	169
Table 4.3	Bill of Quantities	
Table F1	Polyurethane foam association IFD table	276

LIST OF APPENDICES

APPENDIX A	HYDROSTATIC JOINTS	223
APPENDIX B	TRANSLATING THE LIFE MACKEREL MODEL TO A CAD MODEL	231
APPENDIX C	THE FREQUENCY LOSS PATTERN MACHINE	235
APPENDIX D	CODE LIST (PSEUDO CODE) USED IN THE ROBOT FIRMWARE	250
APPENDIX E	PIEZO CRYSTAL BASED ULTRASONIC SENSORS – POSSIBLE REASONS WHY ITS NOT WORKING	260
APPENDIX F	INDENTATION FORCE DEFLECTION (IFD) UNIT	266
APPENDIX G	INTERPRETING THE NYQUIST DIAGRAM	278

CHAPTER ONE

INTRODUCTION

1.1 BACKGROUND

In 1921 - the term "robot" was first used in a play called "R.U.R." (that is "Rossum's Universal Robots") by the Czech writer Karel Capek (Ceska, 2011). This play has led to *many science fiction* writers emerging of which the most well know is Isaac Asimov (Isaac, 1950) who propagated the three laws of robotics as earlier as 1942 and reinstated them in all his science fiction books.

Robots are defined as "*reprogrammable, multifunctional manipulators designed to move material, parts, tools, or specialized devices through various programmed motions for the performance of a variety of tasks*" (Robot Institute of America, 1979) (now renamed Robotic Industries Association – www.robotics.org). Another definition from the Webster dictionary says it is an automatic device that performs functions normally ascribed to humans or a machine in the form of a human. This definition is not too concise as some hazardous functions cannot be done by human beings at all (like handling radioactive waste) and many robots do not have the form or shape of human being at all.

According to Igor (2005), no robot maker has the same definition of what a robot is, all the organization interviewed at RoboNexus 2005 robot exhibition has their own definition of what a robot is supposed to be. Furthermore, there is no consensus on which machines qualify as robots but there is general agreement among experts, and the public, that robots tend to do some or all of the following: move around, operate a mechanical limb, sense and manipulate their environment, and exhibit intelligent behavior — especially behavior which mimics humans or other animals. A robot is a

mechanical device that can perform physical tasks. A robot may act under the direct control of a human (e.g. the robotic arm of the space shuttle) referred to as telerobotic or autonomously under the control of a pre-programmed computer. Autonomy is a key difference between a robot and a remote control gadget, it is the application of artificial intelligence to machine operations. Robots may be used to perform tasks that are too difficult for humans to do directly (e.g. arm disposal, hazardous waste cleaning) or may be used to automate repetitive tasks, which are performed more cheaply by a robot than by the employment of a human (e.g. automobile production).

Robotics has its roots in automatic control, that is, human quest for freedom to have all things done for him at his wish or command. The first recorded attempt was around 350B.C or 450BC by Greek mathematician, Archytas of Tarentum who built a mechanical bird dubbed "the Pigeon" that was propelled by steam. It serves as one of history's earliest studies of flight, not to mention probably the first model airplane. Another one was in 270BC by an ancient Greek engineer named Ctesibus who made organs and water clocks with movable features (James, 2005 and Robotshop, 2008).

Robot development over the years has ranged from toys to space probes and the planet surface explorer, from completely mechanized humanoid to the highly computerized Honda ASIMO and Sony AIBO. In advanced economies, robotic arms have replaced humans in many manufacturing processes because of their consistent precision, absence of fatigue, zero pay and pay rise (except maintenance costs). The scale has now ranged from very large and elaborate space lab arms to nanorobots (Bjorn, 2005) that require microscopes to even view them. Applications range from the hazardous to entertainment, routine jobs like welding and expert works like invasive surgery. The truth of robots capability ranges from fictitious (like star war robots) to makeup ones like the vision based robots – for most are at their infancy but almost all

their makers announce their result as if there is no more need for research in that area – personal opinion. Hundreds of research centers and laboratories, universities, and government agencies as well as industrial giants and startup are into various researches related to robotics.

1.2 ROBOTICS

Robotics is the science and technology of robots, their design, manufacture, and application. Robotic researches are either abstract or biomimetic (biologically inspired). The biologically inspired robots imitate some characteristics of life forms such as mobility (Brooks, 1989), vision (Srinivasan, 1992; Harrison and Koch, 2000; Brett et al, 2003; Zufferey and Floreano, 2005), flying (Srinivasan et al, 2004; Zufferey and Floreano, 2005; Park et al, 2007) and navigational methodology. Biomimetic systems are greatly desired because natural systems are highly optimized and efficient. Srinivasan (1992) calls them shortcuts to mathematically complex issues of life. Take a look at the fly or honey bee. They have very small brain and processing power but no literature has a robot with such visual capabilities like them. Nearly all the five senses of living being i.e. sight or vision (Srinivasan et al, 2004; Zufferey and Floreano, 2005), hearing and touch (http://world.honda.com/ASIMO/ and http://www.sony.net/Products/aibo /index.html), smell - (Grasso, 2000) and taste (http://www.21stcentury.co.uk/ robotics/nomad.asp) are imitated. Zufferey and Floreano (2005) semi-autonomous indoor airplane was only possible because of its mimicry of insect vision using optical flow. The abstract ones are designed to solve specific problems and mostly use the most sophisticated and expensive hardware available. Of these categories are industrial assembly robots. Their design is a direct solution to problem ahead without an attempt to shortcut it, i.e. formal

methods and formal specification are used for designing such robots especially where safety and no failure are important.

Robotics requires a working knowledge of electronics, mechanics, and computer programming. Furthermore, the "development of either biomimetic or biohybrid systems requires a deep understanding of the operation of living systems" according to Convergent Science Network (CSN, 2011).

Robots can be grouped generally as mobile robots (e.g. autonomous vehicles) or manipulator robots (e.g. industrial robots). A list of specific research areas related to robotics is:

1. Behavior based robotics
2. Developmental robotics
3. Epigenetic robotics
4. Evolutionary robotics
5. Cognitive robotics
6. Robot control
7. Automated planning and scheduling
8. Mechatronics
9. Neural networks
10. Cybernetics
11. Artificial consciousness
12. Telerobotics / Telepresence
13. Nanotechnology and Micro-Electrical Mechanical Systems (MEMS)
14. Swarm robotics
15. Robot software

To improve intelligence, knowledge database with inference engine for artificial intelligent programmes exist (Lenat, 1995; Witbrock et al., 2005) such that people all over the world can contribute their common knowledge. An example is the Cyber Corps (CYC) located at http://www.cyc.com/ and is supported by several a number of

organizations such as Microsoft, Apple, Bellcore, Digital Equipment Corporation, US Department of Defense, Interval, and Kodak (Kalev, 2002).

1.3 USES OF ROBOTS

According to Lilianes (2000), some uses of robots include:

1. **Domestic** – Vacuum Cleaner (Irobot's Scooba and Roomba robots.), Errand boy (Honda ASIMO) and Sony's AIBO), Lawn mower, cooking.
2. **Military** – Autonomous Vehicles by Defense Advance Research Project Agency of USA (DARPA), Park robot (used in Afghanistan cave fights)
3. **Industrial** – Industrial arms too numerous to mention. Example is Puma.
4. **Health** – Robot assisted invasive surgery.
5. **Information** - webots, spybots, ircbots used on the internet. Google incorporation uses webot (or webcrawler) for searching and indexing webpages.
6. **Entertainment** or Social robots aim to interact and provide companionship to people. Example of social robots are Ludobot and Wakamaru, Toyota humanoid robot,
7. **Space**, Luna and Mars explorers
8. **Research** - Arrick robots, Leggo robots
9. **Civil purposes**, rescue, road construction
10. **Agriculture** – Harvesting such as picking fruits and repetitive task such as welding (Dohi et al., 2002 and Hirakawa et al., 2002),
11. **Automated Guided Vehicles** (AGVs) are moveable robots that are used in large facilities such as warehouses, hospitals and container ports, for the movement of goods.

1.4 ROBOTIC TRENDS

According to Lilianes (2000), biomimetic robots, evolutionary robots, emotion controlled robots are ideas imitating life with different approaches but with a common goal of improving the adaptivity and learning capabilities of robots, 'breeding' a new generation of robots with better 'survival' chances in their specific operational environments. Another area of technological challenge for the next decade is the

development of microrobots and nanorobots for medical applications (http://www.robovectors.com/trends.html). Robots for cleaning clogged blood vessels or repairing damaged tissues are still to be developed. But still the biggest challenge in robotics for the next decade will be how to find the proper balance between human assisted systems and fully autonomous ones, thus to combine technological capabilities with social expectations and requirements. Several functional biologically inspired robots are already in service (Meyer and Guillot, 2008). Figure 1.1 shows a gallery of some existing biomimetic robots.



(A) Sony Aibo – modeled after dog



(B) A robot modeled after lobster



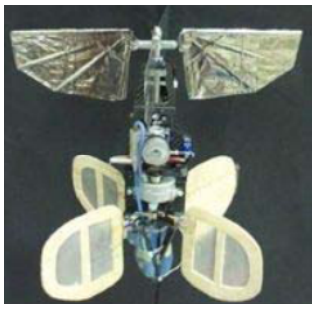
(C) Dinosaur – an example of robotic toy



(D) Toyota Flute playing robot – an example of an android



(E) Robot modeled on dragon



(F) Another flapping wing robot

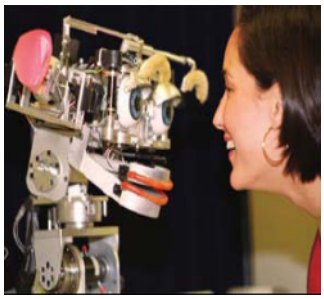
Figure 1.1 Examples of Biomimetic robots – (Meyer and Guillot, 2008)



(G) An android, Geminoid HI-1, developed by the ATR Intelligent Robotics and Communication Laboratories



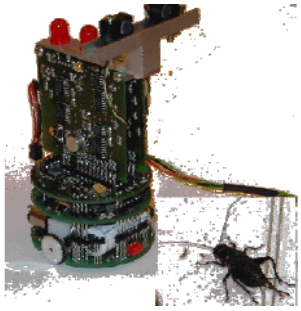
(F) A gynoid, Face robots, developed at the Science University of Tokyo



(H) An humanoid: Kismet from MIT



(I) A worm-inspired robot designed to crawl through intestines



(J) Khepera robot equipped with a cricket-like auditory system.

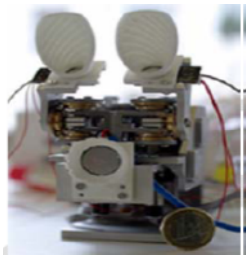


(K) Hopping robot, modeled after grasshopper

Figure 1.1 Examples of Biomimetic robots – (Meyer and Guillot, 2008) - continuation



(L) A gynoid, Uando – model after a woman



(M) Robotic bat head, designed to explore bat object detection methods in the dark



(N) The cricket-robot from Case Western Reserve University.



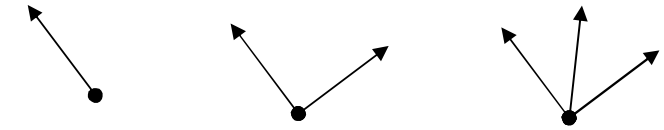
(O) Wall climbing robots at Stanford – a practical application of nano technology for surface adhesion

Figure 1.1 Examples of Biomimetic robots – (Meyer and Guillot, 2008) - continuation

1.5 HYPER-REDUNDANT ROBOTS

These are robots with a very large or infinite relative degree of kinematic redundancy i.e. has many more degrees of freedom than required to perform a certain task. They have the form of serpentine or snake or rod shape. Tentacle, trunk and fish are examples of biological hyper-redundant bodies. The redundancy means different ways to perform the same movement and is usually denoted in terms of degrees of freedom as shown in Figure 1.2. Figure 1.3 further elaborates on the issue of degrees of freedom, an hyper-redundant body can have very large possible configurations to achieve the same task if not constrained. In Figure 1.3, the ends A and B have the same

relative positions to each other for each configuration, while the links have very different arrangements.



1 DOF 2 DOF 3 DOF

Figure 1.2 The meaning of 1, 2 and 3 degree of freedom (DOF) mechanism

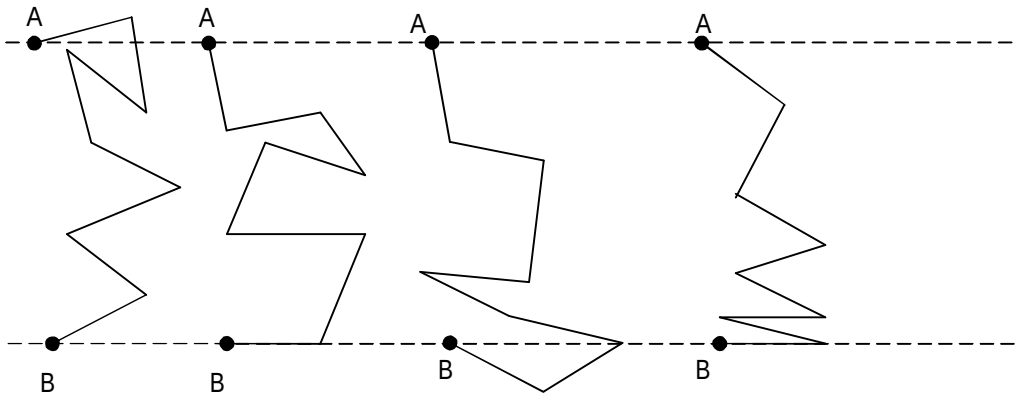


Figure 1.3 An hyper-redundant bodies have large possible configurations without any constraints.

1.6 ADVANTAGES AND DISADVANTAGES OF AN HYPER-REDUNDANT ROBOTS

A hyper-redundant robot has the following **advantages**;

1. The redundancy allows them to still function after losing mobility in one or more sections.
2. Stability in all terrain because of low center of gravity
3. Terrainability which is the ability to traverse rough terrain
4. Traction is very high as the whole body is involved.

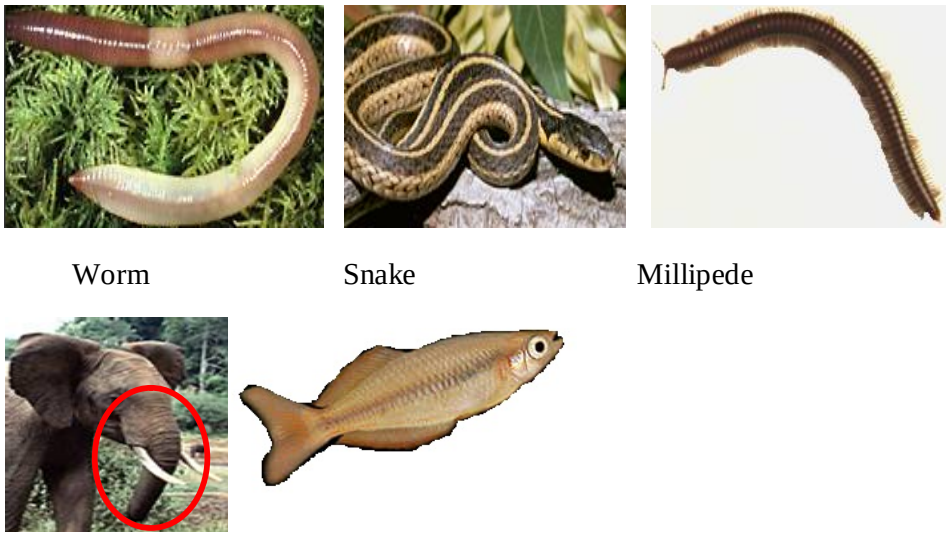
5. High efficiency in energy use as there is no need to lift the body
6. Small size that can penetrate small crevices.
7. Amphibious – by sealing the whole body, the same body motion on land is used for swimming in water as exemplified by ACM-R5 (Yamada et al, 2005 and William, 2006).

The **disadvantages** according to Kevin (1997) include;

1. Low speed as the whole body is used for motion.
2. Poor thermal control because of low surface to volume ratio, (Shugen and Mitsuru, 2002).
3. The need to know how to control, programme and build an efficient control system for the several degrees of freedom (DOF) links or joints.

1.7 EXAMPLES OF BIOLOGICAL HYPER-REDUNDANT BODIES

Figure 1.4 shows some examples of biological hyper-redundant bodies. The worm, millipede and elephant trunk have no bone while the fish and snake have bony support.



Worm Snake Millipede

Elephant trunk Fish

Figure 1.4 Examples of biological hyper-redundant bodies
(Source: Microsoft Encarta Reference Library DVD 2005)

1.8 SCENARIOS WHERE HYPER-REDUNDANT ROBOTS CAN PERFORM

Examples of scenarios requiring hyper-redundant robots are:

1. Under water devices:
    - Military: Anti diver, anti submarine, search operation etc
    - Civil: Oil installation, Oil platform superstructure surveillance
    - Fish decoy, mining, etc
2. Search and rescue among tangle mass of rubbles
3. Cheap and distributed space exploration robots - Brooks and Flynn (1989)
4. Fire fighting – (acting like intelligent fire hose)
5. Manufacturing and machine maintenance in a convoluted environments (Matsuura et al,1985).
6. General manufacturing –can act as robotic arm with great dexterity
7. Minimally invasive surgery – as laparoscope or endoscope that can follow a very complex path without colliding or penetrating organs.
8. Pipe inspection and other underwater facilities inspection.
9. Stealth perimeter surveillance especially if the model is mobile, for example snake form for residential areas, fish form for anti scuba in lagoons and estuaries. If made smaller i.e. as autonomous micro–robots, they can be used for security checks in difficult scenarios e.g. hostage, enemy camps, collapsed structures, pipe inspection, etc where human presence is not desirable.

1.9 STATEMENT OF THE PROBLEM

Hyper-redundant robots have been researched into for over 40 years, they were first documented by Hirose in Japan in 1972 (Kevin, 1997). The problems with this type of robot that every researcher will encounter are as follows:

1. How do we control the multiple degree of freedom joints to produce usable motions? A hyper-redundant body can take a very large number of possible shapes without constraint as shown in Figure 1.3. For every new design, it is still fundamental that a method must be sort on how to make the several joint produce useful motions (Kier and Smith, 1985; Yim, 1994; Skierczynski et al, 1996; Choset and Lee, 2001; Wilbur et al, 2002; Ma and Mitsuru, 2002; Crespi et al, 2005; Masayuki et al, 2008).
2. Which actuator design will have enough strength and tenacity to carry the weight of other links (or parts) and still be fast enough while not generating too much heat? Hyper-redundant bodies have low surface to volume ratio which makes them dense after packaging them and thus heat dissipation is a concern as advised by Skierczynski et al. (1996), Robinson and Davies (1999).
3. Another problem is how a better biomimicry (i.e. imitating living object) can be achieved in designing a hyper-redundant joint. Biological systems, for example hydrostatic joints are commonly found as integral parts of organisms and as parts or complete organs in the case of vertebrates – e.g. tongue and penis. Some invertebrates have *almost* a continuum body while vertebrates such as snakes have over 200 vertebras (200-1 joints) to support their bodies. An elephant trunk has no single joint i.e. it is a continuum.
4. Furthermore, how can we simplify the complex control strategy just like that of the biological systems? Most researchers have been extrapolating convectional joints – hinges, universal, even ball and sockets in an attempt to build a hyper-redundant robot. These approaches have made many of those robots unsuccessful in their imitation of nature. The octopus has no bone in its tentacles but it is still able to control its motion so effectively as to attract researchers

(Yekutieli et al, 2002, Yekutieli et al, 2005a and 2005b). The simplicity of the control strategy it use was referred to as being stereotypical and is worthy of imitating.

1.10 AIM AND OBJECTIVES

The overall objective of this research is to design and develop a biomorphic hyper-redundant joint mechanism for robotic applications.

The specific objectives are;

1. To design a simple hyper-redundant robot joint using materials closest to biological tissues,
2. To assess the possibility of using carbon filled natural rubber as the biomimetic material,
3. To base the designed hyper-redundant joint on hydrostatic skeleton
4. To construct and test a simple robot (in the form of a fish model) to demonstrate the capability of the designed hydrostatic joint in a stationary body of water.
5. To carry out stability analysis on the design control methodology employed.

1.11 JUSTIFICATION

Nigeria has many areas where hyper-redundant robots could contribute significantly. These include;

1. Monitoring and inspecting and repairing leakages of underwater petroleum pipes and other offshore installations. The recent oil leakage at the Gulf of Mexico by BP oils of America (April 2010) was salvaged by underwater robots. Nigeria being one of the largest oil producing countries in the world can face the same problem anytime which will be disastrous and very expensive especially if

Nigerians are not involved in the process of cleaning or management of such a situation.

2. Submarine telecommunications cable inspection: Recently (Radio Nigeria Abuja, August 2010), Globalcom Telecommunication Nigeria Limited (GLO) announced a successful laying of submarine telecommunications cables (GLO-1) from United Kingdom to Lagos. An autonomous underwater device to locate any fault and repair or replace it if there is problem will surely be needed for this cable. A warning device is also needed in case there is sabotage or an accident at any point along the cable lenght.
3. Fresh water ecological monitoring and study: A stationary device may be better, but we can also imagine a portable device that can relocate itself and even take samples back to the base station located somewhere along the river basin or perform on the spot analysis. Rivers passing through jungles can easily be studied ecologically if a robot in the form of a limbless rod is used. The absence of a limb will allow it to pass through tangled mass of twigs and rocks.
4. Military reconnaissance and early warning device:. Any nation with a water boundary – especially oceans and seas can have its security compromised by scuba divers, submarines and even unmanned mobile bombs etc. A distributed and cheap robot can be camouflaged as fish or snake which will then give an early warning to the military for appropriate action.
5. Biomedical engineering can apply the technology into building devices for viewing internal organs and for surgery assistance with minimal body opening – thus lowering operating costs and lengths of stays in hospitals. The devices can be built to resemble a worm that moves among organs while reporting on its findings or in the form of laparoscope for robotic assisted surgery or for

minimally invasive surgery or scar less surgery (that is surgery through natural orifices like the mouth, nose, vagina, anus and the navel).

6. Nigeria does not have much automated manufacturing, but we have a lot of engines that need constant inspection at lower cost. The cost of inspection discourages people from constant engine inspection. Aircraft engines, turbines at power stations etc may be inspected without opening them up using these rod shape robots. A rod-shaped robot that can be made to bend into any shape dynamically under a program and will be able to pass through convoluted spaces.
7. There is a need to acquire a platform for experimenting with bio-hybrid robots as this is the robotic trend and hyper-redundant robot is an example. This research work will allow students and other interested researchers within Ahmadu Bello University to experiment with a bio-hybrid robot in the form of a fish.

1.12 SCOPE OF THE RESEARCH

The scope is limited to:

1. Designing and constructing the joint using biomimetic materials.
2. Assembling it with the necessary electronics and servomotors.
3. Developing (writing) the control program (software) that will be used in the robot.
4. Using a single microcontroller – since biological bodies do not have multiple brains, it is desired not to use more than one microcontroller to control its operations.
5. Testing it in a stationary body of water to confirm that the motion is exactly or at least very close to the biological models.

CHAPTER TWO

LITERATURE REVIEW

2.1 JOINT DESIGNS

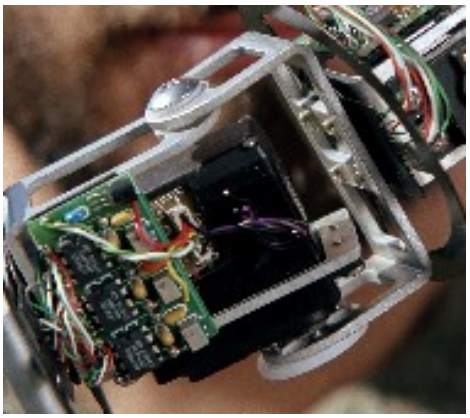
2.1.1 Robotic Joint Designs

Conventional robots can best be described as discrete manipulators (Robinson and Davies, 1999), where the designs are based on a small number of actuatable joints that are serially connected by discrete rigid links. The hyper redundant robots on the other hand have a larger number of joints while continuum robots theoretically have no joints at all or the joints are not distinct.

2.1.1.1 Hyper-redundant robot joint implementations

According to Trimmer et al. (2006), most researchers build their biologically inspired hyper-redundant robots from concatenated rigid modules with multi-axis joints (Shammas et al., 2003) such as universal joint (Yamada, and Hirose, 2006; Mori and Hirose, 2006) or revolute joints (Kevin, 2003), parallel mechanisms (Masayuki et al., 2008) and some are hybrid (Choset and Lee, 2001). Similar modular designs have been used as re-conformable machines (Yim, 1994) and form the basis for many undulating or swimming robots (Wilbur et al., 2002; Crespi et al., 2005). Examples of hyper-redundant robot joint implementations are shown in Figure 2.1.

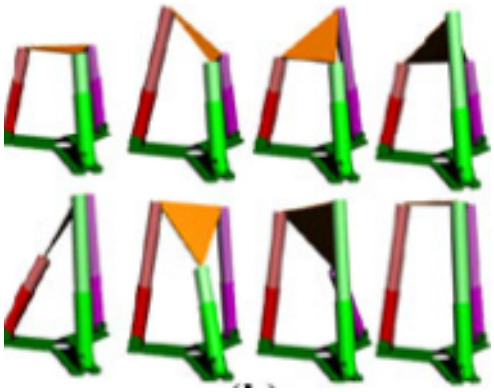
Figure 2.2 shows an obliquely cut mechanism. Joints based on oblique mechanisms are used for slowly changing joint angle such as used by MOGURA (Figure 2.25) for manufacturing and Carnegie Mellon University elephant trunk robot (Figure 2.20).



(A) Revolute Joint as used by NASA snakebot (Kevin, 2003)

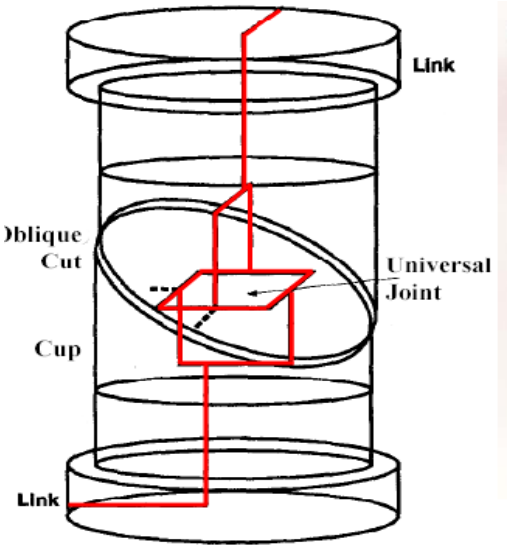


(B) Universal Joint was used by Miller (2010), Hirose ACM -R5 (William, 2006). It is the most popular joint adopted for hyper-redundant robot designs.

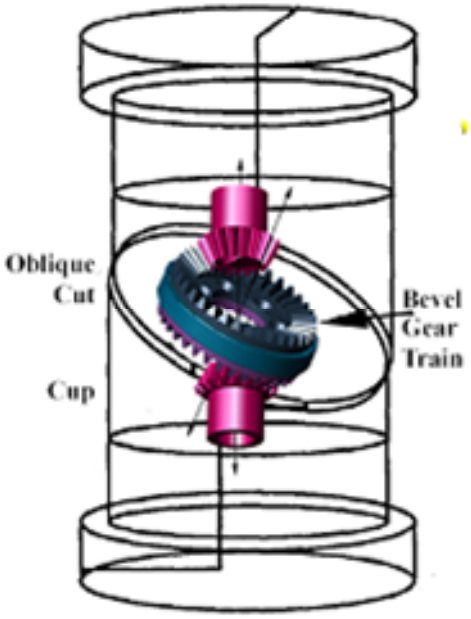


(C) Parallel mechanism as used by Masayuki et al. (2008).

Figure 2.1 Hyper-redundant robot joint type and their implementation



(D) Angular swivel joint with universal joint (Elie et al., 2003)



(E) Angular swivel joint with bevel gear train (Wolf et al., 2003)

Figure 2.1 Hyper-redundant robot joint type and their implementation - continuation

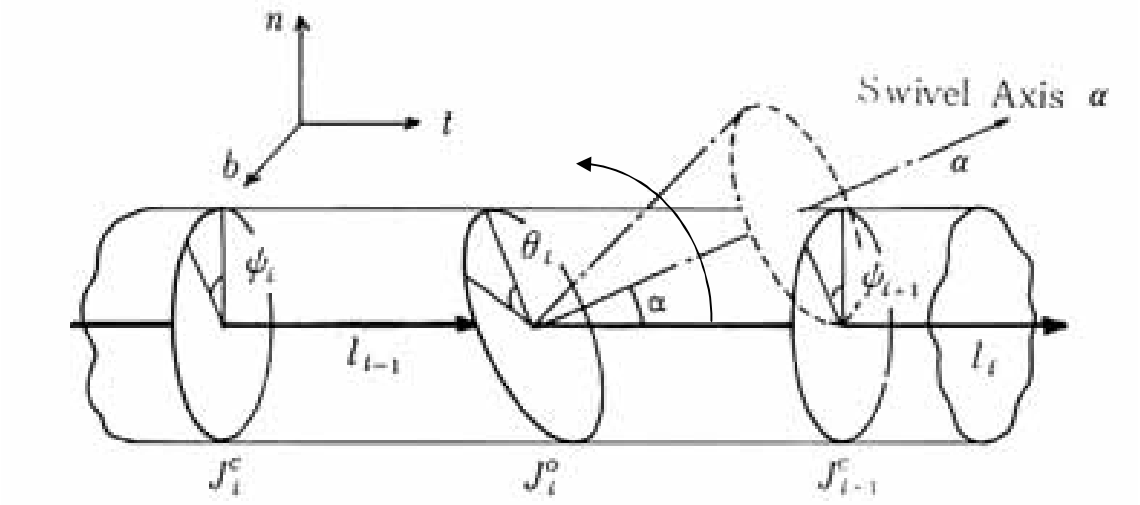


Figure 2.2. Generalized oblique mechanism
(Source http://www-robot.mes.titech.ac.jp/robot/snake/oblix/oblix_e.html)

2.1.2 Joint Types Found in Biological Models

There are two categories of joints found in biological models, they are bony joints and hydrostatic joints.

2.1.2.1 Bony joints

The vertebrates such as mammals, reptiles and birds have these supports (or joints designs) exemplified by the human skeletal system of Figure 2.3.

2.1.2.2 Hydrostatic joints

Most invertebrate organisms have very simple body structures, mostly tubular. Their body is supported by water or their fluidic habitat (Farabee, 2001). For the larger ones, two methods were evolved; one method uses fluid-filled balloon like elastic structure for support (Alscher and Beyn, 1998; Farabee, 2001; Kelly, 2007). The fluid

includes blood, intracellular fluid, seawater etc depending on the animal *Taxa*. The incompressibility of these water based fluids and a flexible restraints/container act as the support – hence hydrostatic skeletons.

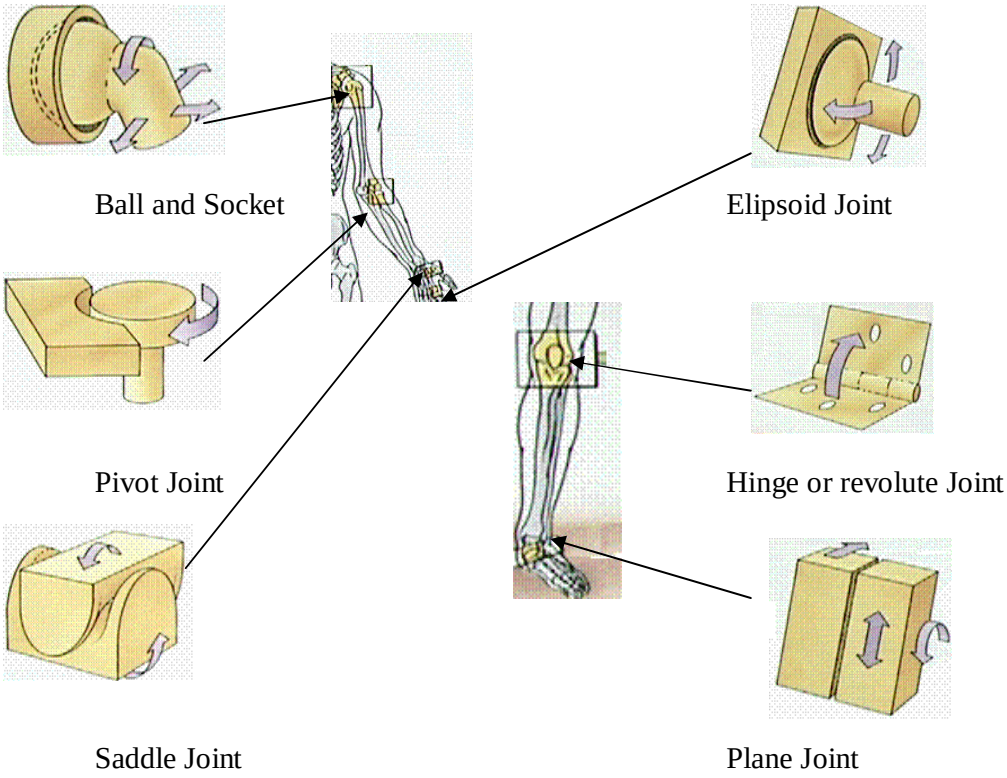


Figure 2.3 Examples of joints found in vertebrates (Source: www.sinauer.com)

The vertebrates also have boneless joints (and supports) referred to as muscular hydrostat (Kier and Smith, 1985) or hydrostatic skeleton (Skierczynski et al., 1996). Examples of muscular hydrostat are the trunk (elephant and opossum), tentacles (octopus and squid), tongue, and intestine and those of the hydrostatic skeleton are the mammalian penis, cochlea (hearing frequency filter which is fluid filled).

2.2 ISOCHORIC NATURE OF HYDROSTATIC JOINTS

Hydrostatic joints (i.e. skeletal system that base their structural rigidity on the incompressibility of water or water based fluid in a container of some sort) are of two forms in terms of volume;

- Sectional isochoric
- Whole body isochoric

2.2.1 Sectional Isochoric Hydrostatic Joint/Support

In the sectional isochoric implementation, the hydrostatic joint is chambered and fluid exchange is not permitted. Each section maintains constant volume (isochoric) while in action by extending and getting thinner diametrically. An example is the leech; *Hirudo medicinalis* (Skierczynski et al.., 1996; Sfakiotakis and Tsakiris, 2006; Alscher, 1990). Figure 2.4 shows a Leech model in extension and contraction while still segmentally isochoric.

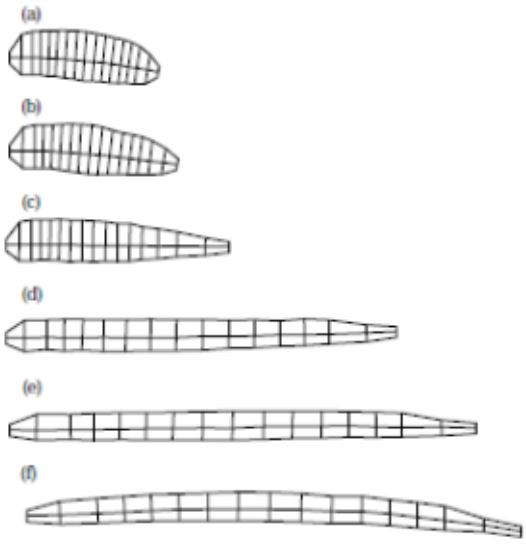


Figure 2.4 Segementally isochoric Leech body.
The body grows thinner when extending to keep volume constant. Also each section maintains constant volume (isochoric) while in action.
(Source: Skierczynski et al.., 1996)

2.2.2 Whole Body Isochoric Hydrostatic Joint/Support

For the whole body isochoric implementations, there may be chamber but fluid exchange is unrestrained. Examples are the hornworm caterpillar (*Manduca sexta)*, Figure 2.5, wild-type nematode, (*Caenorhabditis elegans).* In this nature design, the whole body still exhibits isochoric behaviour so as to maintain rigidity. Any compression (for example) in any part will lead to other parts extending so as to keep the body volume constant, as shown in Figure 2.6, they have internally connected chambers.

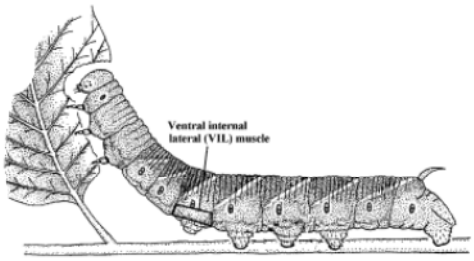


Figure 2.5 *Manduca sexta* Caterpillar.
(Source: Yim, 1994).

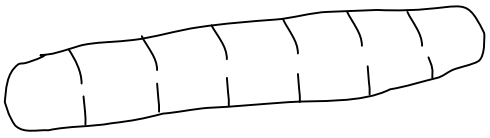


Figure 2.6 *Manduca sexta* Caterpillar body have internally connected chambers

2.3 BIOMECHANISM AND HYDROSTATIC JOINT/SUPPORT

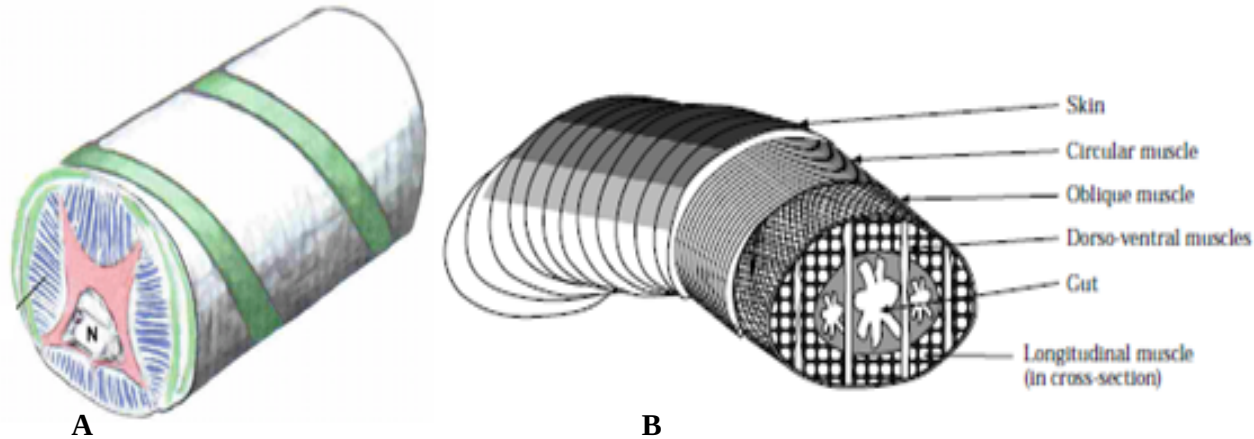
Biomechanics is the study of the structure and function of biological systems by means of the methods of mechanics (Hatze, 1974). “Biomechanics is closely related to engineering, because it often uses traditional engineering sciences to analyze biological systems. Some simple applications of Newtonian mechanics and/or materials sciences

can supply correct approximations to the mechanics of many biological systems. Applied mechanics, most notably mechanical engineering disciplines such as continuum mechanics, mechanism analysis, structural analysis, kinematics and dynamics play prominent roles in the study of biomechanics. Usually biological systems are more complex than man-built systems. Numerical methods are hence applied in almost every biomechanical study. Research is done in an iterative process of hypothesis and verification, including several steps of modeling, computer simulation and experimental measurements" (Peterson and Bronzino, 2008).

Hookes law cannot be used in analyzing biological bodies because the substance they are made of (protein such as collagen and elastin) exhibit nonlinear behaviour. The non linear phenomenon is due to the large strains they normally experienc (>100%). Soft tissues are modeled as hyperelastic materials using models such as Neo-Hookean and Fung-elastic exponential models (Richard and Thomas, 2008).

The biomechanical principle of movement generation is different in vertebrates and invertebrates. The invertebrate uses a dynamic muscle system in combination with fluid or other tissue to form hydrostatic skeleton/ support. The muscle and fluid are incompressible. There are 2 types of hydrostatic support; the first type is called muscular hydrostats. It has muscle and other tissues forming a solid structure without a separate enclosed fluid volume (e.g. cephalopod tentacles, elephant trunks, and vertebrate tongue (Kier and Smith, 1985; Yekutieli et al.., 2005a and 2005b). In the second type, muscle composed of a body wall-like balloon and surrounds a fluid-filled space (e.g. sea anemones and worms), Farabee (2001). According to Kier and Smith (1985), Yekutieli et al.. (2002) and Yekutieli et al.. (2005a and 2005b), a muscular hydrostat consists of closely packed arrays of muscle fibers organized in 3 main directions – parallel, perpendicular and helical or oblique to the long axis (Figure 2.7).

According to Kier and Smith (1985), there are 4 elementary movements that a hydrostat body can make; elongation, shortening, torsion and bending at any point in its length.



A **B**

Figure 2.7 Muscle layouts in Muscular Hydrostat
(Source: **A** - Skierczynski et al, 1996 and **B** - Yekutieli et al, 2002)

2.4 REVIEW OF SELECTED HYDROSTATIC SKELETON MODELS

The hydrostatic skeleton implementation found in nature is highly varied in detail and especially in the neurological control strategy employed. The review here is basically on their mechanical designs.

2.4.1 Leech - *Hirudo Medicinalis*

This is an example of a sectionally isochoric hydrostatic body. Leeches are annelid worms from the class Hirudinea (Figure 2.8). They have a sucker at either end of their body with 21 segments. Adults are 2 to 10cm long and some can reach 20cm when fully extended. Its medicinal use is for painless blood volume reduction (Anne, 1990).

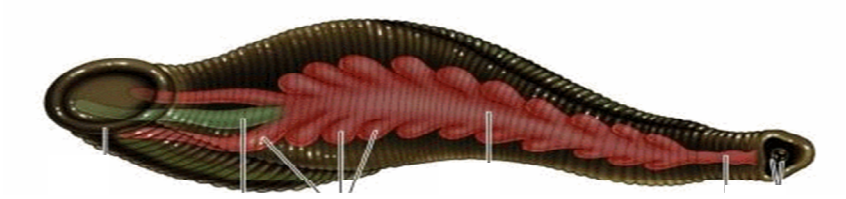


Figure 2.8 Picture of a leech. (Source http//:www. Hirudolab.com)

They have fluid filled compartmentalized cylindrical bodies as shown in Figure 2.6. The muscle arrangement follows Figure 2.7. It moves by crawling or swimming – Kristan et al.. (1974) and Stern et al.. (1986) gave details of the kinematics of these motions. The crawling motion involves sequential grasping and releasing of the front and rear suckers while shortening and elongating the body using the longitudinal and oblique muscles (Alscher and Beyn, 1998). The swimming action is done by a wavy activation of the ventral longitudinal muscles, while the dorsal longitudinal muscles are activated with phase shift. The body is held flattened throughout the movement by activation of the dorso-ventral muscles. The simplicity of these motions has encouraged researchers such as Skierczynski et al.. (1996), Alscher and Beyn (1998) and Alscher (1990) to study it with the hope of gaining insight into how its hydrostatic skeleton functions. Fortunately, its behaviour and physiological structure have been documented by Kristan et al.. (1974) and Stern et al. (1986). The neuronal control and properties of the muscles are well understood also by Mann, (1962). Muller et al. (1981), Wilson et al. (1996). Several models of *Hirudo Medicinalis* exist – *quasi-static model* (Wadepuhl and Beyn (1989), Wadepuhl et al. (1997)), *extended steady state model* (Skierczynski et al., 1996) and a *dynamic model* (Alscher and Beyn, 1998). The *quasi-static model* model was extended by Alscher and Beyn (1998) for dynamic situations such as collision with an object and lift-off behaviour – more or less extending it to 3D behaviour.

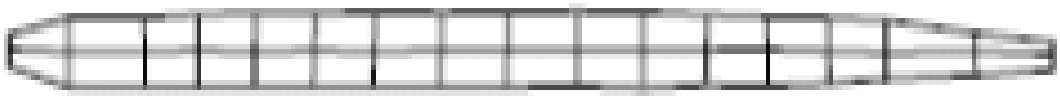


Figure 2.9 Compartmentalized cylindrical model of a leech.
(Source: Skierczynski et al., 1996)

2.4.2 Tobacco Hornworm Caterpillar – (*Manduca sexta*)

Manduca sexta (Figure 2.5) is an example of whole body isochoric hydrostatic body. *Manduca sexta* has been studied much at the neurological level by Woods et al. (2008) and Mezoff et al. (2004), but the material property that accomplished the very interesting movement of such a simple neurological body has started to receive attention as indicated by Mezoff et al. (2004), Dorfmann et al. (2007) and Woods et al. (2008). Most of these works are on kinematics of its motion or neurological control or both. Dorfmann et al. (2007) discussed the biochemical property of *Manduca sexta* muscles as well. *Manduca* is capable of fast crawling, climbing irregular surfaces at any angle, inverted motions, burrowing and tunneling before pupating according to Woods et al. (2008).

Its muscles are small (2-14 fibers and 4-6mm long – typically) with about 70 muscles per segment layered beneath the soft cuticle to which they are attached. Nearly all are oriented longitudinally or obliquely and none circumferentially as in earthworms according to Quillin (2000).

Dorfmann et al. (2007) created a model of the muscle of *Manduca* by comparing it with rubber. The 3rd abdominal segment has been of particular interest in the derivation of this model. The VIL (ventral interior longitudinal) muscle at this 3rd segment (Figure 2.10) was kinematically and neurologically studied by Belanger and Trimmer (2000); Woods et al. (2008). The VIL is a comparatively large muscle in the innermost layers of muscles. The first pro leg is attached to it. The muscle of the lava is different from that of the adult according to Dorfmann et al. (2007), it is slow and stretchy. The adult muscles contract rapidly with little strain of about 7% and at a speed of 0.018m/s, which is good for flight. In contrast, that of the lava strains at 30% and takes a full second to shorten during the crawling cycle (Stevenson and Josephson (1990), Woods et al. (2008)). The strain rate is 0.5 to 1.5 times resting length.

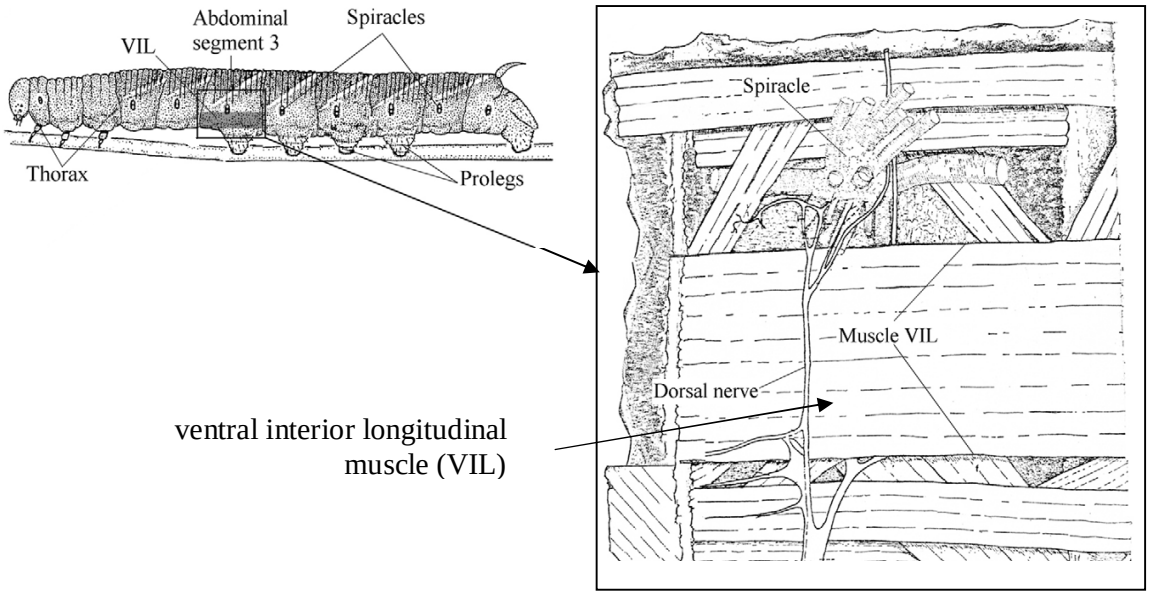
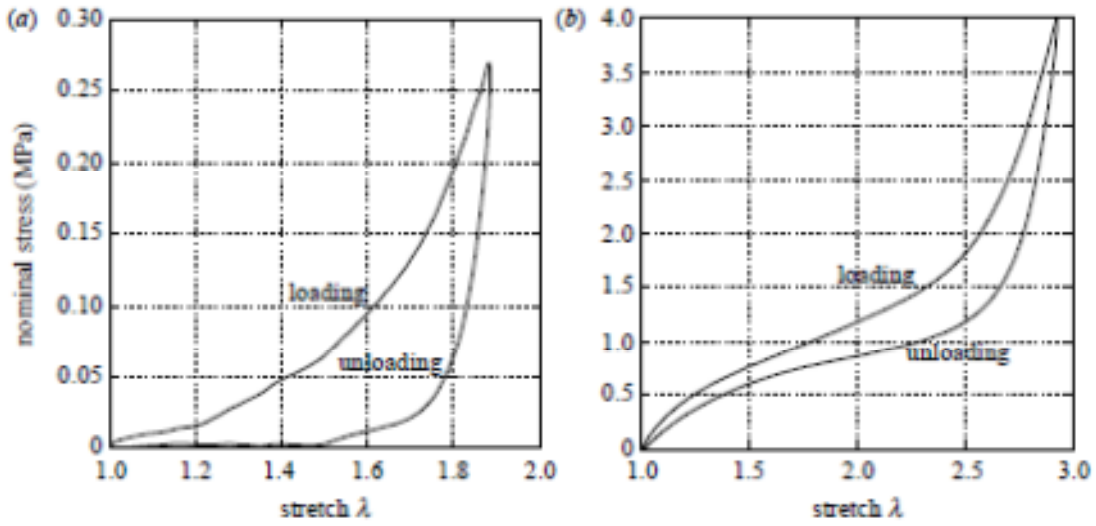


Figure 2.10 The ventral interior longitudinal (VIL) muscle of *M. Sexta.* (Source: Woods et al., 2008).

In deriving the constitutive model, the VIL muscle was subjected to loading and unloading as shown in Figure 2.11. Stress softening effect called Mullins effect was developed – just as found in particle reinforced natural rubber and some elastomers (Dorfmann and Ogden (2003), Dorfmann and Ogden (2004), Horgan et al. (2004)).The *Manduca sexta* muscle is thus a nonlinear pseudo-elastic composite - with isotropic base material embedding a number of fibres. It is also transversely isotropic. According to Fung (1980), a pseudo-elastic material will have the above characteristics. Based on the result, the theory of non-linear elasticity proposed by Ogden and Roxburgh (1999) was used to model *manduca sexta* muscle – *in the passive state*.



(A) (B)

Figure 2.11 Similarity in the pseudo-elastic behaviour of the VIL of *Manduca Muscle* (A) and Carbon-black-reinforced natural rubber (B) during loading and unloading. (Source: Dorfmann et al., 2007).

It is the similarity to rubber that forms the model derivation premises - **the mechanical property of rubber (unfilled and carbon filled) and biological tissues are thus qualitatively similar**. A major difference is that biological tissue is composed of isotropic matrix embedding multiple oriented families of protein fibre hence they have anisotropic behaviour, but rubber is generally isotropic.

2.4.3 *Octopus Vulgaris*

Octopus Vulgaris is an example of large muscular hydrostatic body in the form of tentacles. The octopus, squids and cuttle fish (cephalopoda) are organisms having tentacles. Tentacles have large DOFs like any other hydrostatic muscular system. The reason for its study is the question of how do they manage these DOFs on so many arms? How is the muscle activation coordinated? What lesson can we gain about its control principle? *Octopus Vulgaris* has $\cong 5 \times 10^7$ neuron cells and 30,000 neural cells

in its tentacles, which indicates that the computational task is handled by the tentacle itself – large number of neurons is an indication of computational activities just like the brain.

In its reaching movement, the octopus solved the *non-trivial inverse–kinematics* problem by reducing the degree of freedom (DOF) to three by using *stereotypical* motion. It creates a bend somewhere and propagates it toward an object. If it misses it, it starts all over again. The base of the arm points to the object – 1 DOF, then angle of Yaw – 1 DOF and another for pitch around the arm base – 1 DOF. The forces involved in meeting the inverse kinematics require inverse-dynamics - this shows which muscle forces are needed (Yekutieli et al.; 2005c, 2007).

Gutfreund et al. (1996), Yekutieli et al. (2005c), Yekutieli et al. (2007), have studied the *Octopus Vulgaris* as a muscular hydrostat for more than a decade. Yekutieli et al. (2005c), started by taking a 3D video (using 2 cameras at approximately 90^0 to each other) of three octopus in captivity and estimating the kinematics (position and velocity) from the recording. The 3D position was extracted from the combined video image using direct liner transformation method – between the camera coordinates and external XYZ coordinate

Customized software was developed to tackle the problem associated with 3D kinematics reconstruction of the video images such as occlusion of image by others, background noise and water surface refraction. The process was actually semi-automatic because manual tracking of images were done also.

With good back ground information on the 3D reconstruction of a live *Octopus Vulgaris*, a dynamic model was created that can predict the arm motion and the result used for a flexible robotic manipulator. The model is a 2D array of point masses and springs (Voigt body), the same principle used for modeling leech was applied here. The model is a multi-segment structure shown in Figure 2.12, and each segment contain

longitudinal and transverse muscles and maintains constant volume (isochoric) – a prominent feature of muscle hydrostat. The input to the model is the degree of activation of each of its muscles. The external forces – gravity, buoyancy, water and drag were included in the model. Internal forces by the arm muscles and forces for maintaining constant volume were also included.

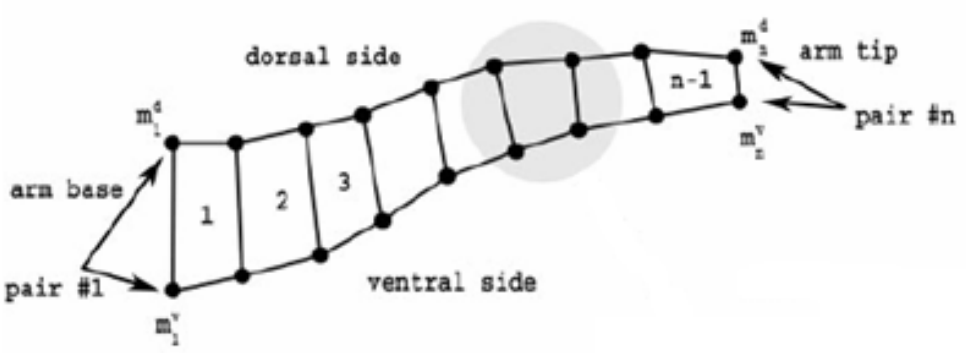


Figure 2.12 A multi-segment model of an octopus arm. (Source: Yekutieli et al., 2005c)

Furthermore the model uses discrete rather than continuous descriptions of the body to simplify the processes – 20 segments were used in all. A single planar force system was also used. To simplify the derivation even more, the drag forces of the reaching arm movement were found experimentally.

The muscle forces were modeled using two methods for comparative purposes:

a) As a nonlinear body – using nonlinear force-length and force-velocity relations
b) As a linear damped spring model

The nonlinear model gave a better result and was used in all their simulation (as expected since living objects are nonlinear (Dorfmann et al., 2007).

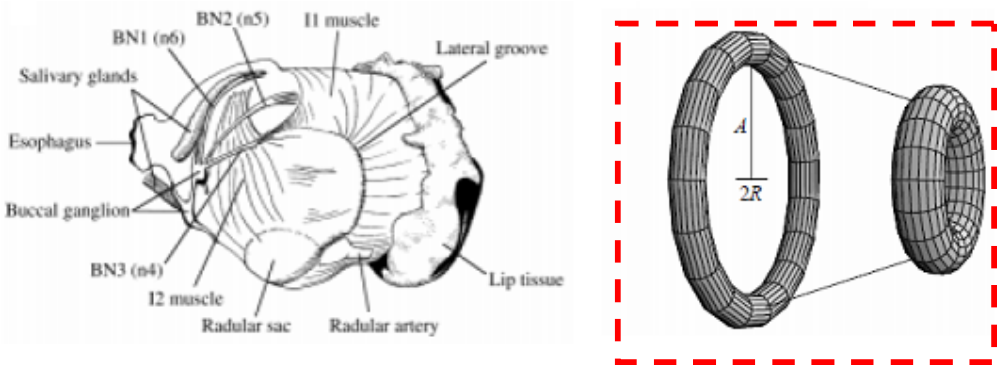
2.4.4 Tongues

Tongues are highly varying muscular hydrostatic bodies among biological models. The tongue as a hydrostatic body was first described by Kier and Smith (1989). Most work related to the tongue has been found to be general in treatment. The following are examples of literature on tongues of different organisms;

- *Aplysia Californica* , a marine mollusk (Neustadter et al., 2007; Drushel et al., 1998)
- Chameleon (Wainwright and Bennett, 1992; Herrel et al., 2001)
- Microhylid frogs (Meyers et al., 2003)
- Python molurus (DeGroot et al., 2004)
- Human being (Gilbert et al., 2007) and
- A generic treatment by Sokoloff (2004).

It was argued by Drushel et al. (1998) that *Aplysia Californica* buccal mass being primarily muscle and cartilage with small internal vascular system are good material for studying muscular hydrostatic systems. The kinetic model developed involves studying a transilluminated specimen swallowing and tearing mouth movement. This process allow them to describe the kinematics of the buccal mass of an intact animal (unlike others that have to deal with anesthetized or dead bodies).

The following diagram - Figure 2.13 shows the modeling of the ***Aplysia Californica*** buccal mass as a torus in which a change in diameter leads to a compensatory change in its cross-sectional area – that is it is whole body isochoric.



Aplysia Californica The torus model of the mouth

Figure 2.13 The torus model used in modeling *Aplysia Californica*.
(Source: Drushel et al., 1998).

Another model is that of the **chameleon**. The ballistic nature of the chameleon and frog/toad and some lizard interested quite a number of researchers (Wainwright and Bennett, 1992; Herrel et al., 2001 and Meyers et al., 2003). A chameleon can extend its tongue by about 600% of its resting length and catches even relatively large pray according to Herrel et al. (2001). ***This extreme behavior is very attractive for actuator design in robotics***. An experiment conducted on *Chamaeleo Onstaleti Mocquard* and *Chamaeleo Calyptraths Dumeril* indicates that there is a constant retractive force due to (i) active hyoid retraction (Figure 2.14). (ii) Large muscle filament overlap at maximal tongue extension and (iii) the super contractile property of the tongue retractor muscles.

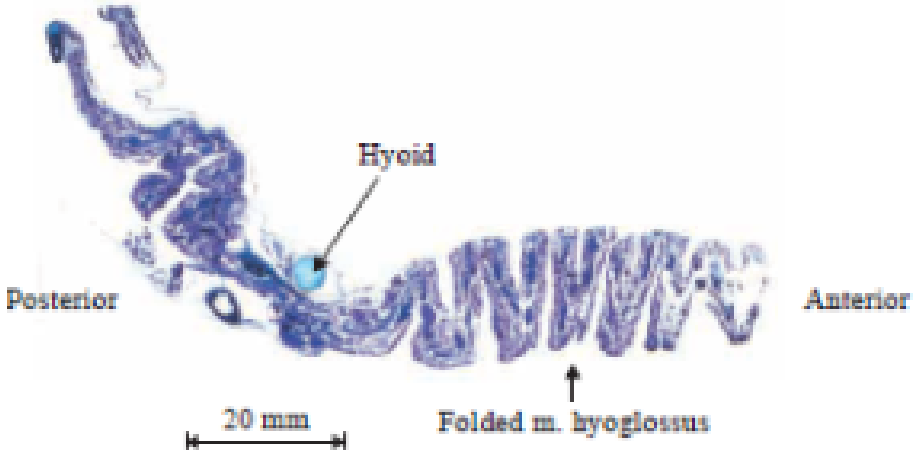


Figure 2.14 A chameleon hyoid. (Source: Herrel et al., 2001).

A 3D kinematic analysis of tongue flickering by ***Python molurus*** was documented by DeGroot et al. (2004). This snake tongue is capable of 1% of the body length in elongation. They found that the posterior protruding part elongates up to 130% and the anterior elongates by 60% maximally. This behaviour was *concluded to be due to the hydrostatic elongation mechanism*. It is only pseudo elastic materials such as **rubber** that have such behavior. Figure 2.15 shows the dorso-ventral representation of the *Python molurus* tongue.

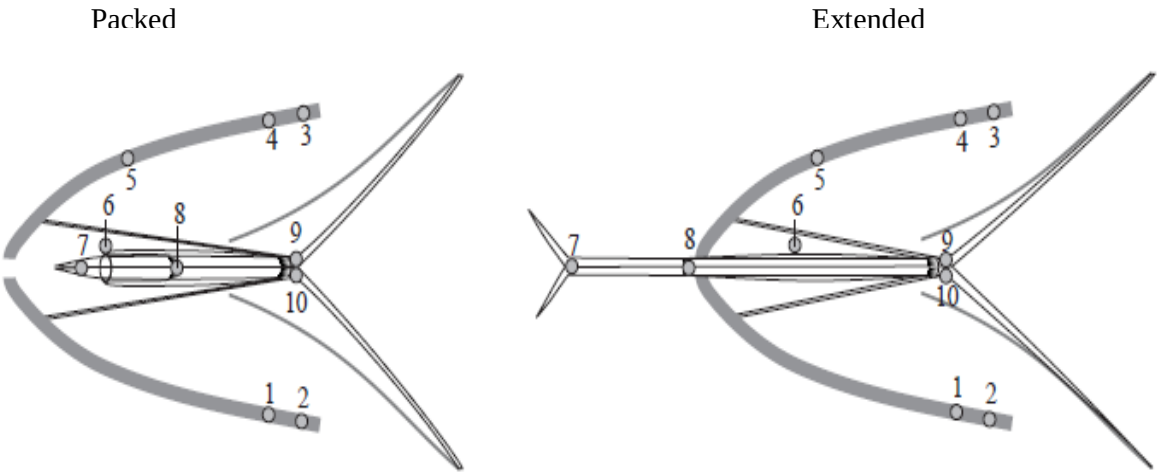


Figure 2.15 Dorso-Ventral model of *Python molurus* – packed and extended (Source: DeGroot et al., 2004).

According to Gilbert et al. (2007), the human tongue working principle was described as based on a hydrostatic mechanism. According to Sokoloff (2004), much work is needed to be done in modeling tongues (generally); the basis for this is the way the tongue muscles are coordinated by the motor neurons. There is a difference in co-ordination during inspiration and expiration for example. He suggested that the tongue entire musculature be studied and not an isolated portion.

2.4.5 Mammalian Penis

The mammalian penis is an example of inflatable hydrostatic skeleton. The mammalian penis has been described as an inflatable hydrostatic skeleton by Hanyu (1988) and Kelly (2002) and has an entirely different design from all the previous hydrostatic skeletons described in this work. When inflated, it can be classified as whole body isochoric. This organ can be stored away when not in use as evidenced by the study of boeciliid fish and many mammals. The design allows quick change in size, shape and flexural stiffness.

This design should greatly interest any designer of portable robots especially hyper-redundant robots or continuum robots such as exemplified by Trimmer et al. (2006) Softbot, though Softbot was modeled after catapillar – *manduca sexta*.

The change in shape and flexural rigidity starts when blood (the main hydrostatic fluid) fills the tunica albugiunea - which comprises primarily thick bundles of type I collagen fibers (Hanyu, 1988 and Moreland et al. 1995) which act as force distributors. This collagen can bear a tensile load of up to 100MPa according to Wainwright (1976). The axial orthogonal array of the collagen fiber arrangement is found by investigators Quillin (2000) and Kelly (2002) to have much higher flexural stiffness than those with cross-helical fiber arrangement as found in most hydrostats such as caterpillars and leeches. Burrowing worms, according to Dorgan et al. (2007) and Koehl et al. (2000), and nematodes (*CaenorhabditIs Elegans*) according to Park et al. (2007), experience very high frontal trust forces. For example, they develop 2-30kPa internal pressure and ability to support this load is attributed to the multilayered collagen.

Conclusively, the behavior of these biological models shows nonlinearity and much varied control strategies. Furthermore, their control scheme is highly tied to their mechanical designs.

2.5 HYPER–ELASTICITY AND BIOLOGICAL MATERIALS

Biological materials stress–strain relationships have been treated and shown to be hyper–elastic in nature according to Dorfmann et al. (2007). The stress–strain behaviour is qualitatively the same with non biological materials, especially rubber as shown in Figure 2.11. For examples, Neo-Hookean and Fung-elastic exponential models (equations) normally used for hyper-elastic materials have been used to model elastin (a protein) according to Richard and Thomas (2008) while *manduca sexta* muscle was modeled by Dorfmann et al. (2007) using Ogden and Roxburgh (1999) hyper elastic model. The stress–strain relationship of the hyper-elastic models are derived from a strain energy density function according to Ogden (1997).

2.5.1 The Nature of Hyper – Elastic Materials

Hyper–elastic materials (also known as green elastic) are ideally elastic materials. The stress–strain patterns are non–linear, the unloading paths do not follow the loading curve. There is residual strain (or memory effect) that goes with time. This phenomenon is referred to as the Mullin effect. Some hyper–elastic materials are isotropic and some are anisotropic. They are incompressible or nearly incompressible with Poisson's ratio of ~0.5.

2.5.2 Hyper – Elastic Materials Mathematical Models (Constitutive Equations)

The models all aimed at describing the loading and unloading behaviour of elastomers as closely as possible. The complexity of elastic materials such as filled elastomers (rubber for example) and biological tissues have led to the creation of various models that are good in some areas and inadequate in others. There are lots of models, and most are modifications to one or more phenomenological models like the

Fung elastic model and the Ogden model or a modification to mechanistic models like the Neo-Hookean model. The phenomenological models are based on observed behaviours while the mechanistic models are based on the underlying material properties.

The following models are reviewed in this work:

- Neo–Hookean
- Mooney – Rivling Model
- Ogden Model
- Yeoh Model
- Polynomial Model

2.5.2.1 Neo–Hookean model

This is a mechanistic model describing the observed stress – strain behaviour (Ogden, 1997). It is an extension of Hooke's law when large deformation is involved. The model was proposed by Ronald Rivling in 1948 and is meant for incompressible materials (plastic and elastic). The strain energy W (using ANSYS Multiphysis 10 software help system) is expressed as;

$$W = \frac{\mu}{2}(\bar{I}_1 - 3) + \frac{1}{d}(J-1)^2 \qquad (2.1)$$

where

J = determinant of the elastic deformation gradient *F*

$\bar{I}_1$ = first deviatoric strain invariant

The initial shear modulus is defined as:

$\mu = 2(c_{10} + c_{01})$

and the initial bulk modulus is defined as:

K = 2/d

where

$d=(1-2*\nu)/ (c_{10} + c_{01})$

2.5.2.2 Mooney – Rivling model

This is a phenomenological based model – (Ogden, 1997). It is a more generalized version of Neo–Hookean's solid created in 1952. Here the strain energy W (from ANSYS Multiphysis 10 software help system); is a linear combination of two invariants $\overline{I_1}$ and $\overline{I_2}$ of finger tensor **B** and is given as:

$$W = c_{10}(\overline{I}_1 - 3) + c_{01}(\overline{I}_2 - 3) + c_{20}(\overline{I}_1 - 3)^2 + c_{11}(\overline{I}_1 - 3)(\overline{I}_2 - 3) + c_{02}(\overline{I}_2 - 3)^2 + c_{30}(\overline{I}_2 - 3)^3 + c_{21}(\overline{I}_1 - 3)^2(\overline{I}_2 - 3) + c_{12}(\overline{I}_1 - 3)(\overline{I}_2 - 3)^2 + c_{03}(\overline{I}_2 - 3)^3 + \frac{1}{d}(J - 1)^2 \quad , \qquad (2.2)$$

where J = determinant of the elastic deformation gradient *F*

$\overline{I_1}$= first deviatoric strain invariant

$\overline{I_2}$= second deviatoric strain invariant

c_{10}, c_{01} = material constants characterizing the deviatoric deformation of the material

d = material incompressibility parameter

The initial shear modulus is defined as:

$\mu = 2(c_{10} + c_{01})$

and the initial bulk modulus is defined as:

K = 2/d,

where

d=(1-2*ν)/ $(c_{10} + c_{01})$

2.5.2.3 Ogden model

This model (also a phenomenological model) is also based on strain energy density function. In the Ogden model, stretches ($l/l_o = \lambda$) are used instead of the strain and is λ_1, λ_2 and λ_3 in the 3 directions. The strain energy W (from equation 2) is taken from ANSYS Multiphysis 10 software help system and defined as follows;

$$W = \sum_{i=1}^{N} \frac{\mu_i}{\alpha_i}\left(\overline{\lambda}_1^{\alpha_i} + \overline{\lambda}_2^{\alpha_i} + \overline{\lambda}_3^{\alpha_i} - 3\right) + \sum_{k=1}^{N} \frac{1}{d_k}(J - 1)^{2k}, \qquad (2.3)$$

where $\bar{\lambda}_p$ (p=1,2,3) = deviatoric principal stretches, defined as $\bar{\lambda}_p = J^{-\frac{1}{3}}\lambda_p$

λ_p = principal stretches of the left Cauchy-Green tensor

J = determinant of the elastic deformation gradient

N, μ_p,α_p and d_p = material constants

The initial shear modulus is defined as:

$\mu = \frac{1}{2}\sum_{i=1}^{N} \alpha_i \mu_i$

and the initial bulk modulus is defined as:

$K = 2/d_1$

2.5.2.4 Yeoh model

For nearly incompressible materials. It is based on Rivlin observation of the effect of incompressibility on the earlier models such as Mooney – Rivlin model which he co-authored. ANSYS Multiphysis 10 software help system stated it as;

$$W = \sum_{i=1}^{N} c_{10}(\bar{I}_1 - 3)^i + \sum_{k=1}^{N} \frac{1}{d_k}(J - 1)^{2k}, \quad (2.4)$$

where

N=3

c_{10}, c_{20}, c_{30}, d_1, d_2, d_3 = material constants

$\bar{\lambda}_p$ (p=1,2,3) = deviatoric principal stretches, defined as $\bar{\lambda}_p = J^{-\frac{1}{3}}\lambda_p$

λ_p = principal stretches of the left Cauchy-Green tensor

J = determinant of the elastic deformation gradient

N, μ_p,α_p and d_p = material constants

The initial shear modulus is defined as:

$\mu = \frac{1}{2}\sum_{i=1}^{N} \alpha_i \mu_i$

and the initial bulk modulus is defined as:

$K = 2/d_1$

The terms/parameters are the same with Mooney Rivling.

2.5.2.5 Polynomial model

The energy density function W, using ANSYS Multiphysis 10 software help system is stated as;

$$W = \sum_{i+j=1}^{N} c_{ij}(\bar{I}_1 - 3)^i(\bar{I}_2 - 3)^j + \sum_{k=1}^{N} \frac{1}{d_k}(J - 1)^{2k} \quad (2.5)$$

The terms/parameters are the same with Mooney Rivling.

If N = 1. This is equivalent to Mooney-Rivlin 2 Parameter.

N = 2. This is equivalent to Mooney-Rivlin 5 Parameter.

N = 3. This is equivalent to Mooney-Rivlin 9 Parameter

N = 1 and $c_{01} = 0$, it is equivalent to Neo-Hookean.

2.5.3 Extensions To The Constitutive Equations And Modifying Factors

In the words of Miller and Arbor, (2008) and also according to Ahmadi and Muhr (2002) the models described earlier do not entirely describe the stress–strain/stress-stretch relationship in a material under all loading conditions. The models are for quasi-static behaviour. This has led many other researchers to create specific models for specific functions. Many products have small dynamic strain behaviour superimposed on a large mean (one time) strain - Figure 2.16. Ogden (2004) summarize some phenomenon not captured without extending the theory. The effect of mean strain on dynamic modulus and the effect of dynamic strain amplitude on dynamic modulus is that the material models such as Ogden, Mooney-Rivlin can only be used with caution and under static or quasi-static loading if they are to give a reliable result.

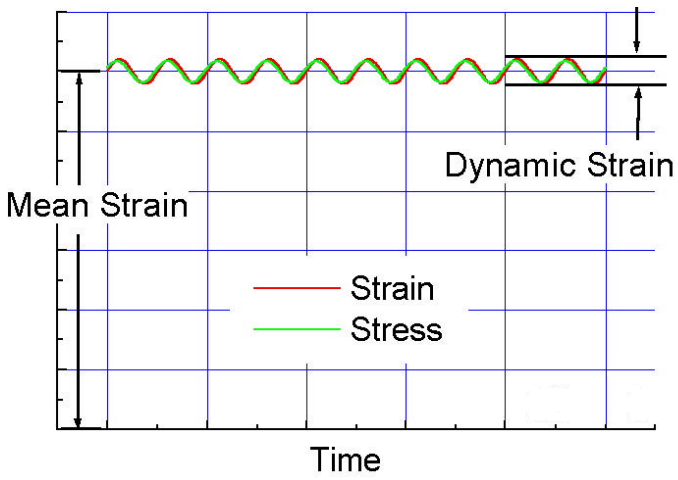


Figure 2.16 Dynamic sinusoidal loading superimposed on a large mean strain in an elastomer. (Source: Miller and Arbor, 2008).

Some common factors that affect the constitutive equations and are not properly captured are temperature, homogeneity of material, compressibility, the Mullin effect, reinforcement, cavitation and the Payne effect.

2.5.3.1 Temperature

Temperature has very strong influence on the stress–strain/ stress–stretch behaviour that the generalized model cannot fit (Dunwoody and Ogden, 2002; Dunwoody, 2005; Miller and Arbor, 2008). It was recommended that the exact temperature at which the experiment is performed should be close to that at which the material will be subjected to when in service.

2.5.3.2 Homogenity of material

Friedrich et al. (1999) cautioned that most models have assumed homogenous materials, which is an ideal situation. An investigator (Bilgili, 2002) had to develop a computerized simulation facility to investigate the shearing deformation of non–

homogenous elastomers and it was found that in homogeneity does cause a localized stress–strain field (not accounted for by the equations).

2.5.3.3 Compressibility

The input data used for creating the constitutive equations are based on uniaxial tensile test, planar biaxial tensile test and volumetric tensile/compressive data and were presumed to be enough to predict the behavior of the material. Compressibility influence (that is if all test data were compressive) was examined by Ogden (2000), Jiang and Ogden (2000) and Kirkinis and Ogden (2002). The azimuth shear of a pseudo elastic circular cylinder such as used in automobile suspension was used to confirm the implication of compression. It was found to give a different result from that predicted.

Furthermore, claims that planar biaxial testing can fully characterize the 3D anisotropic elastic properly of soft tissue was found to be incorrect according to Holzapfel (2008).

2.5.3.4 Mullin effect

The Mullin effect is closely related to the fatigue of elastomers parts - used in engineering applications. It is a memory behavior where a stretched elastomer returns to a residual dimension after some time after removing the tensile load applied to it. It is removed by subjecting the elastomer through a cycle of stretching and removing the load applied. Understanding the Mullins effect will enable the life of a rubber product to be predicted - Beatty (2002).

2.5.3.5 Reinforcement

Rubber for example is normally reinforced with other materials such as carbon black. The influences of exact amounts of reinforcement are not included in the

constitutive equations. Reinforcement effects which show much as Mullins effect during loading and unloading were the focus of Merodio and Ogden (2003), Dorfmann and Ogden (2003), Dorfmann and Ogden (2004), Merodio and Ogden (2005). This led to a model referred to as a reinforcing model according to Merodio and Ogden (2005). Anisotropy influence was also observed in the fiber reinforced incompressible non–linearly elastic solids. Demirxoparan and Pence (2007a and 2007b) link the effects of the reinforcement to swelling – a situation to be found in cylindrical tube and soft body organisms like caterpillars and worms.

2.5.3.6 Cavitation

Cavitation damage occurs when the hyper-elastic material develop spaces or voids internally due to hydrostatic tensile stress. This could cause internal rupture of the material. Dorfmann et al. (2002) present results on cavitation damage and its effect on loss of rubber stiffness. In their work, they noticed void nucleation and the growth of micro cavities in natural rubber which was said to cause the break of bonds in its polymer network. Cavitation effect is not captured along in the constitutive equations, hence the researcher is expected to be aware of its development.

2.5.3.7 Payne effect

The Payne effect is an effect where an elastic material becomes more softened as it is excited by loading and unloading it at a particular frequency. The frequency of excitation in any mode has critical inelastic effects on elastomers according to Beatty (2002), Miller and Arbor (2008). In Beatty (2002) it was noted that fundamental frequencies decrease with increasing softening as exemplified in Figure 2.17, which is the result of the material response to frequency changes. In other words, as the frequency increases, the material becomes softened.

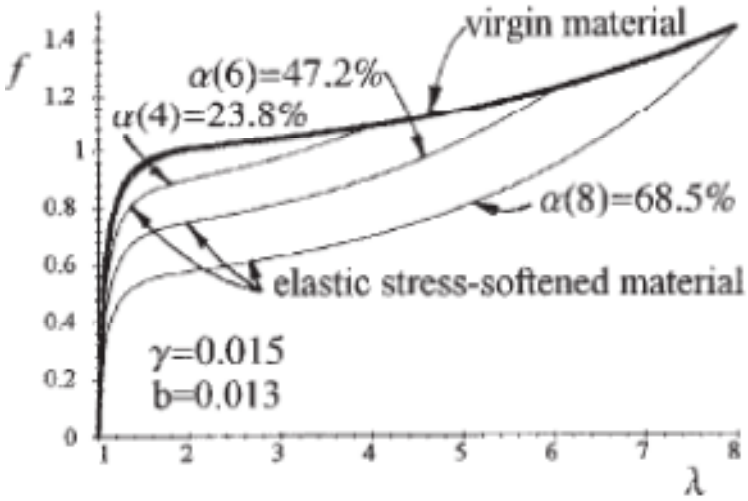


Figure 2.17 Stress-softening effects in the transverse vibrational frequency of a bio-material membrane. (f = frequency of vibration, α = preconditioning extent, γ=a dimensionless constant, λ=stretch. (Source: Beatty, 2002).

2.6 ADVANTAGES OF TRANSFORMING HYDROSTATIC JOINTS AND SUPPORTS INTO ROBOTIC JOINTS

Living organisms are very complex and difficult to imitate - CSN (2011). Truly there is significant progress being made such as Softbot (Trimmer et al., 2006), but on a new frontier, it is better to first understand some basic form and function of the simpler organisms in terms of mobility before moving on to a more complex neurological control of the same organism. A successful prediction in the form of a mathematical model implies a thorough understanding of the organism. Lamprey swimming (Skierczynski et al., 1996) and slime mold - *Physarum polycephalum* (Meyer and Guillot, 2008) are exemplary of lower organism successfully modeled neurologically. Lamprey was even used to control Khepera mobile robot while the slime mold controlled an hexapod robot (Meyer and Guillot, 2008).

There are clear advantages a hydrostatic joint has over the normal musculo-skeletal systems – from the biomimetic point of view, they are:

a) **Simple implementation** – mostly tubular flexible bodies - fluid filled as earlier described. A tubular elastomeric material filled with fluid or stuffed could represent the simplest of this structure.
b) **Unlimited joints** – If the above tube is not chambered, a rigid support with unlimited joints is easily created. The limitation will be due to the number of actuators and the control strategy. How the simple organisms control their bodies with such little brain has been the subject of much research - Skierczynski et al. (1996), Yekutieli et al. (2002), Mezoff et al. (2004), Rooney and Carroll (2007), Gutfreund et al. (1996) and Alscher and Beyn (1998).
c) **Continuum Robotics** – Though this research work is on hyper-redundant robots, the result can be extended to building continuum robots also as exemplified by Hannan and Walker (2003) and Yekutieli et al. (2002).
d) **Anisotropic** (like in caterpillar, *Meduca sexta* and worms), a directional motion can be built and thus simplifying the control.
e) **Isotropism** of hydrostatic body can be used advantageously in the design of robots for search and rescue missions in collapsed structures. The robot (such as softbot of Trimmer et al., (2006) can be extended to become load lifter by inflating it and is extremely simpler than the mechanically complex design used by Shammas et al. (2003).
f) **Weight** – This is debatable but cheaper material can be used for a light weight hydrostatic robot than those complex metal based ones like that of Shammas et al. (2003).

2.7 HYPER REDUNDANT ROBOTS

The term hyper-redundant robots was introduced by Chirikjian and Burdick (Chirikjian and Burdick, 1991) in the early 1990s to describe robots with numerous independent degrees of freedom (DOF). The hyper-redundant robot falls into two broad categories: mobile hyper-redundant robots such as snake robots and serpentine robots and fixed base robots

2.7.1 Mobile Hyper-Redundant Robots Such As Snake Robots And Serpentine Robots

The snake robots are multi-segment mechanisms that derive propulsion from the relative motion of the joints only. They use no wheels, legs, or tracks for propulsion. Examples are Gavin Miller S1 to S7 snake robots (Miller, 2010). Some researchers refer to them as snakebot. The serpentine robots are multi-segment mechanisms that derive propulsion from wheels, legs or tracks. Joints connecting the segments may be powered. Examples are KR-I (Hirose and Morishima, 1990), MOIRA (Osuka and Kitajima, 2003), OmniTread and OmniPede (Grzegorz et al., 2005).

2.7.2 Fixed Base Robots

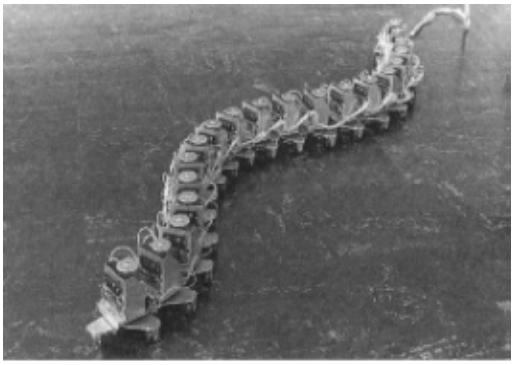
This is a hyper-redundant robot that has one of its ends fixed. An example is the urban search and rescue elephant trunk robot (USAR ETR) from Carnegie Mellon University (http://www.snakerobot.com)).

2.8 SOME EXAMPLES OF HYPER REDUNDANT ROBOTS AND THEIR APPLICATION AREAS

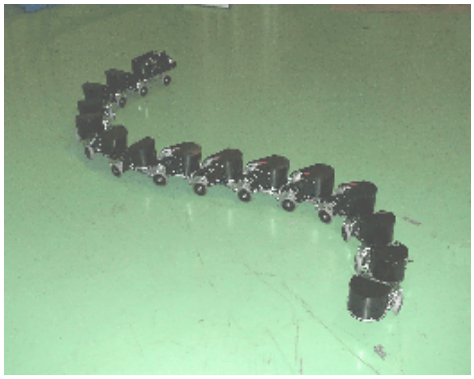
2.8.1 Active Cord Mechanism (ACM)

The first serpentine robot called Active Cord Mechanisms (ACM), (Figure 2.18) was built by Shiego Hirose in 1970 at the Tokyo Institute of Technology. ACM III and

ACM R2 (Revision 2) were both planar. That is each segment can only move in a plane relative to the other (1 degree of freedom). ACM - R3 and ACM - R5 have two degree of freedom joints and ACM-R5 is amphibious with replaceable joints (auto configured) in case of failures. All the ACM have passive wheels except ACM-R3 that uses active wheels for locomotion. ACM-R5 uses 32 bit microcontroller. The joints were made with stainless steel and plastics.



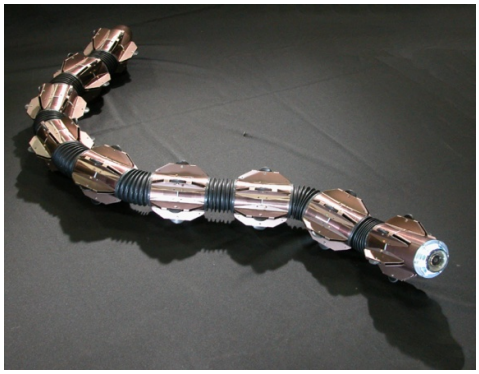
ACM III.



ACM-R2



ACM-R3



ACM-R5 Source Yamada et al., 2005

Figure 2.18 Some Hirose's Active Cord Mechanism (ACM).
(Source: http://www.robot.mess.titech.ac.jp/robot/snakes_e.html)

2.8.2 GMD Robot

Paap's et al. (1996, 1997) in their design of GMD (*Gesellschaft für Mathematik und Datenverarbeitung mbH Bonn* meaning Society for Mathematics and Data Processing) robot used a flexible compression joint actuated by winding and unwinding a wire about a motorized shaft. The shaft was placed in the middle of the joint (Figure 2.19). This approach enhanced the biological accuracy. It increased the smoothness of the body and decreased the discontinuities in motion shapes.

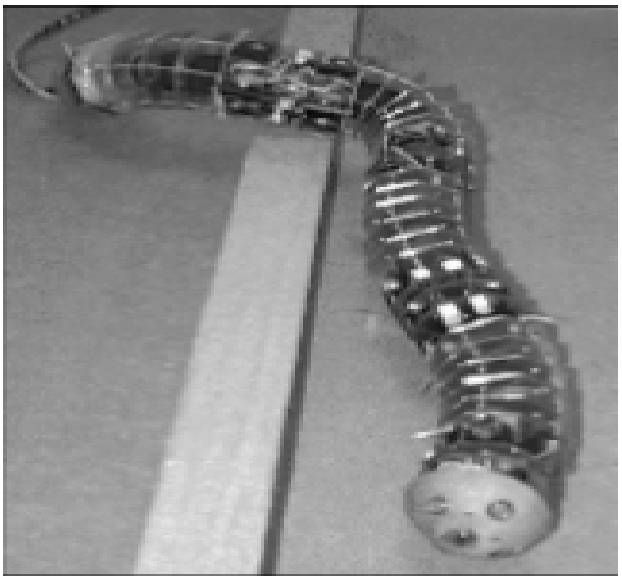


Figure 2.19 Paap's GMD Snake crossing an obstacle.
(Source: Paap et al., 1997)

2.8.3 Carnegie Mellon University Elephant Trunk Robot.

At Carnegie Mellon University, USA, as a response to development of urban search and rescue robot (USAR) (Wolf et al., 2003; Wolf et al., 2005) developed a series of elephant trunk robots (ETR) (Figure 2.20) based on a new (patented) joint design - Figure 2.1D, (Elie et al., 2003 and Wolf et al., 2003). Part of their goal was that the joint should be strong enough to lift up rubble on top victims of disasters. The disaster of the World Trade Center (WTC) –11 September 2001, Mexico city earth quake -19 September 1985, Florida-2009 disasters to mention just three, greatly fueled this work.

The WTC attack saw the first use of USAR in action. The robots used have wheels or tracks and access places unreachable or too dangerous for rescue workers and dogs. It was then many realize that these robots can only show and assist in locating victims but cannot actually rescue them and where there is tangled mesh, they cannot pass through either. They are also mostly tethered hence not autonomous and short ranged. This led attention to robots that could move on all terrain and through small spaces. The joints were made from hardened steel.



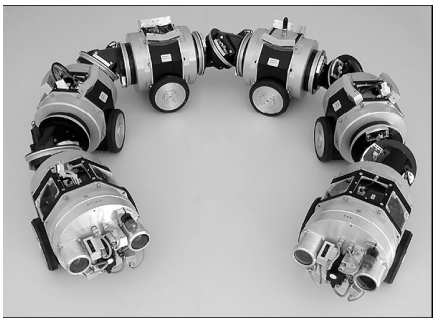
Figure 2.20 Urban Search and Rescue elephant trunk robot with camera on its end. (Source: Wolf et al. 2003)

Similar work on USAR robot was done by Kazuyki et al. (2005), Fumitoshi (2002) and Miller (2010).

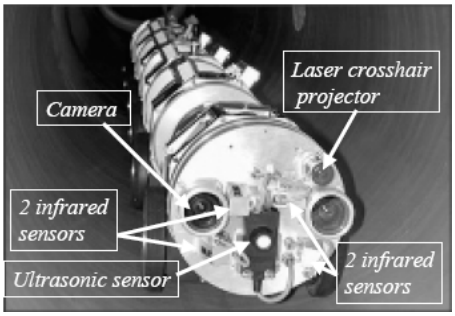
2.8.4 Germany Sewer And Pipe Inspection Robot

The public sewage system in Germany is about 400,000 km long and if it is in no good condition, sewage may leak out, possibly polluting soil and ground water and possibly eroding away building foundations. Most of their sewage piping are circular and are between 30 to 60cm in inner diameter. Teleoperated platforms were used with cabling length of about 200m. The size of the pipe, water presence, slurry, varying construction material will not allow just any robot to operate in such an environment. A

four wheel mobile platform was tested according to Joachim and Frank (1997), Marina and Hermann, (2002) and (Joachim, 2003), but climbing the steps at intersections defeated its use in very slippery sewage environments. The solution was MAKRO (multi-segment robot, operating autonomously in sewer pipes)- Figure 2.21. To aid autonomous navigation it carries several sensors on both ends – Laser cross air, 2-infrared sensor, ultrasonic sensor and transmitter and a camera. The joints are oblique made from steel plates.



View from top



End view showing sensor arrays



MAKRO in action at a T-Joint

Figure 2.21 MAKRO an autonomous robot for sewer inspection
(Source: www.ais.fraunhofer.de/projects/Makro/makro-engl/makro-e.html)

2.8.5 Pneu-Worm Robot or Wormbot

This is a commercial robot and much is not disclosed about its operation. Wormbot (Figure 2.22) is already in service for pipe inspection (Borenstein, 2006). It

uses twin bellow and inchworm motion method for moving within the pipe. The robot is tethered (power and air line supplying the bellows). It carries a camera on its front end and a remote monitor is supplied with it.

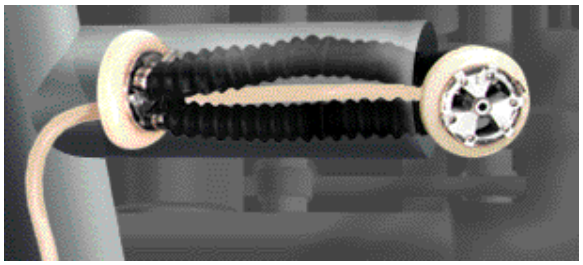


Figure 2.22 Pneu-Worm Robot
(Source: www.ornl.gov/info/ornlreview/rev26-34/text/tramain.html)

2.8.6 NASA Snakebot

Until the publication by Brooks and Flynn of a paper titled "Fast, Cheap and Out of Control: A Robot Invasion of the Solar System" (Brooks and Flynn, 1989), robots for space exploration have always been expensive projects. The paper led to changes in design of the rover (i.e. lunar rovers) research from building the one, big, expensive robot to building lots of little cheap ones.

At NASA's Ames research center, USA, different small scale robots are being developed for space and planet exploration (Kevin, 2003 and Haith et al. 2000), Snakebots is one of them. NASA snakebots (Figure 2.23) are based on Mark Yim polybot - Figure 2.24. The polybot is capable of countless reconfiguration and accidental loss of a segment will not affect the other - in fact, they will be able to function independently as each segment has its own microcontroller. The NASA robot will carry touch sensor over its body. They are expected to help with Martian landscape exploration as they dig into soil, burrow down to depths that other robotic probes can't get into, slither into cracks, navigate rough terrain where wheeled and legged robots will

get stuck or topple. Since they will be more durable and cheaper, a large number can be sent to explore MARS.



A B

Figure 2.23 NASA Snakebot A) closer view of the robot. B) Field test of the robot (Source: Kevin, 2003)

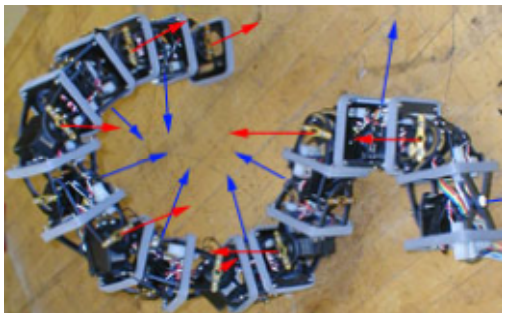


Figure 2.24 Yim's Polybot Robot as used by NASA. (Source: Kevin, 2003)

The polybot was built at Xerox PARC USA. It is planar i.e. 1-degree of freedom per segment. Yims polybot modules are good for quick assembly but produce very weak joints at high cost. The joints were revolute and use stamped metal and plastic.

2.8.7 OBLIX and MOGURA

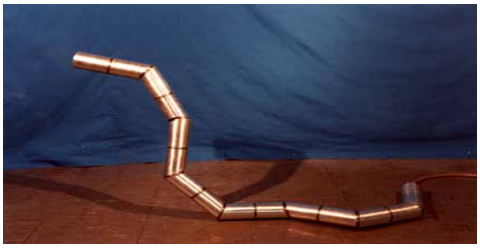
MOGURA (Figure 2.25c) was developed between 1982-84 by Hirose and Yoneda Robotics Lab (Japan) according to Hirobumi (1985), for grinding the water runner of the water wheel for hydro electric power generation. The MOGURA arm which utilizes an oblique swivel mechanism was developed in cooperation with Toshiba Company based on OBLIX (Figure 2.25a and 2.25b). (http://wwwrobot.mes.titech.ac.jp /robot/ snake/oblix/oblix_e.html)

After casting a water wheel for hydroelectric power generation with a diameter of about 4-5m, MOGURA acts as the robot arm that performs the grinding operation on the water runners that follow along the fins of the interior part. Until this time, workers have to climb into the curved runners to measure the surface conditions and do the grinding as shown in Figure 2.6. MOGURA is made from an oblique swivel mechanism that forms a compact and highly rigid arm. It is assembled and used as shown in Figure 2.27. The total length is 2.5m, the diameter is 200 mm, and the oblique swivel angle is 15^0.

The joints used by OBLIX and MOGURA are made from steel.

2.8.8 OmniTread

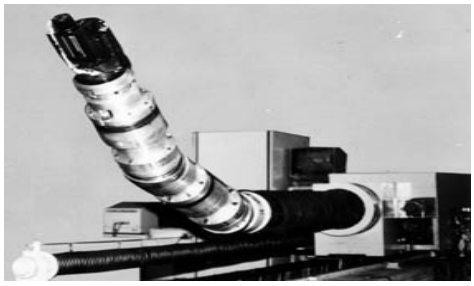
This is an example of serpentine robot**.** The OmniTread is shown in Figure 2.28 in different environments. OmniTread 8" is pneumatically driven externally with dual rubber tracks per side (i.e. 8 per segment). The OmniTread 4" (Figure 2.29) carries its own air supply onboard and has one track per side (or 4 tracks per segment). Both have bellow joint for turning.



A) OBLIX 3D motion



B) OBLIX with wheel



C) MOGURA assembled

Figure 2.25 OBLIX and MOGURA in different configurations
(Source http://www-robot.mes.titech.ac.jp/robot/snake/oblix/ oblix_e.html)

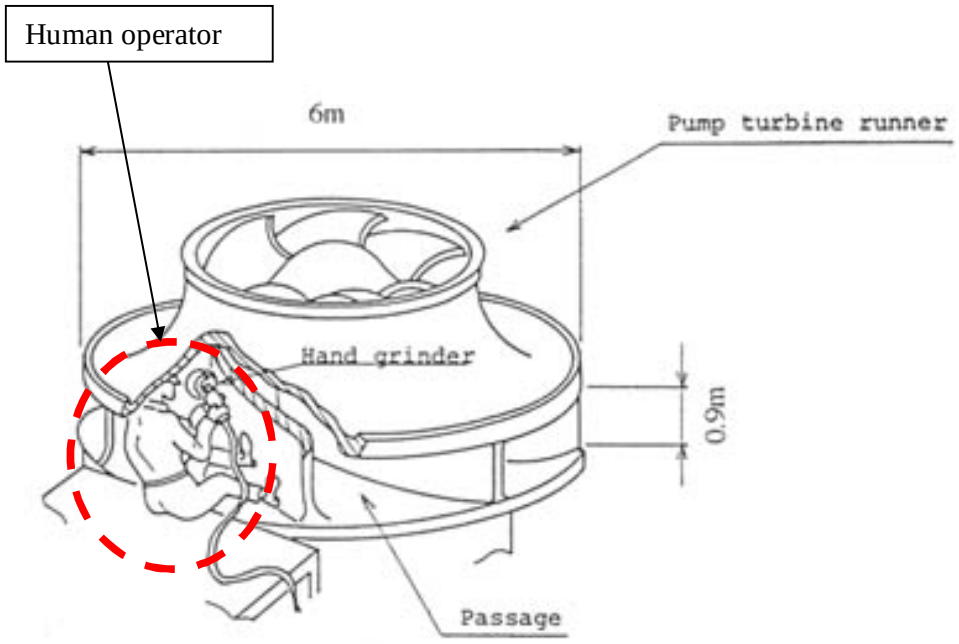


Figure 2.26 Conditions for the waterwheel grinding operations, men have to enter to grind with hand. (Source: http://www-robot.mes.titech.ac.jp /robot/snake/oblix/ oblix_e.html)

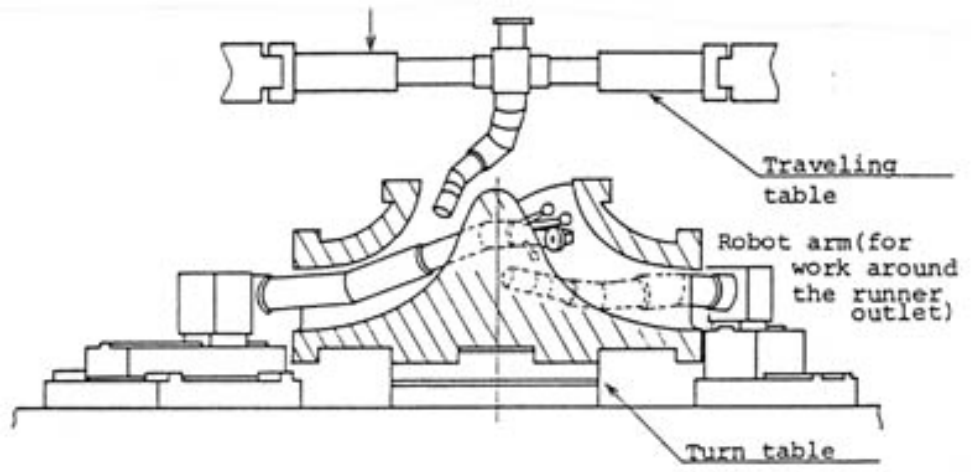
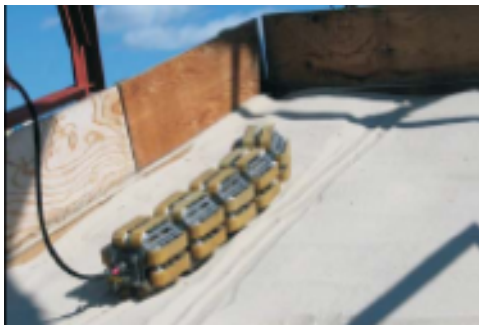


Figure 2.27 Configuration of the MOGURA system when used for grinding operations (Source: http://www-robot.mes.titech.ac.jp/robot/snake /oblix/oblix_e.html)



A Climbing a smooth slope



B At the back of a truck



C Among rocks



D Climbing a pipe

Figure 2.28 OmniTread 8" – (Source: Borenstein, 2006)

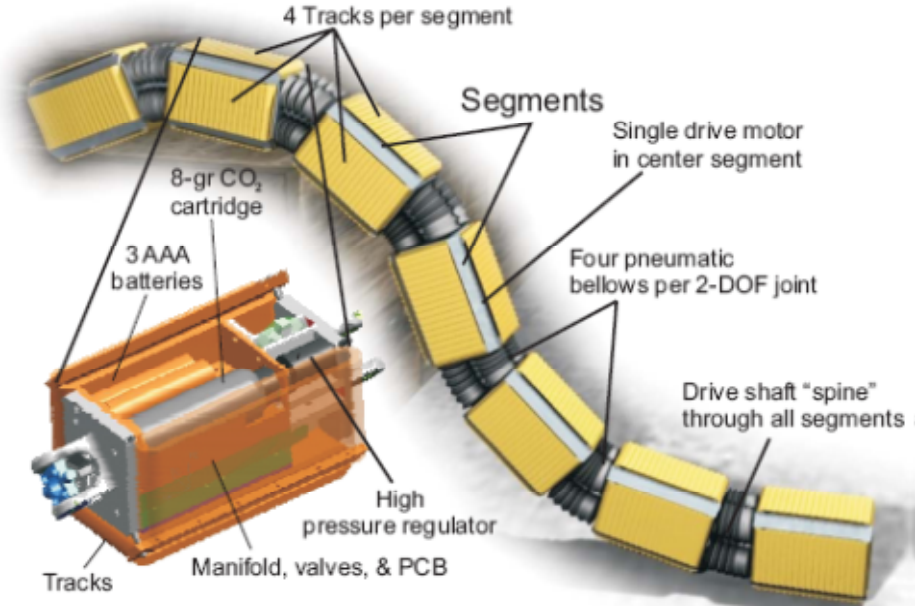


Figure 2.29 OmniTread 4" with the segment internals on the left.
(Source: Borenstein, 2006)

2.9 OTHER APPLICATIONS OF HYPER-REDUNDANT ROBOTS

2.9.1 Military Purposes

They can be used for detonating unexploded ordnance (UXO) and bomb disposal, spying and espionage, surveillance. Wolf et al. (2003) gave description of a surgical bomb disarming robot that moved slowly. It was developed at Pacific Northwest Labs in the USA. It was to be used for probing the internal of UXO without accidentally detonating it - hence its slow motion. The mechanism is kinematically a sequence of linearly actuated universal joints stacked on top of each other - Figure 2.1D.

For stealth purposes, a snake robot will need to be autonomous in selecting its paths among obstacles. This is an undeclared goal by Sensor Base Planning Laboratory of Carnegie Mellon University (http://www.snakerobot.com) and Zhang et al. (2002) in

the development of motion planning for hyper-redundant robots. The extension of the achievement of such a feat is staggering. It means a very slender and camouflaged rod can move about with ability to spy on enemies positions, steal information from them and enter highly fortified places or carrying ordinances even right to the door of the defense head quarter and much more than the mind can conceive now.

Kevin (1997), in his introduction to his works wrote that the FBI and Special Forces of USA made enquiry about his work because they can see future use of it.

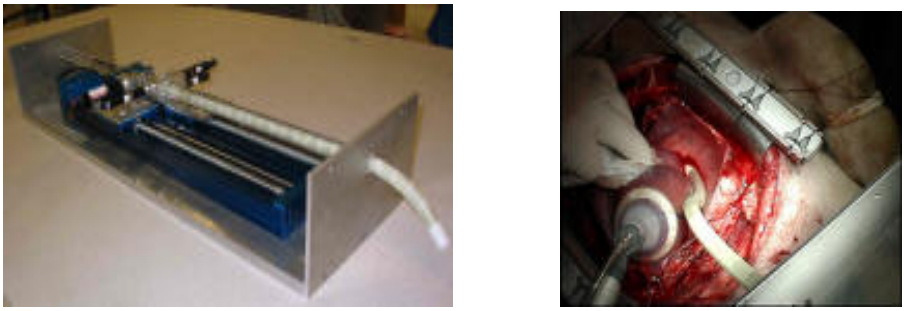
In a 2005 expo at Japan, Hirose demonstrated a very realistic swimming snake robot (Figure 2.18 – ACM R5) to which the most comment on it was that the Japanese will surely load it one day with a bomb.

2.9.2 Medical Purposes (Minimally Invasive Surgery)

Surgery now uses robotic and image processing systems in order to interactively assist medical teams, both in planning surgical interventions, and in their execution. The objective of this new technique is to enhance the quality of surgical procedures by minimizing their side effects (smaller incisions, lesser trauma, more precision etc), thus increasing patient benefit while decreasing the surgical cost. These techniques are being successfully introduced in several areas of surgery: Neurosurgery, orthopaedics, micro-surgery, cardiovascular and general surgery etc (Jean-Pierre, 2000).

Minimally invasive surgery helps patients by accelerating postoperative recovery, Nobuto (2003). It is usually aided by use of laparoscopic and endoscope devices which are used for getting images from remote locations in machines and the human body. The end bending and direction is controlled by cable at its base. The motion of the tip of the laparoscope and endoscope devices are not accurate and complex shapes can neither be followed accurately because they are both rigid tools.

A serpentine device (Figure 2.30) is being tested, that could solve the problem of the endoscope in handling complex path successfully. A successful test was done on a pig (http://www.snakerobot.com) at Carnegie Mellon Biorobotic Laboratory, USA.



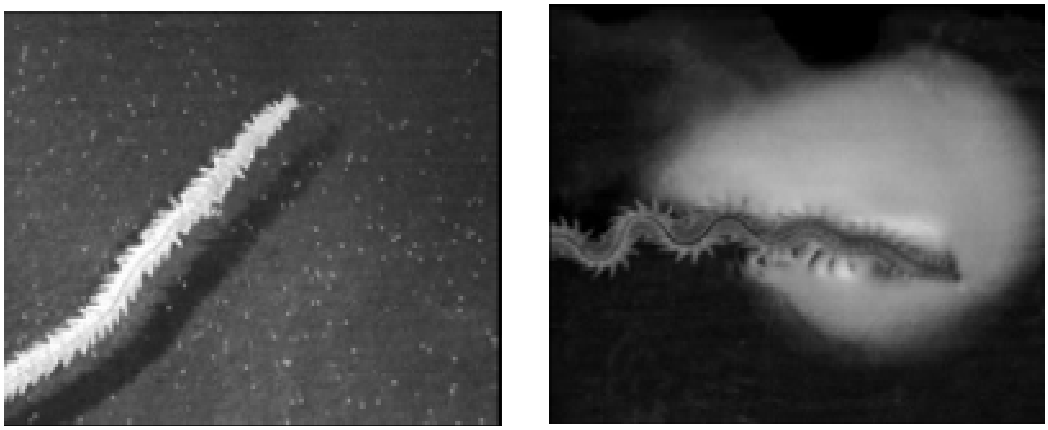
A B

Figure 2.30 An endoscope (A) The endoscope device (B) The endoscope is being inserted behind a pig heart. (Source: http://www.snakerobot.com)

The device was designed to be pushed into the body with a servo motor just like any other endoscope. It uses cable to adjust its direction of bending. According to Kevin, (1997) and Thomas et al. (2005), a self propelled endoscope will open up a wide market and benefit the people as it will reduce discomfort associated with the pushing.

Thomas et al. (2005) presented their investigation on self moving endoscope. They reported that the main problem is the generation of sufficient friction between the device and the slippery mucous-lined tract wall. A biomimetic approach was followed. The common ragworm, *Nereis diversicolor* (Figure 2.31), successfully moves in a variety of slippery environments such as mud and is capable of burrowing through the substrate, crawling over the substrate and swimming in open water. During fast crawling and swimming the body undulates from side to side with each body wave moving from the posterior region to the anterior. Lateral appendages (parapodia) are synchronized with the body waves and aid in thrust generation by acting as paddles

during swimming and legs during crawling. During slow crawling no or only small amplitude body waves are present and thrust is generated by the parapodia. Extruding distally from the parapodium are three bundles of hairs (setae), which are the structures that allow the worm to crawl effectively in slippery substrates.



A B

Figure 2.31 Nereis diversicolor: A) Slow and B) Fast crawling. (Source: Thomas et al., 2005)

2.10 STRATEGIES USED FOR CONTROLLING HYPER-REDUNDANT ROBOT JOINTS

In the cause of developing a biomimetic hyper-redundant robots, various motions employed by the biological counterpart have to be programmed into the robot controller. Biomimicry requires that the object be studied scientifically and its result quantified, this was what Hirose (Hirose and Morishima, 1990) did using live snakes, Figure 2.32. Similarly, Miller (2010) built his S7 prototype as a result of his encounter with a python. Hirose discovered that motion was more than a two-dimensional problem in his study of live snakes. His first ACM robot is planar and has very poor performance. There is a slight body raise called sinus lifting (Figure 2.33) were friction with the surface will rather hamper motion.

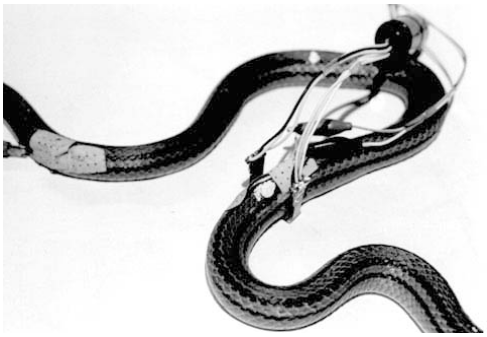
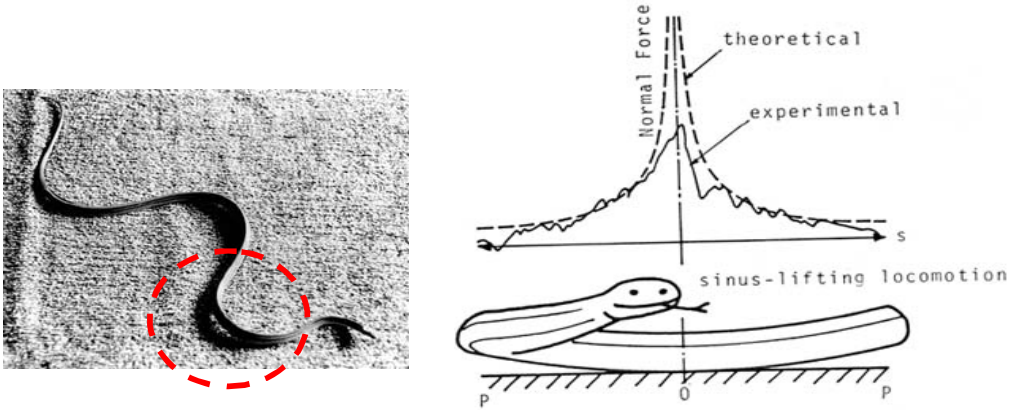


Figure 2.32 A snake equipped with EMG and normal force detectors
(Source: http://www.robot.mess.titech.ac.jp/robot/snakes_e.html)



(A) **(B)**

Figure 2.33 Snake motion (A) Sinus Lifting to reduce friction (B) Sketch of normal force distribution about the sinus
(Source: http://www.robot.mess.titech.ac.jp/robot/snakes_e.html)

There are three approaches according to Kevin (1997) used in controlling hyper-redundant robot joints, they are:

1. Serpenoid curve method
2. Follow the leader approach and
3. Built in motion pattern

2.10.1 The Serpenoid curve

The serpenoid curve (Figure 2.34) was a result of realization of a study on live snakes by Hirose in Japan (http://www.robot.mess.titech.ac.jp/robot/snakes_e.html). The equation for the serpenoid curve is shown in equation 2.5. Snake motion does not follow sine wave as thought earlier.

$$x(s) = sJ_o(\alpha) + \frac{4l}{\pi}\sum_{m=1}\frac{(-1)^m}{2m}J_{2m}(\alpha)\sin\left(m\pi\frac{s}{l}\right) \tag{2.6}$$

$$y(s) = \frac{4l}{\pi}\sum_{m=1}^{\infty}(-1)^{m-1}\frac{J_{2m-1}(\alpha)}{2m-1}\sin\left(\frac{2m-1}{2}\pi\frac{s}{l}\right) \tag{2.7}$$

where

x(s) = displacement in the x directions

y(s) = displacement in the y directions

s = curve length

l = body length

J(α) = Bessel functions

m = joint positions

A plot of this parametric equation will yield Figure 2.34 curves.

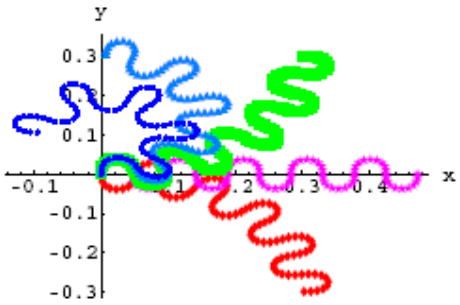


Figure 2.34 Serpenoid curves showing pattern as the snake take turns to left, right and forward motion. (Source: Kevin, 1997)

2.10.2 Follow The Leader Approach

In follow the leader approach, the head (or the tail if reversing) segment is controlled. The information is passed to the next segment till the last segment is reached. The desired motion is mathematically generated.

2.10.3 Built In Motion Pattern

The use of built in motion pattern means that the microcontroller (or microprocessor) will have to adjust each segment according to the predefined motion stored in its memory. This is less mathematically involving but not very flexible. Researchers who use microcontrollers prefer the last two methods as floating point mathematics are avoided. The use of serpenoid curve equation involves floating point calculations.

2.11 PATH PLANNING

Path planning in the parlance of hyper-redundant robotics refers to the methods used in making the joints to form the desired shape and curve and follow a desired path while avoiding obstacles during operation.

Coordinating all the actuators and joints to produce useful motion/gait is a major challenge in hyper-redundant robot implementations. Many of the research work published are those of robots being tested in either an uncluttered environment – i.e. no tangled mass to navigate, or use of geometrically fixed environment as in the MAKRO robot used for sewer environment inspection (Marina and Hermann, 2002). The reason is that each segment activity is not an isolated act. It is a duplication of the first segment on the link (the head) if it is a snake robot, or the memorized path followed by the previous link in case of fixed base ones (i.e. robotic arms). The motion requirement is that of 3-D in an unmapped environment. The problem is referred to as path planning or motion planning. Choset and Henning (1999) are the few researchers working explicitly on serpentine motion planning.

Some solutions tried in hyper-redundant robot motion planning strategy include; roadmap, tunnels, local sensor based planning, generalized voronoi graph (GVG) and Classical planning.

2.11.1 Roadmap

This was introduced by Chirikjian and Burdick (1990b). Roadmaps have the following properties: **accessibility**, **connectivity** and **departability** according to Choset and Wade (1999). The meaning of this is that the end of the robot can move between two points via a path in a connected component of the robot free space by first finding a path onto the roadmap (accessibility), traversing the path to the vicinity of the goal (connectivity) and then constructing a path from the roadmap to the goal (departability).

2.11.2 Tunnels

This is another path planning method by Chirikjian and Burdick (1990a). One suggestion is based on the definition of tunnels through obstacle field into which the serpentine mechanism slips through. They did not prescribe any strategy of constructing such tunnels.

2.11.3 Local Sensor Based Planning.

In this case, the serpentine device maintains its end effector location while it locally adapts to a time varying environment. The entire body fits within a tunnel and then part of the tunnel is continuously adapted away from any object that became unacceptably close as sensed by the mounted body sensor - (Takanashi et al., 1993).

Sensor based planning incorporates sensor information, reflecting the current state of the environment, into a robot's planning process, as opposed to classical planning, where full knowledge of the world's geometry is assumed to be known prior to the planning event. Processing the sensory data for subsequent use in planning also offers many challenges

(http://robotics.caltech.edu/).

A global sensor based planning (Reznik and Lumelsky, 1992) assumed a perfect sensor all over the body of the robot to detect obstacles, research is on-going in this area – such as NASA snakebot which will have sensors all over the body for motion planning or just normal touch sensors.

2.11.4 Generalized Voronoi Graph (GVG)

This is a modified roadmap - Choset and Burdick, (1994, 1995a, 1995b and 1996). GVG is the set of points equidistance to *m* obstacle in *m* dimensions. In the plane, the GVG is simply the generalized Voronoi diagram (O'Dunlaing and Yap, 1985) which is the set of points equidistance to two obstacles. In R^3 (i.e. 3 dimension), the GVG is the one-dimensional set of points equidistant to three obstacles. According to Choset et al. (1997), Konukseven and Choset (1997), Nagatani et al. (2002), Choset and Henning (1999), Lee and Choset (2004), Lee and Choset (2005a, 2005b), **follow-the-leader** approach (section 2.10.2) will be capable of using GVG for its path planning because it is a sensor based planning. The head of the serpentine device moves along the GVG, while the rest of the body follows. This way a set of curves known as backbone curves (Chirikjian and Burdick, 1990b) are created. For example, Figure 2.35 is generated while the segments are adjusted as the serpentine device moves between the obstacles. Where there are sharp corners an approximate curve is formed due to the limit in the mechanical joints – this is referred to as curve deformation (Choset and Lee, 2001).

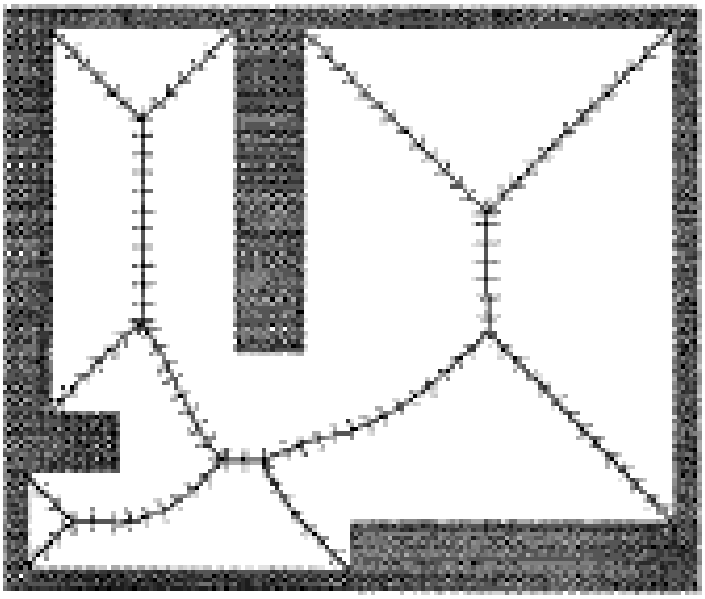
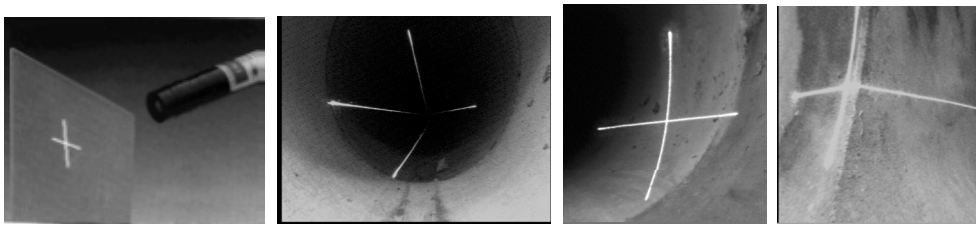


Figure 2.35 The ticked line segments are the planar GVG for the bounded environment. (Source: Choset and Lee, 2001).

2.11.5 Classical Planning

This is a method which requires the full knowledge of the environment in which to operate ahead of time. This is not a realistic method especially in an outdoor environment according to Konukseven and Choset, (1997).

In **geometrically fixed environment** such as sewer pipes that are at right angle to each other, path planning is not needed – (Marina and Hermann, 2002). It was demonstrated that simple vision using shape deformation of Laser cross-hair (Figure 2.36) on surfaces has enabled MAKRO to navigate the sewer networks. The basis for the success was that vision was never to be viewed in isolation but by taking into account the environmental constraints. In other word when a laser pattern is projected onto a scene, the shape of the footprints is like a condensed print, which carries information about the scene geometry from which useful navigational information can be derived. This falls into the class of vision termed cheap vision- Horswill (1992).



A B C D

Figure 2.36 Laser crosshair projector (A). (B), (C) and (D) three surface types with overlaid laser footprints. The pattern is an indicator of the environment configuration. (Source: Marina and Hermann, 2002).

2.11.6 Motion Planning For Fixed Base Hyper-Redundant Robots

For **tethered robot** (i.e. one end fixed as in elephant trunk robot (ETR) an approach for motion planning is based on topological decomposition of space called WAFT (WAve Front Topology) - Ohno and Hirose (2001). This decomposition of space allows for path planning that is path-dependent, meaning that veering left around the first obstacle encountered will change the options that are available in the future as compared to the options had the path to the right of the first obstacle been chosen. The WAFT planner also uses sensor based method (http://voronoi.sbp.ri.cmu.edu /research/rsch_rodgvg.html).

2.12 A REVIEW OF ACTUATORS FOR ROBOTIC JOINTS

The **actuator** is the component that moves the segment under the control of signal from the microprocessor or microcontroller to give it a desired gait/motion. Selection of an actuator is based on things like:

a) Power requirement

b) Speed of operation (of the joint)

c) Torque to lock a link into the generated angle into place

d) Response to control signal

e) Fidelity – faithfulness to the control signal pattern

2.12.1 Brief Description Of Actuators (Kevin, 1997);

a) **Polymer Gels**

Some polymers are capable of converting chemical energy to mechanical work in isothermal conditions. These polymers significantly change their length in response to chemical changes involving altered temperature, pH, or applied electric fields. Volume changes can be as high as a factor of 1000. For polymer gels to be useful there are many technical issues to resolve. There are issues of strength, response, stress-strain relations, fatigue life, thermal and electrical conductivity. Other issues include efficiency, power and force densities.

b) **Shape Memory Alloys (SMA)**

This refers to NiTiNoL (nickel-titanium alloys). These alloys in the form of wires will stretch easily at room temperature but will return to their original forms when carrying current that also heats them up. Longer stretches such as 8% are possible for a few cycles of operation but a shorter strain like 5% will allow millions of cycles. The 8% strain will correspond to 600N/mm^2. The response time is slow, and depends on the rate of heat removal.

c) **Piezoelectric Devices**

These are crystalline materials that change size when electric voltage is applied. They also generate electric voltage when strained. Their limitation is that the size changes are very small, they have non-linear behaviour, high hysterisis and creep. They however have very fast response and could produce very large forces.

d) **Electrostriction Devices**

These are similar to piezo crystal materials but with the fact that electrostrictive crystals are symmetric. The strain is proportional to the square of electric field. This

property is independent of piezoelectric effect and is due to rotation of polar domains in ceramic through the field. It has the advantages that it can use lower voltages - compared to piezo crystals. It also has very low length changes and some of piezo crystals problems according to Kelvin (1997).

e) **Magnetostriction**

Magnetostriction is the mechanical deformation of a ferromagnetic material when subjected to a uniform magnetic field. Unlike piezo electrics, the displacement per unit field actually increases with length. Internal stresses in the material due to anisotropy energy are required to magnetize it in certain directions relative to the crystal axes and vice versa. The strains and displacements can be significantly more than piezo electrics but piezo electric materials can be stacked to give nearly the same stroke per length. Terfenol-D, used in several magnetostrictive commercial products, offers high forces and good strain.

f) **MEMS (Micro-Electrical Mechanical Systems) actuator**

These are actuators based on the use of semiconductor technology to fabricate mechanical parts that can move objects.

g) **Thermal actuators**

They use the thermal expansion property of materials to actuate. We see this in the electric pressing iron for example. The force generated is very high but the speed of response is slow. Thermopolymers are new materials that have faster response and are being researched upon.

h) **Electro-magnetic motors**

The current carrying conductor within a magnetic field will generate motion. This is used to form an electric motor. The technology is well established and is improving

as power density of the conductor increases with newer superconductors.

i) **Pneumatic actuators**

These use compressed air or other gas to move a ram or pneumatic motor. High force, high speed actuation can be generated within a small space. The limitation however has to do with the gas source/supply and precision position control. Another limitation is possible leakage and material wear.

j) **Hydraulic actuators**

Hydraulic actuators work similarly to pneumatic actuator but uses fluid instead of air.

The most desired actuating device is artificial muscle using any of the above technology, but up till now, research is still vigorously on. Some progress has been made, for example, platinum plated perfluorosulfonic acid polymer (ICPF) operating in water (a must condition) has been used to design an underwater robot that operate as linear (muscle like) actuator – Guo et al. (1998).

2.12.2 Tested Method Of Actuating Hyper-Redundant Robots

Various actuating devices have been tested all with the aim of higher power to weight ratio and lower power consumption and small volume.

The commonest approach of actuating the segment of hyper-redundant robot is to place a motor inside each one. For planar robot such as Hirose ACM, a single motor is used per joint giving each joint a single degree of freedom. Those that have two or more DOFs are equipped with two motors. This arrangement has the advantage of ease of controlling each segment independently. However, the large number of motors used increase weight, power consumption and reduced maneuverability.

Examples of tried actuators are:

1. **Remote control servomotors** (Kevin, 1997 and Miller, 2010)
2. **Permanent magnet DC motors** (Anani et al., 2004),
3. **Pneumatic motor** (Grzegorz et al., 2005; Ohno and Hirose, 2000; Paulina and Jörg, 2003 and Hitoshi et al., 2006)
4. **Hydraulic (water) motor** - Hitoshi et al. 2006,
5. **Artificial muscle** platinum plated perfluorosulfonic acid polymer (ICPF), Guo et al. (2004), electro-actuated polymer (EAP)), Piezocrystal, Magnetostrictive, Shape-Memory Alloy (SMA), Shigeo et al. (1989).

Examples of tried mechanisms are:

1. **Cable** - Wolf et al. (2003), Ma et al. (1992)
2. **Hydraulic cylinders** - http://www.act.sys.okayama-u.ac.jp/wormrobot.html
3. **Gear box** - Paulina and Jörg (2003), Miller (2010)

For the serpentine robots, a variety of methods have been employed in driving the mechanism for locomotion used by serpentine robots. Most are the same as with snake robots. The locomotion devices tested are

1. Legs - Grzegorz et al. (2005),
2. Tracks - Grzegorz et al. (2005), Paulina and Jörg (2003), Kazuyki et al. (2005)
3. Wheels - Marina and Hermann (2002), Joachim (2002)
4. Scale (rubber) - Charles and Antonio (1998).

2.13 REVIEW OF PAST WORKS ON ROBOTIC FISH

Fish are known for their fulgurating acceleration inside water. “It is well known that the tuna swims with high speed and high efficiency, the pike accelerates in a flash

and the eel swims skillfully into narrow holes. Such astonishing swimming ability inspired researchers (Streitlien, et al., 1996; Anderson, 1996; Guo et al., 1998; Kato, 2000; Liang, 2002; Yu, 2002; Jindong and Huosheng, 2004) to improve the performance of aquatic man-made systems. Instead of the conventional rotary propeller used in ships or underwater vehicles, the undulation movement like fish provides the main energy of the robotic fish. The observation on the real fish shows that this kind of propulsion is more noiseless, effective, and manoeuvrable than the propeller-based propulsion" - Jindong and Huosheng, (2003).

Four robotic fish models will be reviewed in this work; they are Robotuna, Robopike, PF series and University of Essex fish robot.

2.13.1 Robotuna

Description: David (1994) developed Robotuna (Figure 2.37) in MIT. Delrin plastic was used for most of its construction and epoxy for sealing. The electronics is Onset model 8 computer (68332) with digital wireless modem and DC-DC converter. The tail (Figure 2.38) is made of rings of delrin plastic.

Limitation: It could not float nor swim because of its weight (3.6kg) and other heavy material used for its construction.

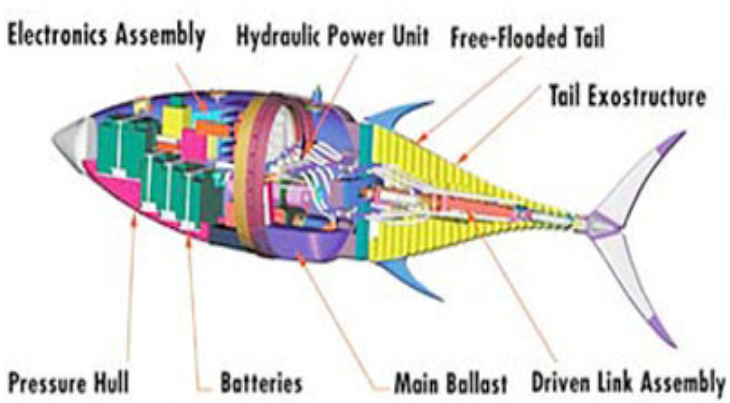


Figure 2.37 Robotuna (Source: http://web.mit.edu/towtank/www/Tuna/tuna.html)

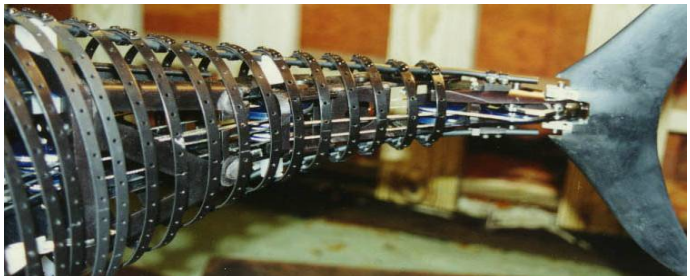


Figure 2.38 Robotuna tail construction
(Source: http://web.mit.edu/towtank/www/Tuna/tuna.html)

2.13.2 Robopike

Description: Robopike (Figure 2.39) is also from MIT and is a creation of John Muir Kumph (Kumph, 1996). It was a continuation of work on Robottuna. The pike (a fish) was chosen because of its excellent accelerating and turning abilities. Pike has very quick turning and fast acceleration from rest. In the wild, the pike accelerates at rates of 8-12 m/s^2.

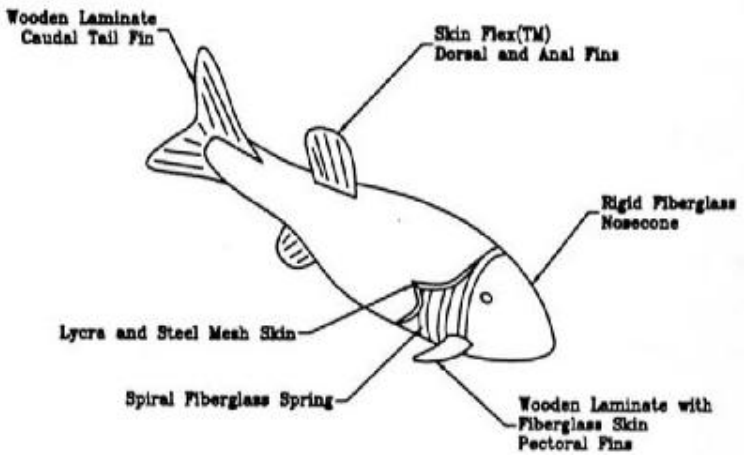


Figure 2.39 Robopike (Source: http://web.mit.edu/towtank/www/Pike/pike.html)

Robopike is controlled by a supervisory controller. The navigation is performed by a human, and a computer interprets the controls so that the robot can perform as expected.

Comment: Robopike uses only three segments, thus the size of the fish is reduced, allowing the use of inexpensive actuators. This means that while the shape of the fish cannot be made to resemble exactly the shape of a real fish, a close shape can be obtained. The tail is made up of spiral spring exoskeleton (Figure 2.40) using delrin. Robopike was used for studying drag reduction in fish like locomotion.



Figure 2.40 Robopike spiral spring exoskeleton of the tail section.
(Source: http://web.mit.edu/towtank/www/Pike/pike.html)

2.13.3 Japanese PF-300, PF-600, PF-700,UPF-2001 Robotic Fishes

Description: These Japanese robotic fishes (http://www.nmri.go.jp/eng/ khirata/fish) were designed for different purposes.

1. The **PF-300** (Figure 2.41) was for studying turning performance and straight line propulsion.
2. The **PF-600** is designed to study propulsion and improve on PF-300.
3. **PF-700** was designed for high speed, and had a DC motor as a power source. The shape was modeled after mackerel and pike, so PF-700 had a very slim body. A maximum speed of 0.6m/s was obtained by PF-700 at tail swing of 15^{o} amplitude.
4. **PF-2001** (Figure 2.42) was designed to exploit 3D motion. It has the up -down motion mechanism with a moving weight. A maximum speed of 0.97m/s was obtained by the PF 2001.

Comment: These fishes carried their own float (i.e. they have fixed depth) except PF-2001. They all have their flexible parts made up of plastic revolute joints.

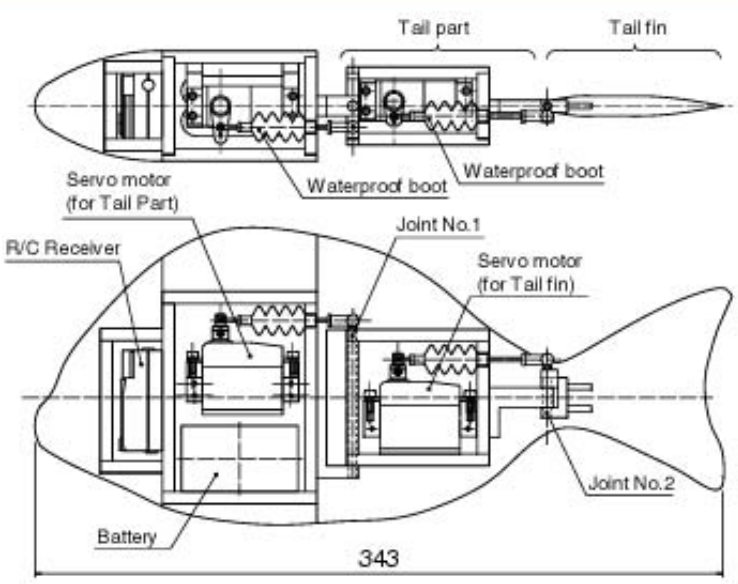


Figure 2.41 PF-300 robot (Source: http://www.nmri.go.jp/eng/khirata/fish)

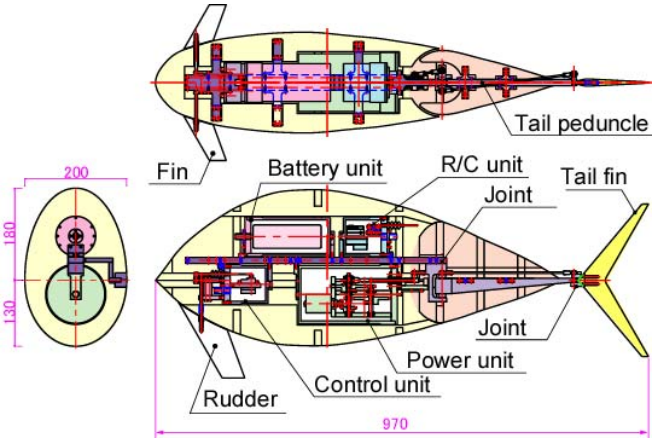


Figure 2.42 PF-2001 robot (Source: http://www.nmri.go.jp/eng/khirata/fish)

2.13.4 Essex G9 Robotic Fish

Description: Essex G9 robotic fish (Figure 2.43) is about 32cm long and has 3 R/C servo motors and 2 DC motors. Three servomotors are concatenated together in the tail to act as 3 joints (for the G9 but more than that for other series like the one shown in Figure 2.44), 1 DC motor is fixed in the head to change center of gravity (COG) of the

fish and 1 DC motor controls the micro-pump for float control. On the back of the fish body, a dorsal fin is fixed vertically to keep the fish from swaging. The central controller of the robotic fish is based on a 400Mhz Gumstix Linux computer and is responsible for sampling data from sensors, processing data and making decisions.

Comments: It has a linear speed of 0.2m/s, at maximum tail beat frequency of 0.5Hz. It is able to bend its body at a big angle in a short time (about 90°/0.20sec). The researcher idea is to directly link the servomotors (thus the motors themselves form the joints), this introduces inertial and hence low tail oscillation speed obtainable to 0.5Hz.

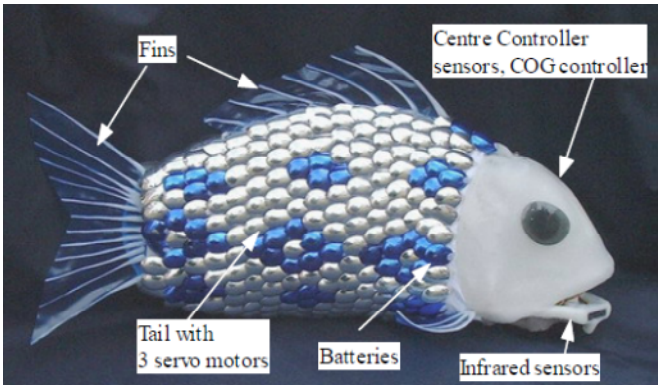


Figure 2.43 Essex G9 robotic fish – (Source: Jindong and Huosheng, 2003)

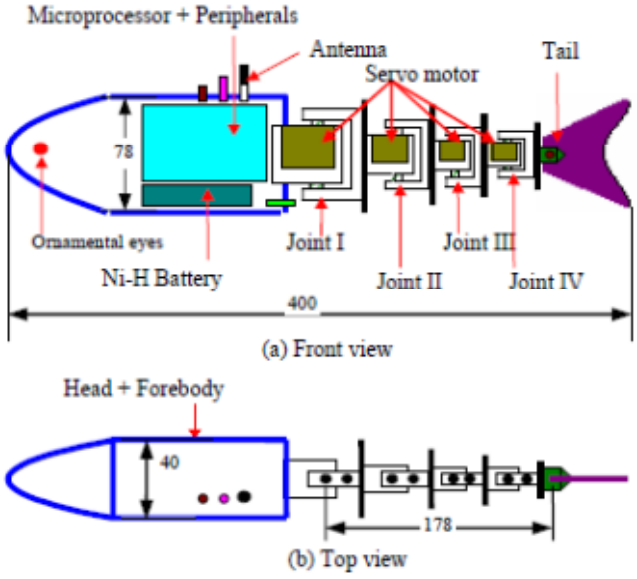


Figure 2.44 Mechanical Configuration of the Essex Robot Fish.
(Source: Jindong and Huosheng, 2004)

CHAPTER THREE

DESIGN CONSIDERATIONS, THEORIES AND CALCULATIONS

3.1 DESIGN CONSIDERATIONS

The design considerations are (1) biomimicry, (2) simplified control scheme of the hyper-redundant joints (3) simplified and functional joint design, (4) material selection and (5) capturing the model geometry/design.

3.1.1 Biomimicry

This refers to close performance to the biological model being imitated specifically in motion pattern. To achieve this design consideration, carbon-black-reinforced rubbers is used. It is has been shown to have very close mechanical properties to biological tissues.

Natural rubber (polyisoprene) is a flexible material with very wide compositions. Fundamentally, they are made from latex extracted from the para rubber tree (*Hevea brasiliensis*) plus carbon sooth (as filler), sulphur (as vulcanizing ingredient) and several other proprietary materials added for different end purposes.

Using rubber for artificial hydrostatic joint design requires that Mullins effect, Payne effect and temperature be taken into cognizance as shown in the literature review; they have significant effect on the performance of the end product. Rubber was also shown earlier to have similarity to living tissue especially hydrostatic support used by invertebrate bodies.

3.1.2 Simplified Control Scheme Of The Hyper-Redundant Joints

It is desired to use control scheme on the joints that is achievable without very high computational cost. The use of built in pattern(s) for motion control strategy simplifies the need for floating point calculations especially for the serpenoid curves that describe hyper-redundant body motions. Furthermore, sensor based path planning is computationally less tasking and is hereby adapted for this work.

3.1.3 Simplified And Functional Joint Design

Biological bodies have simple mechanical designs that function because of the nature of the materials used in building them, and actuating them. The goal of achieving this is possible by copying nature and using materials very close to those used by nature. One of the simplest and functional joints found in nature is the hydrostatic joint.

3.1.4 Material Selection

Carbon-black-reinforced rubbers have mechanical properties close to those of living tissues and hence qualify for use for the hydrostatic components. A fluid filled design is not desired, therefore the design will imitate muscular hydrostat as closely as possible – with a more rigid support equivalent to cuticle (the hardened coat of an insect). Cuticle itself is equivalent to plastic in nature. Wood and any plastic can therefore be a perfect artificial support.

3.1.5 Capturing The Model Geometry/Design

Copying a biological model design is essential if biomimicry is to actually take place. Fish as the model used in this work vary greatly in their designs. A life model has to be measured and used to build the robotic model.

3.2 FRAMEWORK FOR THE HYDROSTATIC JOINTS

The design presented in this work is hereby named diamond cross-sectional design. It is an hydrostatic joint modeled using lessons from hornworm caterpillar- *maduca sexta*. The lessons are:

1. The caterpillar is whole body isochoric which means no change to the geometry. Rubber also does not change volume when stretched or compressed.

2. The rubber stress-stretch nature has very close resemblance to that of the muscle (qualitatively)

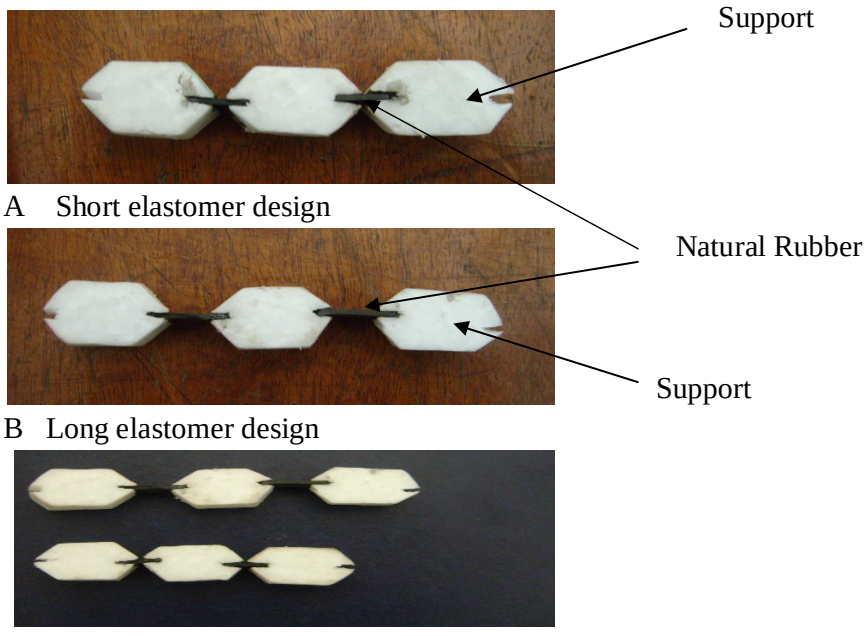
3. It is round and long, qualifying it adequately as an hyper-redundant body

Though it is fluid filled, muscular hydrostat such as the human tongue approach of control is imitated, that is, the actuator will pull on the support structure to generate motions.

Appendix A shows other design that could also be exploited for translating rubber into artificial hydrostatic joint.

3.2.1 Description Of The Rubber Based Artificial Hydrostatic Joint

The diamond design – Figure 3.1, is of two types – the shorter model that uses much smaller elastomer length and the longer one that uses longer elastomer length in between the supports. Figure 3.2 shows the cross-sectional sketch of the design. The diamond shape is needed to avoid interference from adjacent support during bending. The elastomer strip will be held in the support using glue or screws.



A Short elastomer design

B Long elastomer design

C The two designs put side by side for length comparison

Figure 3.1 Diamond design of the evolved joint – short and long elastomer designs

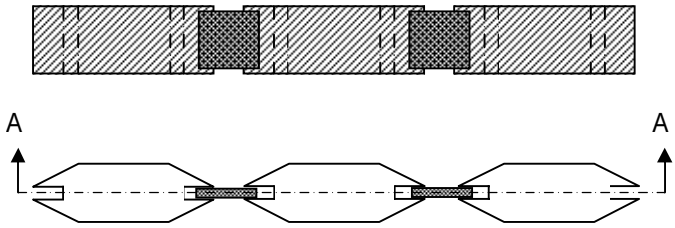
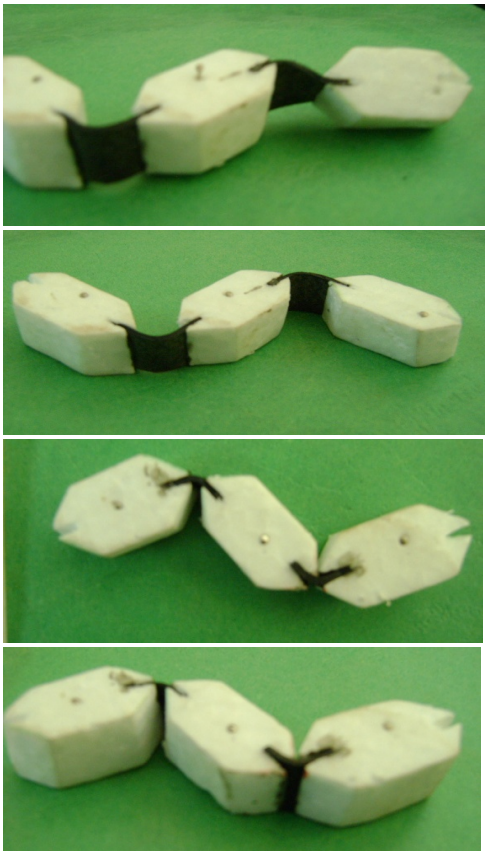


Figure 3.2 The diamond design - cross-section of the model

3.2.2 Kinematics Of The Model

The kinematic of the model gives a visualization of the joints and a comparison can be made in terms of potential for 3D motions, rigidity, minimum curvature or radius and twisting. The kinematics of the two models are presented in Figure 3.3.



A
Long elastomer model showing twist and planar bending simultaneously

B
Long elastomer model showing planar bending only

C
Short elastomer model showing planar bending - viewed from the top

D
Short elastomer model showing planar bending – oblique view

Figure 3.3 Kinematics of the diamond designs

3.2.3 Comparison Of The Two Diamond Design

1. On **potential for 3D motions**, the model with longer elastomer can be used for a hyper-redundant robot that requires 3D body motion. The shorter model is too rigid to twist.
2. On **rigidity**, the shorter model will excel since it is more compact and has less elastomer exposure.
3. **Minimum curvature** – the three segments shown for the model with longer elastomer will easily form a complete circle while the shorter model will require more number of links to form a circle. Larger number of links will translate to more number of actuators to manage each link and more complex control schemes will ultimately be needed.

Summarily, an hyper-redundant joint system that will operate mostly in plain should not have too long rubber in between the supports while those that will require 3D motions should not use too little rubber length that will hamper motion. An optimum should be based on the following criteria:

(1) The minimum radius of curvature (r) expected of the joint as shown in Figure 3.4.

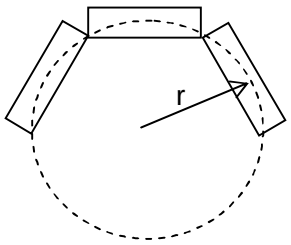


Figure 3.4 The minimum radius of curvature of the joints

(2) The amount of 3D motion expected if it will not be a pure planar motion, Figure 3.5 shows motion about θ and β polar axis.

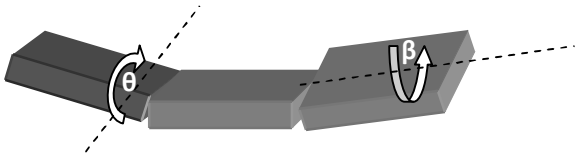


Figure 3.5 3-Dimensional motions capabilities about other axis

(3) The presence of cantilever (Figure 3.6), that is the ability to carry other links or segments without collapsing. This calls for a rigid design.

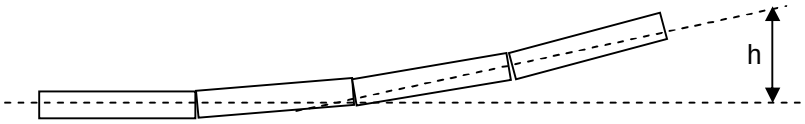


Figure 3.6 Cantilever of multiple links

3.2.4 Strength And Weakness Of The Evolved Artificial Hydrostatic Joint

The following are the advantages expected of the evolved artificial hydrostatic joint

1. It has potential for miniaturization – which may be extremely difficult to achieve using rigid metal joints.
2. Cheaper material – rubber and any rigid support – wood, plastic etc
3. Mass production will be easier
4. High speed of bending
5. It can be made with medical grade rubber like silicones and used for medical purposes without causing hazard to the organ. In event of collusion with organ, damage will be minimal or nonexistence.
6. It can be used for precision positioning purposes if used with micro stepper motors.
7. Maintenance will be low as the rubber will need no lubrication or adjustment
8. Noiseless operations will be possible with the design

Also there are obvious/inherent weaknesses of the design which are a carry-over from biological models. They are:

1. The design cannot be used where there is an extremely high temperature or very low temperature. The rubber used and the support materials will determine the useful temperature range.
2. Since this is not an inflatable design, it cannot be used to lift heavy load
3. The design will not work in a radioactive environment, as the rubber may dissociate.

Appendix A shows other configurations/ design and possible use of the evolved artificial hydrostatic joint.

3.3 ADAPTATION OF THE ARTIFICIAL HYDROSTATIC JOINTS TO A FISH MODEL

3.3.1 Selection Of A Biological Hyper-Redundant Body Model

This work requires that a biological hyper-redundant body model be selected for imitation. Biological hyper-redundant bodies vary in length, some are longer like the snake and some are relatively short – like the fish. The control system grows in complexity with their length; many actuators ("muscles") will have to be managed simultaneously. A shorter model (fish) is adapted as a model for demonstrating the use of the artificial hydrostatic joint in this work.

3.3.2 Selection Of A Fish Model

The high speed *teleost* species of fish is selected for this work. Table 3.1 shows some common member of the families of the *teleost* fish and their peak speed in increasing order. The specie of *teleost* fish selected was mackerel (Figure 3.7) because of the following reasons;

1 It is very common

2 It is capable of fair speed, 11 km/h, (fastest fish is sail fish with speed > 96km/h)

3 The natural ones move in schools (up to 20km long). It means that they can be concealed easily among fish schools for military purpose and also used as fish tracker by fishermen and biologists.

4 It is small enough for stream monitoring and ecological study.

3.3.3 The Active Joint Area Of The Fish Model

For the *teleost* species of fish, the tail is where the oscillation is based and it is where the hyper-redundancy is significant. It is also the main organ of propulsion, therefore, the main area of the joint design will focus on the tail; the frontal part is considered rigid.

3.3.4 Description of the Hydrostatic Joint Mechanism As Adapted for the Fish Model

Figure 3.8 is the computer aided design (CAD) model of the live fish assembled, while figures 3.9 and 3.10 are the isometric views of the haul and tail assembly (both CAD drawings). A more detailed drawings of the design are found in the assembly drawings 1, 2 and 3 and parts drawings 4 to 23. The dimensions are directly taken from the live fish at 1:1 scale – **Appendix B** shows the steps taken in translating the life fish to the CAD model. Figure 3.11 shows the critical dimensions. To be noted in this design are:

1. The rubber strips are 5mm wide – since the motion expected will be planar
2. The 5mm is also adequate to prevent interference between adjacent supports when bending
3. Maximum bending will not exceed 90^{o}.

Table 3.1 Some common family member of *teleost* species of fish with their peak speed, average body length, speed to length ratio (V/L)

 Herring	Speed = 6 km/h = 1.67 m/s = 3.7 MPH Length = 0.3 m V/L = 5.6
 Pike	Speed = 6 km/h = 1.67 m/s = 3.7 MPH Length = 0.5 m V/L = 3.3
 Carp	Speed = 6 km/h = 1.67 m/s = 3.7 MPH Length = 0.8 m V/L = 2.1
 Cod	Speed = 8 km/h = 2.22 m/s = 5 MPH Length = 1.2 m V/L = 1.9
 Mackerel	Speed = 11 km/h = 3.06 m/s = 6.8 MPH Length = 0.5 m V/L = 6.1
 Salmon	Speed = 45 km/h = 12.5 m/s = 28 MPH Length = 1.0 m V/L = 12.5
 Bonito	Speed = 60 km/h = 16.7 m/s = 37 MPH Length = 0.9 m V/L = 18.6
 Small Tuna	Speed = 60 km/h = 16.7 m/s = 37 MPH Length = 3.0 m V/L = 5.6
 Black Tuna	Speed = 80 km/h = 22.2 m/s = 50 MPH Length = 3.0 m V/L = 7.4
 Swordfish	Speed = 96 km/h = 26.7 m/s = 60 MPH Length = 4.0 m V/L = 6.7

(Source http://www.nmri.go.jp/eng/khirata/fish/general/speed/speede.htm)



Figure 3.7 A lateral view of the Mackerel used for this project.

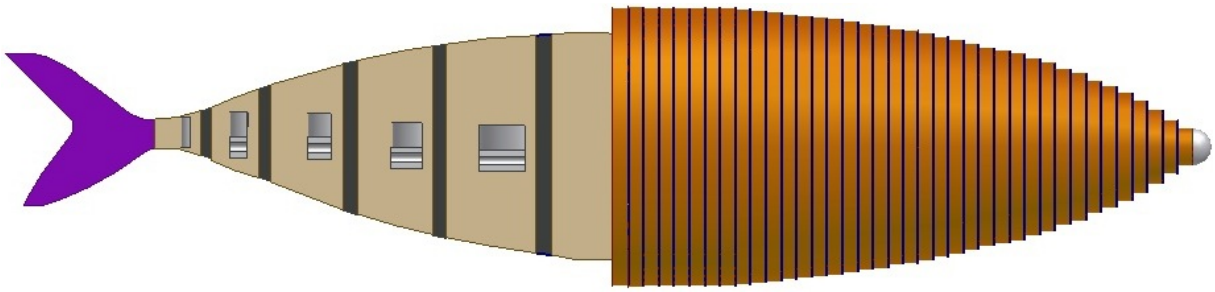


Figure 3.8 The CAD model of the Mackerel shown in Figure 4.6. – not to scale

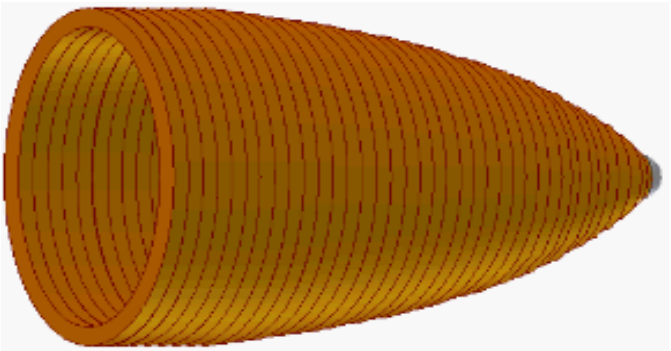


Figure 3.9 Isometric CAD view of the haul (front rigid part) – not to scale

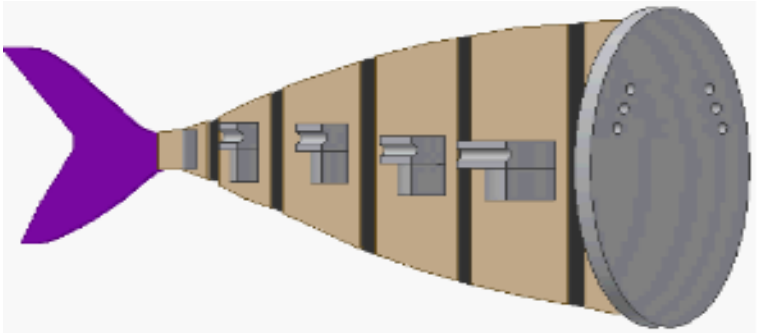


Figure 3.10 Isometric CAD view of the tail section (flexible part) – not to scale

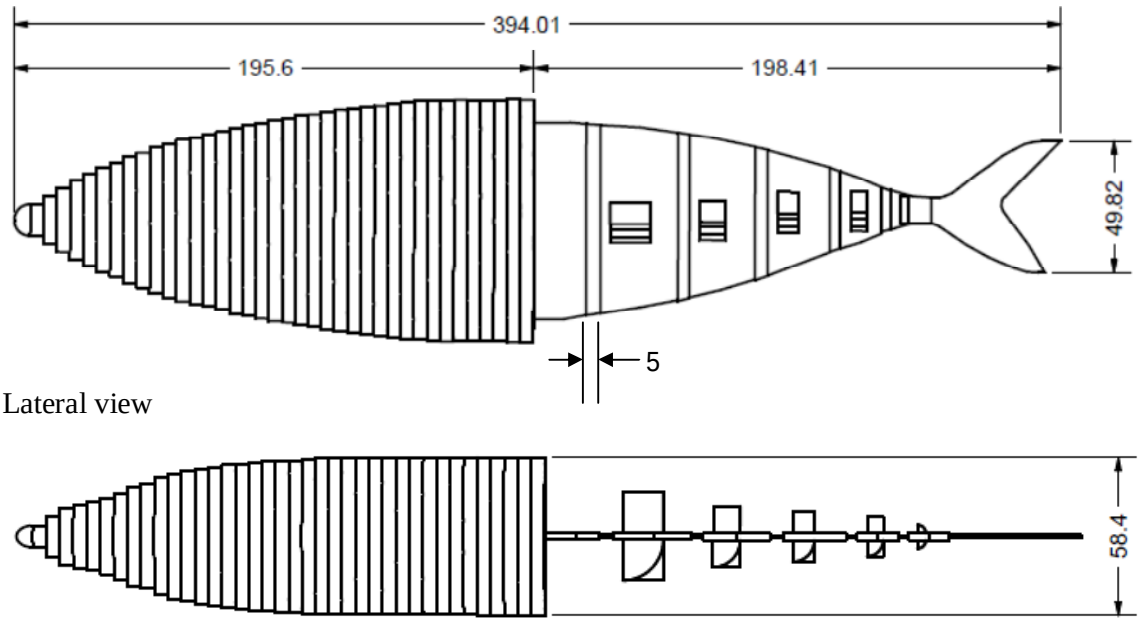


Figure 3.11 The critical dimensions (in mm) of the model

The active part of the robotic fish model described here is the tail section, the front part is a rigid haul. Using the sketch model shown in Figure 3.12 – 3.14, the manner the joint works is described as follows;

1. From Figure 3.12 the rubber joint (A) (strips of rubber) is sandwiched between pairs of rigid support segments (1) to (6).
2. The support (6) is attached to oval support (B) having six pass through holes (C) for the cables support.
3. The servo motor (D) is attached to the oval support (B) having pass through holes for the cables.
4. The cables are connected to the servo motor horn (E) by tying
5. The servo motor horn oscillates at angle (F). To get a serpentine motion, the microcontroller uses its built in pattern generator to control the sequence of turning of

the servo motors (D). It sends the angular displacement information to the servo motors in such a manner that its horn (E) will oscillate +/- angle (F).

6. On both sides of each segment (1) to (6) are located quarter pulleys (H) over which the nylon cable (G) passes before hooking to those segments. Only one cable is shown for clarity.
7. The nylon cables (G) are attached to the servo motor horn (E). Its support passes through the pass-through holes (C).
8. To get a serpentine motion, the microcontroller uses its built in pattern generator to control the sequence of segment (1 to 6) turning by activating the servo motors (B) (one is shown for clarity) according to the pattern.
9. The segments (1), (3) and (5) are connected to a servomotor each.
10. The other segment simplifies the design as they act to restore the joints to their static states. Also, they help in getting the desired serpentine shape without complicated design – just like nature has simplified its designs by appropriate use of material. Furthermore this approach simplifies the number of motors required and hence the control scheme.
11. Figure 3.13 shows how the tail fin will bend to the left or right when the left or right cable is pulled respectively by the servomotor (D).
12. Figure 3.14 shows the detail of the Nylon cable (H) design that will connect the motor horn to the support structure (segments). It uses clutch cable design (as used in bicycles and cars). It is made up of flexible plastic with the nylon cable running inside it.
13. For swimming to take place, the microcontroller sends angle data to each servo motor using pulse-width-modulated scheme. The servo motors then turn to that angle which is at 60^{o} phase difference to the next servo motor. The servo motor then pulls the cable which in turn pulls the segment it is attached to. In this manner, the tail generates a travelling wave that has its origin at the segment (6) and ends at segment (1). The amplitude increases from segment (6) to segment (1).

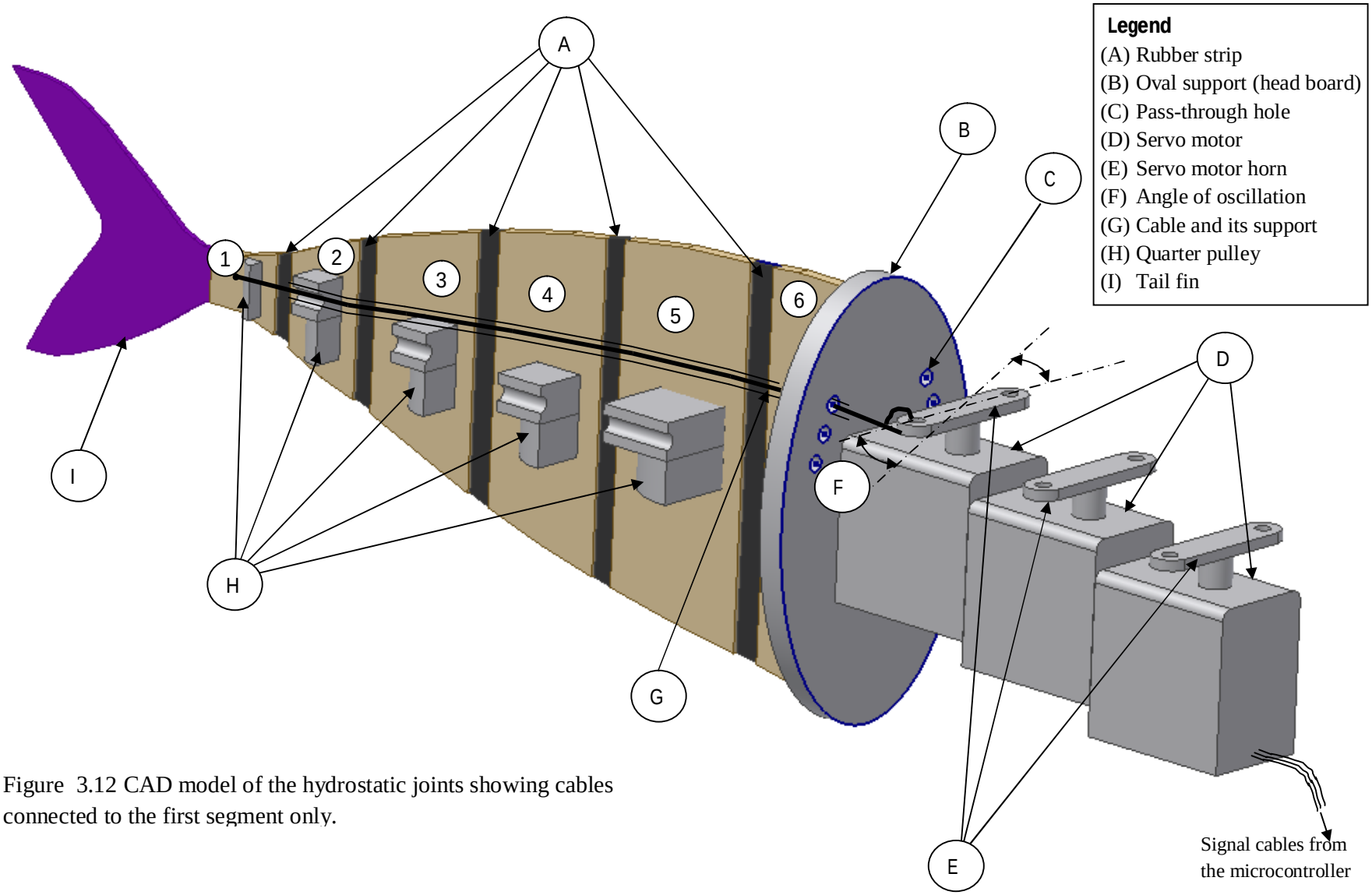


Figure 3.12 CAD model of the hydrostatic joints showing cables connected to the first segment only.

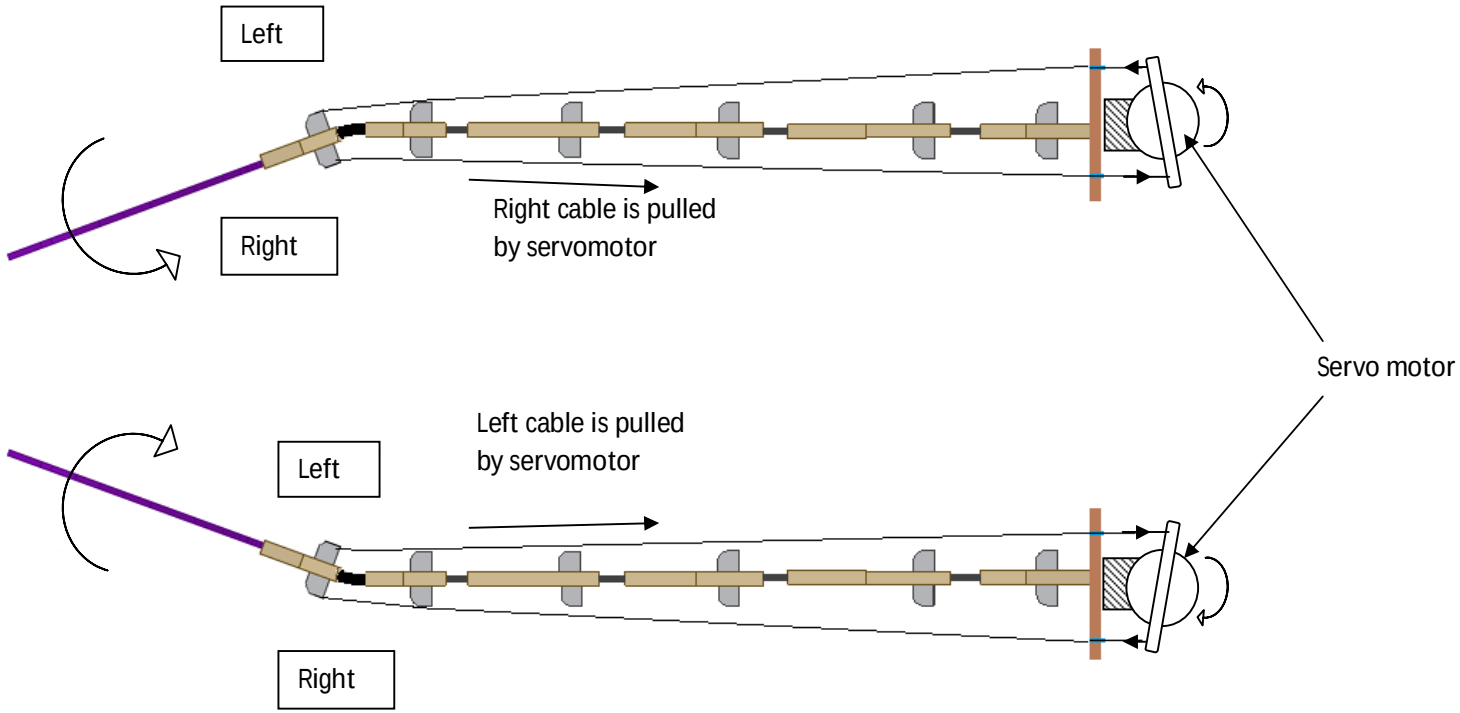


Figure 3.13 How the tail fin will respond as the servo motor pull on the cables

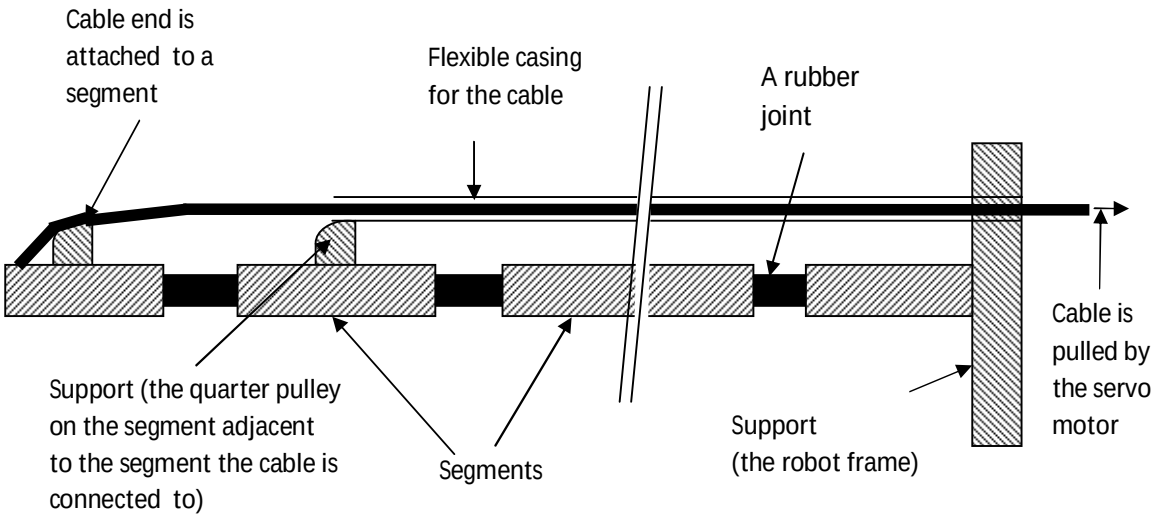


Figure 3.14 The detail design of the cable showing one side only

3.4 MATERIALS SELECTION

The forces and loads the artificial hydrostatic joint will experience are dependent on its function and to some extent on the materials that are used in constructing it. Also, the use of rubber means that the way and the manner it will be used will affect its performance, specifically the oscillatory motion will incur the frequency softening effect (Payne effect).

3.4.1 List of Materials

The following materials were used in constructing the fish robot;

1. Vulcanized rubber – 1.5mm thick.
2. 1/8 inch (3.175mm) thick seasoned plywood.
3. ¾ (19.05mm) inch plywood.
4. ABRO® steel reinforced 4 minutes setting Epoxy glue – Araldite.
5. Nylon 1010 cables – 0.5mm diameter.
6. 2.5mm diameter unplasticized PVC tubing.
7. Remote control servomotors (Futaba 3003 and Futaba 148).
8. Microcontroller – PIC18F4520
9. Latex rubber – from Population Services International (PSI)
10. Silicone rubber
11. Micro switches.
12. Parallax Ping)))
13. Collapsed polyurethane foam
14. Cyanoacrylate glue (super glue)

3.4.2 Description Of The Materials

The **rubber** is carbon filled vulcanized motor car inner tube (14inch or

35.56cm) from King Rubber Tire Company of China. This rubber was used for the artificial hydrostatic joint. The **1/8 inch thick seasoned plywood** acts as the support for the rubber material. The open air seasoning is for dimensional stability. The ¾ **inch plywood** is used for the pulleys. The **epoxy glue** is used for assembly of the parts. ABRO® 4 minute epoxy glue is selected because the manufacturer states on its label that it does not shrink after setting, meaning the parts will maintain their dimensions after setting. The 0.5mm **nylon cables** connect the servo motor horn (lever) to the joints supports (the plywood). The **2.5mm unplasticized PVC tubing** acts as support for the nylon cables. The remote control **servo motors** (Futaba 3003) are the programmable actuators. The **microcontroller** manages the control of the artificial joints so that a usable and varying motion can be achieved. The **latex rubber** and silicone rubber are used for sealing against water. The **micro switch** is used as the sensor for collision detection. Two pieces were used, one to detect collision on the left, the other is for the right. The **parallax ping)))** are ultrasonic transmitter-receiver pairs that are used for detecting objects. The **polyurethane** foam is used for padding purposes. The **cyanoacrylate glue** was used for water proofing all the wooden parts – wood easily absorbs it to form a water phobic layer.

3.5 COMPONENTS DESIGN

The components are designed based on the following theories; finite element analysis, stress behavior in elastomers, stress in elastic materials, forces experienced by a moving foil inside water, large-amplitude elongated-body motion theory, Mulling and Payne effects. These are finally used in selecting the actuator for driving the joints and assembling it.

3.5.1 Finite Element Analysis (FEA) for General Simulation

Finite element analysis (FEA) is a numerical technique for finding approximate solutions of partial differential equations (PDE) as well as of integral equations. A structure is normally partitioned into small sections referred to as elements, with depth added for a 3-D environment. The connection between them is referred to as nodes. At **each node**, there are forces F_1, F_2, F_3, F_4, F_5 and F_6 operating in the direction +x, -x, +y, -y, +z and -z with displacements u_1,u_2, u_3, u_4, u_5, and u_6 (for 3-D situation); adapted from Jason (2011) .

$$k_{ij} * u_j = F_i$$

and k_{ij} is the stiffness coefficient relating F_j to u_j (linearity is assumed here for simplicity)

For two linked node we can write a matrix of the relationship as:

$$\begin{bmatrix} F_1 \\ F_2 \\ F_3 \\ F_4 \\ F_5 \\ F_6 \end{bmatrix} = \begin{bmatrix} k_{11} & k_{12} & k_{13} & k_{14} & k_{15} & k_{16} \\ k_{21} & k_{22} & k_{23} & k_{24} & k_{25} & k_{26} \\ k_{31} & k_{32} & k_{33} & k_{34} & k_{35} & k_{36} \\ k_{41} & k_{42} & k_{43} & k_{44} & k_{45} & k_{46} \\ k_{51} & k_{52} & k_{53} & k_{54} & k_{55} & k_{56} \\ k_{61} & k_{62} & k_{63} & k_{64} & k_{65} & k_{66} \end{bmatrix} \begin{bmatrix} u_1 \\ u_2 \\ u_3 \\ u_4 \\ u_5 \\ u_6 \end{bmatrix} \quad (3.1)$$

This matrix is called the stiffness matrix and it defines the geometric and material properties of the object being analyzed. This matrix is solved for each linked node and in relation to adjacent nodes to get all the unknowns i.e the loads experienced and the corresponding displacements. Thus, the more the elements, the more the nodes, and irregular shapes or boundary elements usually have more nodes to capture the geometry

of the structure. More elements means that the analysis can be more accurate as it will be more refined in its capture of the structure geometry.

3.5.2 Stress Within An Elastomer (Rubber)

The loads in the rubber are determined using finite strain elasticity theory or constitutive equations because it has unique properties, in particular exceptionally low shear modulus and high elastic strain capability. The equations are solved using finite element analysis (FEA). The equations relating the displacements *u* to the load *F* (see equation 3.1) are defined by constitutive equations and are normally solved using a computer because of the matrix of matrix in algebraic form (i.e. tensors) involved (Kolecki, 2002).

3.5.3 Stress Within The Plywood Material

The plywood is treated as a linear material (i.e. Hooke's law is used) and the following mechanical properties are used in its finite element analysis **(**Ryder, 1990; Kelly, 2011);

a. Stress $$\sigma = \frac{Load}{Area} \quad (3.2)$$

b. Strain $$\epsilon = \frac{change\ in\ length}{original\ length} \quad (3.3)$$

c. Modulus of elasticity or Young's modulus; $$E = \frac{Stress}{Strain} \quad (3.4)$$

d. Poisson's ratio $$\nu = \frac{lateral\ strain}{longitudinal\ strain} \quad (3.5)$$

e. Density, $$\rho = \frac{mass}{volume} \quad (3.6)$$

f. Yield strength

Yielding occurs when the design stress exceeds the material yield strength. Design stress is typically maximum surface stress (simple loading) or von Mises stress (complex loading conditions). The von Mises yield criterion states that yielding occurs when the von Mises stress, σ_v exceeds the yield strength in tension. Often, finite element analysis stress results use von Mises stresses. von Mises stress is:

$$\sigma_v = \sqrt{\frac{(\sigma_1 - \sigma_2)^2 + (\sigma_2 - \sigma_3)^2 + (\sigma_1 - \sigma_3)^2}{2}} \quad (3.7)$$

where σ_1, σ_2 and σ_3 are the principal stresses

3.5.4 Forces Experienced By A Moving Foil (Or Plate) Inside Water

When the fish tail oscillates inside the water, it behaves like a plate. The main force acting on the plate with area **A** is the drag force, F_d. (John, 1993).

The drag force is given as $F_d = \frac{1}{2}\rho v^2 C_d A$ (3.8)

where ρ = density of fluid (water in this case)

C_d = coefficient of drag. It is shape dependent, in this work, it is assumed to be perfectly flat.

A = Area of plate

v = velocity of the plate (peduncle)

3.5.5 Forces On Rings

The rings are hereby treated as thin cylinders, Figure 3.15, with internal pressure P_i and external pressure, P_e

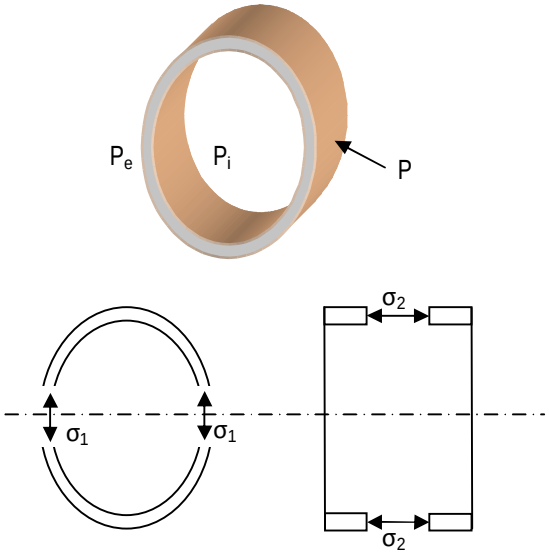


Figure 3.15 The ring geometry

If the internal diameter is d and the thickness t, and σ_1, σ_2 are the hoop and longitudinal stress, then

$$\sigma_1 = Pd/2t \quad (3.9)$$

$$\sigma_2 = Pd/4t \quad (3.10)$$

where $P = P_e - P_i$ (3.11)

3.5.6 Bending Stress Within A Cantilevered Object

The classic formula **(**Ryder, 1990) for determining the bending stress in a beam under

simple bending is:

$$\sigma_b = \frac{My}{I_{xx}} \quad (3.12)$$

$$I_{xx} = \frac{bd^3}{12} \quad (3.13)$$

where σ_b = the bending stress

M = the moment about the neutral axis

y = the perpendicular distance to the neutral axis

I_{xx} = the second moment of area about the neutral axis x

b = the width of the beam

d = height of the beam

3.5.7 Stress In The Nylon Cable

According to Ryder, 1990, the stress in the nylon cable is calculated as

$$\sigma_c = \frac{P_c}{A_c} \quad (3.14)$$

where P_c= pull acting on the cable

A_c= area of the cable

3.5.8 Tensile Stress Within A Glue

$$\sigma_g = \frac{P_g}{A_g} \quad (3.15)$$

where P_g= separating forces acting on the glued bodies

A_g= area of glue

Mechanical interlocking theory is assumed which is based on the fact that at the

microscopic level all surfaces are very rough consisting of crevices, cracks and pores. The adhesive penetrates these features and hardens such that it keys into the surfaces and forms a strong surface bond (Roy, 2010).

3.5.9 Large-Amplitude Elongated-Body Motion Theory

The dynamic pressure, P_v caused by the tail pushing water at velocity ω is given by Bernoulli's equation of the form

$$P_v = 0.5\ \rho\ \omega_v^2 \quad (N\ m^{-2}), \tag{3.16}$$

according to John (1993)

where P_v = dynamic pressure

ρ = water density

ω_v = angular velocity of the fish tail

This dynamic pressure was derived using large-amplitude elongated-body motion theory by Lighthill (1971) which allowed the prediction of instantaneous reactive force between fish and water for fish motions of arbitrary amplitude. Figure 3.16 is used to explain all the parameters involved in the derivation of the dynamic torque. It shows the force components and velocity components of a fish peduncle as well as the torque and angular velocity experienced by it. The Force F_v is zero (F_v=0 N) for a fish that is stationary or coasting; also ω=0. Coasting arises when a fish stops wagging its tail and just glides along its path in a straight manner. Force F_v is non zero when there is tail motion.

Thus we have (with equation 3.16)

$$F_v = \begin{cases} 0 & coasting \\ 0.5\rho\omega_v^2 & swiming \end{cases} \tag{3.17}$$

From which the dynamic torque T, is calculated.

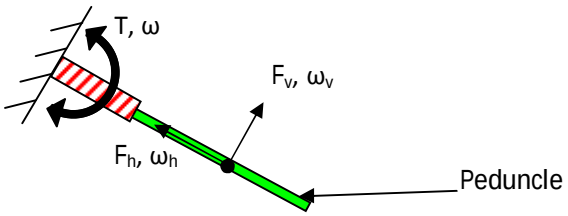


Figure 3.16 Instantaneous force and velocity component of an active tail fin

Horizontal velocity component ω_h is assumed negligible - disturbance to water along that axis is small (John, 1993).

3.5.10 Mullins Effect – Preconditioning

Preconditioning rubber material by uniaxial loading and unloading is known as stress-softening and is referred to as Mullins effect. Stress-softening of elastomer is an incompressible, isotropic and nonlinear behaviour whose mechanical response depends on its deformation history. Mullins materials have a selective memory of only previous maximum strain experienced during its deformation history but not how it got there. The magnitude of strain *m* is defined as

$$m \equiv \|\mathbf{B}\| = \sqrt{\mathbf{B}.\mathbf{B}} \qquad \text{Beatty (2002)} \qquad (3.18)$$

in terms of the left Cauchy-Green deformation tensor $\mathbf{B} \equiv \mathbf{F}\mathbf{F}^{\mathbf{T}}$.

In the undistorted state for which $\mathbf{B} = 1$, we have $m=\sqrt{3}$; otherwise, $m>\sqrt{3}$ for all isochoric deformations. For a virgin material, the maximum previous strain is the current value of *m*. When the material is stretched, the magnitude of strain value changes to $M=m_{max}$ it experienced. As long as any subsequent stretching does not pass this *M*, it retraces its steps / pattern when stretched again.

3.5.11 Payne Effect – Frequency Induced Softening

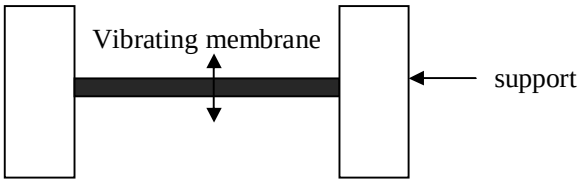


Figure 3.17 Experimental elastomer membrane subjected to stress induced softening - Beatty (2002)

Using Figure 3.17, a membrane with mass density of ρ will have fundamental/ natural frequency ν as

$$\nu = \gamma\sqrt{\frac{T}{\rho A}} \quad , \tag{3.19}$$

where T = the tension within the elastomer

ρ = mass density

A = Area of elastomer

γ= a dimensionless constant

For a virgin material the frequency can be written as

$$\nu = \nu(T,\lambda) = \nu_0\sqrt{\frac{T}{\mu_{0}\lambda^2}} \quad , \tag{3.20}$$

where λ = the isochoric equibaxial stretch

μ_o = shear modulus of the material in its undisturbed state

$\nu_o = \gamma\sqrt{t_0\mu_0/\rho_0 A_0}$

t_0 = current elastomer thickness

ρ_0 = current density

A_0 = current area of elastomer

For a stress-softened material, the frequency is

$$\nu_s = \nu(\tau,\lambda) = \nu_0 \sqrt{\frac{\tau}{\mu_0 \lambda^2}} \quad , \tag{3.21}$$

where τ = the stress within the softened material

and $$T \geq \tau \quad , \tag{3.22}$$

therefore $$\frac{v}{v_s} = \sqrt{\frac{T}{\tau}} \geq 1 \quad , \tag{3.23}$$

hence the vibration frequency of the virgin material is greater than the corresponding frequency of the stress-softened material for each fixed stretch value.

3.5.12 Power Requirements Of An Electric Motor

The power to drive an ordinary permanent magnet motor is given as

$$w = (V*I)/\eta \quad , \tag{3.24}$$

where V = applied voltage

I = current flowing = $I_{running} + I_{idle}$

$I_{running}$ = current consumed while running

I_{idle} = current consumed while idle

η = efficiency of the motor

Also $$\mathbf{W} = 2\pi*N*T \quad , \tag{3.25}$$

where N = circular speed (rev /s)

T = Torque (Nm)

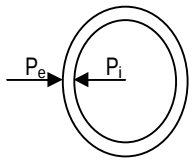
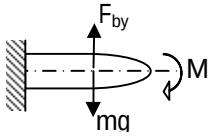
3.6 CALCULATIONS OF FORCES AND LOADS EXPERIENCED BY THE COMPONENTS

The forces and loads experienced by the components are hereby calculated.

3.6.1 Component: Rings.

Forces acting on the rings that will be used for building the rigid haul is calculated as shown in Table 3.2

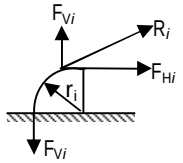
Table 3.2 Forces within the rings for building the hauls

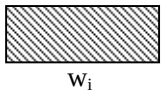
Initial data	Calculations	Result	Remark
	P = Pe - Pi	hoop stress = 0 longitudinal stress = 0	Flood filled approach is intended, therefore the internal and
P_e = external water pressure P_i = internal haul pressure	= 0	bending stress = 0	external pressure will be equal. The robot haul will not be sealed
hoop stress= σ_1	from equation 3.9 σ_1 = Pd/2t =0		i.e. water is allowed to enter it.
longitudinal stress= σ_2	from equation 3.10 σ_2 = Pd/4t =0		The bending stress is expected to be 0 for a weightless object because buoyancy
bending stress on the haul assembly = σ_b 	from equation 3.12 F_{by} = mg therefore M = 0 $\sigma_b = \frac{My}{I_{xx}} = 0$		force F_{by} is cancelled by the force of gravity mg while inside water

3.6.2 Component: Quarter Pulleys

Forces acting on the quarter pulleys that will be used for supporting the nylon cable and the nylon cable container are calculated as shown in Table 3.3

Table 3.3 Forces acting on the quarter pulleys

Initial data	**Calculations**	**Result**	**Remark**
 *i* denote ith segement F_{Hi} = the cable pull F_{Vi} = vertical reaction R_i = resultant pull r_i = radius T_i = Torque Maximum torque the intended motor can generate is 0.29Nm at a (horn) radius of 15mm, therefore assumed maximum cable pull on any pulley is approx. 20N F_{H1}=F_{H3}=F_{H5}= 20N F_{H2}=F_{H4}=0 as they are idlers. r_1 = 3mm r_2 = 6mm r_3 = 8mm r_4 = 10mm r_5 = 15mm	From tail fin <u>Segment 1</u> T_1 = 20N x 3= 0.06Nm F_{V1} = F_{H1} = 20N $R_1 = \sqrt{F_{V1}^2 + F_{H1}^2}$ = 28.28N Segment 3 T_3 =20N x8= 0.16Nm F_{V3} = F_{H3} = 20N $R_3 = \sqrt{F_{V3}^2 + F_{H3}^2}$ = 28.28N Segment 5 T_5 =20N x 15= 0.30Nm F_{V5} = F_{H5} =20N $R_5 = \sqrt{F_{V5}^2 + F_{H5}^2}$ = 28.28N	Torque on the segments are; T_1 = 0.06Nm T_3 = 0.16Nm T_5 = 0.30Nm T_2 =T_4 = 0Nm Maximum vertical reaction forces on the segments are all equal to the pulls = 28.28N	The pull varies with speed of oscillation. Therefore maximum value is used. The radius are selected to be less than the width of the fish robot at each position, guided by measuring live fish

Initial data	Calculations	Result	Remark
stress within the glue  $A = r_i \times w_i$ w_1 = 10mm $w_3 = w_5$ = 15mm w_i = width of pulley	from equation 3.15 σ_{g1}= 20N/3x10 = 0.67N/mm^2= 670kPa σ_{g3}= 20N/8x15 = 0.167N/mm^2= 167kPa σ_{g5}= 20N/15x15 = 0.088N/mm^2= 88kPa	Stress within the glue σ_{g1}= 670kPa σ_{g3}=167kPa σ_{g5}=88kPa	This is the stress the glue will have to withstand in operation

3.6.3 Component: Nylon Cable

Forces acting within the nylon cable that will be used for connecting the servomotor horns to the tail segments are calculated as shown in Table 3.4

Table 3.4 Stress within the nylon cable

Initial data	Calculation	Result	Remark
The cable is treated as a rod undergoing tensile loading  P = 20N Radius, r = 0.25mm	$A = \pi r^2$ $= \pi \times 0.25^2$ = 0.1963mm^2 = 1.963x10^{-7} m^2 from equation 3.14 σ = P / A σ = 20N/1.963x10^{-7} m^2 = 101,884,870 N/m^2 $\cong$ 102Mpa	$\sigma \cong$ 102Mpa	Nylon 1010 is used and has the tenacity required, it has tensile strength of about 210 MPa

3.6.4 The Wooden Supports, Rubber Stripes And The Fin For The Peduncle

The forces within this set of three components are interrelated – that is, each component cannot be treated in isolation. Since rubber is involved, the stresses within the components are found using computer simulation and finite element analysis.

Practical finite element analysis is known to be mathematically involving (Cadiff, 2006) as shown in equation 3.1, generally and even much more for non-linear materials like rubber - which requires constitutive equations**.** A multi-cluster system or super computer is needed for solving such equations to get a very accurate result; there is a limitation to what an office computer can do. The approach here is to concentrate on the part that will experience the most loading and make it the reference for all other parts. This was what Frank et al (2011) also did in their experimental verification of their soft-robot gaits.

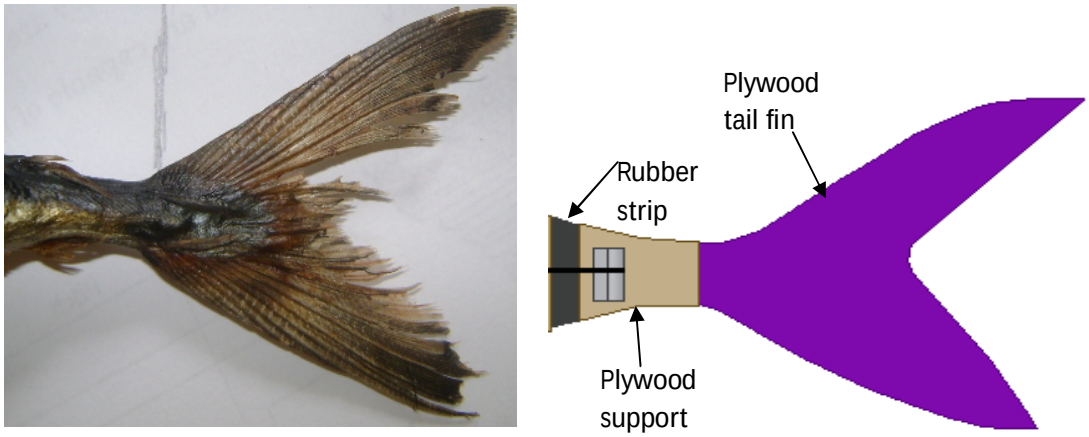
Because of the computing power limitation above, the stress within the tail peduncle (Figure 3.18) will be simulated and the result used as the basis for the design of the other tail portion. The peduncle is unique for the following reasons;

1. The tail peduncle is the main propulsive organ for *teleost* species of fish (like mackerel) and is thus expected to experience the greatest load.
2. It is required to bend at about $\pm 45^{o}$ while in action.
3. It is the thinnest portion of the whole body – thus it is the "weakest link of a chain".
4. It has the highest angular velocity than the other tail sections.

3.6.4.1 Parameters that were simulated are;

1. Stress within the peduncle assembly

2. Stress due to static weight of the fin (or links) – cantilever effect
3. Glue tenacity between the rubber and the support, the support and the tail fin.
4. Warping/rigidity of the assembly



Live fish CAD model

Figure 3.18 A fish peduncle

3.6.4.2 Setup of the finite element tool and the constraints used for the simulation

The finite element tool selected is ANSYS Multiphysis version 10. For all the geometry, Autodesk Inventor 7 was used i.e. the 3D diagrams of the tail peduncle. The following steps were taken in setting up the finite element tool;

1. Input of material physical data
2. Selecting the constitutive equation to use
3. Design of mesh element pattern,
4. Input of simulated loads,

(I) Specification of the material physical data

The following data was used as the physical property of the materials;

Input data for the plywood material

Young's modulus	$5x10^9$ Pa	Plywood is used for the support forming the segment and the fin.
Poisson's ratio	0.25	
Density	$500kg/m^3$	
Tensile yield strength	$1.5x10^7$ Pa	
Compressive yield strength	$3.6\ x10^7$ Pa	
Tensile ultimate strength	$3.1\ x10^7$ Pa	
Compressive ultimate strength	$2.0\ x10^7$ Pa	

Input data for the rubber material

The inputs are uniaxial and biaxial test data shown graphically in Figure 3.19 and Figure 3.20 respectively.

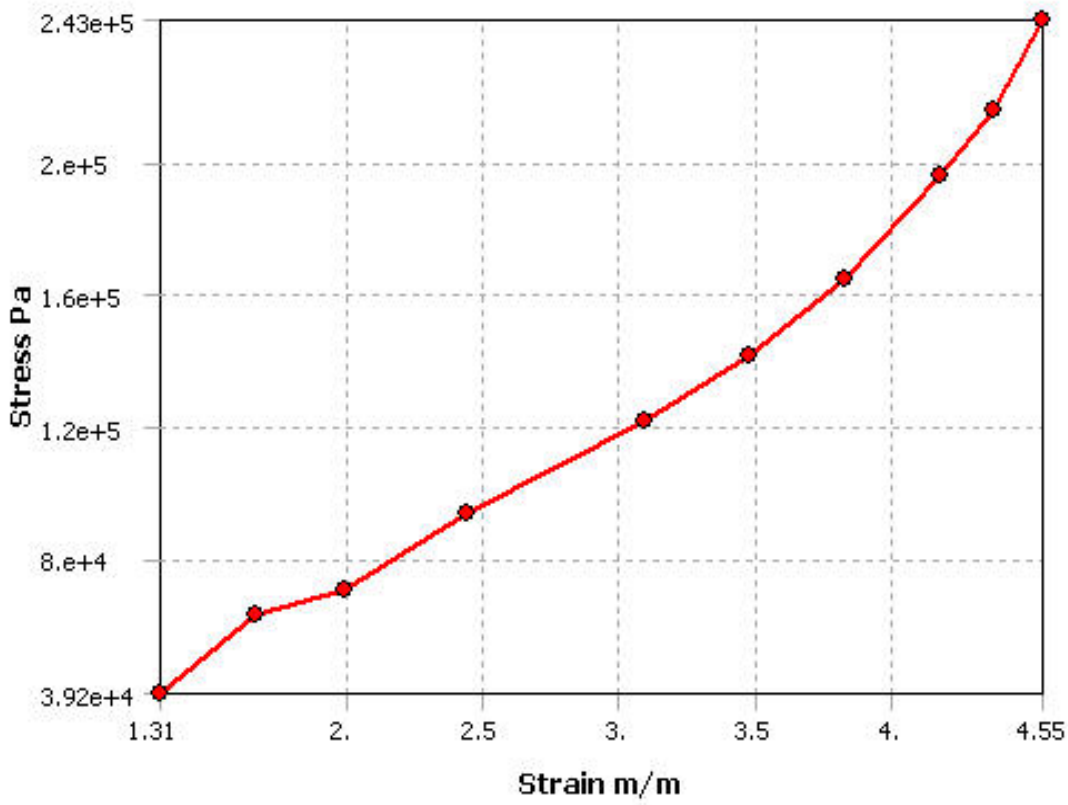


Figure 3.19 Uniaxial tensile test data plotted using ANSYS multiphysis 10

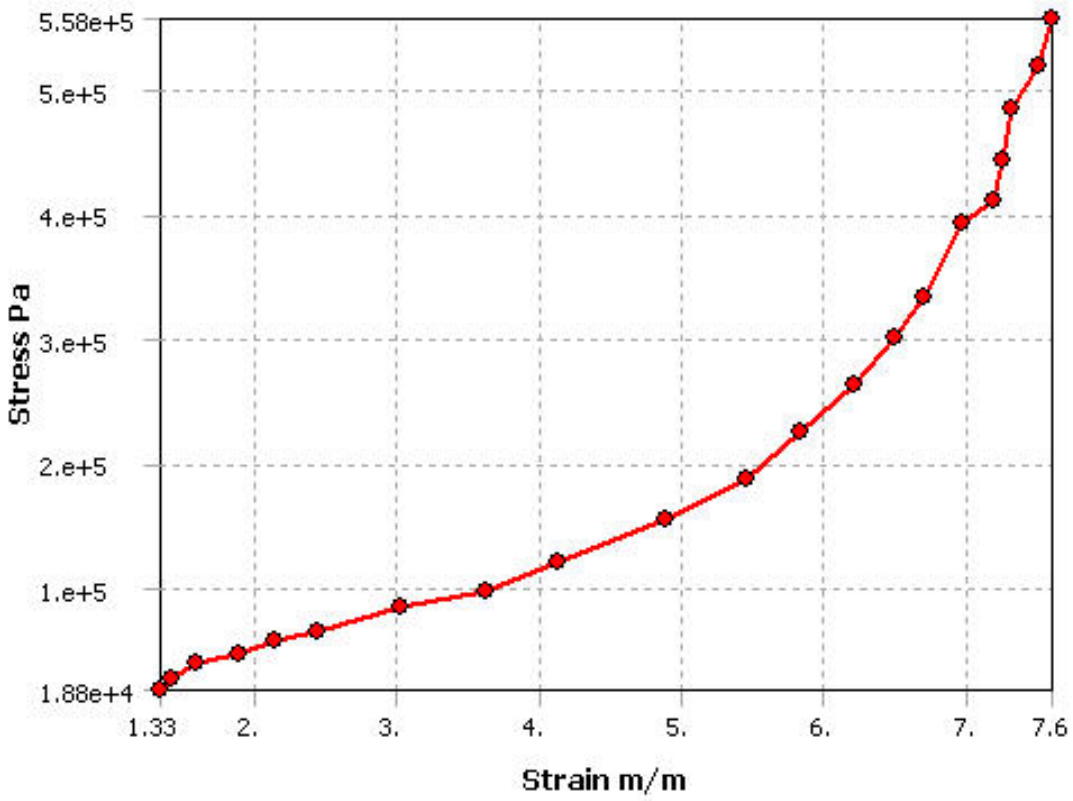


Figure 3.20 Biaxial tensile test data plotted using ANSYS multiphysis 10

(II) Selecting constitutive equation

Determining which constitutive equation will best predict the beahaviour of the particular sample being tested require curve fiting using the tools provided in the ANSYS Multiphysis version 10. The tool indicates that Mooney –Rivlin parameter (equation 3.24) constitituve equation is adequate to predict the behaviour of the rubber sample.

$$W = c_{10}(\bar{I}_1 - 3) + c_{01}(\bar{I}_2 - 3) + c_{20}(\bar{I}_1 - 3)^2 + c_{11}(\bar{I}_1 - 3)(\bar{I}_2 - 3) + c_{02}(\bar{I}_2 - 3)^2 + c_{30}(\bar{I}_2 - 3)^3 + c_{21}(\bar{I}_1 - 3)^2(\bar{I}_2 - 3) + c_{12}(\bar{I}_1 - 3)(\bar{I}_2 - 3)^2 + c_{03}(\bar{I}_2 - 3)^3 + \frac{1}{d}(J - 1)^2 \quad , \qquad (3.24)$$

where W = strain energy

J = determinant of the elastic deformation gradient F

$\bar{I}_1$= first deviatoric strain invariant

$\bar{I}_2$= second deviatoric strain invariant

c_{10}, c_{01} = material constants characterizing the deviatoric deformation of the material

d = material incompressibility parameter

The initial shear modulus is defined as:

$\mu = 2(c_{10} + c_{01})$

and the initial bulk modulus is defined as:

$K = 2/d$ where $d=(1-2*\nu)/ (c_{10} + c_{01})$

To use this model in ANSYS, minimum of two inputs are required, biaxial and uniaxial tension test results on the rubber. Figure 3.21 shows the inputs and the predicted plot using Mooney –Rivlin parameter constitutive equation. The dotted lines are the predicted, while the smoothlines are the inputs (biaxial and uniaxial).

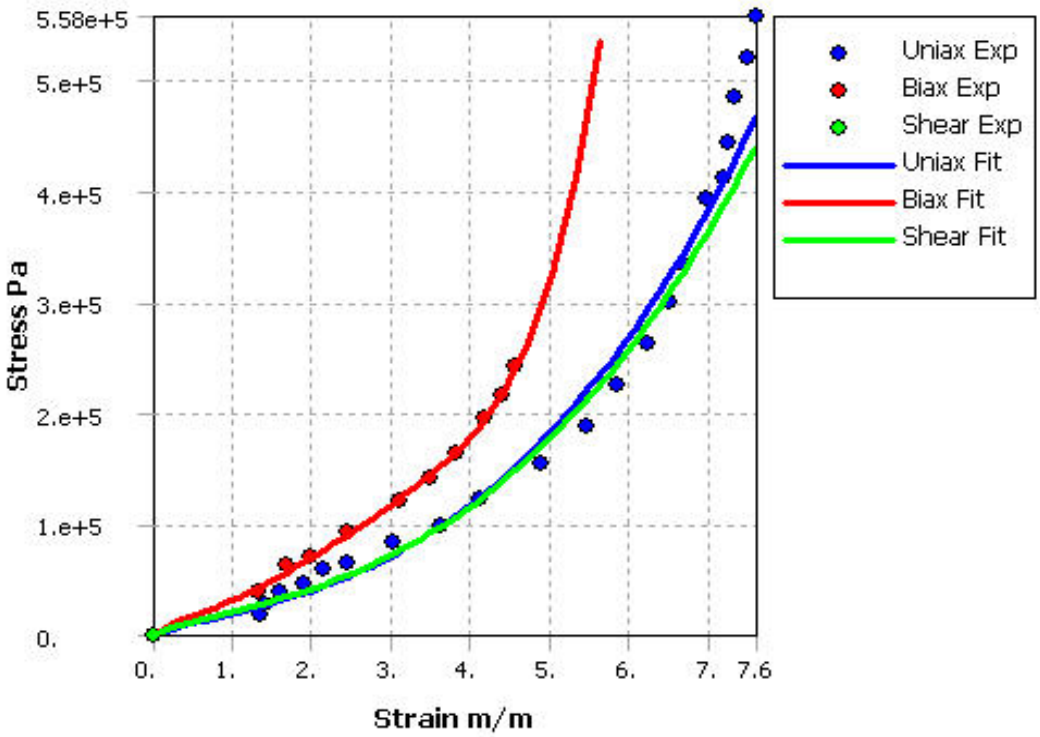


Figure 3.21 Mooney-Rivling parameter constitutive equation used within the ANSYS 10 shows very close prediction of the rubber sample behavior. It means that Mooney-Rivling parameter can be safely used for the Finite element analysis of the rubber sample.

(III) Mesh element design

The mesh element design Figure 3.22 was done using the mesh tools built into the ANSYS multiphysis 10. The number of elements = 7442, the number of nodes = 11817 and the depth of refinement = 2. These values were arrived at by trial and error based on the combination that was able to give convergence (i.e. solution). Higher values will also work but experience shows for each increase in refinement for example, the processing time increases exponentially – this is the core reason while a multi-cluster system or supercomputers are used for such simulations.

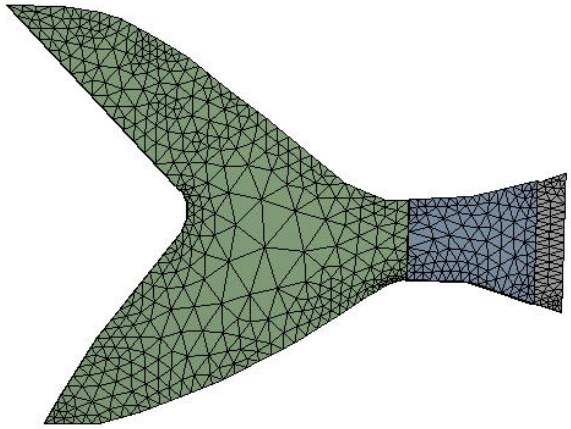


Figure 3.22 Optimized ANSYS 10 generated mesh pattern used for the finite element analysis.

(IV) Simulated inputs loads and its derivation for the finite element analysis

The simulated loads are shown in Figure 3.23. The following assumptions were made:

1 The tail section is oscillating at max of 90^{o} ($+45^{o}$ to -45^{o})

2 It is oscillating at frequency of 1Hz

3 It will operate in water with density of $990kg/m^{3}$ (sea water)

The simulated loads are derived as follows as shown in Table 3.5;

Table 3.5 Simulated inputs loads for the finite element analysis and how they were derived

Initial data	**Calculation**	**Result**	**Remark**
Angular velocity, ω over 90^o (from $+45^o$) to $-45^{o)}$	$\omega = 2\pi \times 90^o/360^o = ¼ \times 2\pi$	½π rad/s	Angular velocity (from the assumption earlier made) Speed is the frequency of oscillation of the peduncle
Centroid, r		≈ 20mm	The non standard shape was estimated by CAD program. See figures 3.23 and 3.24
Area, A		0.002427 m^2	
Drag force, F_d C_d = 1.28 $\rho = 990kg/m^3$	From equation 3.8 ½ x 990 x $(0.03142)^2$ x 1.28 x 0.002427	= 0.001N	The force that will act on the peduncle will be equal to the drag force on the fin It's interaction with water will be as a flat plate with area A, hence C_d = 1.28
Perpendicular load on the peduncle = Drag force, F_d		0.001N	Perpendicular loading across its surface is expected to be the major load as it moves inside water which is the same as the drag force See figures 3.23 and 3.24
Load on the wooden segment (plywood)	Z axes = 0.001N X axes = 0.001N	0.00141421N	Vector sum
Contact specification		Sticking	ANSYS Multiphysis 10 did not provide a place to specify the nature of the glue except the mode of it.

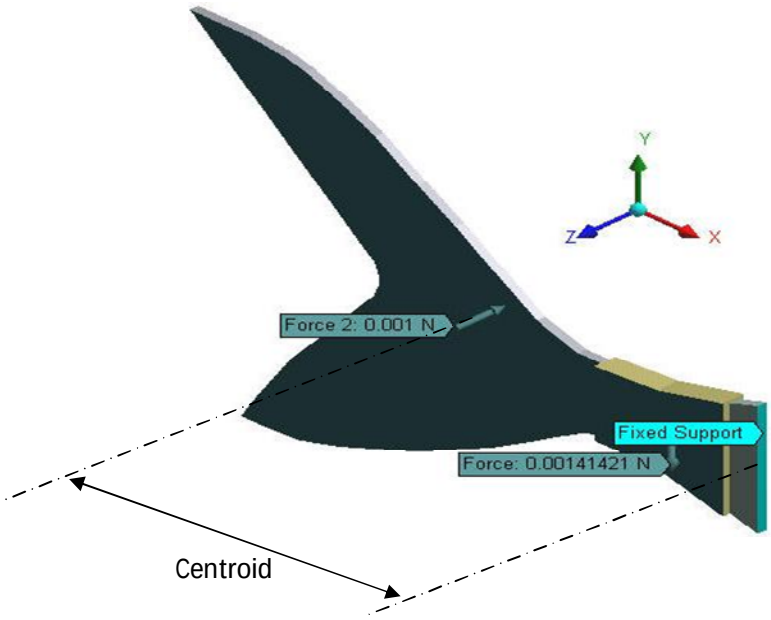


Figure 3.23 The simulation inputs: 0.001N on the fin, 0.00141421N (vector sum of 0.001N –z axis and 0.001 N - x axis) on the plywood support.

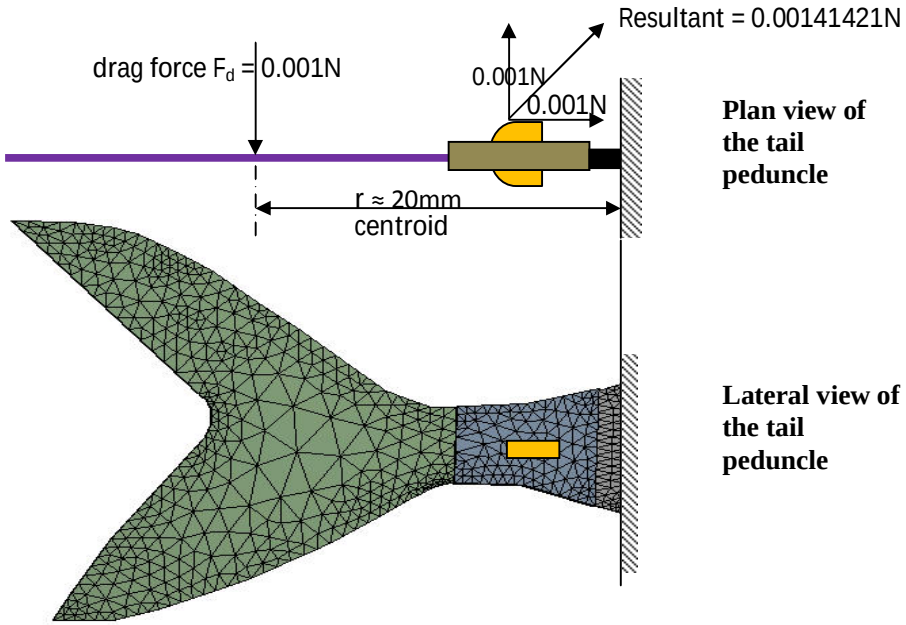


Figure 3.24 Simulated input loads – plan and side views. The finite element tool determines the centroid of the area.

3.6.5 The Servo Motor

Servo motor designed for remote controlled gadgets will be used as the actuators for the artificial hydrostatic joint developed. The motor requirements are estimated as shown in Table 3.6. The step by step calculation of the dynamic torque for a 1Hz oscillation speed of the tail is shown in Table 3.6.

Table 3.6 Estimating the motor requirements

	Parameter	**Value**	**Remark**
1	Torque to overcome drag force F_d of the oscillating tail fin	0.002Nm	F_d = 0.001N r = 20mm Torque = F_d * r
2	Reaction time	50ms or less	Oscillation expected will not exceed 20Hz i.e. a period of 50ms cycle. The motor response must be less than this value
3	Dynamic Torque	0.0000949Nm at 1Hz	The torque that will be experienced by the motor driving the tail fin at 1Hz. Table 3.7 shows how the dynamic torque is derived for 1Hz

Table 3.7 Calculating the dynamic torque for 1Hz oscillation speed

Parameter	**Calculation**	**Result**	**Remark**
$\rho \sim= 990$ kg/m^3			Water density
A= 0.002427 m^2			Tail fin surface area is calculated using AutoCAD Inventor 7 – since it is an irregular shape
R~=20mm			approximately centroid from AutoCAD Inventor 7
maximum oscillating angle	(+45^o to -45^o) = 90 ^{o} = π/2	π/2	The maximum oscillating angle is = 90 ^{o} = π/2
angular displacement	= π/2 * 2	π	maximum oscillating angle * 2 (a complete cycle)
time to perform the displacement	1/1Hz	1s	period of oscillation = 1/frequency of oscillation using the simulation frequency of 1Hz
angular velocity	π * 1	π rad/s	angular displacement / time to perform the displacement
Linear velocity	π rad/s * 0.02m	0.0628m/s	= angular velocity * r
ω_v is equivalent to the linear	ω_v = Linear velocity	0.0628m/s	Instantaneous velocity of the tail.

Parameter	Calculation	Result	Remark
velocity in this scenario (John, 1993).			The minimum is 0m/s (stationary or coasting).
dynamic pressure	from equation 3.17 0.5 * 990 kg/m^3 * $(0.0628m/s)^2$	1.9522 N/m^2	
$F_v = P_v * A$	1.9522 N/m^2 * 0.002427m^2	0.00474 N	
Dynamic torque = $F_v * r$	0.00474 N * 0.02m	0.0000949Nm	torque at the peduncle centroid. This is the torque required for 1Hz tail beat frequency at 90^o angular displacement inside water of density 990kg/m^3.

3.6.6 Battery Size Required

For a remote control (RC) servo motor by www.Futaba-rc.com, the following condition exist;

1. input voltage is fixed and can be between 4.8V to 6.0V
2. torque output when activated is also a range (0.3 - 0.4 Nm) and is dependent on the current flowing at a given time
3. current demand is dependent on the angle it transverses at any time
4. rotation is not continuous at least as used in this project and is intermittent

The limiting factor is therefore the current demand to drive the motor. Therefore equation 3.24 is rearranged as

$$I = w / V^* \eta \,, \qquad (3.25)$$

where

w will be the maximum power the motor will encountered

V = applied voltage = 4.8v for this project

η = is less than 100% as the motor is servo motor, a worst scenario of 50% is assumed

Therefore

$$I > w/(4.8*0.5) \qquad (3.26)$$

3.6.7 The Rubber Joints; Estimating The Mullins Effect

From section 3.2.8, Mullins effect is a memory effect, where the elastomer stays within the bound of previous maximum strain when unloaded. All that is needed is to precondition the rubber used for the artificial hydrostatic joint by stretching the sample to maximum range it will ever encounter in operations 10-20 times or more – imitating the experience it will encounter.

The maximum bending the rubber joint will encounter is $+45^o$ to -45^o and all we need to do is to bend it a couple of times say 20 times slowly to get it preconditioned permanently.

3.6.8 The Rubber Joints; Estimating The Payne Effect

The Payne effect was estimated experimentally as the rubber constituents could not be verified from the manufacturer. A precision computerized machine (Figure 3.25) was therefore setup to estimate it - see Appendix C for detailed information on the machine and how it was used.

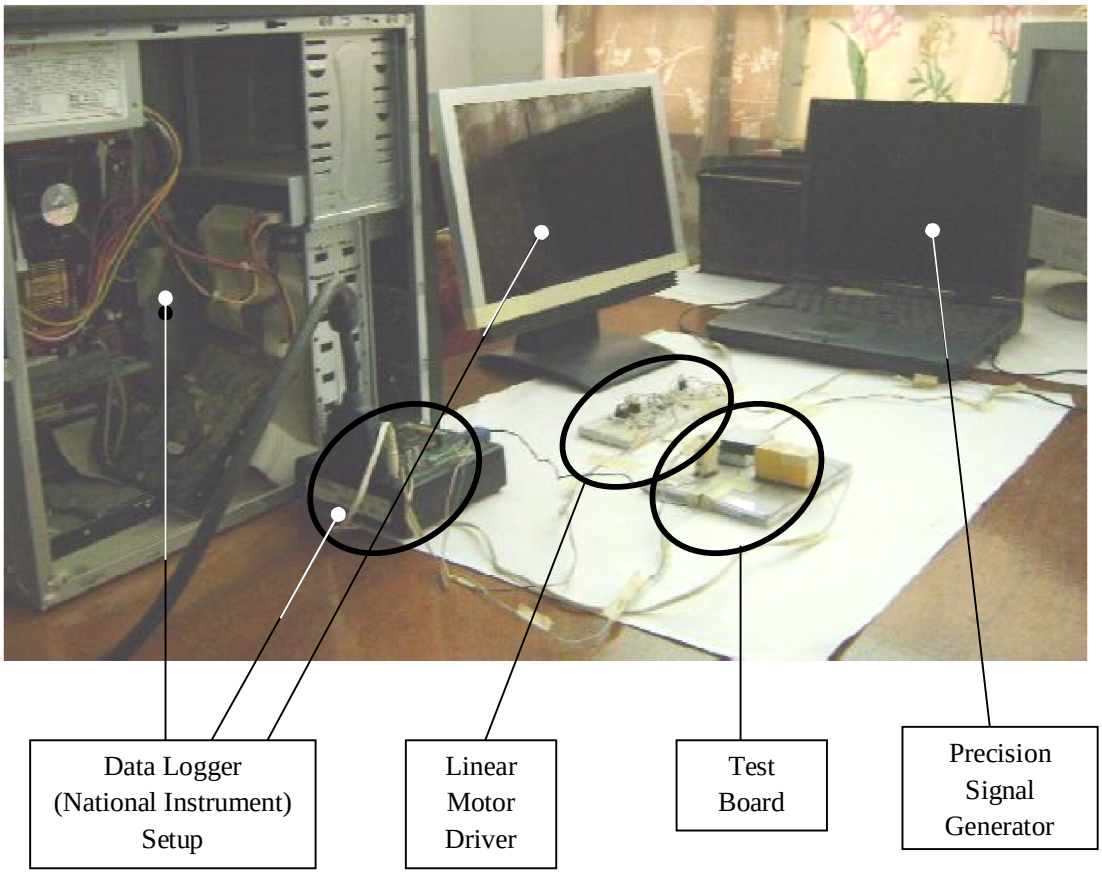


Figure 3.25 The precision frequency induced machine assembled for the frequency induced softening test

3.7 STABILITY AND SENSITIVITY ANALYSIS OF THE DEVELOPED ROBOTIC FISH

This analysis is done by creating a mathematical model of each major component in time domain and then translating it into complex domain using Laplace transform. The transformed equations are then used in MATLAB/SIMULINK block. Thereafter the input-output response was carried out and various charts like step response, Nyquist diagram, Bode diagram were created in the MATLAB/SIMULINK environment. These charts were then used for the stability and sensitivity analysis of the robotic system.

The fish body dynamic model is based on the parameters indicated in figure 3.26 and table 3.8. These parameters are used within MATLAB/SIMULINK environment to

determine the stability and sensitivity of the control system built into the robotic fish.

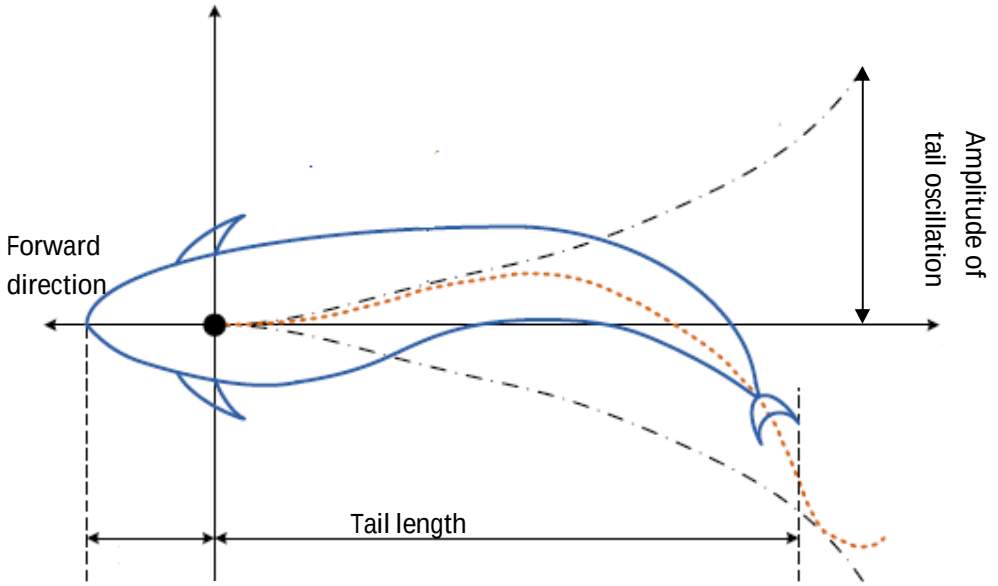


Figure 3.26 The geometrical parameter used in modeling the robotic fish

Table 3.8 Other parameters used in simulating the control action of the robotic fish.

Parameter	**Value**
Armature resistance, R	2 Ω
Inductance, L	0.5H
Back emf constant, K_{emf}	0.1 V
Friction coefficient, K_f	0.2
Inertial load, J	0.1Nm
Damping ratio zeta, ζ	0.5
Tail oscillation frequency, *f*	1 rad/s
Tail length, L_T	0.24 m
Linear wave amplitude factor, c1	0.1
Quadratic wave amplitude factor, c2	0.05

Peduncle (Tail fin Area), T_a	0.002427
Water Density, ρ	990
Coefficient of drag: Tail , Cd_T	1.28
Coefficient of drag: Body, Cd_B	0.04
Strouhal Number, S_h	0.3
Area the fish uses to for the drag, S_a	$0.00094m^2$
Rubber Spring constant - linear model assumed, K_{spring}	0.01
Kinematic viscosity of water, υ	$00.00000112\ m^2/s$

3.7.1 The Hydrodynamic Drag

Hydrodynamic drag is the resistant force the robotic fish will encounter while swimming, it is given as (Jindong and Huosheng, 2004);

$$Dv = ½*Cd*Sa*V^2* \rho \quad (3.27)$$

where the terms are as defined in table 3.8.

And

$$Cf = 1.328Re^{-0.5} + 0.074Re^{-0.2} \quad (3.28)$$

Where Cf is the a sum of laminar and turbulent component of the drag derived from Reynolds number given as

$$Re = L_T V/ \upsilon \quad (3.29)$$

3.7.2 *Teleost* Fish Swimming Equation (Jindong and Huosheng, 2004)

For fishes that use their tails mostly for swimming, to which group *teleost* species belong, the forward speed, V is given as

$$V = fA / S_t \quad (3.30)$$

and

the peak to peak amplitude of the tail motion is given as

$$A = 2(c1*L_T - c2*L_T^2) \quad (3.31)$$

3.7.3 Derivation Of The Mathematical Model And Transfer Function Of The Fish Model

The major components involved in deriving the mathematical model of the fish are discussed in this section. Note that TF stands for transfer function of the component (the subscript) in each section.

3.7.3.1 The servo motor

The RC servomotor is modeled as a DC motor since it is an open loop device. In Laplace transform it is derived as

$$TF_{motor} = (K_m/(L.s + R) * (1/(J.s + K_f)) \quad (3.32)$$

where the first term models the motor electrical system and the second term models the mechanical aspects.

3.7.3.2 The hydrodynamic drag

The hydrodynamic drag (D_{hydro}) is first separated into laminar ($D_{laminar}$) and turbulent ($D_{turbulent}$) portion as follows

$$D_{hydro} = D_{laminar} + D_{turbulent}$$

$$D_{laminar} = ½ *S_a*\rho*V^2(1.328* L_T *V/\upsilon)^{-0.5} \quad (3.33)$$

The transfer function is determined using MATLAB as

$$TF_{laminar} = k_A /s \quad , \quad (3.34)$$

where $k_A = ½ *S_a*\rho*(1.328L_T/\upsilon)^{-0.5}$

$$D_{turbulent} = ½ *S_a*\rho*V^2(0.074*L_T*V/\upsilon)^{-0.2} \quad (3.35)$$

The transfer function is determined using MATLAB as

$$TF_{turbulent} = k_B /s \quad , \quad (3.36)$$

where $k_B = ½ *S_a*\rho*(0.074L_T/\upsilon)^{-0.2}$

3.7.3.3 The rubber joint resistance to bending

The rubber joint is modeled as a voigt body (linear resistance is assumed)

$F_{rubber} = K_{spring} * x$

$$TF_{rubber} = K_{spring} * X_{(s)} \quad (3.37)$$

3.7.3.4 The tail fin resistance to paddling

The dynamic load on the tail fin is given in equation 3.8. The velocity in this case (unlike equation 3.27) is the angular velocity, ω. The transfer function between the fin angular velocity and dynamic load Fv is determined to be

$$TF_{fin} = X(s)/Fv(s) = 1/k_c \,.\, s \quad (3.38)$$

3.7.4 Mathematical Model Of The Robotic Fish

To derive the mathematical model, MATLAB/SIMULINK was used. A model was designed as shown in figure 3.27 and thereafter the overall transfer function was derived between the main input (the driving clock) and output which is the speed of the fish.

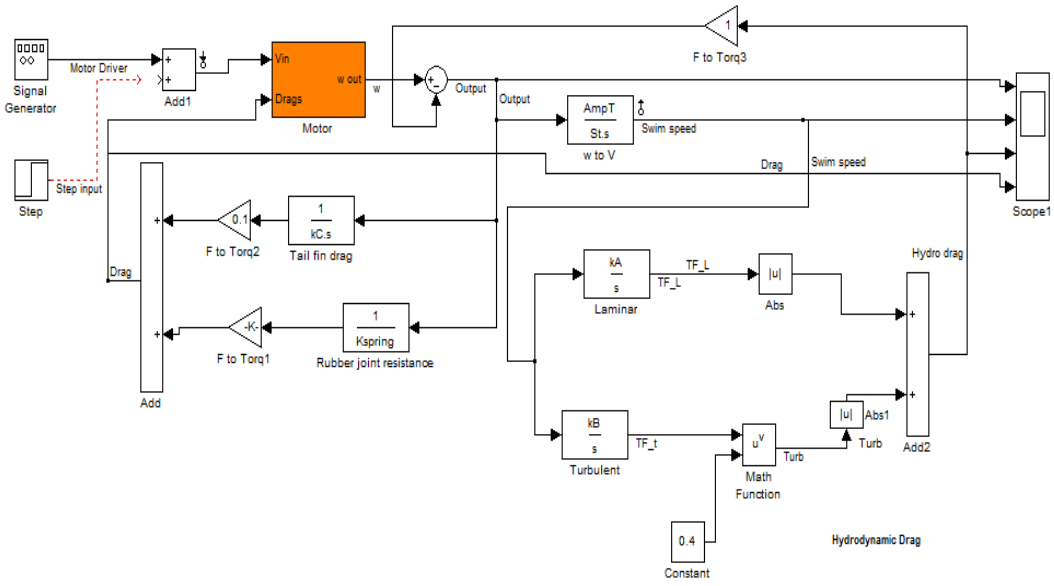


Figure 3.27 The SIMULINK block diagram of the robotic fish model

(1) The overall transfer function of the model fish is given as

$$\frac{0.2816\ s}{s^4 + 26s^3 + 141.8s^2 + 214.4s} \qquad (3.39)$$

(2) The state space representation is given as

$$x' = Ax + B\,u \qquad (3.40)$$

$$y = Cx + Du$$

where

A =

	x1	x2	x3	x4
x1	-4	-1	0	0
x2	0.2	-22	-5.359	0
x3	0	10	0	0
x4	0	10	0	0

B =

	Trigger point (input)
x1	1
x2	0
x3	0
x4	0

C =

	x1	x2	x3	x4
Swim speed	0	0	0	0.1408

D =

	Trigger point
Swim speed	0

State Names:

x1 - Motor System - Electrical

x2 - Motor System1 - Mechanical

x3 - Tail fin

x4 – Angular to Forward speed converter

(3) The zero pole gain (zpg) representation is given as

$$\frac{0.2816\ s}{s\ (s+19.2)\ (s+4.043)\ (s+2.762)} \qquad (3.41)$$

3.7.5 Stability Response Of The Robotic Fish Control

The mathematical model was subjected to a step input defined as

$f(t) = 0$, for $t<0$

$= A$, for $t>0$

where A = amplitude of the step input signal and is set to unity (1) in this work. And the following results were gotten from the step response (figure 3.28), they are the Nyquist plot (figure 3.29), Pole-Zero map (figure 3.30), Bode Plot (figure 3.31), and the Nichols plot (figure 3.32). An impulse response of the control (figure 3.33) was also investigated in the work.

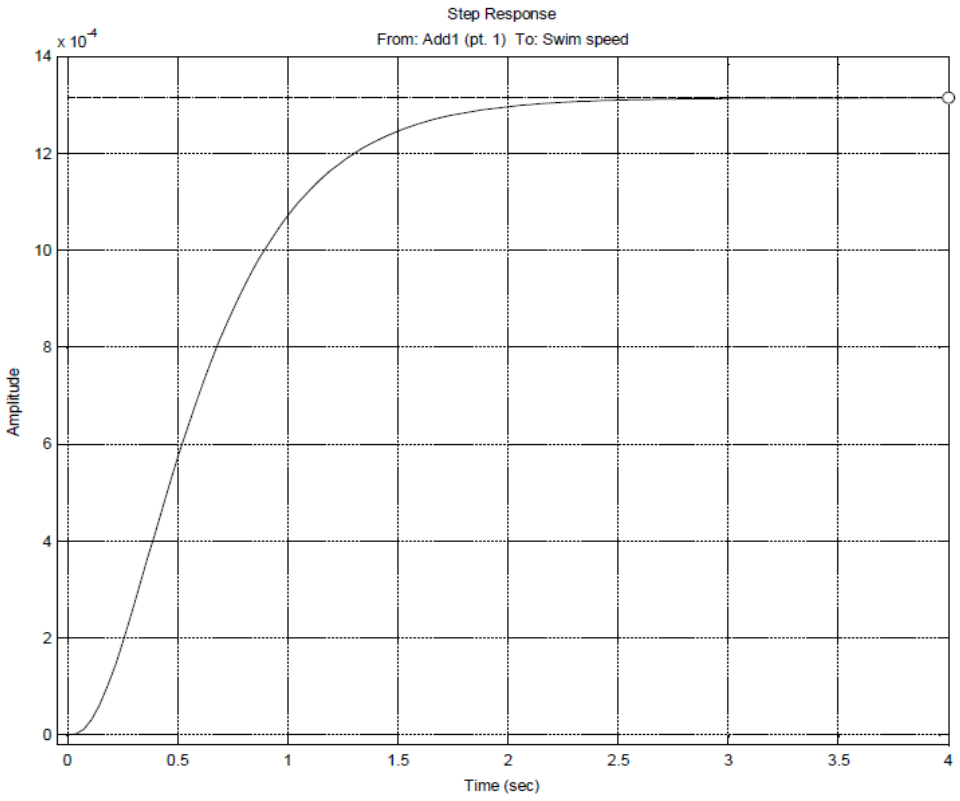


Figure 3.28 Step response of the robotic fish control system

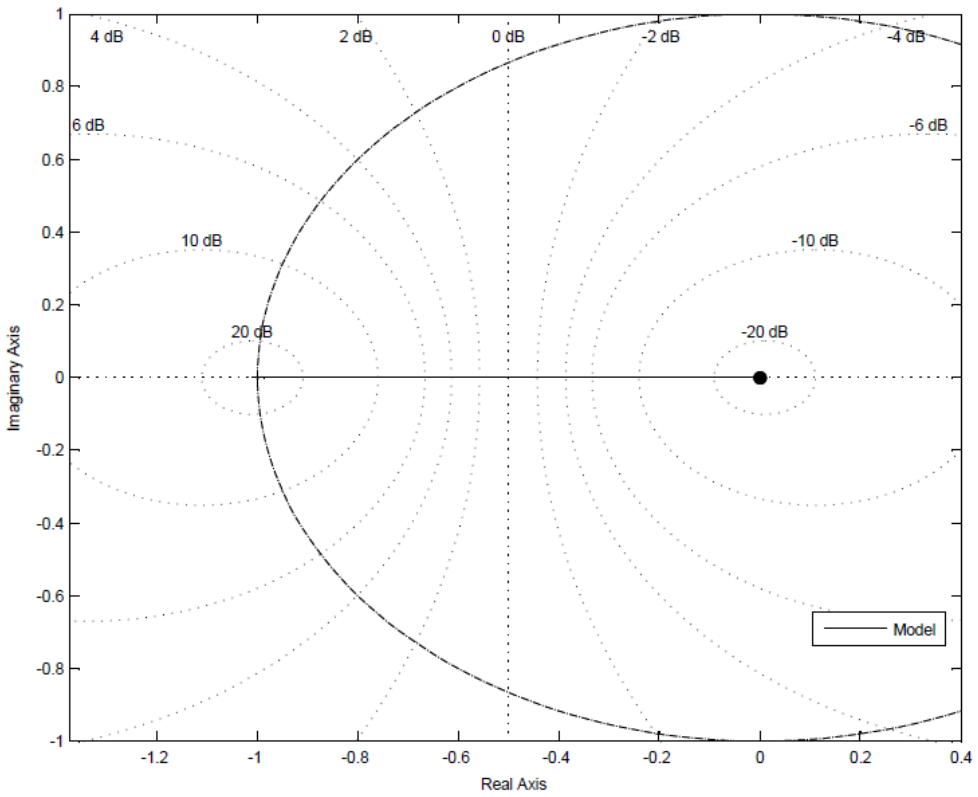


Figure 3.29 Nyquist Diagram for the robotic fish control system

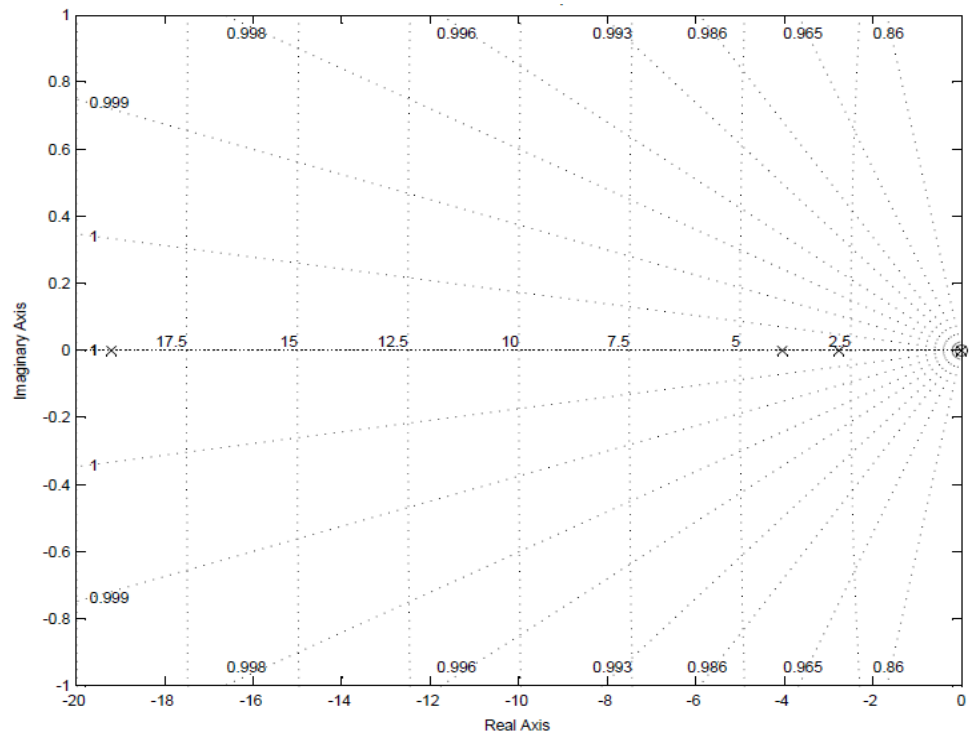


Figure 3.30 Pole-Zero Map Diagram for the robotic fish control system

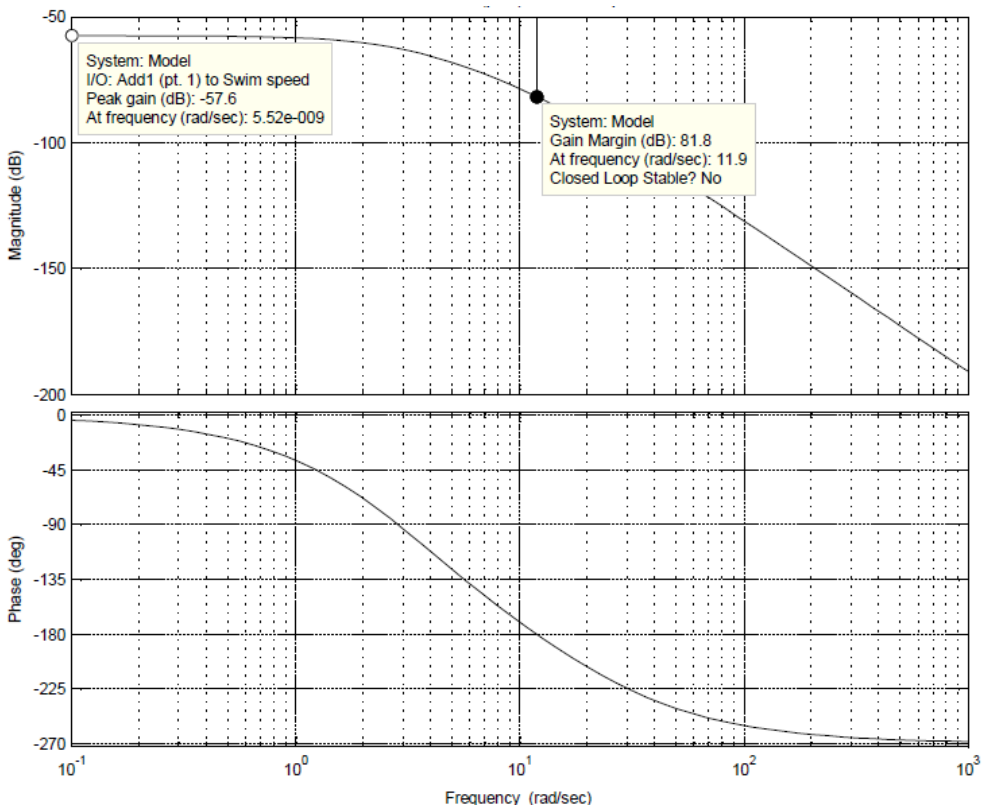


Figure 3.31 Bode diagram for the robotic fish control system

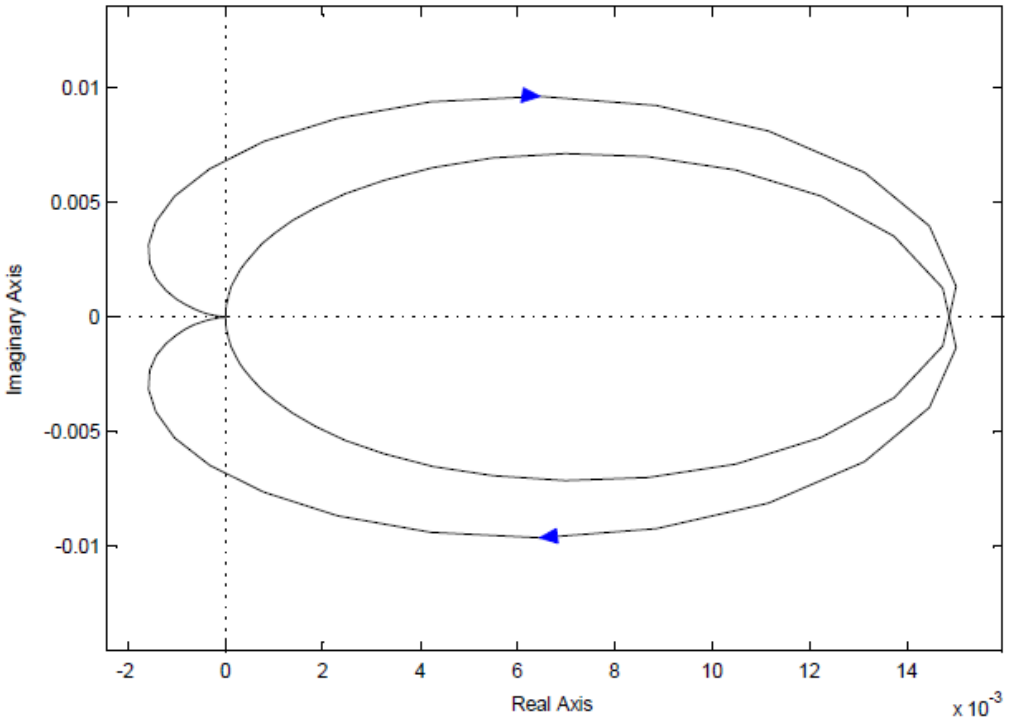


Figure 3.32 Nyquist Diagram for the robotic fish motor control system (equivalent tobehaviour outside water – no hydrodynamic drag)

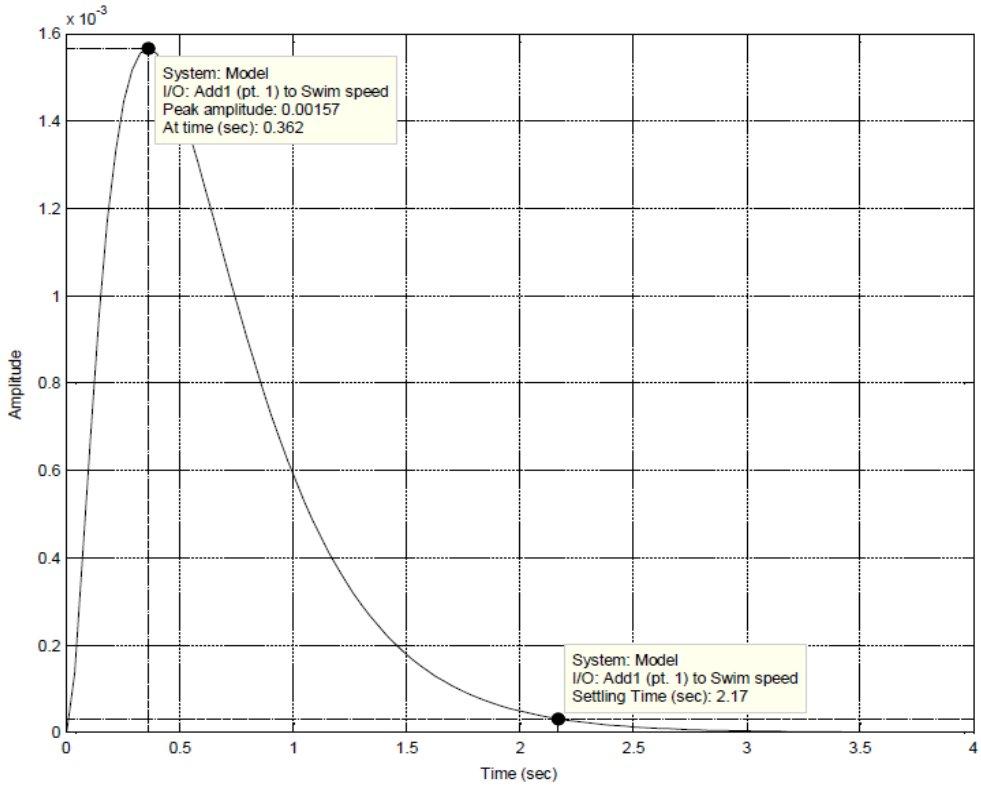


Figure 3.33 Impulse response of the robotic fish control system

3.8 RESULTS OF THE CALCULATIONS AND SIMULATIONS

3.8.1 Forces On Rings

Since flood filled approach is to be used, the water pressure inside and outside the rings for constructing the robot fish haul will be equal, leading to these results as derived in Table 3.2;

Pressure difference P = Pe - Pi = 0, therefore

hoop stress = 0

longitudinal stress = 0

bending stress = 0

3.8.2 Bending Stress Experienced By The Haul

The haul is lumped as a single rod supported at the end (see Table 3.2). The fact that flood filled approach will be used implies that the upward thrust due to buoyancy will be canceled by the downward force due to gravitational pull. There will be a weightlessness of the body. This is the same principle used by submarine and supertankers to get support despite their lengths. Thus

the bending stress = $\sigma_b = \frac{My}{I_x} = 0$, $M_y = 0$

3.8.3 Stress The Cables Will Experience

The stress the Nylon 1010 cable will experience is ≅102MPa as shown in Table 3.4. This falls within the range of commercial values of the Nylon 1010 which is about 210MPa.

3.8.4 The Forces Acting On The Quarter Pulleys

There are 5 quarter pulleys out of which 2 are idlers and the remaining 3 bear loads. The resultant loads on them from Table 3.3 are:

Segment 1 quarter pulley

Torque = 0.06Nm

Vertical reaction/separating forces = 28.28N

Segment 3 quarter pulley

Torque = 0.16Nm

Vertical reaction/separating forces = 28.28N

Segment 5 quarter pulley

Torque = 0.30Nm

Vertical reaction/separating forces = 28.28N

Segment 2 and 4_ quarter pulleys

Torque = 0Nm

Vertical reaction/separating forces = 28.28N

3.8.5 Tensile Stress Within The Glue

Stress within the glue for the segments 1, 3 and 5 that are bearing loads are (using Table 3.3)

σ_{g1}= 670kPa

σ_{g3}=167kPa

σ_{g5}=88kPa

Furthermore Figure 3.34 shows the contact analysis result after the simulation. It was scaled as being sticking, sliding, near and far. The two contacts analyzed show that both are sticking, that is, the materials will be bonded properly.

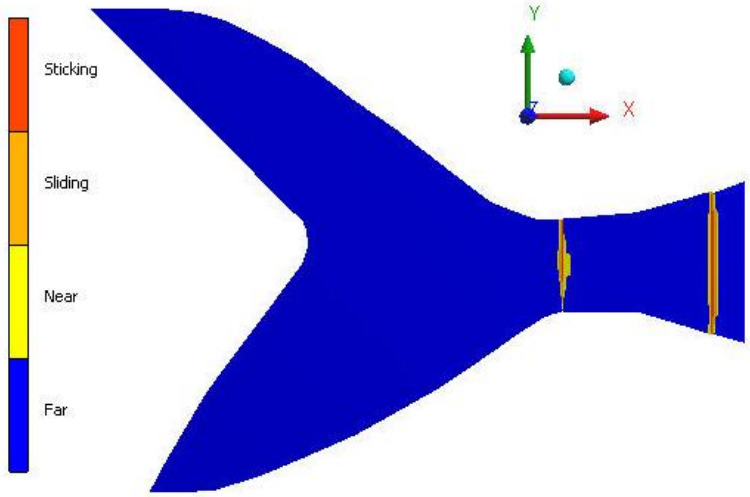


Figure 3.34 The contact analysis of the composite material. All the glued contacts shows a complete sticking which implies that the weight and loads will be spread/absorbed properly.

3.8.6 Stress Within The Rubber Joints

The result of the computer simulation of forces on the surface of the peduncle is shown in Figure 3.35 from which the von Mises maximum stress in the rubber is $0.464x10^4$Pa = 4.64kN/m^2 and the minimum is $0.003x10^4$Pa = 0.03kN/m^2.

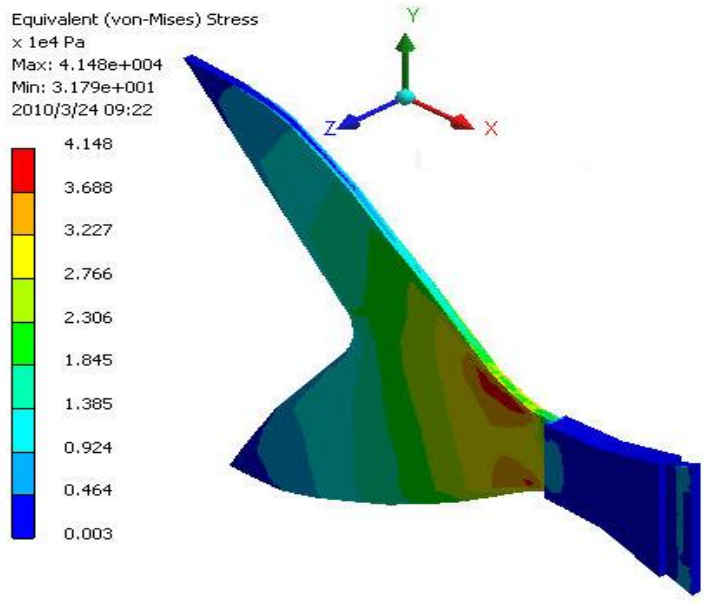


Figure 3.35 Simulation Result – von Mises stress acting within the peduncle using the simulated loads

If the result is extrapolated for each rubber section, the stress factor for any rubber joint will be approximated by:

$$\sigma_x = \frac{H_p}{H_x} \times \sigma_p \qquad (3.42)$$

where H_p = Average height of rubber at the peduncle

H_x = Average height of rubber at any section

σ_p = Stress within the rubber at the peduncle

σ_x = Stress at any section of the tail

for each section we have the result shown in Table 3.9 using average dimensions from the drawing No's 12 to 16. Furthermore, Figure 3.26 elaborates on the stress distribution pattern, it drops rapidly toward the head board.

Table 3.9 The maximum and minimum stress within the rubber joints

Section	Maximum stress within the rubber joints	Minimum stress within the rubber joints
1	4.64 kN/m^2	0.030kN/m^2
2	2.37 kN/m^2	0.015kN/m^2
3	1.46 kN/m^2	0.009kN/m^2
4	1.14 kN/m^2	0.007kN/m^2
5	1.00 kN/m^2	0.006kN/m^2

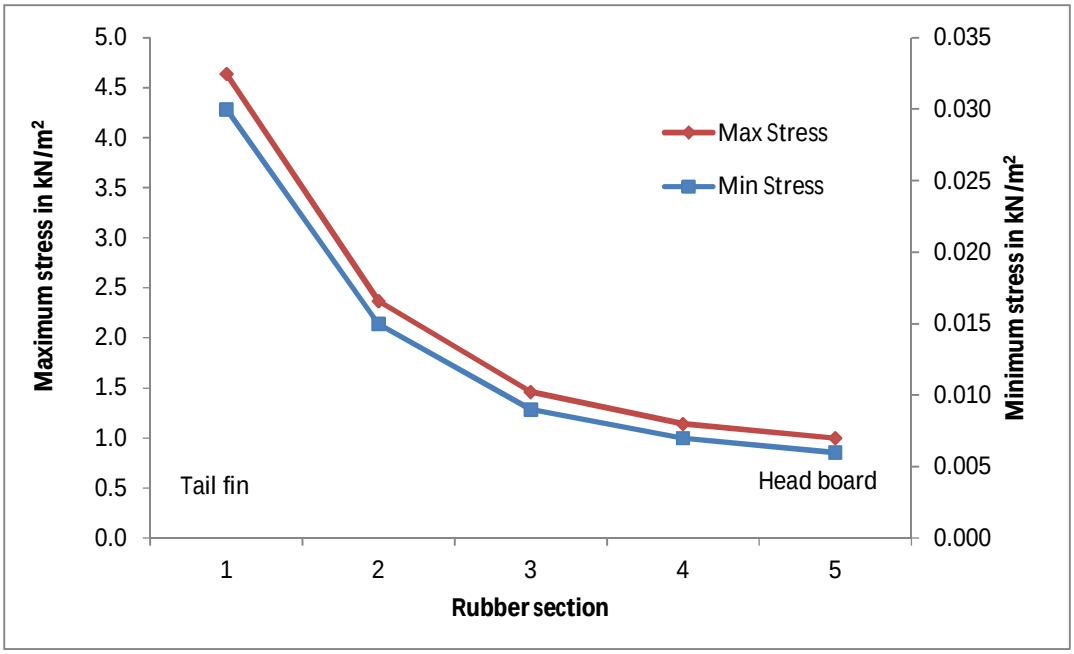


Figure 3.36 The maximum and minimum stress within the rubber used for the joints

Figure 3.37 shows the simulation result of the peduncle under vertical loading or its own weight (i.e. the cantilever effect). For the rubber component the maximum von Mises stress experienced in the rubber is 3.803x10^{3}Pa = 3.8kN/m^2 and the minimum von Mises stress experienced is 0 Pa = 0 kN/m^2

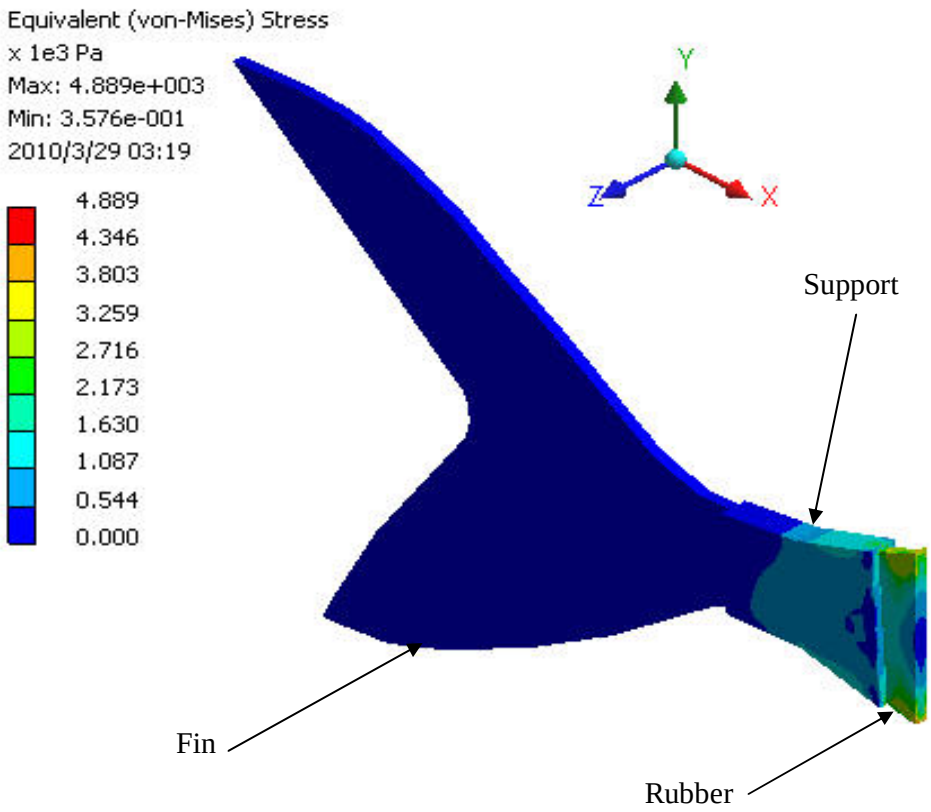


Figure 3.37 von Mises stress within the peduncle under its own static weight.

Using Figure 3.38, the stress acting on the links of the tail is arrived at as follows;

The weight of each part made with ply wood are FP_6, FP_5 ,FP_4,FP_3,FP_2, FP_1 and those of the rubber joints are FR_5, FR_4,FR_3,FR_2, FR_1. The weight of these irregularly shaped bodies are computed with ANSYS 10 multiphysis during simulation. To derive the centroid of each element relative to the head board, Autodesk Inventor 7.0 was used. Geometrical data (average height of each element) were taken from the drawing nos 5 to 16. The result of the loads, separating torque due to localized weight and cumulative torque due to other links (cantilever effect) and average stress are tabulated in Table 3.10 using equation 3.42. The centroid r for each part relative to the head board is shown in Figure 3.38, only one is shown for clarity.

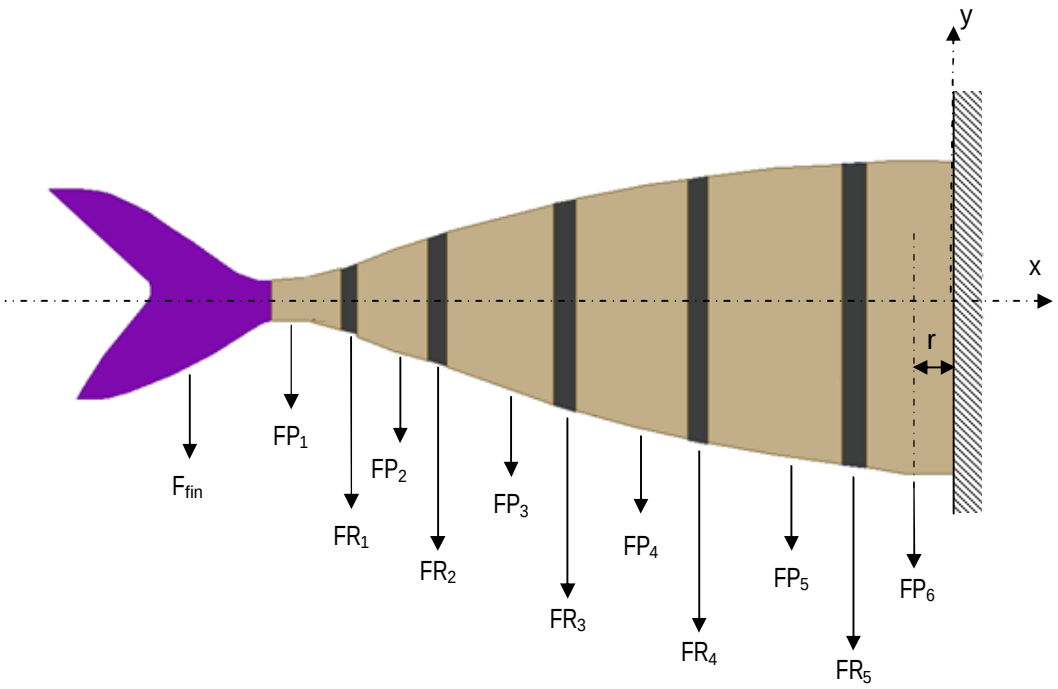


Figure 3.38 The load distributions on the tail due to the components weights

Table 3.11 The weights and centroid of action of the rubber joints and the supports

Part	Weight	Centroid (x-axis) in mm	Separating torque (Nm)	Cumulative torque	Cumulative load due to weight of previous link	Stress (N/m^2)
FP_6	0.28110555N	2.238	0.000629	0.000676	1.198177	5145.58
FP_5	0.38000016N	10.395	0.000047	0.010449	0.917072	8531.69
FP_4	0.26762661N	27.373	0.010402	0.010544	0.91253	4274.04
FP_3	0.17935623N	44.417	0.000142	0.015808	0.53253	5663.10
FP_2	0.07039558N	58.536	0.015666	0.015867	0.529325	2946.10
FP_1	0.00208875N	73.643	0.000201	0.015799	0.261698	3550.02
FR_5	0.00454199N	86.966	0.015598	0.015745	0.258971	2047.20
FR_4	0.00320469N	101.434	0.000147	0.007933	0.079615	1754.31
FR_3	0.00272722N	110.602	0.007786	0.007861	0.078168	1060.90
FR_2	0.00144725N	120.670	0.000075	0.000346	0.007772	335.04
FR_1	0.00062426N	129.457	0.000270	0.001084	0.007148	185.31
F_{fin}	0.00505912N	160.735	0.000813	0.000813	0.005059	0.53

3.8.7 Stress Within The Plywood Material

The result of the computer simulation of forces on the surface of the peduncle is shown in Figure 3.25. For the plywood support, the von Mises Maximum stress is $0.924x10^4Pa = 8.24kN/m^2$ occurring at the junction between it and the fin. The minimum von Mises stress is $0.003x10^4Pa = 0.03kN/m^2$ occurring at the junction between it and the rubber joint. Equation 3.42 is also used to approximate the stress experienced by the other supports. The result for other plywood parts is shown in Table 3.11 using equation 3.42. The graphical representation is shown in Figure 3.39 which shows a rapidly declining pattern toward the head board.

Table 3.11 The maximum and minimum stress within the plywood support

Section	Maximum stress within the plywood support	Minimum stress within the plywood support
1	9.24 kN/m^2	0.03kN/m^2
2	4.62 kN/m^2	0.015kN/m^2
3	2.68 kN/m^2	0.009kN/m^2
4	1.94 kN/m^2	0.006kN/m^2
5	1.57 kN/m^2	0.005kN/m^2
6	1.48 kN/m^2	0.005kN/m^2

3.8.8 Maximum Stress Within The Fin

The result of the computer simulation of forces on the surface of the fin is shown in peduncle stress simulation of Figure 3.35 from which the von Mises maximum stress in the fin is $4.148x10^4Pa = 41.48kN/m^2$ and the minimum is $0.003x10^4Pa = 0.03kN/m^2$.

The maximum occurred at the top bend and lower bend just before the connector to the last segment rubber.

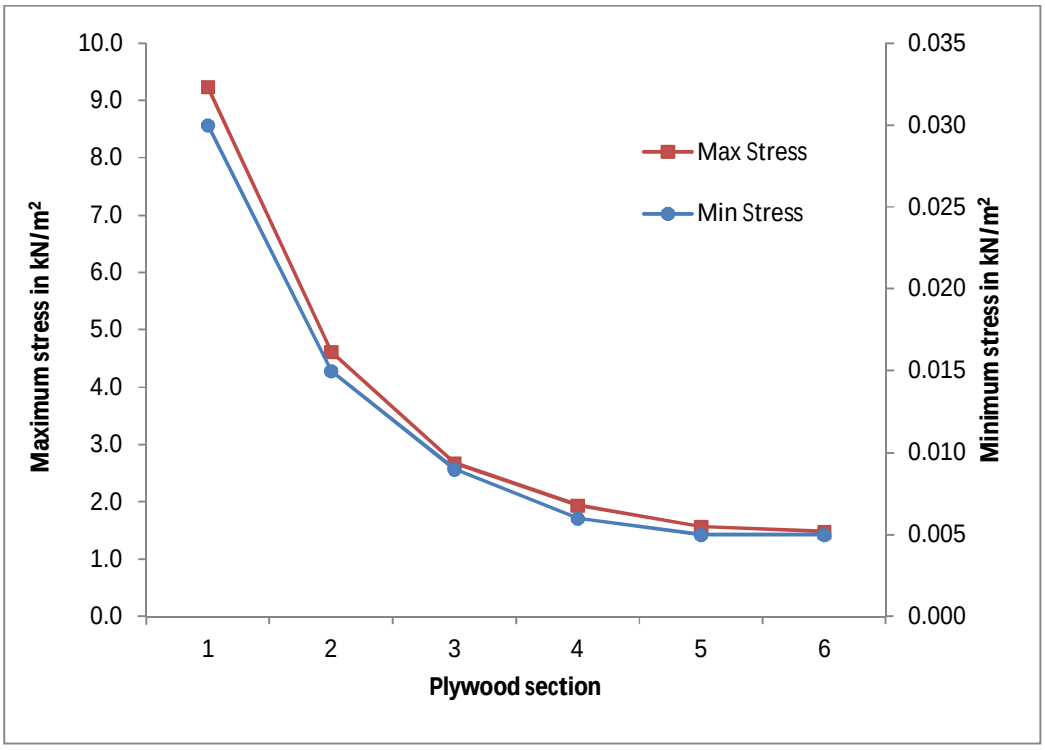


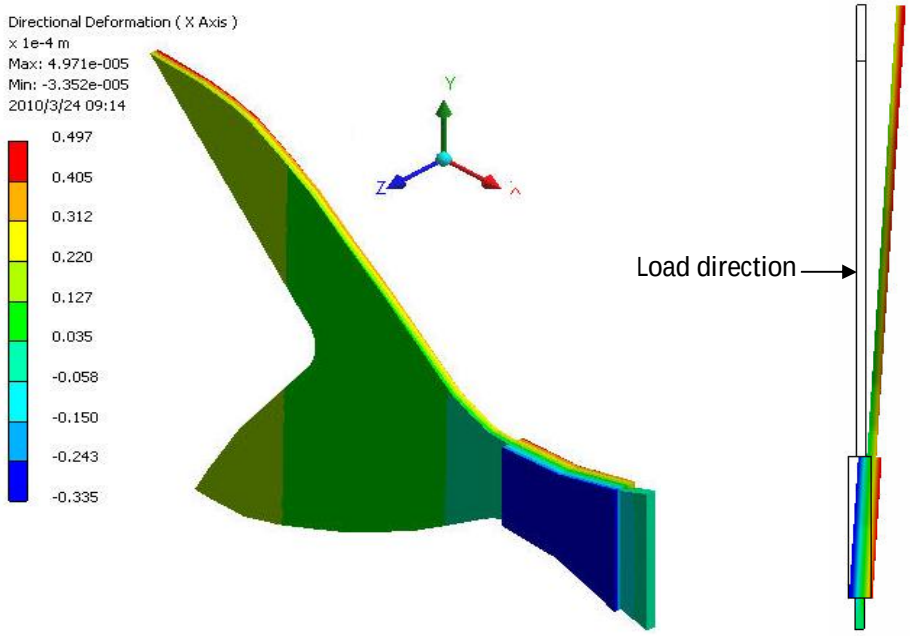
Figure 3.39 The maximum and minimum stress within the plywood support

3.8.9 Test For Warping/ Bending Result

Figure 3.40 shows the deformation (or warping) simulation result. The isoline shows straight pattern. A warped assembly will show contoured lines. It can thus be concluded that the assembly will maintain the rigidity required in operation.

3.8.10 Frequency Induced Softening

Figures 3.41 to 3.48 show the lags due to the rubber stiffness at various experimental frequencies used. The frequencies used are 0.5Hz, 1Hz, 5Hz, 10Hz, 15Hz, 20Hz, 25Hz and 30Hz. Three experiments were conducted for each frequency at the



Isometric View Top view

Figure 3.40 Simulation Result – Directional deformation – It shows vertical straight patterns. The top view further shows the evidence of rigid non warping bending. The implication of this is that a rigid support is guaranteed for the Hydrostatic skeleton.

temperatures shown in Figure 3.49. The x-axis indicates the number of data used for the plots. Some outlier data were discarded. Figure 3.50 is a consolidated data from figures 3.41 to 3.48. From Figure 3.50 it is observed that there is progressive drop in the response time as frequency increases. The meaning is that the material becomes softer as the frequency increases. At above 25Hz, softening becomes more glaring and therefore this particular rubber should not be used above that value for oscillatory motions. The artificial hydrostatic joint should not be run at a frequency above 25Hz for this particular rubber sample.

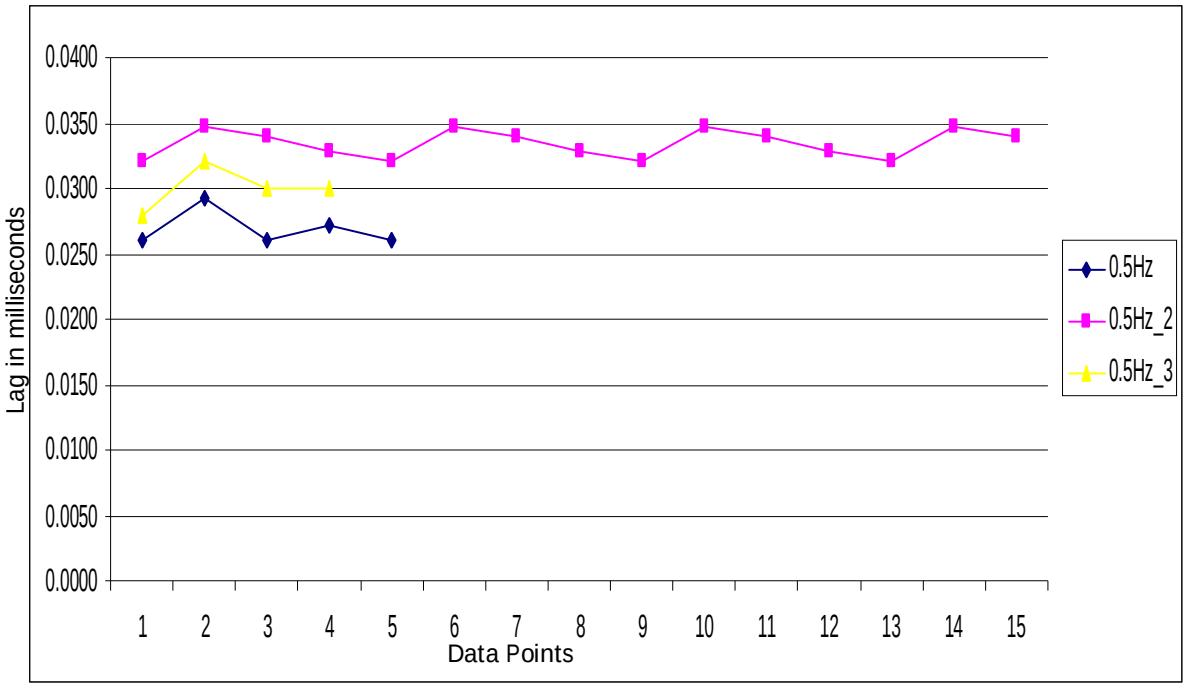


Figure 3.41 Lag at 0.5Hz frequency of oscillation.
The legends 0.5Hz, 0.5Hz_2, 0.5Hz_3 correspond to temperature a, b and c of Figure 3.49 respectively.

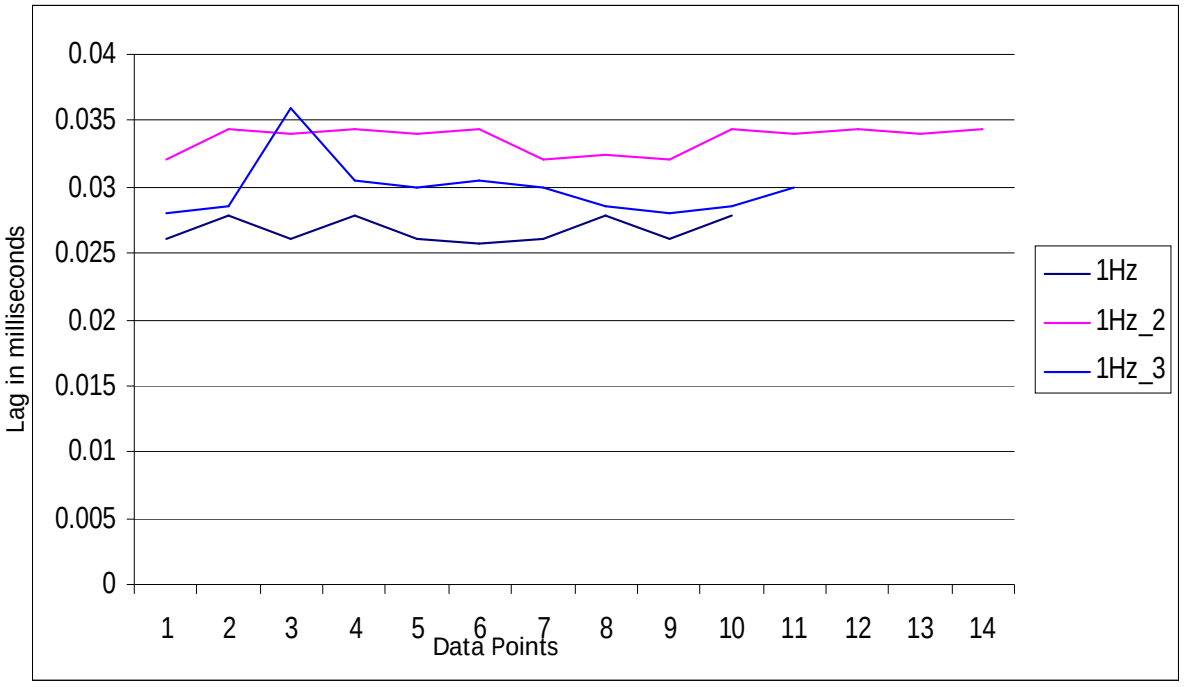


Figure 3.42 Lag at 1Hz frequency of oscillation.
The legends 1Hz, 1Hz_2, 1Hz_3 correspond to temperature a, b and c of Figure 3.49 respectively.

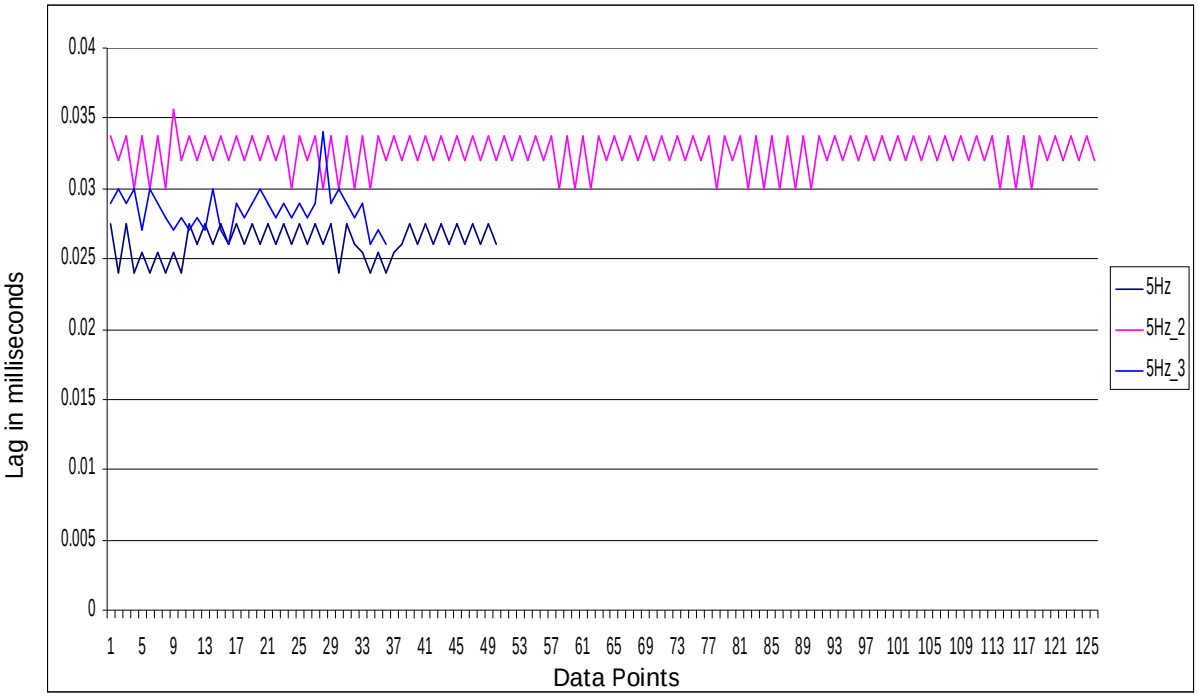


Figure 3.43 Lag at 5Hz frequency of oscillation.

The legends 5Hz, 5Hz_2, 5Hz_3 correspond to temperature a, b and c of Figure 3.49 respectively.

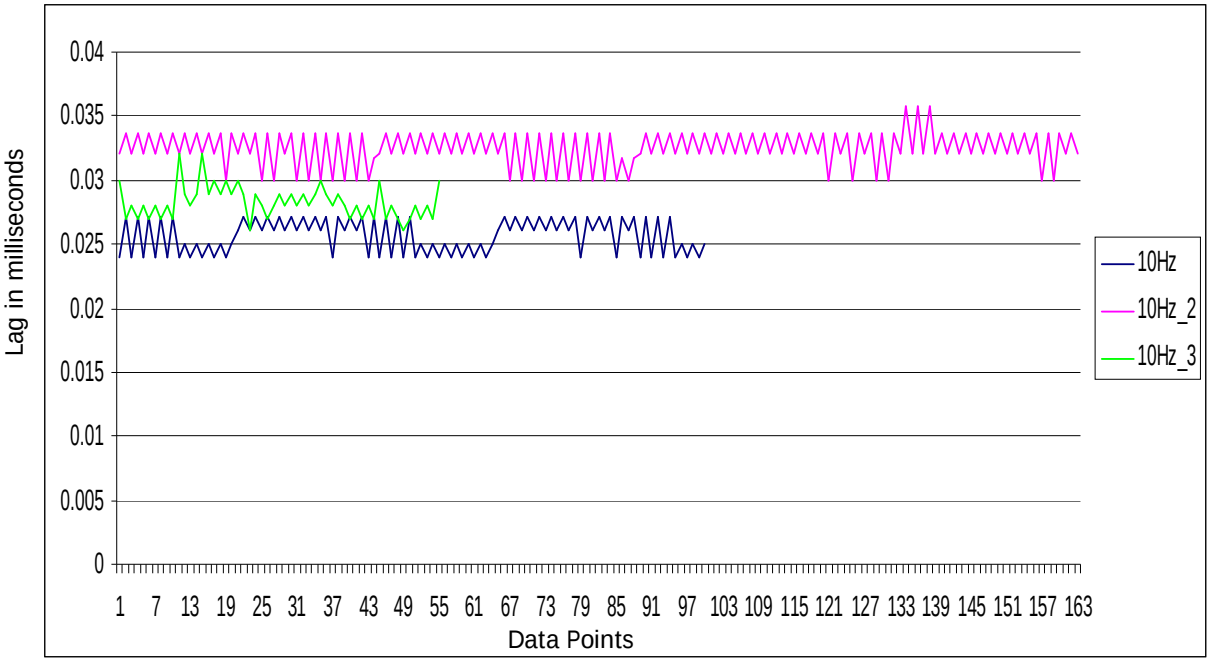


Figure 3.44 Lag at 10Hz frequency of oscillation.

The legends 10Hz, 10Hz_2, 10Hz_3 correspond to temperature a, b and c of Figure 3.49 respectively.

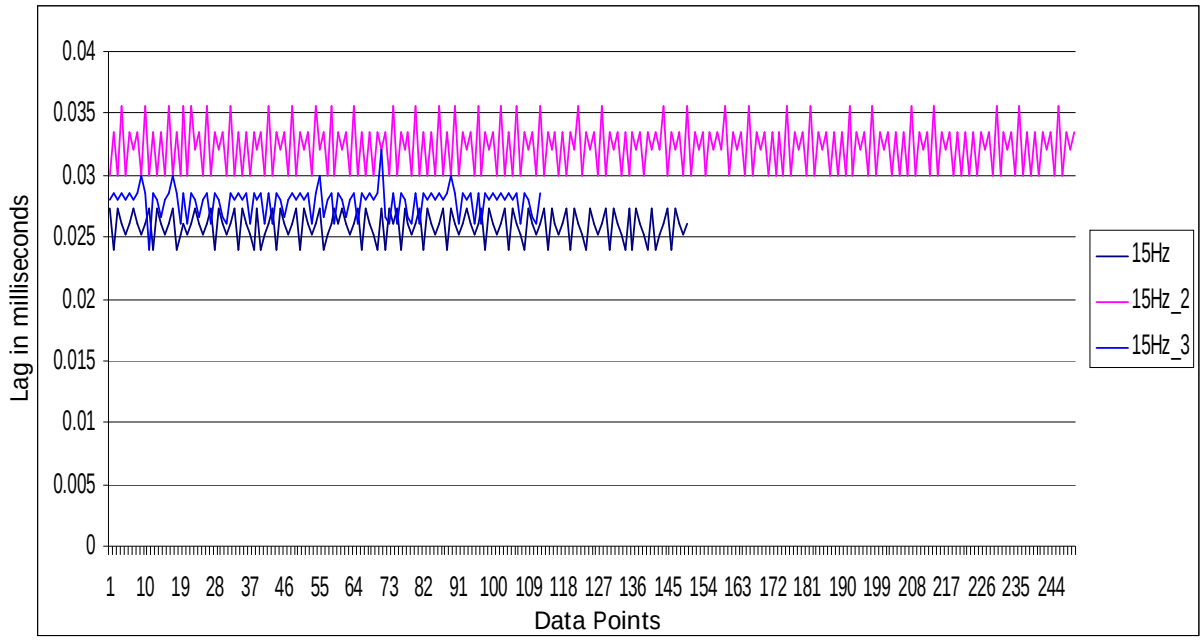


Figure 3.45 Lag at 15Hz frequency of oscillation.
The legends 15Hz, 15Hz_2, 15Hz_3 correspond to temperature a, b and c of Figure 3. 49 respectively.

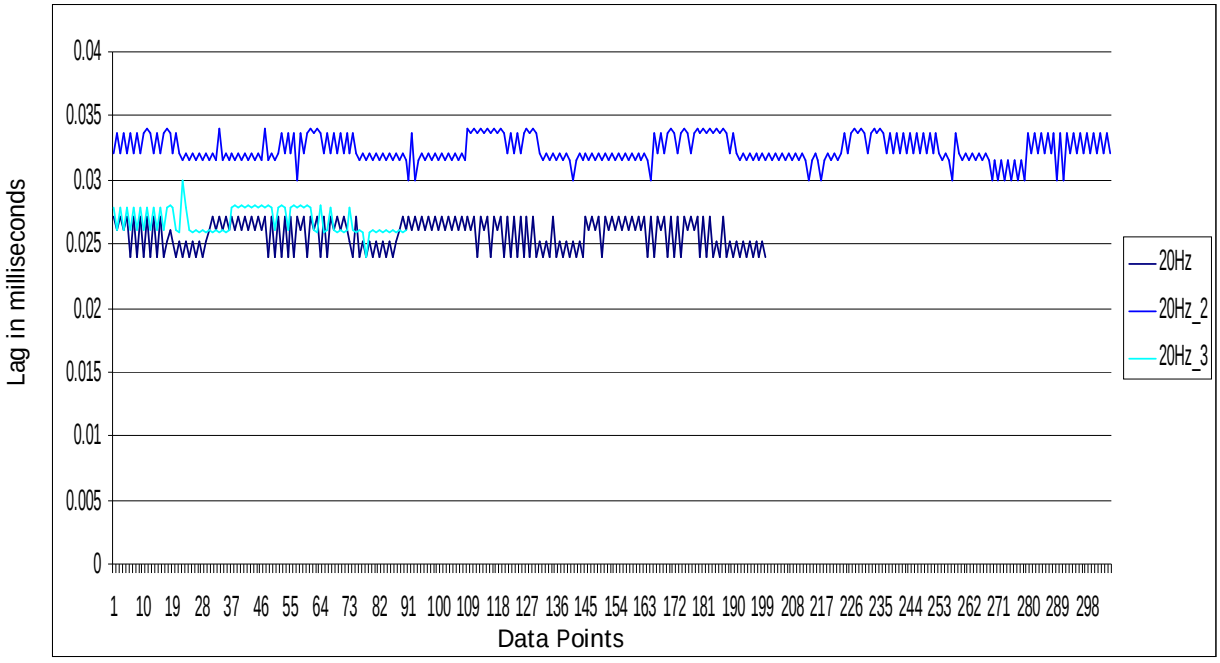


Figure 3.46 Lag at 20Hz frequency of oscillation.
The legends 20Hz, 20Hz_2, 20Hz_3 correspond to temperature a, b and c of Figure 3. 49 respectively.

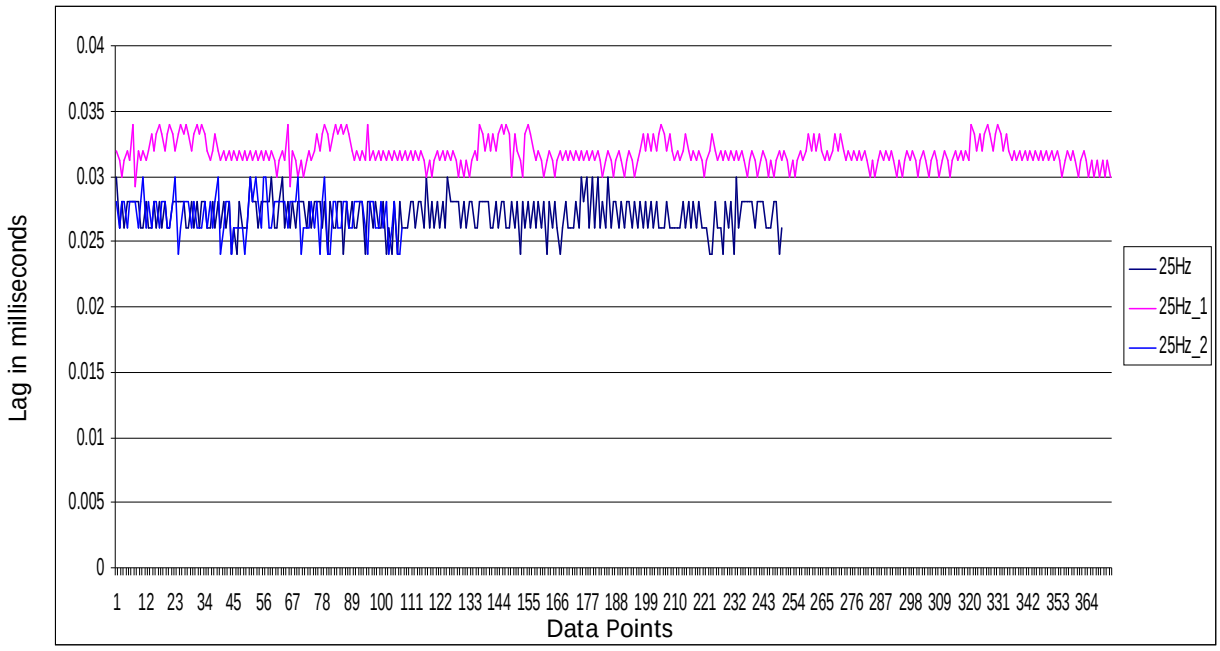


Figure 3.47 Lag at 25Hz frequency of oscillation.

The legends 25Hz, 25Hz_2, 25Hz_3 correspond to temperature a, b and c of Figure 3. 49 respectively.

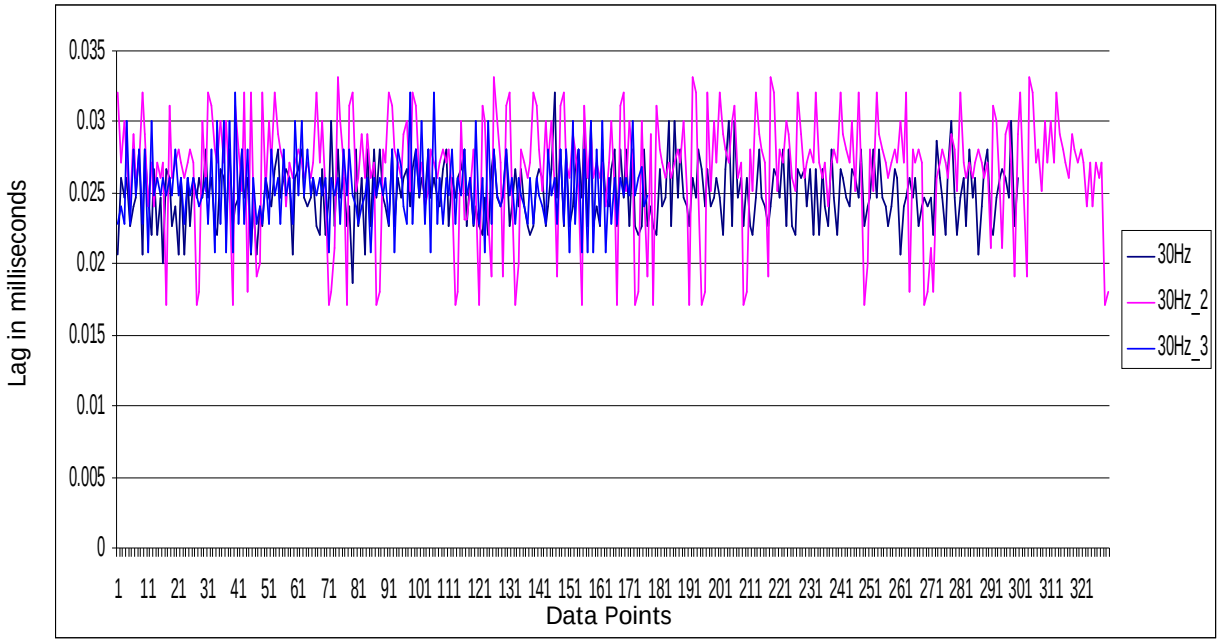


Figure 3.48 Lag at 30Hz frequency of oscillation.

The legends 30Hz, 30Hz_2, 30Hz_3 correspond to temperature a, b and c of Figure 3. 41 respectively.

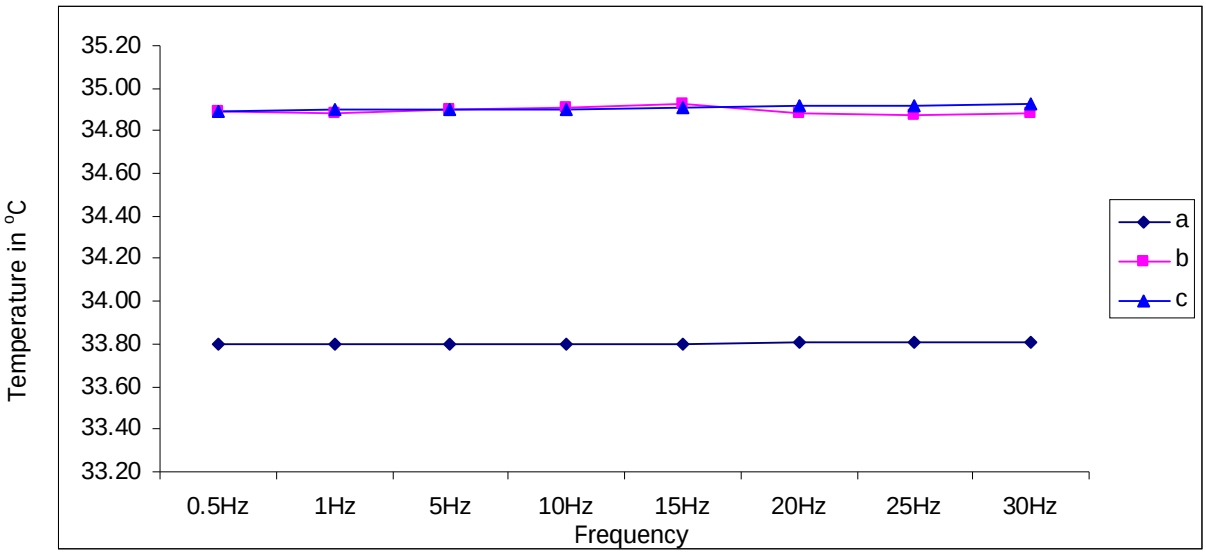


Figure 3.49 Different room temperature at which test was carried out. Maximum variation is 1.1°C.

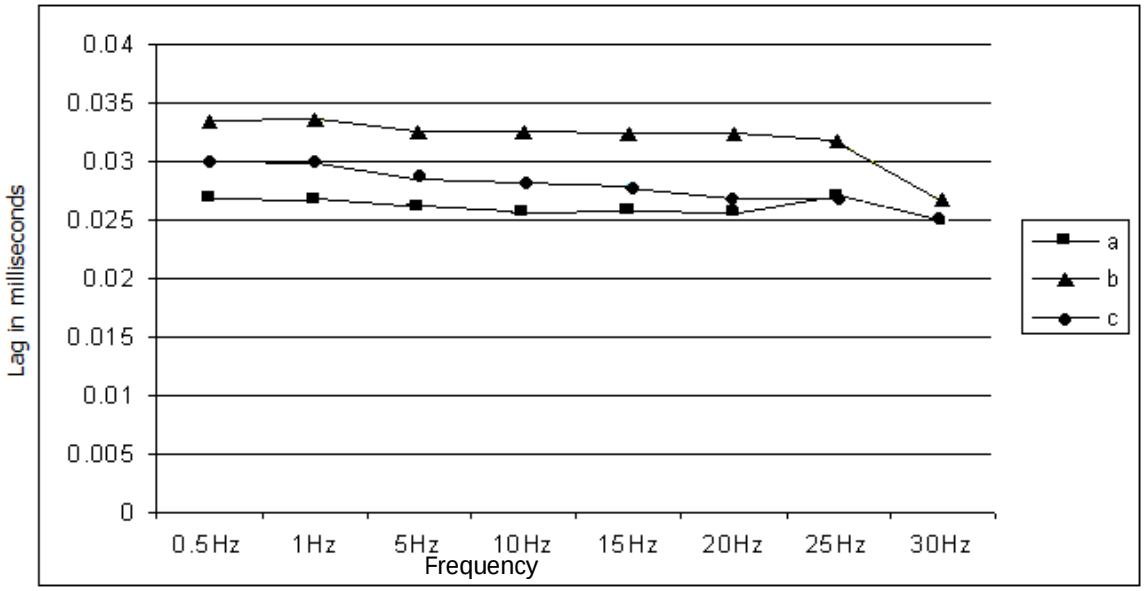


Figure 3.50 Progressive drops in response time with increasing frequency. The legend (a,b,c) refers to the environmental temperature as shown in Figure 3.49

3.8.11 Result Of Dynamic Torque / Motor Loads For Various Mode (Frequency, Angle Of Oscillation) Of The Peduncle

The summary of the torque the motor attached to the peduncle will encountered

for different frequency ranges and various angles of oscillation is shown in Table 3.12. The steps used in Table 3.6 and 3.7 were applied for each combination of frequencies and angles of oscillation to arrive at the dynamic torque developed. The frequencies indicated here were selected to tally with those used for the frequency softening effect experimentation. The maximum torque that will be encountered within the designed limit of 0 to 25Hz and peak displacement is 0.0592850Nm. From Futaba S3003 servo motor datasheet, its rating is 0.29Nm, which means that it is capable of handling the dynamic load effectively as it is greater than the largest value of 0.0592850Nm expected.

Furthermore, Figure 3.51 which is the graphical representation of the Table 3.12, shows that the torque requirement increases greatly with the angle of oscillation.

Table 3.12 Summary of dynamic torque (Nm) developed as a function of angle of oscillation and its frequency (medium is water of density=990kg/m^3)

	Angle of oscillation in degree					
Freq (Hz)	90	45	30	20	10	5
0.5	0.0000237	0.0000059	0.00000263	0.0000012	0.0000003	0.00000007
1	0.0000949	0.0000237	0.00001054	0.0000047	0.0000012	0.00000029
5	0.0023714	0.0005929	0.00026349	0.0001171	0.0000293	0.00000732
10	0.0094856	0.0023714	0.00105396	0.0004684	0.0001171	0.00002928
15	0.0213426	0.0053357	0.00237140	0.0010540	0.0002635	0.00006587
20	0.0379424	0.0094856	0.00421582	0.0018737	0.0004684	0.00011711
25	**0.0592850**	0.0148213	0.00658722	0.0029277	0.0007320	0.00018298

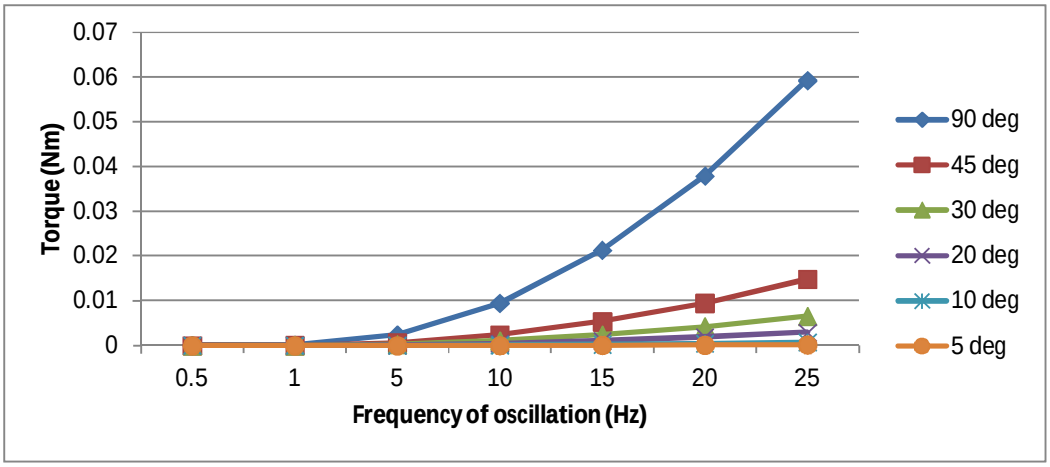


Figure 3.51 Torque developed at different peduncle oscillation frequency and swing angle

3.8.12 The Battery Requirement To Drive The Servo Motor

From Table 3.12, the maximum dynamic torque that will be encountered is 0.0592850Nm.

Rated speed for Futaba S3003 at 4.8v = 0.23 sec/60^{o} = 0.72 rev/s

Hence maximum power needed from equation 3.42 = 2π * 0.72 * 0.0592850 ≈ 0.27W

Hence current requirement is I > w/(4.8*0.5) = 0.27/(4.8*0.5) = 0.11A

For 3 servo motors

Current to drive them = 3 * 0.11A= 0.33A=333mA

An LiPo battery rated 900mAh will drive the three motors successfully for

900/333 h= 2.7hrs

3.8.13 Stability Response Of The Robotic Fish Control

Using MATLAB pole(sys) command, the system was found to have four poles; 0, -2.7631, -4.0426, and -19.1943. Although three of the poles are negative real value with 3 of them greater than -1 on the real axis of figure 3.29, it can be safely said that the system is stable for open loop design but as confirmed by the Bode diagram, Figure 3.31, the system is unstable if used in closed loop mode, a negative gain margin is an indication of an unstable system. From Figure 3.30 Pole-Zero Map diagram, all the

poles lies on zero imaginary axis meaning a non oscillatory system. From figure 3.29 the system maximum gain is -20dB, see appendix G.

3.8.14 Sensitivity Of The Robotic Fish Control

On the system sensitivity, it can be seen from Figure 3.33 that the system swim speed response to impulsive input is rather slow, it takes about 2.17 seconds to settle after an impulsive perturbation. It means that the system is very sensitive to perturbation (Ashish, 2002). From the Nyquist diagram of Figure 3.32, which is for the robot controller without hydrodynamic drag, the stability is within a very narrow range, its characteristic equation roots are -19.1943, -4.0426 and -2.7631 and are all far from the frequency ($j\omega$) plot as indicated in the Nyquist diagram.

CHAPTER FOUR

CONSTRUCTION PROCESSES AND PERFORMANCE EVALUATION OF THE FISH ROBOT

4.1 CONSTRUCTION SEQUENCE

The construction and assembly of this robot was done on two fronts; the hardware and the firmware. The hardware is all about the tangible components including the artificial hydrostatic joints while the firmware is all about the software that controls the joints so that biomimicry can be achieved.

4.2 CONSTRUCTION PROCESS OF THE HARDWARE

The following steps were taken in translating the biological model (394.01mm long mackerel) into a 1:1 scale robotic model of figure 4.1:

Table 4.1 Step by step construction process of the hardware

Component	Material	Construction process	Equipment used
Haul	6.35mm (1/4inch) Plywood	The haul is made from plywood rings constructed according to drawing no 4. These rings (figure 4.1) were cut using a jig saw. The rings were then glued according to their positions as indicated in the drawing no 2 using epoxy glue to form the haul (figure 4.2). However, the ring at position 10 was not used as its position was replaced by the micro switch of figure 4.3.	Jig saw, Epoxy glue

Component	Material	Construction process	Equipment used
Bump switch	1. Micro switch 2. Wires 3. Vero board	The bump switch is a micro switch and is made as an integral part of the haul as shown in figure 4.3. The two switches are first soldered on a circuit board and then glued to the 3mm deep recess on the haul using epoxy glue.	Soldering iron Epoxy glue
Ultrasonic sensor assembly	Parallax Ping))) pair	The cone of the hauls (after ring no 10) holds the ultrasonic sensors – figure 4.4. The receiver was glued to the ring no 1 (see drawing no 2) with epoxy glue and the transmitter was glued to the base of the cone as shown in figure 4.4.	Soldering Iron Epoxy glue
Water proofing of the haul	Plywood Haul	The haul was water proofed in stages. 1. First, the outside of the haul was given a foundation coat of TOP BOND® wood glue (figure 4.5). 2. Then a coat of wood glue soaked fine sawdust was applied (~3mm thick) – figure 4.6. The aim is to produce a smooth outer coat. 3. The haul was then oven dried for 5 min at 100watt using Samsung microwave oven - figure 4.7 to prevent soaking of the haul. 4. The haul was left in open air to allow it to dry slowly for 1 year (August 2010 to August 2011) – to allow stability and strength. 5. A blue silicone layer was added to the external to make it impermeable to water. At this stage, the bump switch was already in place. Figure 4.8. 6. The inside was coated with cyanoacrylate glue (super glue) to make the inside of the haul water proof.	Wood glue (TOP BOND) Fine saw dust (sieve size = Mesh 10 = 2.0mm maximum particle size) Microwave oven Blue silicone Cyanoacrylate glue (super glue)

Component	Material	Construction process	Equipment used
The tail support structure	3.175 mm (1/8inch) Ply wood	The tail support structure is made from plywood slabs constructed according to drawing nos 6 to 11. These slabs (figure 4.9) were cut using jig saw.	Jig saw
The tail rubber joints	Rubber strips from Kings tire rubber	The tail rubber joints were made from Kings tire rubber tube (size=165/175-13) (figure 4.10). The dimensions were taken from drawing nos 12 to 16 to get the shapes of figure 4.11. A Tiger razor blade and scissors were used to get the contours from paper stencils with the drawing printed on them	1. Tiger razor blade 2. Scissors 3. Paper (as stencil)
Quarter pulleys assembly	¾inch (19.05mm) plywood PVC tubings	The quarter pulleys were made from ¾inch (19.05mm) plywood using drawing nos 17 to 21 dimensions. The cuttings were made with a power jig saw (Bosh PST 54E), fine grained sand paper was used for polishing it. A 2.5mm round file was used for creating the slots to hold the 2.5mm unplasticized PVC tubings – figure 4.12. The tubes were held in place with epoxy glue.	1. Power jig saw (Bosh PST 54E) 2. Fine grained sand paper 3. 2.5mm round file 4. Epoxy glue
The cable and flexible plastic support	Nylon 1010, Unplasticised Polyvinly chloride (PVC) tubes	The nylon cables were threaded through the PVC tubings using thin nichrome wires. Each cable length was made much longer than the length of the tail assembly (198.41mm from drawing no 1).	Nichrome wire for threading purposes

Component	Material	Construction process	Equipment used
The tail fin	¾inch (19.05mm) plywood	The fin structure is made from plywood slabs constructed according to drawing no 5. Its contour was traced out on the 1/8 inch (3.175mm) thick plywood board - figure 4.13.	Jig saw
The tail – wooden and foams half rings	6.35mm (1/4inch) plywood Collapsed polyurethane foam	The tail rings and foam (figure 4.14) are to give the tail the streamline contour while still allowing flexibility. The dimensions were taken from drawing no 22. The wooden part was cut using a jig saw while the foam was cut using a hot nichrome wire cutter. A paper stencil with the shape printed out was used for the tracing. The rings were then cut into half.	1. Jig saw 2. Hot Nichrome wire cutter 3. Paper stencil
The head board	6.35mm (1/4inch) plywood	The oval head board is made from plywood slabs constructed according to drawing no 23. This head board (figure 4.15) was an off cut from the last ring used for the haul- this will ensure a perfect fit. The pass thru holes were created with nails and expanded with a round file all in accordance to drawing no 23.	Jig saw 3mm diameter nails 2.5mm file
The servomotor – water proofing process	Futaba 3003 Remote Control Servomotor	The servomotors were opened up (figure 4.16A) and the electronic components covered with blue gasket silicone (figure 4.16–D,E) . The rotor shaft was covered with vaseline (figure 4.16–B, F). The	Philip screw driver Blue gasket silicone Vaseline Light

Component	Material	Construction process	Equipment used
		gear area was filled with light mineral oil (sewing machine oil) (figure 4.16 -C). The casing joints were then sealed with cyanoacrylte glue after closing it back.	mineral oil Cyanoacrylte glue
The battery – waterproofing and assembly of the Lithium ion-Polymer battery	Lithium-Polymer battery	The four onboard Lithium ion-Polymer batteries were water proofed by covering them with epoxy glue as shown in figure 4.17. The wires were also coated with cyanoacrylate glue to cover any crack or bruise in them. They were then glued to the side of the servomotors (2 on each side) as shown in figure 4.18 and 4.19. The 4 batteries were then wired in parallel to give 4.3v 4x900mAh capacity.	1. Epoxy glue 2. Cyanoacrylate glue
Assembly of tail components	1. Plywood fin 2. Plywood support structure 3. Rubber strips 4. quarter pulley (with the PVC cable support	1. The tail was assembled first by arranging the wood support (see table 4.5) in their correct order. 2. The rubber strips (see table 4.6) were then placed in between the wood support. 3. These were then glued using epoxy glue and allowed to set. The spacing between the plywood supports is 5mm.	Epoxy glue

Component	Material	Construction process	Equipment used
	5. head board 6. half rings (plywoods) 7. Futaba 3003 servomotors	4. Next, the quarter pulley (with the PVC cable support already attached – table 4.7) were placed on the wooden support according to the drawing no 3 5. The head board drawing no 23 (item 18 on drawing no 3) was then glued to item no 5 on drawing no 3 – the last wooden support of the tail using epoxy glue 6. The cables were then run through the pass thru holes in the head board – to be connected to the servomotor horns. 7. The half rings were then glued as shown in figure 4.20 to give the tail its streamline shape. The foam (not shown) come in between the wooden ones according to drawing 22. 8. The Futaba 3003 servomotors were then attached to the head board serially (figure 4.21) and the cables connected to their horns. The servomotors are glued to each other before gluing them to the head board. The serial arrangement is to help with weight distribution	

Component	Material	Construction process	Equipment used
		9. Figure 4.22 shows the final assembly of the tail.	
Water proofing the tail structure	The assembled tail	All the wooden parts used for the tail were water proofed by applying a coat of cyanoacrylate glue to them with care not to allow it to touch the rubber joint, the nylon cables and the PVC tubing parts. This hardens within 1 to 3 minutes depending on the quantity applied. The treatment was done in a well ventilated environment.	Cyanoacrylate glue
The tail outer skin	The assembled tail	The outer skin was made from blue coloured pvc sheet. This sheet was cut with tailor scissors and glued with epoxy over the tail rings to cover the gaps – they had no specific dimensions (length or breadth).	Epoxy glue Tailor scissors
The electronic and controller components	1. PIC18F4520 microcontroller 2. Diodes (1N400) 3. Resistors (1kΩ, 10kΩ, 100 kΩ), 5W 10% tolerance	Drawing no 24 shows the complete schematic of the electronic devices used for the robotic fish. The final assembly was soldered on two Vero boards – figure 4.23. One Vero board carries the input diode conditioner while the other carries the microcontroller, resistors, capacitors and the debugger connectors. The third board is a 4	1. 3W soldering iron 2. Soldering tin 3. Candle-vaseline wax (50:50 ratio) 4. Latex rubber

Component	Material	Construction process	Equipment used
	4. 10µF electrolytic capacitor 5. Remote control receiver 6. Vero board 7. 6 pins programmer debugger connectors	channels remote control receiver. The components were then waterproofed by covering them in candle-vaseline wax (50:50 ratio) to allow easy removal if need be. Also each board was wrapped in latex rubber and the mouth sealed with epoxy glue and cyanocrylate glue. The outer layer was finally coated with silicone to make it scratch and puncture resistant – figure 4.24. The wire junctions were also coated with epoxy glue and cynoacrylate glue to prevent shorting. The waterproofed electronic and controller were placed below the haul as shown in figure 4.25	5. Epoxy glue 6. Cyanocrylate glue 7. Blue gasket silicone

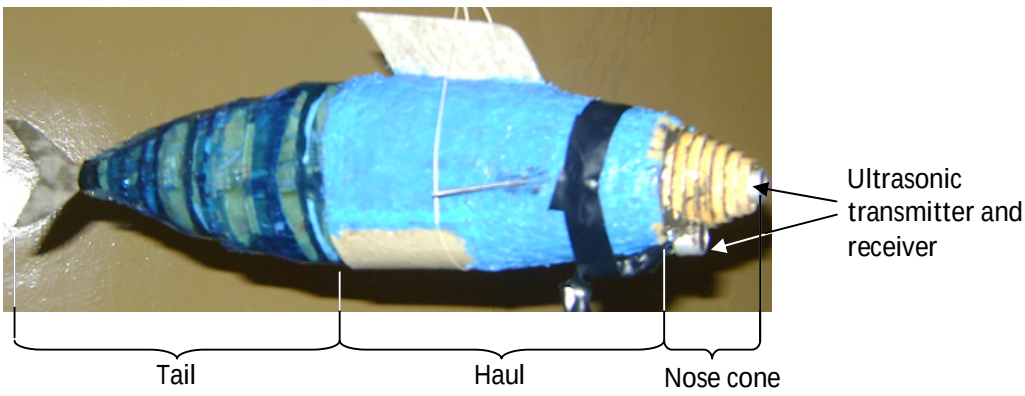


Figure 4.1 The assembled fish robot



A



B

Figure 4.2 The rings (**A**) for building the robot haul which are then glued together to form the front part of the robot fish (**B**).



Figure 4.3 Assembling the bump detector on the haul

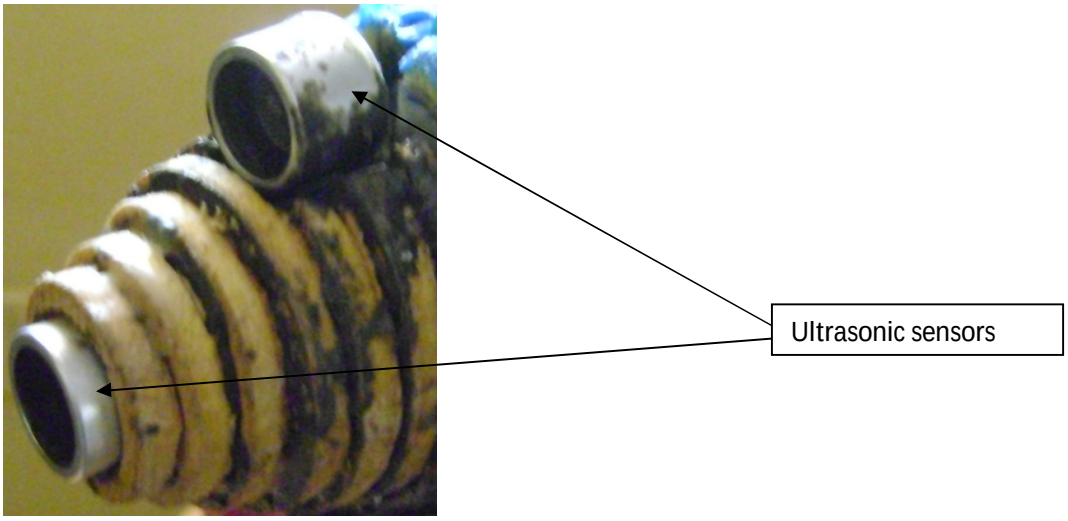


Figure 4.4 The cone holds the ultrasonic sensors – the receiver is at the tip and the transmitter is at the top.



Figure 4.5 The haul with foundation coating of TOP BOND® wood glue



Figure 4.6 The haul with wood glue soaked fine sawdust ~3mm



Figure 4.7 Microwave oven being used for preliminary drying at 5 min at 100watt. This will quickly eliminate the water in the applied mixture.

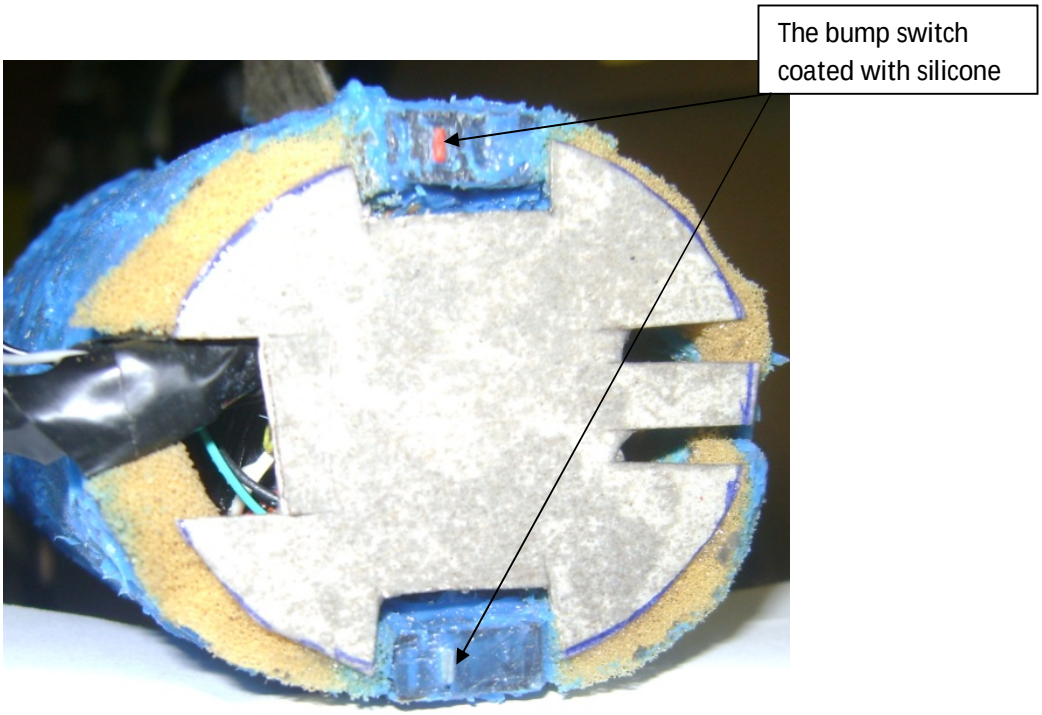


Figure 4.8 The bump switch was waterproofed with the haul using silicone rubber.

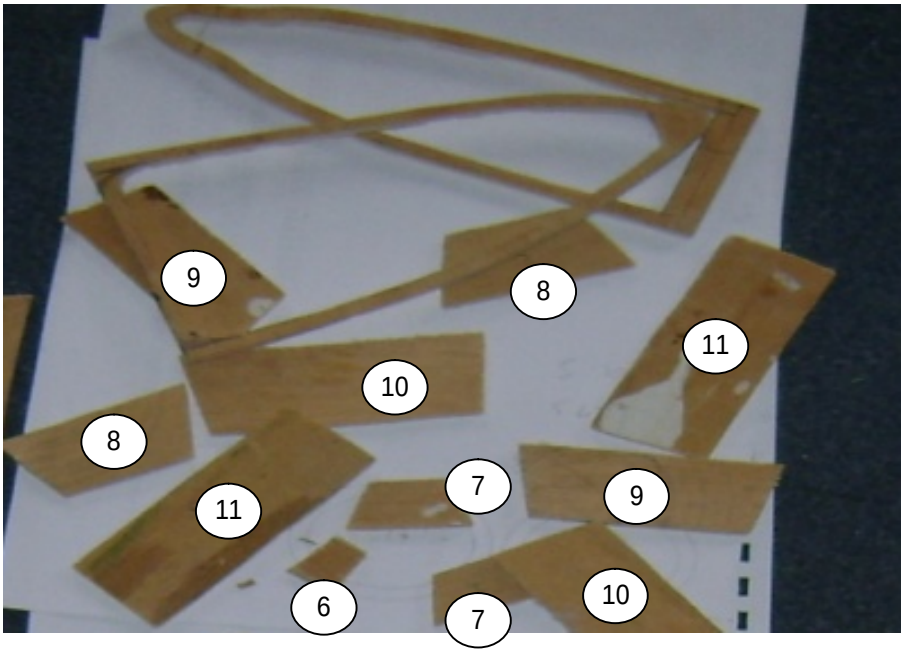


Figure 4.9 The slabs used for building the robot tail support structures according to drawing nos 6 to 11. The labels tallies with the drawing numbers and are in pairs



Figure 4.10 Kings tire rubber tube used (size=165/175-13)

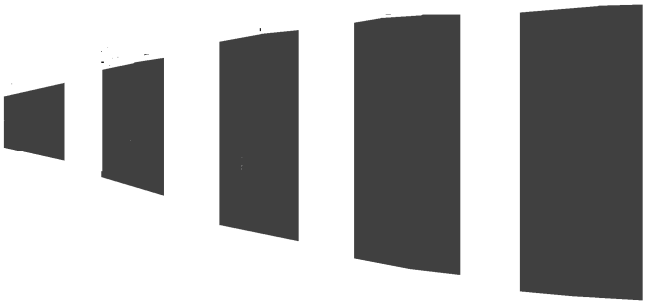


Figure 4.11 The rubber is cut according to the dimensions taken from drawing nos 12 to 16. The first 2 stripes from the tail fin (left on this picture are 20mm wide and the remaining ones are 25mm wide).

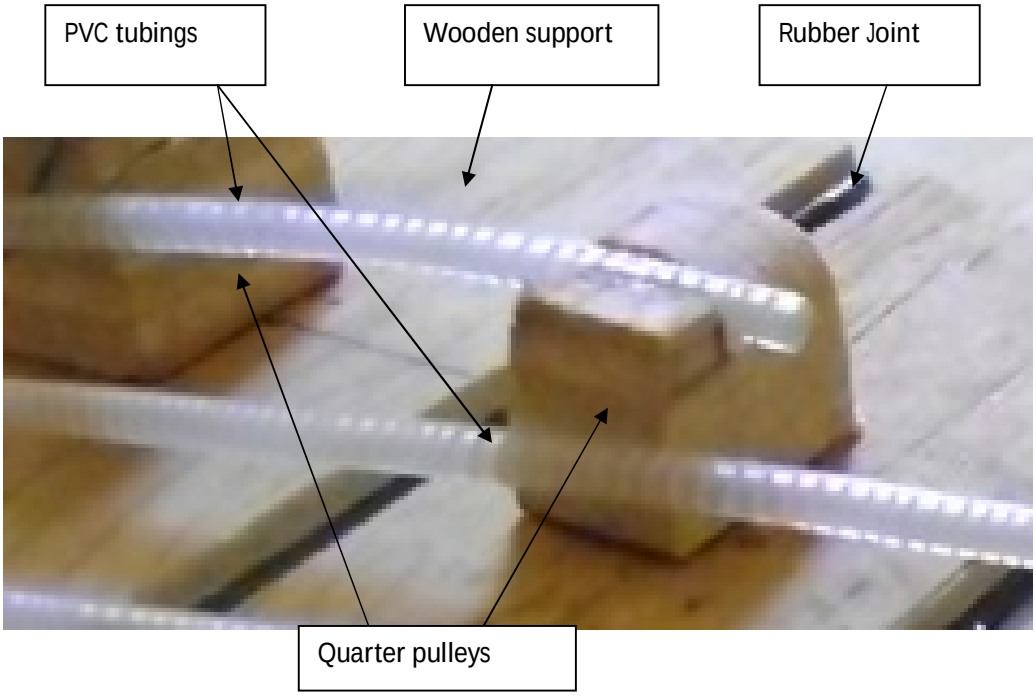


Figure 4.12 The quarter pulleys and unplasticized PVC tubings glued in place



Figure 4.13 The fin, made from plywood board.



Figure 4.14 The rings – half ring pairs used for the tail contour

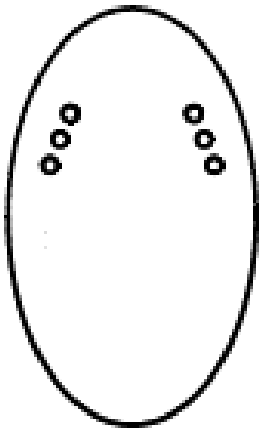


Figure 4.15 The head board



The original servomotor



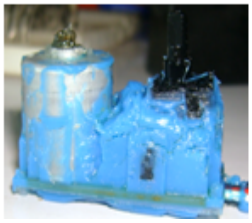
A



B



C



D



E



F

Figure 4.16 Water proofing the servomotor.





. A B

Figure 4.17 The battery before (A) and after (B) it was covered with epoxy glue.

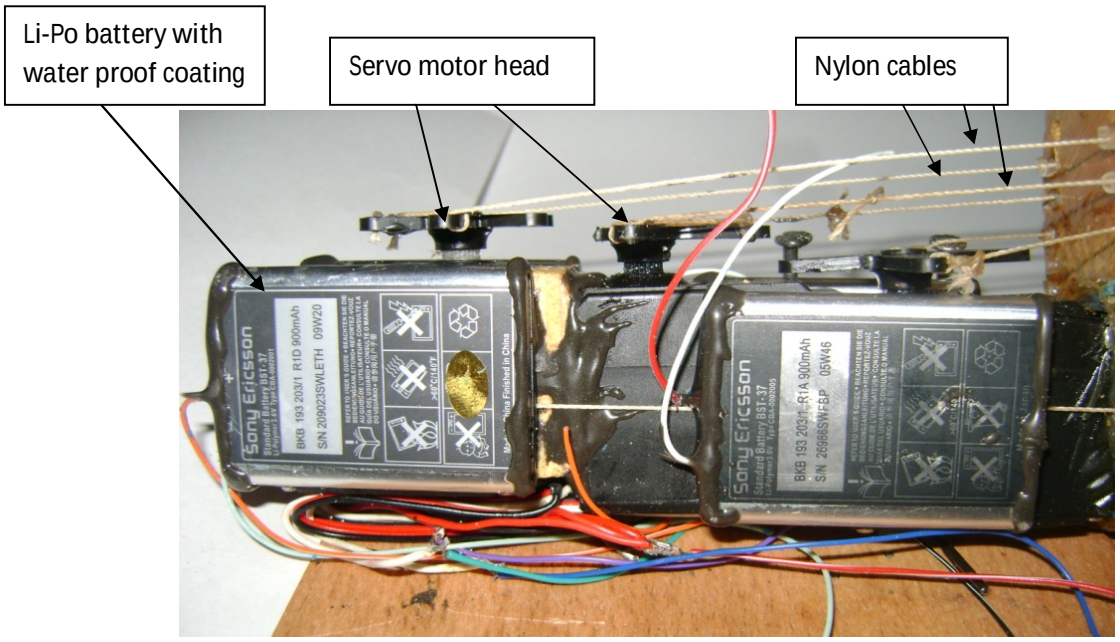


Figure 4.18 The Li-Po battery were glued to the side of the motors, 2 per side, viewed from the side

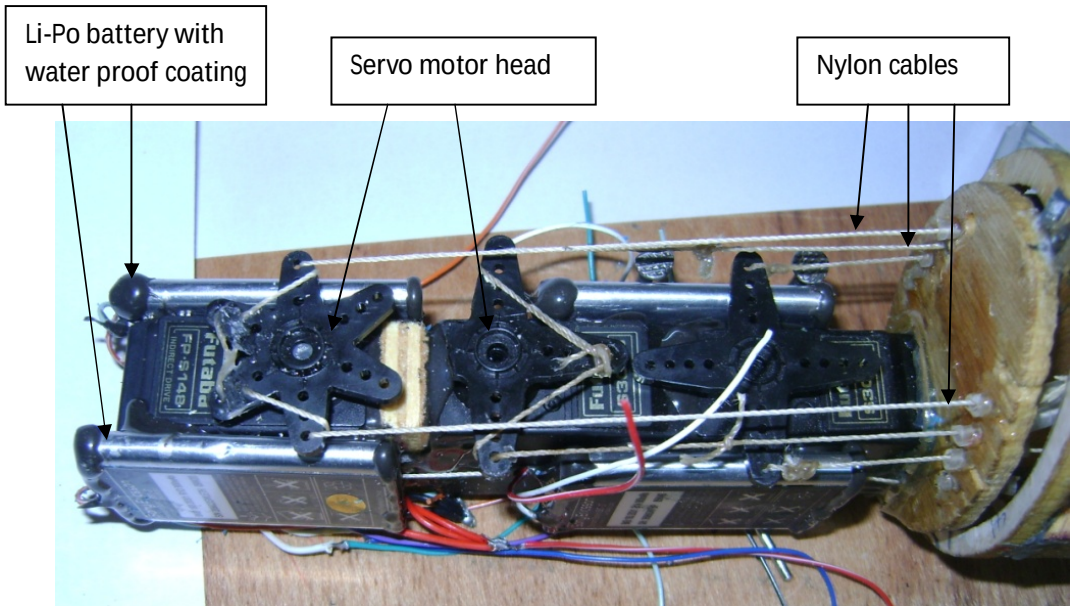


Figure 4.19 The Li-Po battery were glued to the side of the motors, 2 per side, viewed from above

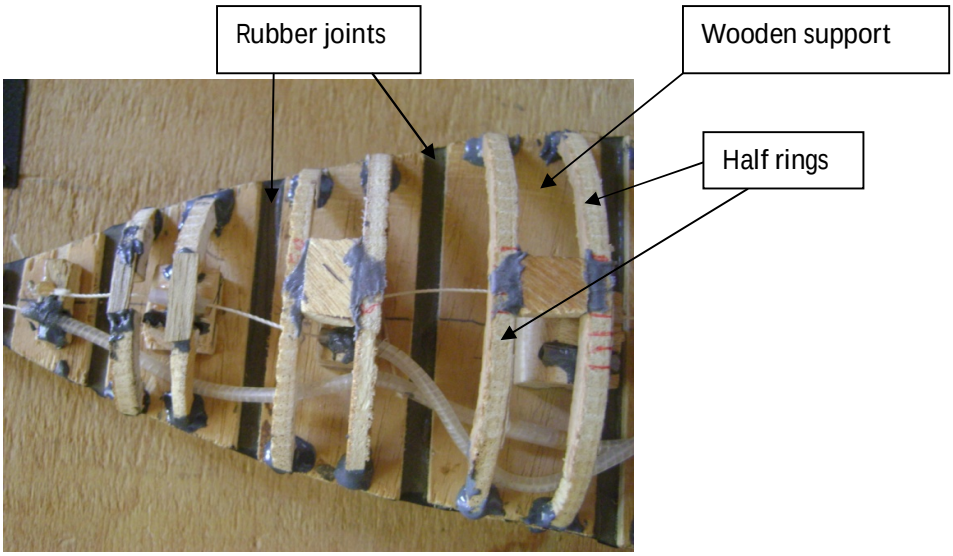


Figure 4.20 The half rings glued to the supporting board with epoxy glue

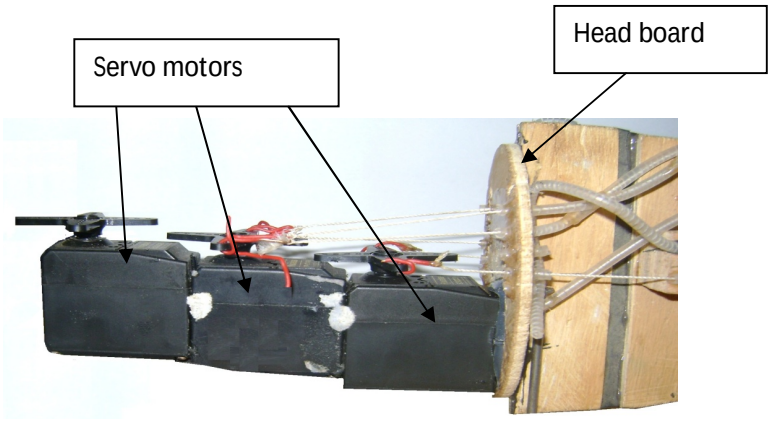


Figure 4.21 The three servomotors are connected serially and then glued to the head board

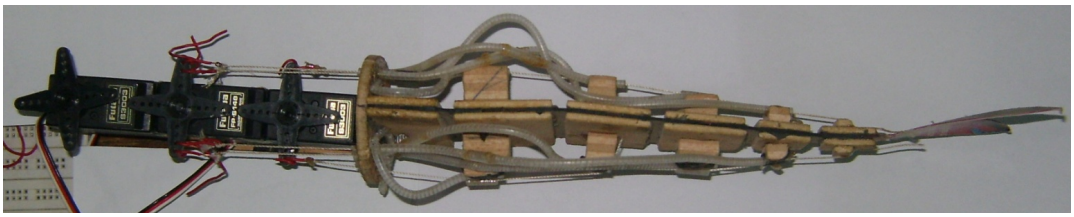


Figure 4.22 The final tail assembly

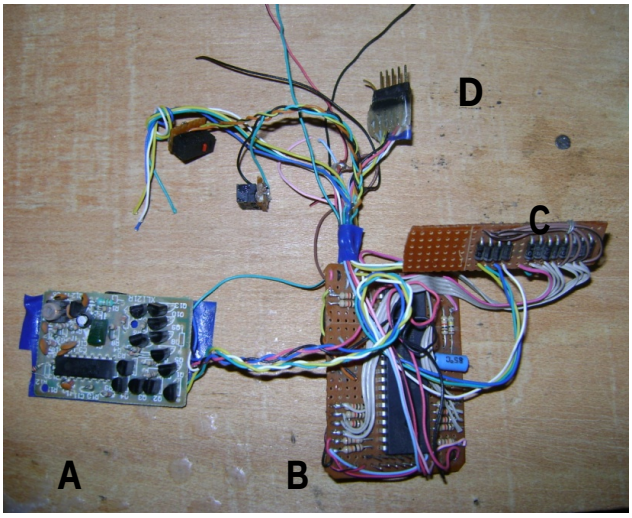


Figure 4.23 The assembled electronic and controller parts showing the remote control receiver (A), the microcontroller board (B), the inputs diode board (C), the programmer/debugger connectors (D)



Figure 4.24 The electronic and controller after covering with silicone.

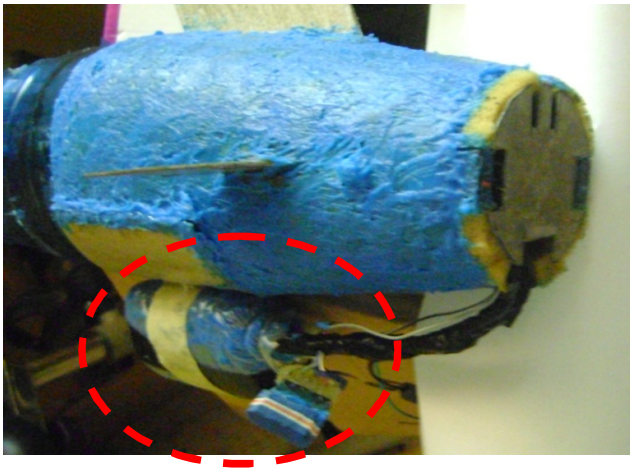


Figure 4.25 The finished electronic and controller assembly is placed externally to the haul, just at the middle of the robot

4.3 FIRMWARE (SOFTWARE) CODE ASSEMBLY

4.3.1 Development Environment

The development environments are the utilities used in assembling the firmware used in programming the robot microcontroller, they are;

4.3.1.1 Integrated development environment (Microchip MPLAB v8.56.00 IDE)

This is the software that manages all the source codes and other utilities.

4.3.1.2 Assembler (MPASM Assembler v5.37)

This is the software utility that parses the assembly source code and handles all the assembly language syntax. Assembly languages are hardware and vendor (manufacturer) specific.

4.3.1.3 Linker (MPLINK Object Linker v4.37)

This is the software utility that translate the assembly language to intermediate language (called object code or op-code) and then (based on the instruction given) translate it into machine language or executable program often called hex code/file.

4.3.1.4 Library (MPLIB v4.37)

The library is a software utility that merges object codes generated by the assembler and feeds them into the linker. This is a tool needed especially when the program has multiple parts (multipart).

4.3.1.5 Debugger (MPLAB SIM and PICkit 2)

Debugger is the software (MPLAB SIM) or hardware (PICkit 2) utility that is used to locate errors in program construct or flow that often prevent the program from executing as intended.

4.3.1.6 Programmer (PICkit 2)

The programmer is the software cum hardware utility that copies and burn the hex code (executable code) generated into the targeted microcontroller. It also configure the microcontroller functions like clock speed, watch dog timer (WDT), power-on reset (POR), brown-out reset (BOR) etc.

The clock directs all the timing and synchronizations of signals, the watchdog timer (WDT) gives the code developer a way to reset the device in the event of unexpected code operation. Power-on reset (POR) is a reset that occurs at microcontroller power on. Brown-out reset (BOR) is a circuit that forces the microprocessor to reset if there is a short interruption of power - one that is long enough to disrupt operation, but not long enough to force a normal power on reset.

4.3.1.7 Clock (8MIP or 32Mhz)

The Microchip microcontroller uses ¼ of its system (or input) clock. This project uses 8MIP (million instructions per second) which is ¼ of the 32Mhz built in clock.

4.3.1.8 Operating system (OS) - Windows 7 Home Basic, 6.1.7601.2 SP1

This is the host computer instruction language on which all the development of the robot code was performed.

4.3.1.9 Oscilloscope (TFD Scope v2.0 http://www.adrosoft.com)

The TFD scope is a software based oscilloscope that comes with a spectrum analyzer built in. The maximum frequency it handles is 22kHz.

4.3.1.10 Logic analyzer (MPLAB SIM Simulator Logic Analyzer)

The logic analyzer is also a software based utility that shows the status of each input or output pin (logic levels) of the microcontroller when being debugged in real time.

4.3.2 Capabilities Built Into The Robot Firmware

The following abilities were programmed into the robot microcontroller;

1. turning left/ right while swimming
2. sharp/ quick turn
3. increase/decrease oscillation amplitude,
4. increase/decrease speed,
5. detect obstacle and avoid it by intelligently choosing which direction to go,
6. locate a simulated object – a sonar source
7. permit human override as long as the override is valid.

Appendix D contains the complete listing of the firmware pseudo code.

4.3.3 Description Of The Robot Firmware

The flowcharts (figures 4.26 to 4.32) describe the internal workings/logic of the firmware used within the microcontroller (PIC18F4520) used for the robotic fish.

4.3.3.1 The firmware generalize flowchart

Figure 4.26 is the generalized flowchart of the firmware. It is sectioned into three – (1) bump sensor based obstacle detection, (2) ultrasonic based obstacle detection and (3) human override controller all interacting with the turning, tail speed and tail oscillation amplitude routines.

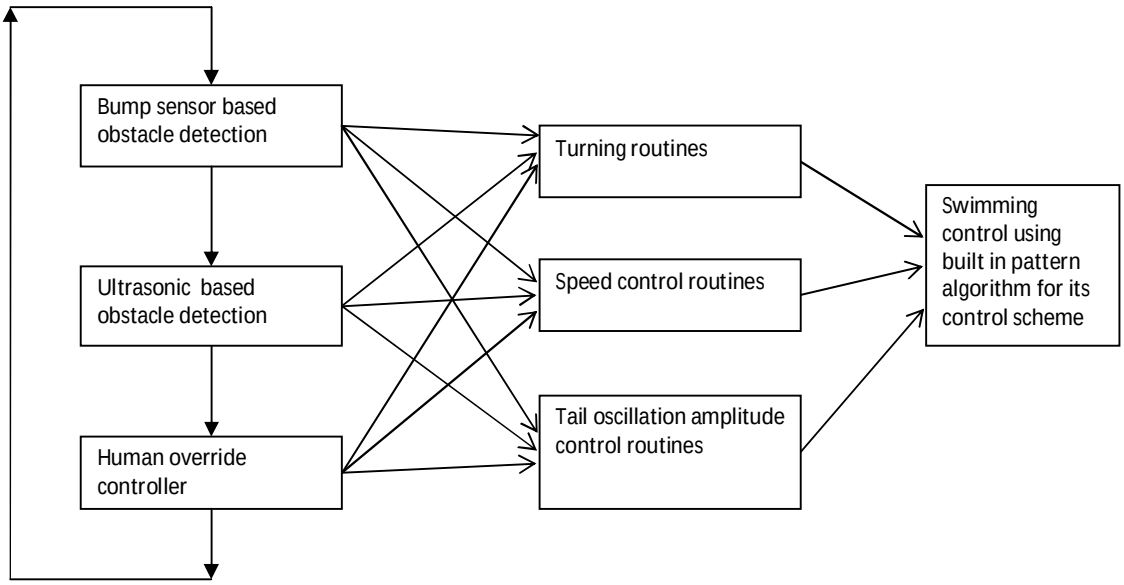


Figure 4.26 The generalized flow chart of the firmware controlling the robot.

4.3.3.2 Bump switch based obstacle detection subroutine flowchart

Figure 4.27 shows the details of the bump switch based obstacle detection and avoidance routine. It uses the bump sensor information for its inputs. The time the two are on are measured and compared. The one with the larger value is the one that got switched on first and longer and therefore, the robot is stirred away from it. If the results are equal, a random number is generated, an odd value implies stir left and even value implies stir right.

4.3.3.3 Ultrasonic based obstacle detection subroutine flowchart

Figure 4.28 is the ultrasonic based object detection flowchart, it works similar to the bump switch obstacle detection. It uses 40kHz ultrasonic piezo crystal transmitter receiver pair.

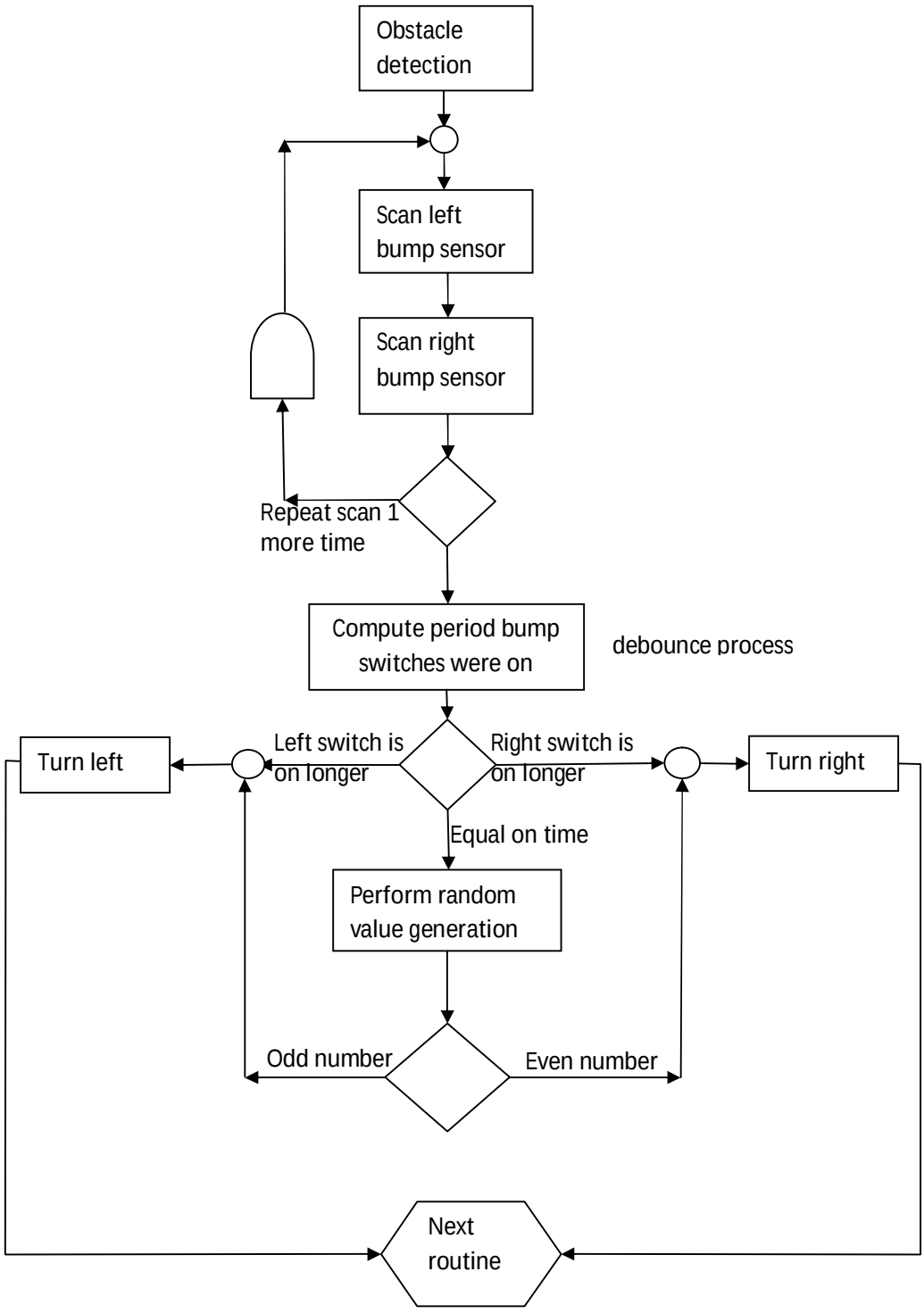


Figure 4.27 Bump switch based obstacle detection subroutine

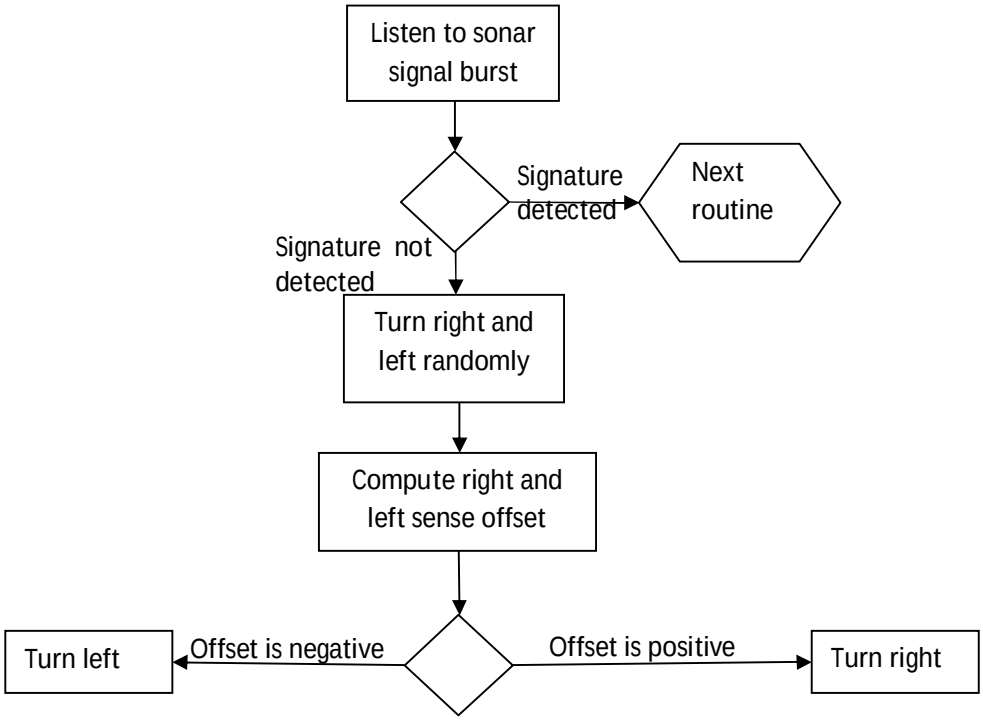


Figure 4.28 Ultrasonic based obstacle detection subroutine

4.3.3.4 Human override subroutine flowchart

The human override subroutine (figure 4.32) uses a 4 channels remote control that works on bang-bang protocol, that is, the output is either ON or OFF not a proportional output. The firmware scans the receiver 4 outputs through the microcontroller 4 input ports in turn continuously and generates an interrupt whenever it senses an input is ON. The input is then used to control the behavior of the robot firmware instruction execution/branching. The following HEX code shows the port input order –PORTC,4; PORTC,5; PORTC,6 and PORTC,7 and their state is used to set a corresponding bit in a symbol (a memory location) named `temp_temp`. Thus a maximum of 4 bits of `temp_temp` can be set as 1 or 0 as shown in the following assembly code line `478-486`:

```
473:   ;----code list: Remote control output polling--------
474:   Ext_Int_Code
475:   bcf INTCON,1
476:
477:   ;Capture port state
478:       clrf    temp_temp
479:       btfss   PORTC,4
480:       bsf     temp_temp,4
481:       btfss   PORTC,5
482:       bsf     temp_temp,5
483:       btfss   PORTC,6
484:       bsf     temp_temp,6
485:       btfss   PORTC,7
486:       bsf     temp_temp,7
```

This means that from a 4 bit input, we can make a controller with 16 possible outputs as shown in the table 4.2. The routine polls the value of `temp_temp` and branch to the code that is appropriate.

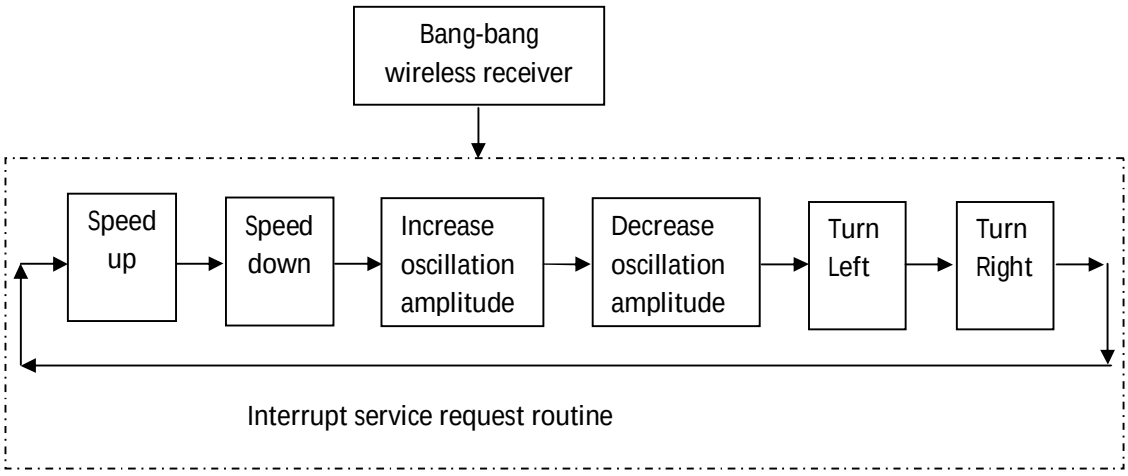


Figure 4.29 Human override control subroutine

Table 4.2 The 16 possible combination a 4 bit can generate. The counting start from 0

sno	Bit 1	Bit 2	Bit 3	Bit 4
0	0	0	0	0
1	0	0	0	1
2	0	0	1	0
3	0	0	1	1
4	0	1	0	0
5	0	1	0	1
6	0	1	1	0
7	0	1	1	1
8	1	0	0	0
9	1	0	0	1
10	1	0	1	0
11	1	0	1	1
12	1	1	0	0
13	1	1	0	1
14	1	1	1	0
15	1	1	1	1

4.3.3.5 The tail oscillation amplitude control subroutine flowchart

Figure 4.30 is the flowchart for the tail amplitude control. The amplitude is the amount of excursion the tail will make from left to right. The bigger it is the more the fluid in its environment is affected. The width of the pulse determines the angle to

which the motor will move to. Changing the pulse width data causes the PWM generator for each servomotor to adjust accordingly. See section 4.3.3.7 for more information on the PWM generator.

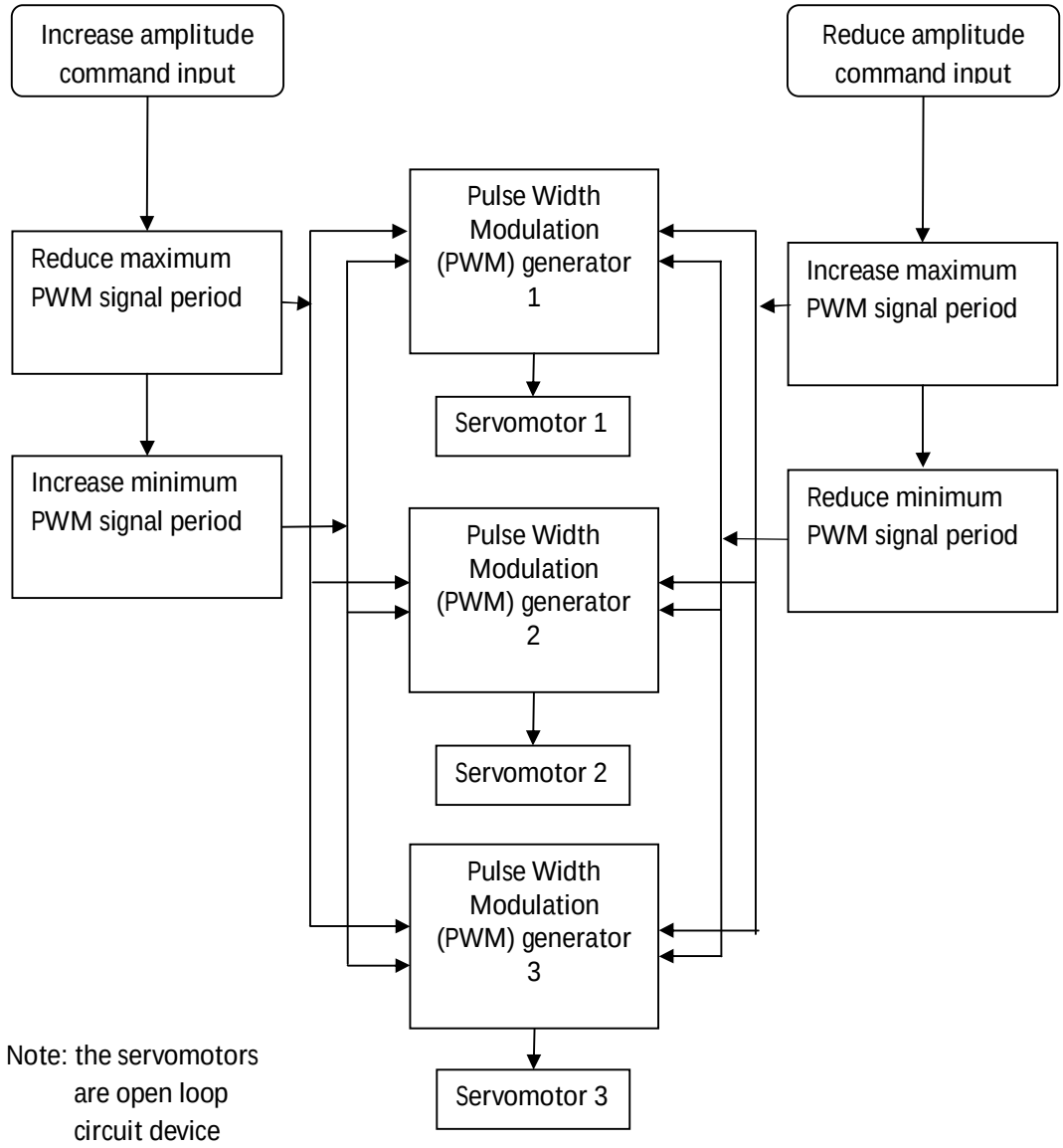


Figure 4.30 Tail oscillation amplitude control routine

4.3.3.6 The speed of oscillation control subroutine flowchart

Figure 4.31 is the flowchart of the speed of oscillation control. The speed is managed by changing the pulse-width-modulation (PWM) signal width and how long it remain so before changing the value again in either direction during oscillation. Essentially, the delay are what is adjusted. If the delay is longer, the speed is lowered and vice versa for each servomotor. See section 4.3.3.8 for more information on the PWM generator.

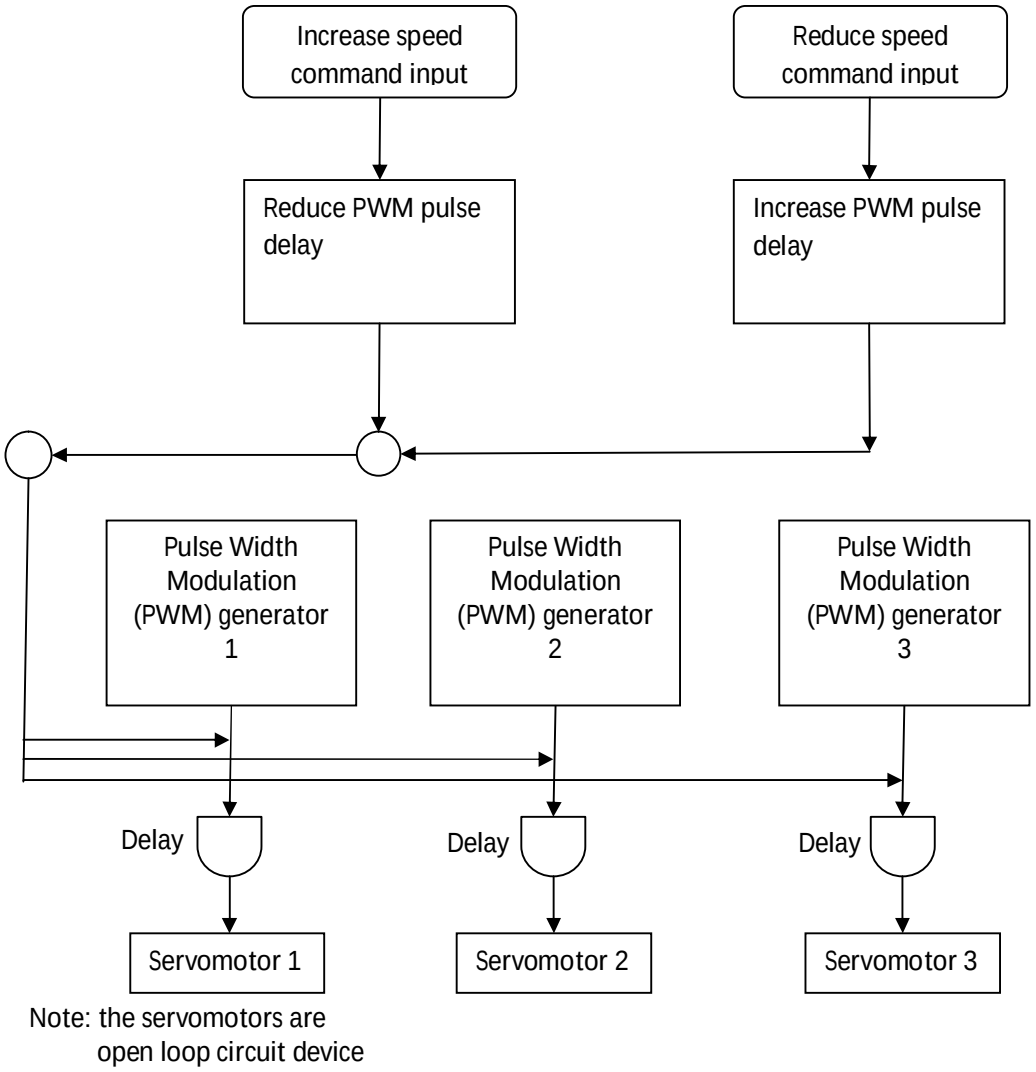
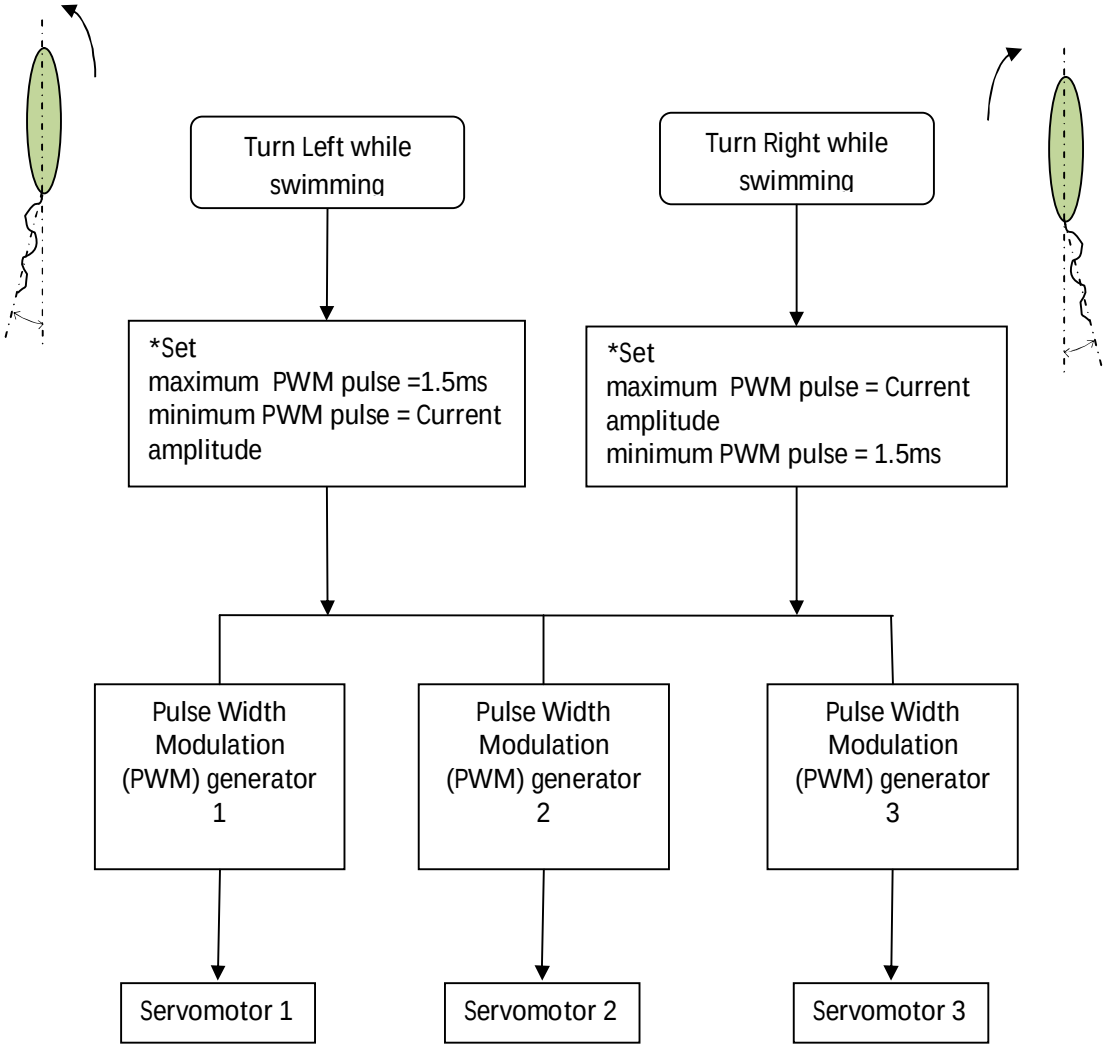


Figure 4.31 Tail oscillation speed control routine

4.3.3.7 The turning subroutine flow chart

Figure 4.32 is the flowchart of the turning routine. The turning is done by restraining the motion to half of the fish midline as shown in figure 4.32. The PWM generator is commanded to keep the maximum PWM pulse width to 1.5ms if turning to left and minimum PWM pulse width to 1.5ms if turning to right. The 1.5ms is approximately the pulse width command for the servomotor to turn to the middle or 90^{o}.



Note: 1.5ms is the approximate PWM at which the servomotor is set to their middle line.

Figure 4.32 Turning routine

4.3.3.8 Pulse width modulator (PWM) protocol generator

For this project, the specifications for the PWM signal needed are:

1 Three concurrent (or rigidly coupled) PWM signal that is out of phase by 60^{o}.

2 Continuously varying duty cycle

3 Different duty cycles at any point in time

4 The three PWM signal will have the same period

5 Repeated (introduced dead band)

6 Less load on the microcontroller time

The flow chart shown in figure 4.33 is used for describing the working of the concurrent PWM protocol generator being described here. The concurrent PWM signal generator is a modified timer based interrupt method with much contribution from instruction time method. Timer0 interrupt (INT0) was used as the trigger. The period is to be fixed at ≈20ms. The pulse length is a table of pre calculated values (built in motion pattern). It could also be mathematically generated also. The processes involved in calculating the pulse length are performed during the microcontroller idle time.

As soon as there is an interrupt, critical register are saved and the Timer0 is prepared for the next interruption. The ports are all set high, the difference (lag) between the start of the first and the last is calculated as follows:

If Port 0 start time = T_{port0}

Then Port X start time $= T_{port0} + T_{port1} + T_{port2} + \ldots + T_{port\ x-1}$

$= T_{port0} + (x-1)* T_{CY,}$

where T_{CY} is the length of an instruction cycle

The PIC microcontroller used was run at 32Mhz and

therefore the $T_{CY} = (1/32Mhz)*4 = 0.000000125s$ or 125ns

lag for Port X = $(x-1)* T_{CY} = (x-1) * 125ns$

As an example, the lag between the first port and last port of a 3 PWM concurrent generator will be

Lag = (3-1) * 125ns = 250ns

Fortunately, this lag will be fixed as the PWM signals have the same reference, i.e. they have the same period that is fired up by a single timer (Timer0). The period for any channel will therefore remain constant at ≈20ms as designed. Using figure 4.34,

$T_1 = T_2 = T_3 \approx 20ms.$

The count down process checked and compared the RAM value of the pulse against the current count, if greater or equal, the corresponding port is set low. The routine is exited as soon as all the ports are set low.

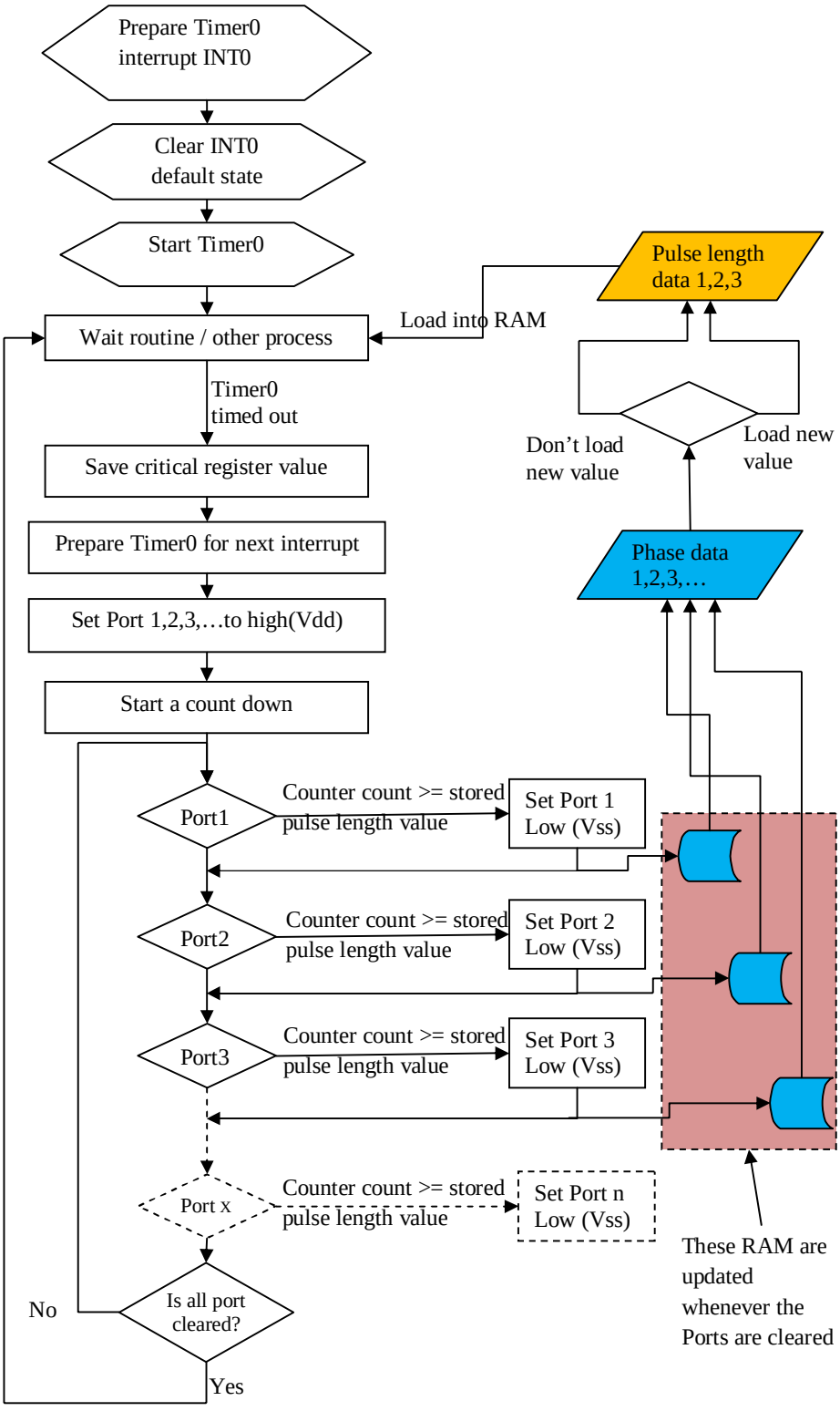


Figure 4.33 Concurrent Pulse Width Modulator (PWM) generation routine

A phase difference is needed for the robotic fish segment for motion to take place. These motors can be made to rotate at different phase angle by adjusting their duty cycles at different rate. The phase data is a table of pre calculated values (it can be mathematically generated also). The reference to when to change the motor phases is derived from the current state of the ports. The phase data modifies the pulse length data by simply controlling whether to load new values or not. This automatically creates a dead band. This dead band is used advantageously by the fact that the inertia of the servomotor motor, shaft and gear cannot keep up with a rapidly changing PWM duty

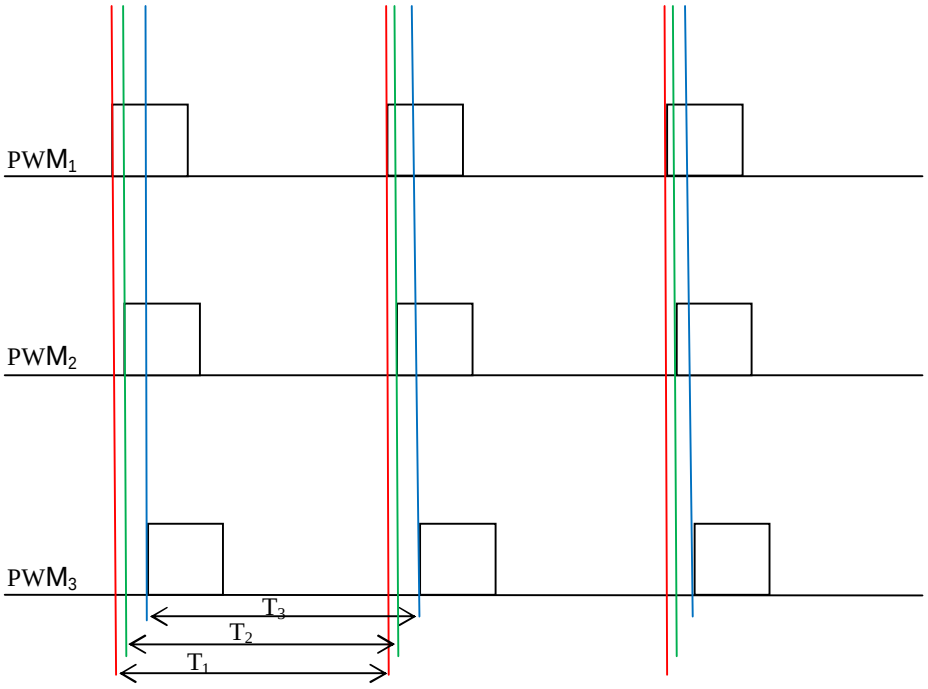


Figure 4.34 An exaggerated illustration of lag present in the concurrent PWM generator.

cycle. The phase controller is therefore actually causing the PWM signal generator to "wait" for the motor to finish up. These waiting periods are varied for different servo motor and thus lead to phase lags or leads.

4.4 THE LABORATORY TESTS

The laboratory tests were tests performed while the robot is out of water. An exception is the water leakage tests which require that the parts be placed inside water while the power supply is disconnected. The following laboratory tests were conducted;

1. Test on the concurrent PWM (pulse-width-modulation) generation module
2. Test for correct angular displacement (swing) of the motors
3. Test of the sonar sensor fidelity to input signal and the peak response test.
4. Test of the bump sensor routine
5. Test of the Left/Right turning while swimming
6. Test of the Left/Right sharp turn
7. Test of the human override control
8. Test for water leakages

4.4.1 Test On The Pulse Width Modulation (PWM) Code Generation

According to the remote control servomotor manufacturer (Futaba incorporation of USA), the PWM control scheme is a pulse signal (<=5V+ peak) lasting for 1 to 2 ms and repeated at 20ms (50Hz) interval –depicted in Figure 4.35.

4.4.1.1 Equipment used

1. PICkit 1 signal analysis Oscilloscope
2. An Acer Aspire 5600 computer USB 2.0 port

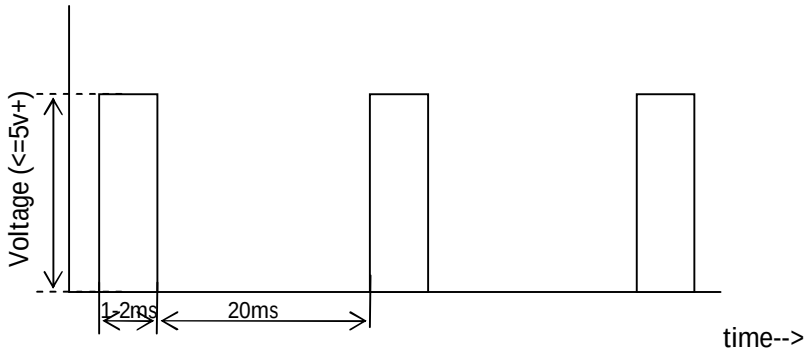


Figure 4.35 PWM control scheme for Futaba remote control servomotors.

4.4.1.2 Test procedure

1. The microcontroller was switched on and powered with 5v input
2. The output pin that will go to the servomotors input pins were connected to the PICkit 1 signal analysis oscilloscope input.
3. The PICkit 1 signal analysis oscilloscope output was then connected through a USB port of the computer used.
4. The PICkit 1 signal analysis oscilloscope was set to Continuous
5. The computer output was then capture and saved.

4.4.2 Test For The Microcontroller Concurrent Pulse Width Modulation (PWM) Code Generation

The microcontroller is to generate three PWM code at the same time. Each is to drive the one of the three servomotors in real time. A delay will cause the servomotor to treat

it as a new command and will respond to it by turning left or right. This could lead to jittering of the motors.

4.4.2.1 Equipment used

1. Logic analyzer built into the MPLAB IDE (integrated development environment) used for the firmware development.
2. MPLab SIM simulator

4.4.2.2 Test procedure

1. The MPLAB IDE was switched to debug mode.
2. MPLab SIM simulator was started – which automatically starts a virtual model of the PIC18F4520 microcontroller being programmed
3. The logic analyzer was started also
4. The software was then started
5. The logic analyzer was then used to capture the signal level on the output pins of the virtual microcontroller.

4.4.3 Test For Establishing Correct Angular Displacement (Swing) Of The Motor

The servomotors are capable of 0 to 180^o swing, these angles do not precisely correspond to 1ms and 2ms nor 1.5ms equal 90^o, a test is required to establish the center timing signal. This test automatically leads to calibrating the servomotor.

4.4.3.1 Equipment used

1. A Futaba 3003 servomotor
2. An ordinary transparent plastic protractor

3. Three 5cm long nails to support the protractor
4. A wooden board to hold the nail, protractor and a servomotor
5. PICKit 2 debugger
6. MPLAB v8.56 simulator software stopwatch

4.4.3.2 Test procedure

1. The equipment was setup as shown in Figure 4.36.
2. The microcontroller was connected to the computer using PICkit 2 debugger
3. The development environment was started and switched to debug mode
4. The firmware was instructed to generate 1.5ms width pulse length which will approximately correspond to mid value of the servomotor. MPLAB v8.56 simulator software stopwatch was used to measure the timing intervals.
5. The code for generating the center signal was adjusted until the servomotor points to 90^{o} approximately. The initial and final values were noted

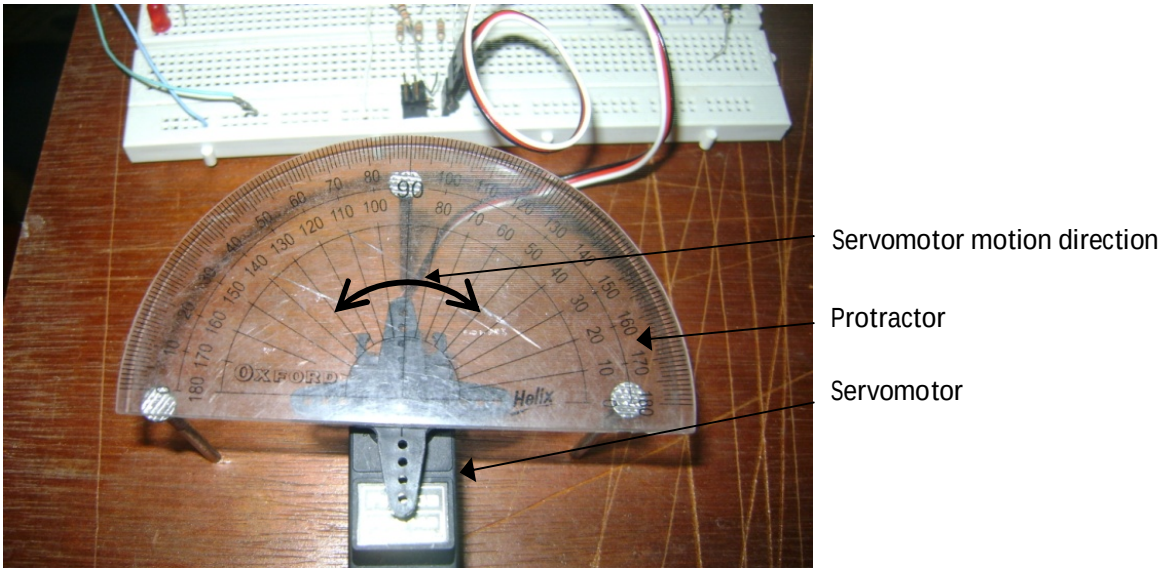


Figure 4.36 Angular displacement measurement setup using protractor

4.4.4 Test Of The Sonar Sensor

Test on the sonar sensors was performed to see if it will respond as designed and detect objects also. Tests carried out are;

1 Maximum distance covered, that is the distance between the transmitter and the receiver

2 Beam arc – this is the arc of coverage of the transmitted signal. See appendix E for the sensor datasheet for more information on this.

3 Placing different obstacles between the transmitter and sensors

4 Making the objects to reflect the sent signal to the sensors

4.4.4.1 Equipment used

1. A dedicated 1Hz pulse rate sonar transmitter. Sonar signal is at 40kHz.
2. A matched pair of 5mm diaphragm piezo crystal transducers, one for transmitter and the other one is the receiver.
3. Obstacles – CD plastic, plastic with oil inside, A4 paper sheet, human hand, glass lens.
4. Ruler for distance measurement and protractor for angular displacements
5. Water tank of 60.96cm x 121.92cm x 60.96cm made up of wood filled with water to depth of 30cm or pressure head of 2.91kPa.

Furthermore, the environmental condition (July 2011) for the open air test was

- Mean temperature (ºC) = 25.9
- Maximum temperature (ºC) = 28.2
- Minimum temperature (ºC) = 24.1
- Mean humidity (%) = 77

while environmental condition (July 2011) for test in the water (rain water) is

- Water Temperature (ºC) = 23
- Water density kg/m^3 = 997

4.4.4.2 Test procedure

1. The setup of Figure 4.37 was used inside and outside the water.
2. The dedicated 1Hz pulse rate sonar transmitter is switched on
3. The receiver respond by blinking an LED at 1s interval. The LED is connected to the receiver output of the microcontroller.
4. The arrangement of Figure 4.37 (A) was used to test for distance between the receiver and sender. The receiver LED will stop blinking if it could no longer detect any signal sent to it. The distance between them was measured.
5. The arrangement of Figure 4.37 (A) was also used to measure the beam arc at a very close range of 30cm by moving the receiver about an arc in a plane perpendicular to them. The protractor was placed underneath for measuring the angle.
6. The arrangement of Figure 4.37 (B) was used for the obstacle detection. Obstacle were placed from the transmitter-receiver pairs at 30cm.
7. The environmental condition were also noted during the tests

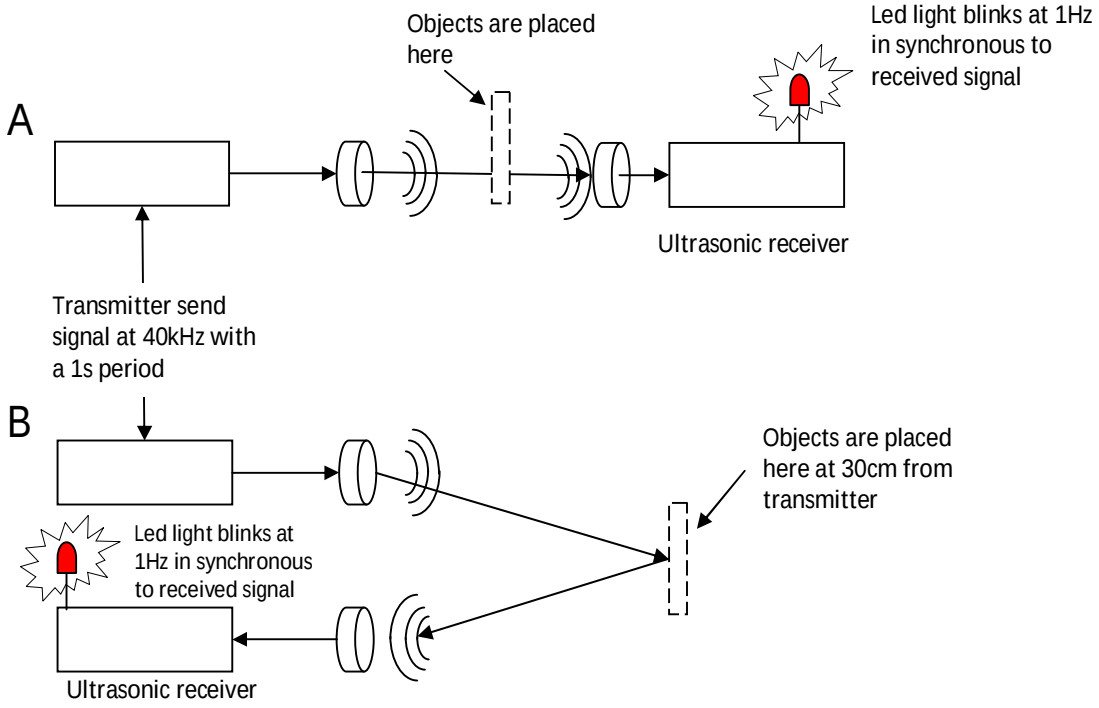


Figure 4.37 The setups (A and B) used to test the ultrasonic sender and receiver fidelity.

4.4.5 Test Of The Bump Sensor Routine And Performance

Two type of test were performed, the debounce test and activation load test.

A. The bump sensor (Figure 4.38) is a plain mechanical switch (a micro switch), therefore there will be bouncing of the contact (the click noise). To the microcontroller running at 32MHz (or 8MIP (million instructions per second) for Microchip microcontrollers), a single click can be interpreted to mean thousands of inputs and that will be a meaningless input to it. A way out is to debounce it in the firmware – this is done by waiting for the switch to stabilize before beginning to take readings.

B. The activation load test involved finding out the minimum force to actually cause a response (or to close the switch). The lower the force is, the likelihood of the switch closing when the robot hits an object especially at slow speed. The micro switch requires 0.015N to depress according to the manufacturer (*www.ck-components.com*).

4.4.5.1 Equipment for the switch debounce test

1. MPLAB IDE (integrated development environment)
2. PICkit 2 as debugger
3. TFD Scope 2.0 Spectrum analyzer and Oscilloscope

4.4.5.2 Test procedure

1. The MPLAB IDE was started and switched to debug mode
2. The PICkit 2 was connected to the microcontroller and the computer hosting the MPLAB IDE.
3. The buttons were pressed slowly and then fast to see if the program execution will branch appropriately.

4. Both were pressed at once to see if a random number will be generated as an indication that the collision was headlong.
5. Furthermore, the micro switch frequency spectrum and time series value were captured by the TFD scope 2.0 spectrum analyzer and oscilloscope respectively.



Figure 4.38 The micro switch used for the bump sensor

4.4.5.3 Equipment for activation load test

1. CAMRY® Load cell with digital output
2. 1 cm^3 sample of the collapsed polyurethane foam used in between the haul and the cone.

4.4.5.4 Test procedure

1. The robot nose cone was depressed on one side with the load cell until a click of the micro switch was heard. The diagram of Figure 4.39 shows a sketch of this arrangement.
2. The load cell reading was then taken.
3. Both sides were treated 5 times to get an average reading.
4. The polyurethane foam sample was also subjected to a compressive test by putting it on the load cell and depressing to 50% of its original height. This is a modification to Polyurethane Foam Association standard (PFA,1994).

Polyurethane Foam Association uses IFD (Indentation Force Deflection) table (see appendix F) which is defined as the amount of force, in pounds, required to indent a fifty square inch, round indentor foot into a predefined foam specimen a certain percentage of the specimen's total thickness. This modification allows the resistive force to compression to be determined.

5. The compressive test was performed for each side of the 1 cm^3 foam sample. Five samples were tested.

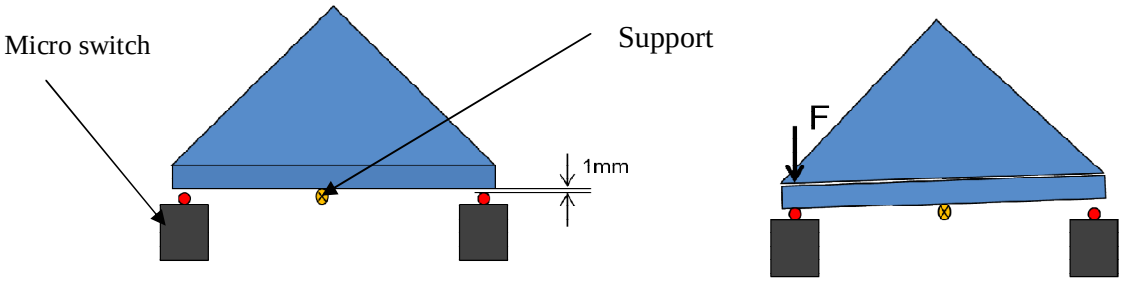


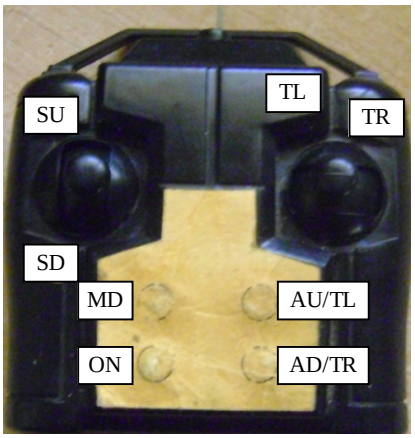
Figure 4.39 Measuring the force required to activate the bump switch

4.4.6 Test Of The Human Override Control i.e. The Remote Control

The remote control transmitter (Figure 4.40) and receiver have 4 channels and that means without further modification only 4 items can be controlled. It was modified to produce 12 more channels and thus giving a total of 16 possible outcomes. 11 are actually used in the robot, they are

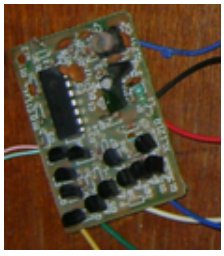
1. speed oscillation up
2. speed oscillation down
3. amplitude up
4. amplitude down,
5. turn left while swimming

6. turn right while swimming,
7. sharp turn left
8. sharp turn right
9. pause (and straighten up),
10. switch mode – allows a button to be used for other purposes like shift key on computer keyboard
11. start up/switch off



Legend
SU – Speed up
SD – Speed down
ON – Start up/Pause
MD – Mode 1/ Mode 2 Switch
AU – Amplitude Up
AD – Amplitude Down
TL – Turn left (while swimming
(sharp turn left, mode 1 on – joystick only)
TR – Turn right (while swimming
(sharp turn right, mode 1 on – joystick only)

The transmitter (modified by adding extra buttons)



The receiver

Figure 4.40 The modified remote control transmitter and receiver

4.4.6.1 Equipment used

1. The remote control itself
2. MPLAB SIM simulator (within MPLAB IDE)
3. PICkit 2

4.4.6.2 Test procedure

1. The MPLAB IDE was started and the MPLAB SIM simulator was started also.
2. The PICkit 2 was connected to the microcontroller and to the computer hosting the MPLAB IDE.
3. The MPLAB IDE debugger mode was started.
4. On the remote control, key combinations were pressed to see if the correct routine was executed.
5. The MPLAB SIM simulator built into the development environment was used to confirm the routine branched into.

4.4.7 Test For Motion Pattern

There are three strategies employed for controlling hyper-redundant robot joints – the serpenoid curve, follow the leader approach and built in motion pattern. For mobile robots, onboard power is much limited and the processing is commonly done by microcontrollers. This implies a method that uses less power and is less mathematically involving will be preferred automatically. Built in motion pattern is the best at handling this limitation; pre-calculated values or lookup table are used for determining the motion patterns. In this project, six motion patterns were built into the robot firmware;

1. Swim only mode – moving wave pattern of the tail
2. Turn left while swimming
3. Turn right while swimming
4. Sharp turn – left
5. Sharp turn – right
6. Pause (coasting)

The motion pattern requires studying of life fish while swimming and turning and watching a slowed motion video of the fish. The **swimming motion** is a sine wave but with the amplitude increasing toward the tail fin – Figure 4.41. Lighthill (1960) described it as a travelling wave. The **sharp turning left** and **right** involves bending suddenly in the direction of interest and forming a curve that increases in its radius of curvature from the tail towards the head – much like a spring, and then uncoiling it rapidly – Figure 4.42. **Turning while swimming** involve one sided swinging of the tail.

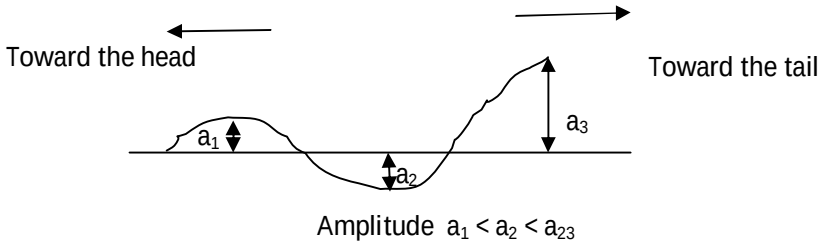
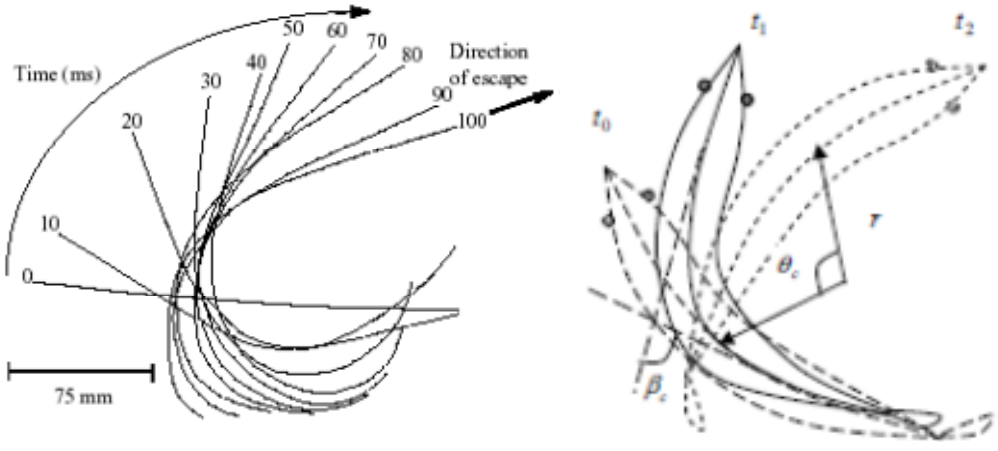


Figure 4.41 *Teleost* fish swimming pattern – tail amplitude increases toward the tail fin



A **B**

Figure 4.42 Sharp turning behavior – sources (A) (Jindong and Huosheng, 2005) (B) (Huosheng et al, 2006)

4.4.7.1 Equipment used

1. A digital camera - Sony Cyber-shot digital camera (model DSC-S730) set to VGA mode for video capture.

4.4.7.2 Test procedure

1. The test was carried out by issuing the commands (i.e. pressing the buttons on the remote control transmitter) and documenting the responses of the robot to each command – listed in section 4.4.7.

4.4.8 Test For Water Leakages

Since the robot is intended to work inside water, any leakage will damage the electronic components. The wooden parts will also get soaked and the glues will part if there is any leak.

4.4.8.1 Equipment used

1. A plastic bucket for water - capacity – 30cl
2. Stop watch – for timing purposes.

4.4.8.2 Test procedure

1. The bucket was filled with water to a depth of 30cm as shown in Figure 4.43. Thus the pressure head is
   $= (\rho * a * h) = 2{,}913.57 \text{ Pa} \approx 2.91\text{kPa}$
   where
   $h=30\text{cm} = 0.3\text{m}$ = height of water in the bucket used for the test
   $\rho=990\text{kg/m}^3$ = density of the water
   $a=9.81\text{m/s}^2$ = acceleration due to gravity
2. The parts (the tail assembly with the servomotors, the electronic and controller pod, the battery, the sensors, the wires) were immersed inside water for 30minutes
3. A visual inspection was done on them to see if there were any leakages.
4. Furthermore, the servomotors were tested for leakages by powering them up and applying control signals to see if they will still work.



Figure 4.43 The tail and servomotors are placed inside a bucket of water for test against water leakages and soaking of wood.

4.5 FIELD TESTS

The purpose of the field tests are;

1. To find out if the joint developed can work effectively with the control scheme built into the microcontroller controlling it and
2. To also find out the performance of the fish robot inside a body of water

The field tests were done in two environments:

1. **Water tank** – to demonstrate turning in a tight corner (sharp turning) and test the behaviour of the bump sensor.
2. **A shallow pool** - to demonstrate dynamic turning, effect of amplitude of tail oscillation, frequency of tail oscillation, linear speed.

4.5.1 Experimental Conditions – Water Tank

This is about test carried out in the water tank.

4.5.1.1 Equipment required for the experiment in the water tank

1. The water tank is a 60.96cm x 121.92cm x 60.96cm wooden box filled with water to a depth of 30cm or pressure head of 2.91kPa. (Figure 4.44).

2. A digital camera - Sony Cyber-shot digital camera (model DSC-S730) set to VGA mode for video capture.
3. Ballast material; polystyrene foam block, black tape and stones.

4.5.1.2 Test procedure

1. The ballast materials were attached to the robot bottom using black tape. The foam was used to lift the head/haul as it is heavier.
2. The robot was then placed inside the tank previously filled with water to a depth of 30cm.
3. Control signals were then applied, that is, the remote control was used to start it up, then the robot was allowed to swim freely.
4. The video camera was used to capture all the motions for evaluation.

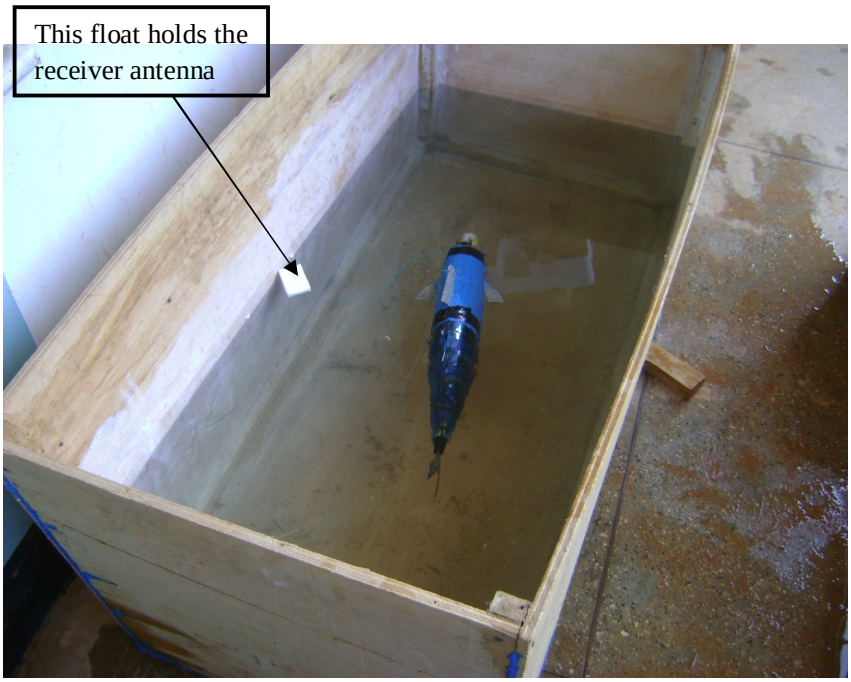


Figure 4.44– The robot inside the wooden water tank

4.5.2 Experimental Conditions – Shallow Pond

4.5.2.1 Equipment required for the experiment in the shallow pond

1. The shallow pond located at Ahmadu Bello University, Faculty of Engineering quadrangle – with a depth range of 25cm to 50cm (equivalent pressure head of 2.4kPa – 4.9kPa). Figure 4.45 shows the static picture of the robot inside the pond.
2. A digital camera - Sony Cyber-shot digital camera (model DSC-S730) set to VGA mode for video capture.
3. Ballast material such as polystyrene foam block, black tape and stones.

4.5.2.2 Test procedure

1. The ballast materials were attached to the robot bottom using black tape. The foam was used to lift the head/haul as it is heavier.
2. The robot was then placed inside the pond at the lower side.
3. The maximum depth at which the experiment was performed was 10cm because of visibility inside the murky water. The depth was adjusted using different ballast weights.
4. The control signals were then applied in turn, that is, the remote control was used to start it up, then the various instructions was made to be executed by pressing the corresponding buttons.
5. The video camera was used to document all the experimental processes for evaluation later on.



Figure 4.45 Static picture of the robotic fish swimming in the shallow pond of Ahmadu Bello University Faculty of Engineering quadrangle pond.

Table 4.3 BILL OF QUANTITIES

s/no	Material	Dimension	Quantity	Cost (NGN)
1	Vulcanized rubber – 1.5mm thick.	100cmX100cm	1	500.00
2	1/8 inch (3.175mm) thick seasoned plywood.	60.96cmX60.96cm (12” by 12”)	1	750.00
3	¾ (19.05mm) inch plywood.	15.24cmX30.48cm (6” by 12”)	1	750.00

4	ABRO® steel reinforced 4 minutes setting Epoxy glue – Araldite.	-	5	1000.00
5	Nylon 1010 cables – 0.5mm diameter.	1m	1	50.00
6	2.5mm diameter unplasticized PVC tubing.	1m	1	200.00
7	Remote Control Servomotors (Futaba 3003 and Futaba 148).	-	3	10500.00
8	Microcontroller – PIC18F4520	-	1	600.00
9	Latex Rubber – from Population Services International (PSI)	-	2	40.00
10	Silicone rubber	-	2	400.00
11	Micro switches.	-	2	100.00
12	Parallax Ping)))	-	1	5000.00
13	Collapsed polyurethane foam	15.24cmX30.48cm (6” by 12”)	1	100.00
14	Cyanoacrylate glue (super	-	20	1000.00

	glue)			
15	Resistor 1kΩ	-	15	75.00
16	Resistor 100kΩ	-	12	60.00
	Resistor 100kΩ	-	1	5.00
17	Diode 1N400	-	9	45.00
18	PCB Board	5cm X 10cm	1	200.00
19	Remote control (transmitter and receiver)	-	1	4500.00
20	Capacitor 10µF	-	1	10.00
21	Candle wax	-	1	20.00
22	Vaseline	-	1	100.00
23	Lithium polymer battery	-	4	2000.00
24	Power switch	-	1	100.00
			Total material cost	**₦28,105.00**

CHAPTER FIVE

RESULTS AND DISCUSSIONS

5.1 LABORATORY TEST RESULTS

5.1.1 Results Of Tests On The Pulse Width Modulation (PWM) Code Generation

Figure 5.1 shows the oscilloscope output of the microcontroller generating the PWM control signal at 1ms latency and 20ms period accurately.

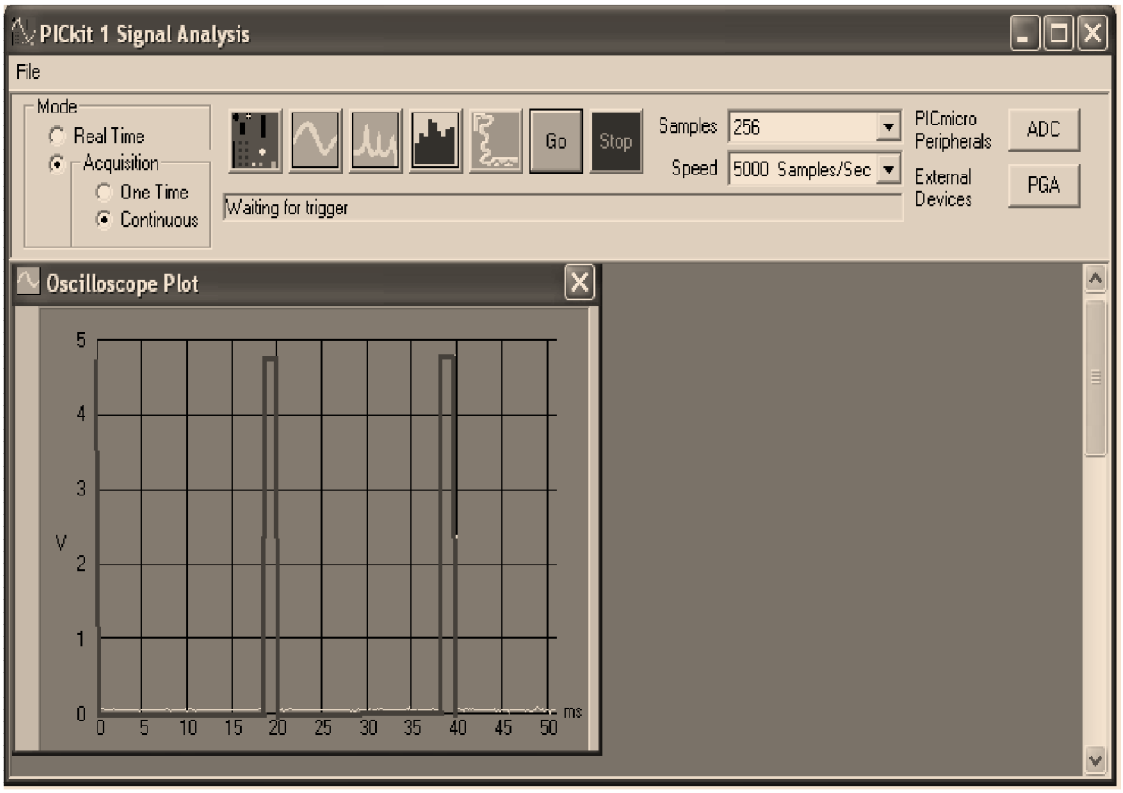


Figure 5.1 Oscilloscope output of the microcontroller generating the PWM

5.1.2 Result Of Concurrency Pulse Width Modulation (PWM) Code Generation

Figure 5.2 shows the Logic analyzer output of the microcontroller generating 3 concurrent PWM control signals for the three servomotor output pin labeled RD0, RD1 and RD2. The horizontal axis is the time scale in microseconds.

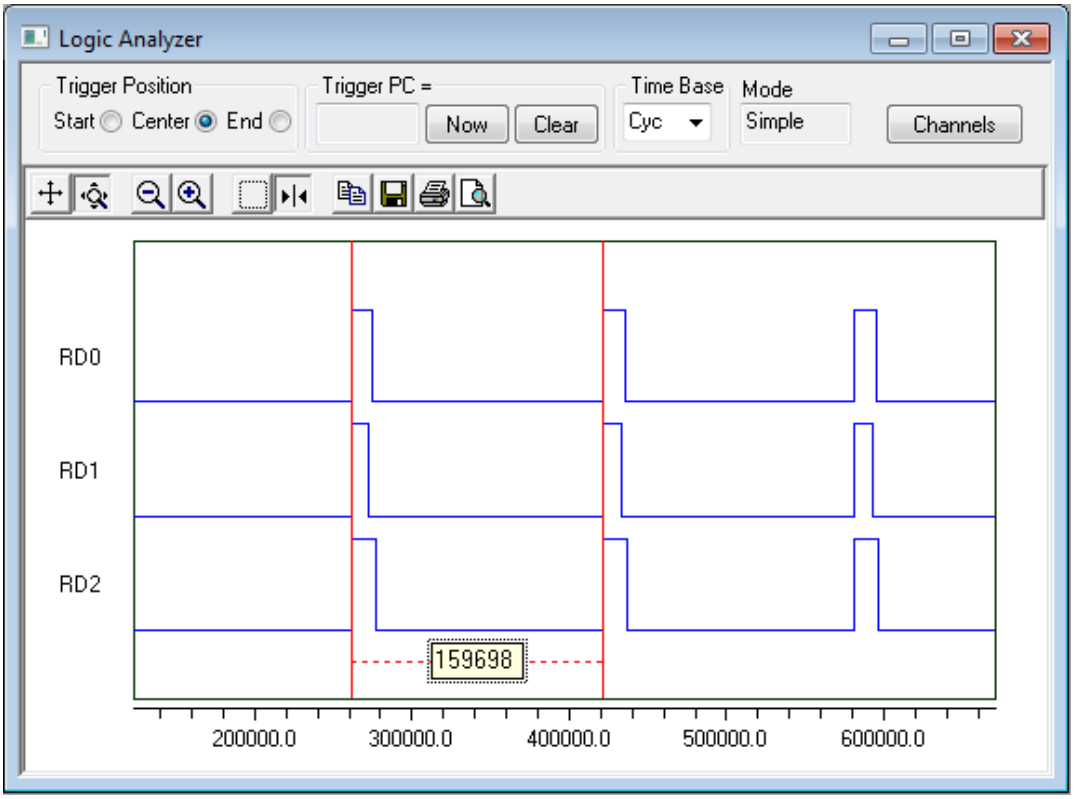


Figure 5.2 Logic analyzer output of the microcontroller generating 3 concurrent pulse width modulated signal

5.1.3 Result Of The Test For Correct Angular Displacement (Swing) Of The Motor

For the Futaba 3003 servo motors used, it was found to be 1.5275ms, the time was measured using MPLAB v8.56 simulator software stopwatch.

5.1.4 The Result Of The Test On The Sonar Sensor

5.1.4.1 The result of the test on the sonar sensor in the air

Maximum distance at which signal was sensed = ~3m

Beam arc at 3m = θ = 30cm

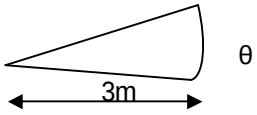


Table 5.1 shows the result of the object detection tests in the air for signal blocking and signal reflection modes.

Table 5.1 Results of different objects effect on sonar signal transmitted and received in the air

Material	Signal blocking	Signal reflection (at 30cm)
CD plastic	Blocked	Perfect reflector
Plastic with sewing machine oil	Blocked	Fair reflector, as the oil seems to absorb the signal
Paper sheet	Blocked at about 1m (effective as distance increases)	Poor reflector – although signal is still detected
Human hand	Blocked	Poor reflector – although signal is still detected
Glass lens	Blocked	As a lens, the signal is scattered but sensed if properly aligned

5.1.4.2 The result of the test on the sonar sensor in the water

Maximum distance covered = 0m

Beam arc; no signal detected

5.1.5 Result Of The Test Of The Bump Sensor Routine And Performance

5.1.5.1 The switch debounce test result

The undebounced micro switch signal output is shown in Figure 5.3, while Figure 5.4 shows the spectrum analyzer output of the micro switch.

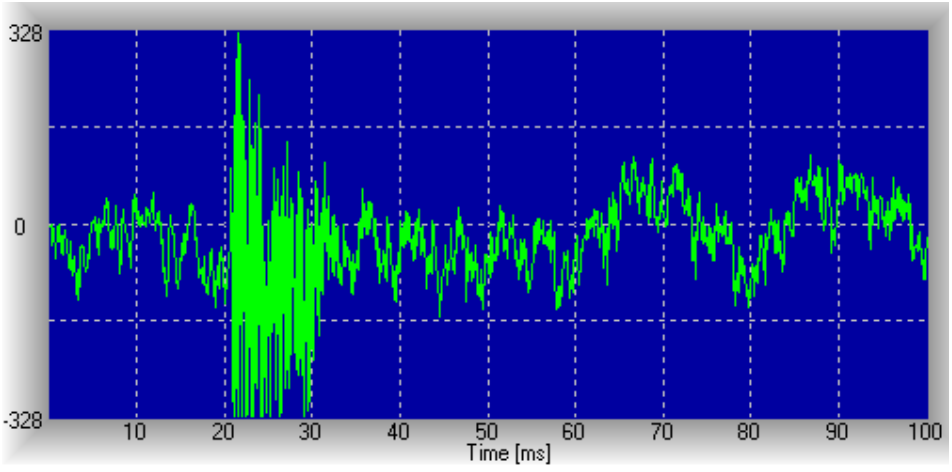


Figure 5.3 Oscilloscope displaying the undebounced micro switch signal output. Signals from 0-20ms and 30-100ms are artifact due to the 50Hz power line

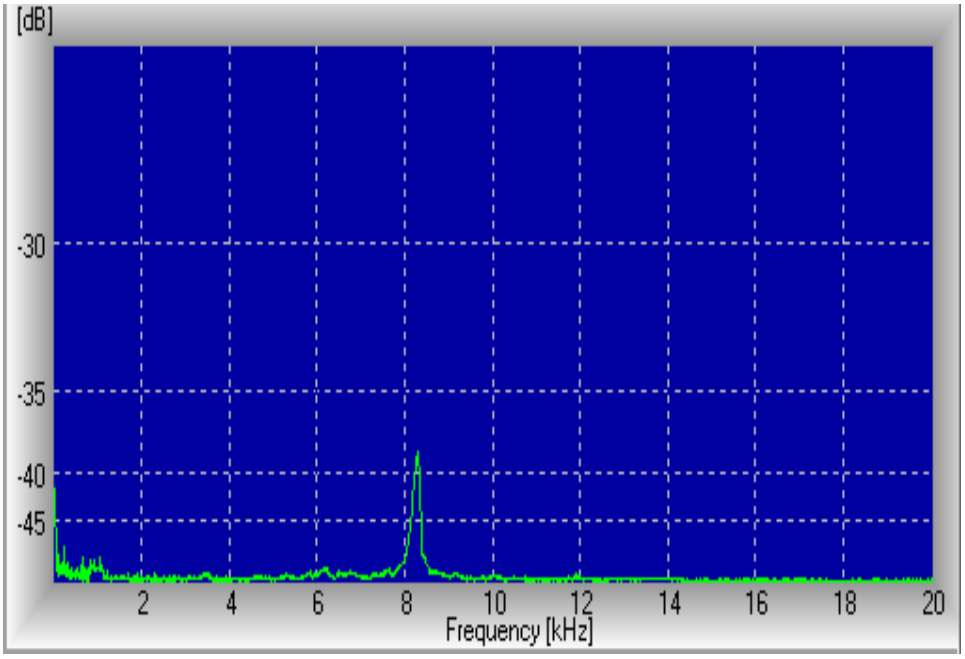


Figure 5.4 Spectrum analyzer display of the undebounced micro switch signal output

5.1.5.2 Activation load test result

The force to cause each button to be activated is shown in Table 5.2 and Figure 5.5.

Table 5.2 Activation force (in N) to cause the left and right bump switch (micro switch) to be activated.

Time in minutes	Left button (N)	Right button (N)
0	3.88	6.06
5	3.85	6.11
10	3.73	5.87
15	3.78	5.59
20	3.70	5.75
25	3.72	5.79
Mean	3.78	5.86
Standard deviation	0.07	0.18

A dorsal view is implied in identifying the left and right switch

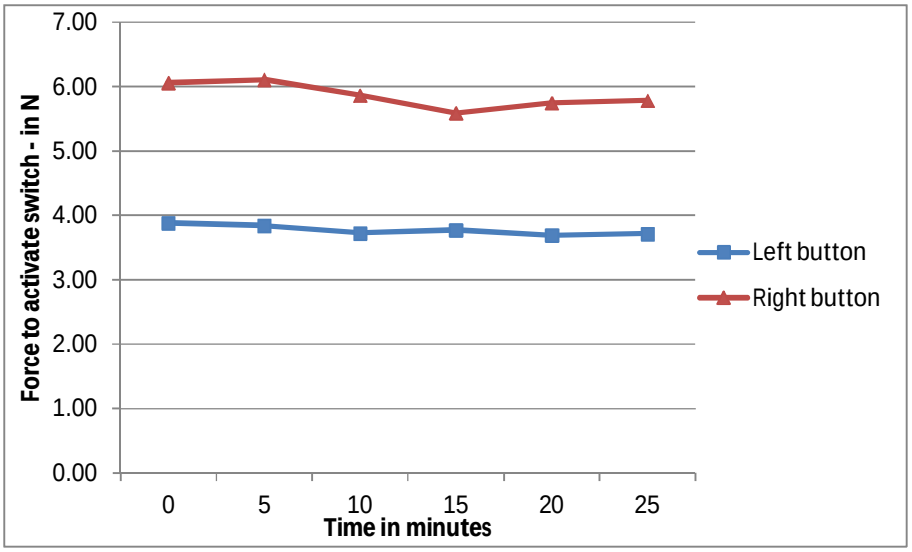


Figure 5.5 A plot of force to activate the left and right bump switch

5.1.5.2 Foam compressive test result

The result of the modified IFD test (compressive tests) on five samples of the 1 cm^3 collapsed polyurethane foams is shown in Table 5.3 and Figure 5.6.

Table 5.3 shows the result of the modified IFD test (compressive tests) on five samples of the 1 cm^3 collapsed polyurethane foams. Values are in Newton.

	Foam sample				
Side	**Sample 1**	**Sample 2**	**Sample 3**	**Sample 4**	**Sample 5**
1	0.44	0.29	0.37	0.29	0.47
2	0.48	0.24	0.35	0.31	0.31
3	0.34	0.25	0.26	0.28	0.30
4	0.36	0.48	0.28	0.29	0.26
5	0.45	0.34	0.39	0.39	0.41
6	0.39	0.33	0.36	0.39	0.35
Mean	0.41	0.32	0.34	0.33	0.35
STD	0.05	0.08	0.05	0.05	0.07

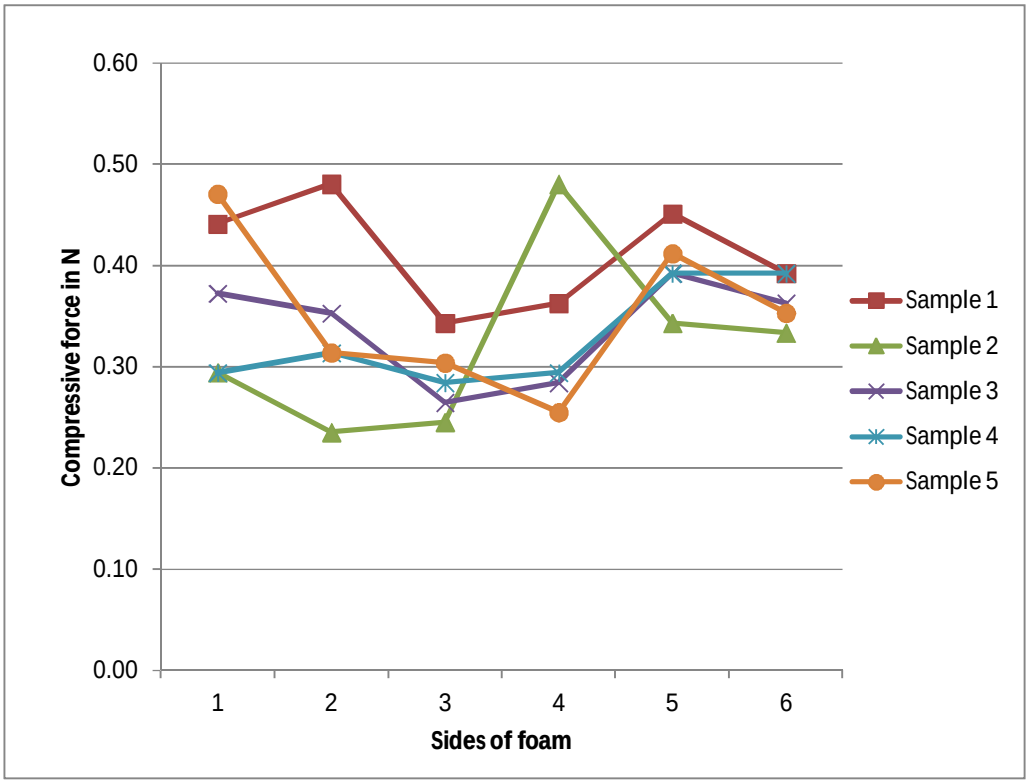


Figure 5.6 A plot of force to activate the left and right bump switch

5.1.6 Result Of The Test Of The Human Override Control

There were no errors or wrong response to the control signals, however the robot responds randomly whenever the robot battery drops to 4.0v or less.

5.1.7 Test For Motion Pattern

Figure 5.7 shows the static result of the 3 patterns – straight swim, sharp turn left and sharp turn right. The pause/coasting pattern means the robot should straighten up as shown in Figure 5.8. In the swimming mode, the maximum tail frequency achieved was 4.3Hz in the air.

Straight swim



Five sequence of still picture of the robot showing swimming mode.
Frame interval is 0.5s. Maximum frequency achieved was 4.3Hz

Turning left



Robotic fish tail developed showing bend pattern when executing left turn

Turning right



Robotic fish tail developed showing bend pattern when executing right turn

Figure 5.7 Result of the motion pattern



Figure 5.8 Pause/coasting mode – in this mode, the robot is straighten up. the servomotors are receiving commands to turn their horns to 90^o and remains at it.

5.2 FIELD TEST RESULTS

The results presented here are for tests performed while the robot is swimming in the water tank and shallow pond.

5.2.1 Tail Oscillation Speed

1 Maximum oscillation achieved = 1.7Hz, measured with slowed video capture of the fish robot.

2 Minimum oscillation – 0Hz implies coasting – or no oscillation of the tail

5.2.2 Dynamic Turning (Turning While Swimming)

The following results were obtained;

1 Peduncle angle was able to transits from 0^o +/- 45^o

2 Peak frequency is equal to current tail oscillation frequency while performing the motion.

3 The transition between normal swimming and dynamic turning is noticeably smooth.

5.2.3 Amplitude Of Oscillation Of The Tail

This is the amount of excursion the tail section makes from the middle line to either side. Table 5.4 shows the results obtained.

Table 5.4 The result of the amplitude variation of the tail sections

Segment	Maximum	Minimum	Steps/division
1 (close to base)	~10° from center	~5° from center	0x40/0x5 =C=d12
2 (middle)	~45° from center	~10° from center	- do -
3 (Attached to peduncle)	~90° from center	~45° from center	- do -

5.2.4 Sharp Turning

The following results were obtained;

1 Minimum turning radius was 0.8m

2 The uncoiling delay was approximately 1second.

5.2.5 Swimming Speed At Different Peduncle Amplitude And Different Tail Frequencies

Figure 5.9 shows in graphical form the swimming speed with respect to different tail (peduncle) amplitudes at frequencies of 0.5, 0.7, 0.9, 1.1, 1.3, 1.5 and at the maximum (1.7Hz obtained inside water). Frequencies 0.7, 0.9, 1.1, 1.3, 1.5 were estimated by interpolation from the slowed video of the swimming robot.

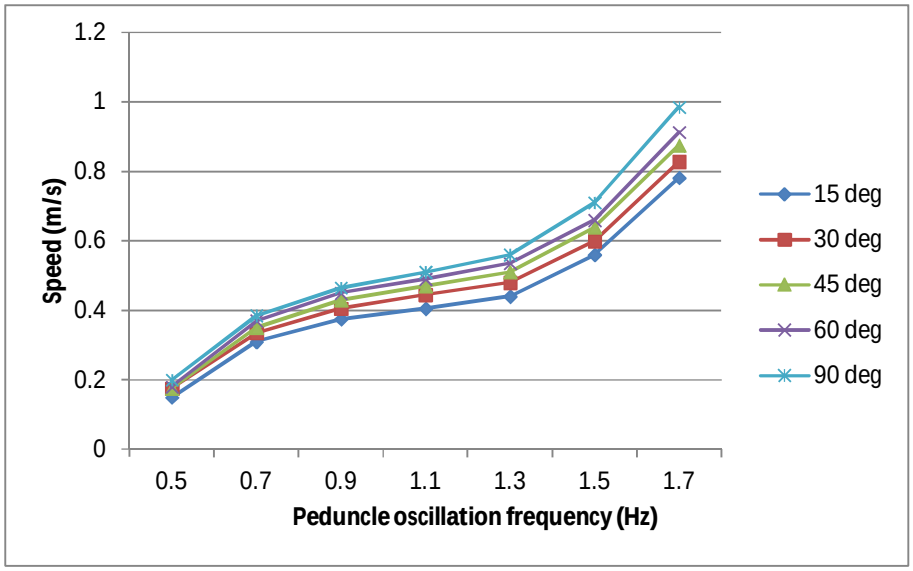


Figure 5.9 Speed of robot against peduncle (last segment) oscillation at different peduncle amplitude

5.2.6 Maximum Linear Speed

From Figure 5.9, the average maximum linear speed achieved was 0.985 m/s at maximum tail beat frequency of 1.7Hz inside water.

5.2.7 Other Field Test Results

The sealing worked perfectly as water would have destroyed the electronics if there is any leakage. In one of the test, a little leakage damaged the wireless receiver transistors and the whole receiver (transmitter and receiver pair had to be changed)

5.3 DISCUSSION OF THE LABORATORY TESTS RESULTS

5.3.1 Pulse Width Modulation (PWM) Code Generation

From Figure 5.1, the microcontroller output is reliably accurate or rather the code for the PWM scheme generation is working fine. If the code is faulty, there will be jittering of the motor and the output will not also be as desired.

5.3.2 Concurrent Pulse Width Modulation (PWM) Code Generation

Since the three concurrent PWM control signals have different latency and starting up simultaneously, it means the servomotors are at different angles; or precisely 60^o out of phase to each other as designed (Figure 5.2). If servomotor connected to RD0 is at 120^o, then that connected to RD1 will be at 60^o and RD2 will be at 180^o.

5.3.3 Angular Displacement (Swing) Of The Motor

The servomotors swing from 0^o to 180^o with 1ms PWM input corresponding to 0^o and 2ms corresponding to 180^o. Naturally, 1.5ms PWM input to the motor is supposed to give 90^o. For the servomotors used it was found to be 1.5275ms. This value was updated in the firmware after the test so as to correct this error.

5.3.4 The Sonar Sensor

5.3.4.1 The test of the sonar sensor in the air

The value are consistent with the manufacturer data as shown in Appendix E.

5.3.4.2 The test of the sonar sensor in the water

The reason for the zero signal detection is attributed to diaphragm overloading as explained in appendix E.

5.3.5 The Bump Sensor Routine And Performance

5.3.5.1 The switch debounce test

This test aim at removing false signal input to the microcontroller due to switch contact bounce. From the spectrum analyzer display, the switch bounce frequency is at 8.5khz approximately. From this information we can deduce;

The number of inputs to the microcontroller as

=Microcontroller MIP / Switch bounce frequency

where

Microcontroller MIP = microcontroller clock/4 (for microchip microcontrollers)

= 32Mhz/4 = 8Mhz = 8,000,000Hz

Therefore, the number of inputs to the microcontroller is;

= 8,000,000/85000

=941.18 inputs per second (that is one click of the switch will generate > 941 inputs)

In periodic notation, this is equal to

T = 1/941.18

= 0.0010625 seconds

= 1,062.5 μs

The microcontroller execute one instruction in 0.125μs, it implies that it will always have to wait or idle for T / 0.125 instructions before deciding whether the switch contact was closed or opened and is given as;

= 1,0625.5μs /0.125μs

= 8,500 instructions Or (0x100)*(0x21) in hexadecimal notations

5.3.5.2 Activation load test

From Table 5.2 and Figure 5.5, the right button is stiffer, requiring 5.86N on average to activate it. This value is about 35% higher than the left button average activation force.

From Table 5.3 and Figure 5.6 it can be seen that the force ranges between 0.24N to 0.48N with the mean varying between 0.32 to 0.41. The standard deviation for three samples is 0.5 meaning the other two are skewed perhaps due to measurement errors.

According to the manufacturer datasheet, 0.015N is required to activate the micro switches. The 0.24N to 0.48N require for the foam is 16 to 32 times additional load required to depress the micro switch. Therefore, the actual force required to activate the switch is

(3.78-0.24) to (3.78-0.48) **For left bump switch**

= 3.54N to 3.30N

Or averagely 3.42N

(5.86-0.24) or (5.86-0.48) **For right bump switch**

= 5.62 to 5.38

Or averagely 5.50N

These high values (compared to 0.015N by the manufacturer of the micro switches) are due to the water proof coating using silicone.

The question that arise is that, at what minimum speed should the robot be moving so as to activate the bump switches.

If we work by the right bump switch that requires maximum force to depress it i.e. 5.50N and drag forces are ignored, then from Newton's second law of motion, impulse is defined as

$F.t = mv_1 - mv_2$

F= force acting

t=period of action

m=mass of the body

v_1=final velocity after impact

v_0=initial velocity before impact

The minimum speed will be just enough to bring the robot to stand still, i.e.

$v_1 = 0$

m = 592g = mass of the robot

F = 5.86N the total force required to depress the switch

therefore

$F*t = mv_1 - mv_2$ = $5.86 * t = 0.592*0 - 0.592*v_2$

Or $5.86 = - 0.592*v_2/t$ implying a deceleration

$v_2/t = 0.592/5.86 = 0.096 m/s^2$

and hence

$v_2 = 0.096$ m/s over a period of 1s

5.3.6 The Human Override Control i.e. The Remote Control

The random behavior of the robot whenever its battery drops to 4.0V and less is expected as the documentation for the PIC18F4520 used for the microcontroller specifies that the nominal voltage should be 4.5V to 5V.

Furthermore, the robot was made to "swim" for over 10minute before the anomaly started showing up against the calculated 2.7 hours. This is the result of the use of battery in which the label and manufacturer name and logo had been compromised or are false.

5.3.7 Discussion On The Test For Motion Pattern

The other two patterns (turn left while swimming and turn right while swimming) are best appreciated when viewed as video. The pause/coasting pattern means the robot should straighten up as shown in Figure 5.8. In the swimming mode, the maximum tail frequency achieved was 4.3Hz – (in the air).

5.4 DISCUSSION OF THE FIELD TESTS RESULTS

5.4.1 Tail Oscillation Speed

This is the frequency at which the tail section moves from left to right and back again, the;

1 Maximum oscillation achieved = 1.7Hz, measure with slowed video capture of the fish robot.

2 Minimum oscillation – 0Hz which implies coasting – or no oscillation of the tail

5.4.2 Dynamic Turning (Turning While Swimming)

This is the turning performed while cruising and involve the tail oscillation being restricted to one axis. The transition between normal swimming and dynamic turning is noticeably smooth, this is essential for successful swimming. If transition is not smooth, a jerky or wobbling motion may result.

5.4.3 Amplitude Of Oscillation Of The Tail

This is the amount of excursion the tail section makes from the middle line to either side. For the values shown in Table 5.4,

1 the segments referred to are the positions the cables from the motors are attached to, also

2 the measurements are in degree from center line, and

3 the values were taken with respect to the peduncle as it has the largest excursion.

The ~90^{o} maximum for the peduncle is an out of bound data resulting from the water pressure on it, that is the peduncle was forced to bend that far while pushing the water away.

5.4.4 Sharp Turning

Sharp turning routine is only activated by the bump switch. The turn involves bending like a coil or letter C and then uncoiling rapidly (limited by the current tail oscillation frequency that is, fast oscillation, fast coiling or uncoiling). The turning radius is always the minimum as maximum turning radius implies straight line motion.

On the uncoiling delay which is approximately 1second, the built in delay was set to 0x1E which by the program structure, it will yield 600ms, the extra 400ms lag (1s minus 600ms) is due to the motor inertia and the water environment.

5.4.5 Swimming Speed At Different Peduncle Amplitude And Different Tail Frequencies

Figure 5.9 shows in graphical form the swimming speed with respect to different tail (peduncle) amplitudes at frequencies of 0.5, 0.7, 0.9, 1.1, 1.3, 1.5 and at the maximum (1.7Hz obtained inside water). The result is comparable to that obtained by Jindong and Huosheng (2007) reproduced here in Figure 5.10 for comparison. For this work and theirs, the speed of the fish robots increases with tail frequency. Also the increase amplitude leads to a relative increment in speed for each tail oscillation frequency. The relationship between tail frequency and speed is not linear.

5.4.6 Maximum Linear Speed

From Figure 5.9, the average maximum linear speed achieved was 0.985 m/s at maximum tail beat frequency of 1.7Hz inside water. This is approximately 1/3 of that of live mackerel which is 3.06m/s (http://www.nmri.go.jp/eng/khirata/fish /general/speed/speede.htm).

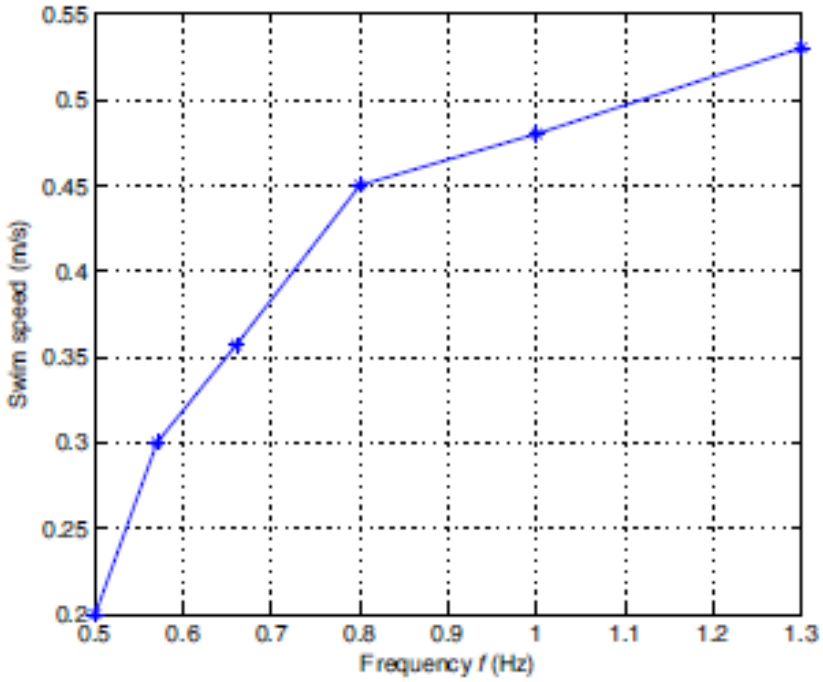


Figure 5.10 Relationship between swim speed and tail flapping speed.
Source: Jindong and Huosheng (2007)

Compared to UPF-2001 robotic fish that has 0.97m/s (http://www.nmri.go.jp/eng /khirata/fish) and the Essex G9 robotic fish (Jindong and Huosheng (2007) with linear speed of 0.2m/s, this robot fish is faster at 0.985m/s. This can be attributed to the tail design which used light material and thus allows faster tail beat (1.7Hz inside water, 4.3Hz in the air) than the Essex G9 fish that actually placed motors inside the tail which reduces its tail beat frequencies to 0.5Hz. The UPF-2001 is also fast because it does not have motor in its tail, it uses lever to control its tail fin.

CHAPTER SIX

CONCLUSIONS AND RECOMMENDATIONS

6.1 CONCLUSIONS

The following conclusions are hereby drawn from this research work;

1. A biomorphic hyper-redundant joint mechanism for robotic applications has been successfully designed and developed,
2. Carbon filled natural rubber was found to be a suitable biomimetic material and was used successfully for building the robot joints. Other researchers have shown it to have qualitatively similar mechanical properties to living tissues.
3. Muscular hydrostatic skeleton was successfully imitated in achieving the goal of using hydrostatic skeleton as the structural design basis.
4. The goal of constructing and testing a simple robot based on the joint developed and designed was achieved by applying the designed joint to a fish robot tail – specifically a *teleost* specie of fish, mackerel.
5. The robot fish developed was successfully tested inside stationary body of water and had a linear speed that is one third (1/3) of a live mackerel fish, and a maximum tail beat frequency of 1.7Hz inside water and 4.3Hz outside water.
6. The control scheme is simple as three (3) servo motors were used for actuation and one microcontroller for their control compared to an earlier version of Essex G9 robotic fish which uses up to 5 motors.
7. The computer simulations that predicted the maximum stress ($4.64kN/m^2$ for rubber, and 9.24 kN/m^2 for plywood material) that the peduncle will experience were also accurate as peduncle did not fail in any of the tests (laboratory and field) carried out on the robot. Also, the design did not warp as predicted especially as the oscillation did not reach the critical speed of 25Hz where Payne effect will occur

and cause frequency induced softening. The servo motors rating (0.29Nm) is adequate enough to handle the torque of 0.0000237Nm (at 0.5Hz) to 0.00088804Nm (at 1.7Hz) and peduncle displacement of 90^{o} actually experienced by the robot while being tested.

8. Furthermore, stability analysis indicates that the controller design is unstable when hydro dynamic drag is considered and marginally stable without it. The controller is also very sensitive to perturbation as implemented.

6.2 RECOMMENDATIONS

The followings are therefore recommended in a future work on this same project or any similar one to it;

1. There is still much work to be done especially on the sonar navigation system. In the course of this research exhaustive literature search for documents or publications on sonar navigation underwater at a small scale (less 0.5m) was not found. There is need to solve this problem as the object detection using visible light or infrared light or even ultraviolet rays may likely not be effective inside mucky water.
2. Furthermore, a bigger model will allow much onboard power, more instrumentations and capabilities to be built in. For example, the model developed could have demonstrated 3D motion also, but there was no place to put buoyancy devices inside it.
3. Rubber is a nonlinear material and simulating its behavior is a non trivial issue. It is recommended that further work be done on simulating the complete fish model with a cluster computing system or super computer. The design is very promising as the robot was able to swim at about 1/3 that of a live fish, it is good to perform a complete simulation to find out how to improve on this speed even more.

REFERENCES

Afolayan, M.O. (2010). Potential of Watch Buzzer as Underwater Navigation Device in Shallow Water Streams. *Research Journal of Applied Sciences, Engineering and Technology* 2(5): 436-446.

Afolayan, M.O. and Madakson, P.B. (2009). A design description of mobile robotic endoscope. *Proceedings of the 28th Committee of directors of health services in Nigerian universities & 13th National Association of Doctors in University health Services, held at Institute for Development Research (I.D.R.), Ahmadu Bello University, Zaria*. pp 100-108.

Ahmadi, H. and Muhr, A. (2002). Design of elastomeric engineering components using FEA: current practice and future trends. FENet Thematic Network Competitive and Sustainable growth programme. *Available online at: http://www.fe-net.org/downloads/FENet_Meetings/Wiesbaden_Germany_Nov_2001/FENET_Wiesbaden_Nov2001_Tech_Issues_DLE_Ahmadi.pdf*. pp 1-10.

Alessandro, C., Auke, J. I. (2008). *Salamandra robotica*: a biologically inspired amphibious robot that swims and walks. *Internal Review of Biologically Inspired Robotics Group, Ecole Polytechnique Federale De Lausanne (EPFL) Biorobotic Laboratory internal review, Lausanne, Switzerland*. pp 1-20.

Alscher, C. (1990). Numerical Simulation of impact and Lift-off events in the Hydrostatic Skeleton of the Leech. *Department of Mathematics, University of Bielefeld, Bielefeld, Germany*. pp 1-20.

Alscher, C. and Beyn, W.J. (1998). Simulating the motion of the Leech, A biomechanical application of DAEs, *Numerical Algorithms* 19 (1998): 1-12.

Anani, A., Ivan, K., Evgeni, P. and Banko, H. (2004). Single-Motor Driven Construction of Hyper-Redundant Robot. *Available online at: www.oru.se/oru-upload/institutioner/teknik/document/forskining/ASS/publication%202004 %20single-motor.pdf*

Anderson, J.M. (1996). "Vorticity control for efficient propulsion," *Ph.D. dissertation, Massachusetts Inst. Technol./Woods Hole Oceanographic Inst. Joint Program, Woods Hole, MA,* 1996.

Anne, P. (1990). Leech - Biology for Bushwalkers. *Australian Zoologist*, 26: 3 – 4.

Ashish, T. (2002). Modern Control Design with MATLAB and SIMULINK. *John Wiley and Sons Ltd*. pp 13-124.

Beatty, M.F. (2002). The Mullins Effect in the Vibration of Stretched Rubber Membrane. *Mathematics and Mechanics of Solids*. 8: 435-445

Belanger, J.H. and Trimmer, B.A. (2000). Combined kinematic and Electromyography analysis of proleg function during crawling by the caterpillar *manduca sexta*. *J. Comparative. Physiology*. A (2000). 186: 1031-1039.

Bilgili, E. (2002). Computer Simulation as a Tool to Investigate the Shearing Deformation of Nonhomogeneous Elastomers. *Journal of Elastomers and Plastics* 34; 239.

Bjorn, C. (2005). The World Smallest Robot. *http://www.livescience.com/ technology/050915_smallest_robot.html.* Accessed 21/07/2006

Brett, R. F., William, H. W, Selim, T. and Leslie P. K. (2003). A dynamic Model of Visually- Guided Steering, Obstacle Avoidance, and Route Selection. *International Journal of Computer Vision* 54(1/2/3), 13-34, 2003.

Brooks, R. A. (1989). A Robot That Walks; Emergent Behaviours from Carefully Evolved Network. *MIT AI Lab Memo 1091, February 1989. A Book about Genghis. Available online at http://groups.csail.mit.edu/people/brooks/papers*

Brooks, R. A. and Flynn, A. M. (1989). Fast, Cheap and Out of Control: A Robot Invasion of the Solar System. *Journal of The British Interplanetary Society*, 42: 478-485.

Cardiff, M. (2006). Introduction to Finite Element Modeling & COMSOL (a mini-course) CEE-268, Winter 2006 pg 10. *Available online at www.stanford.edu /~mcardiff/COMSOL/ Presentation1.ppt*

Ceska, V. (2011). Who did actually invent the word "robot" and what does it mean? *Available online at http://capek.misto.cz/english/robot.html*.

Charles, W. E. and Antonio, A. A. (1998). Jormungand, an Autonomous Robotic Snake. *Machine Intelligent Laboratory, University of Florida, Department of Electrical Engineering*.

Chirikjian, G.S. and Burdick, J.W. (1990). An Obstacle Avoidance Algorithm for Hyper-Redundant Manipulators. *Proceeding of IEEE International Conference on Robotics and Automation.* pp 625-631

Chirikjian, G.S. and Burdick, J.W. (1990). Kinematics of Hyper-Redundant Manipulators. *Proceeding of ASME Mechanism Conference*. pp 391-396.

Chirikjian, G.S. and Burdick, J. (1991). Kinematics of Hyper-redundant locomotion with applications to grqasping. *In Proceeding of IEEE International Conference on Robotics and Automation*, pp 720-727.

Choset, H. and Burdick, J. (1994). Sensor Based Planning and Nonsmooth Analysis. In *Proceeding of IEEE International Conference on Robotics and Automation*, pp 3034-3041.

Choset, H. and Burdick, J. (1995a). Sensor Based Planning, Part I: The Generalized Voronoi Graph. *IEEE International Conference on Robotics and Automation*. 2: 1649-1655.

Choset, H. and Burdick, J. (1995b). Sensor Based Planning, Part II: Incremental Construction of the Generalized Voronoi Graph. *IEEE International Conference on Robotics and Automation*. 2:1643-1648.

Choset, H. and Burdick, J. (1996). Sensor Based Planning for a Planar Rod Robot. *Proceedings of IEEE International Conference on Robotics and Automation, Minneapolis, Minnesota* – April 1996. 4: 3584 - 3591

Choset, H. and Henning, W. (1999). A Follow-The-Leader Approach to Serpentine Robot Motion Planning. *ASCE Journal of Aerospace Engineering*. pp 1-25.

Choset, H., Konukseven, I. and Rizzi, A. (1997). Sensor Based Planning: A Control law for Generating the Generalized Voronoi Graph. *ICAR '97, Montery, CA* July 7-9, 1997. pp 435-449.

Choset, H and Lee, J. Y. (2001). Sensor-Based Construction of a Retract-Like Structure for a Planar Rod Robot. *IEEE Transactions on Robotics*. pp 435- 449.

Crespi, A, Badertscher, A, Guignard, A and Ijspeert, A. J. (2005). Amphibot I: an amphibious snake-like robot. *Robots and Autonomous System*, 50: 163-175.

CSN, (2011). Convergent Science Network of biomimetic and biohybrid systems. *http://csnetwork.eu/conf2012/conference*. Accessed 7.35pm 24, November 2011

David, B. (1994). Robotuna. *Available online at: http://web.mit.edu/towtank/www /Tuna/tuna.html.* Accessed 8.00pm 24, August 2010

Degani, A., Choset, H., Wolf, A. and Zenati, M.A. (2006). Highly articulated robotic probe for minimally invasive surgery. *ICRA 2006. Proceedings 2006 IEEE International Conference* on *Robotics and Automation, 2006*. 15(19) : 4167 - 4172. DOI 10.1109 / ROBOT.2006.1642343

DeGroot, J.H., van der Sluijs, I., Snelderwaard, P.C. and van Leeuwen, J.L. (2004). A three-dimensional kinematic analysis of tongue flicking Python Molurus. *Journal of Experimenatl Biology*. 207:827-839.

Demirkoparan, H. and Pence, T.J. (2007a). Swelling of an internally pressurized nonlinearly elastic tube with fiber reinforcing. *International Journal of Solids and Structures* 44 :4009-4029. (doi:10.1016/j.ijsolstr.2006.11.006).

Demirkoparan, H. and Pence, T.J. (2007b). The effect of fiber recruitment on the swelling of a pressurized anisotropic nonlinearly elastic tube. *International Journal of Nonlinear Mechanics* 42 :258-270. (doi: 10.1016/j.ijnonlinmec. 2007.01.013).

Dohi, M., Fujiura, T and Yano, A. (2002). Hexapod Walking Robot for Agricultural Field (i) – Mechanism of leg and gait control. *Automation Technology for Off-Road*

Equipment, Proceedings of the July 26-27, 2002 Conference (Chicago, Illinois, USA) 701P0502. PP 196-203.

Dorfmann, A., Fuller, K.N.G., Ogden, R.W. (2002). Shear, compressive and dilatational response of rubberlike solids subject to cavitation damage. *International Journal of Solids and Structures*, 39 (7):1845-1861

Dorfmann, A. and Ogden, R.W. (2003). A pseudo-elastic model for loading, partial unloading and reloading of particle-reinforced rubber. *International Journal of Solids and Structures* 40: 2699-2714.

Dorfmann, A. and Ogden, R.W. (2004). A constitutive Model for the Mullins effect with permanent set in particle-reinforced rubber. *International Journal of Solids and Structures* 41:1855-1878.

Dorfmann, A., Trimmer, B.A. and Woods, W.A. Jr. (2007). A constitutive Model for Muscle properties in Soft-bodied Arthropod. *Journal of Royal Society International*. 4: 257-269.

Dorgan, K.M., Arwade, S.R. and Jumars, P.A. (2007). Burrowing in marine muds by crack propagation: kinematics and forces. *The Journal of Experimental Biology* 210: 4198-4212.

Drushel, R.F., Neustadter, D.M., Hurwitz, I., Crago, P.E. and Chiel, H.J. (1998). Kinematic Models of the Bucca Mass *Aplysia Californica*. *The Journal of Experimental Biology*. 1563-1583.

Dunwoody, J. (2005) Heat Conduction and Controlled Deformations in Incompressible Isotropic Elasticity. *Mathematics and Mechanics of Solids*, 10 (5): 487-502.

Dunwoody, J. and Ogden, R. W. (2002). On the Thermodynamic Stability of Elastic Heat-Conducting Solids Subject to a Deformation—Temperature Constraint. *Mathematics and Mechanics of Solids*. 7: 285-306.

Elie, S., Wolf, A., Brown, H.B., Jr. and Choset, H. (2003). New Joint Design for Three-dimensional Hyper Redundant Robots. *Proceedings of the 2005 IEEE*

International Conference on Robotics and Automation, Las Vegas, Nevada, October 2003. pp 3594- 3599.

Farabee, M.J. (2001). Muscular and Skeletal Systems. *Available online at: www.emc.maricopa.edu/faculty/farabee/BIOBK/BioBookMUSSKEL.html* (Accessed 10/23/2008 6:29pm)

Frank, S., Ethan, G., Robert, D. W. and Jason, R. (2011). Experimental verification of soft-robot gaits evolved by a lumped dynamic model. *Robotica*. 29(6):823-830.

Friedrich, M., Baltes, J., Schütz, M. and Gärtner, H. (1999). Automatic Shape Optimisation of Elastomeric Products. *Available online: www.mscsoftware.com/support/library/conf/auto99/p02199.pdf*. pp 1-10

Fumitoshi, M. (2002). A mobile robot for collecting disaster information and a snake robot for searching. *Advanced Robotics*. 16(6): 517-520.

Fung, Y.C. (1980). On Pseudo-elasticity of living tissues mechanics today. *Vol 5 (ed S.N. Nasser), Pergamon Mechanics Today series,. New York NY Pergamon Press.* pp. 49-66.

Gilbert, R. J., Napadow, V. J., Gaige, T. A. and Wedeen, V. J. (2007). Anatomical basis of lingual hydrostatic deformation. *Journal of Experimental Biology,* 210 (23): 4069-4082.

Grasso, F. W. (2000). Flow and Chemo~sense for Robot and Lobster Guidance in Odor Source Tracking. Neurotechnology for Biomimetic Robots Conference May-14-16, 2000 at Northeastern University East Point, Nahant, MA 01908. pp 1-10.

Grzegorz, G., Malik, G. H. and Johann, B. (2005). Industrial Robots. *International Journal on Industrial Robots, Special Issue on Mobile Robots,* vol IR32-2, March 18th, 2005, pp. 139-148.

Guo, S., Fukuda, T., Kato, N. and Oguro, K. (1998). "Development of Underwater Microrobot Using ICPF Actuator". *Proceedings of the 1998 IEEE International Conference on Robotics & Automation*. Pp 1829-1834.

Gutfreund, Y., Flash, T, Yarom, Y., Fiorito, G., Segev, I. and Hochner, B. (1996). Organization of Octopus Arm movements: a Model System for Studying the Control of Flexible Arms. *The Journal of Neuroscience*. 16(22): 7292-7307.

Haith, G.L., Thomas, H., Wright, A. (2000). A Serpentine Robot for Planetary and Asteroid Surface Exploration. *Oral Presentation at the Fourth IAA International Conference on Low-Cost Planetary Missions*, May 2-5, 2000, Laurel, MD. pp 1-10.

Hannan, M.W. and Walker, I.D. (2003). Kinematics and the implementation of an Elephant's Trunk manipulator and other continuum style Robots. *Journal of Robot System*. 20(2):45-63.

Hanyu, S. (1988). Morphological changes in penile vessels during erection: The mechanism of obstruction of arteries and veins at the tunica albuginea in dog corpora cavernosa. *Urology International*. 43: 219–224.

Harrison, R. R. and Koch, C. (2000). A Silicon Implementation of the Fly's Optomotor Control System *In: Letter by M.V. Srinivasan and Stephen DeWeerth. Neural Computation, Massachusetts Institute of Technology*. 12: 2291-2304

Hatze, H. (1974). "The meaning of the term biomechanics". *Journal of Biomechanics*. 7: 189–190.

Herrel, A., Meyers, J.J., Aerts, P. and Nishikawa, K.C. (2001). Functional implications of Supercontracting muscles in the Chameleon tongue retractors. *Journal of Experimental Biology*. 204: 3621-3627.

Hirakawa, A. R., Saraiva, A. M. and Cugnasca, C. E. (2002). Wireless Robust Robot for Agricultural Applications. *Proceedings of the World Congress of Computers in Agriculture and Natural Resources* (13-15, March 2002, Iguacu Falls, Brazil) 701P0301. pp 414-420

Hirobumi, M., Morihiro, M., Yoshihiro, M., Hiroshi, S.A., Shigeo, H., Yoji, U. (1985). Measuring/Grinding System for Water Turbine Runner, *Proceeding 2nd International Conference on Advanced Research*, pp.199-206

Hirose, S. and Morishima, A. (1990). "Design and Control of a Mobile Robot with an Articulated Body", *The International Journal of Robotics Research*. 9(2):99-113.

Hitoshi, K., Fumihiro, K., Daisuke, M., Michihiko, K., and Norio, I. (2006). Flexible Hermetically-Sealed Mobile Robot for Narrow Spaces Using Hydrostatic Skeleton Driving Mechanism. *Proceedings of the 2006 IEEE/RSJ International Conference on Intelligent Robots and Systems October 9 - 15, 2006, Beijing, China*. pp 4006 - 4011

Horgan, C.O., Ogden, R.W. and Saccomandi, G. (2004). A theory of stress softening of Elastomers based on finite chain extensibility. *Proceeding Royal. Society*. pp 1737-1754.

Horswill, I. (1992). Characterizing adaptation by constraint. In F. J. Varela and P. Bourgine (Eds.), Toward a practice of autonomous systems: *Proceedings of the First European Conference on Artificial Life*. pp 58-64.

Igor, P. (2005). What is a robot? RoboNexus 2005 robot exhibition virtual tour November 16, 2005. *Available online at: http://www.virtuar.com/click/2005/ robonexus/index.htm* Accessed on 23/03/2005

Isaac, A. (1950) I, Robot. *Gnome Press, available through http://www.asimovonline.com/oldsite/asimov_titles.html*

James, I. (2005). A Brief History of Robotics. *Available online at: http://robotics.megagiant.com/history.html.* Accessed on 23/03/2005

Jason, M. (2011). Fracture. *Available online at http://www.sv.vt.edu/ classes/MSE2094_NoteBook/97ClassProj/num/midkiff/theory.html*

Jean-Pierre, M. (2000). The Design of the MIPS Micro-Robot for Endoscopy Applications in European Research Consortium for Information and Mathematics, *ERIC NEWS*, July 2000, Number 42. Special Theme: Robotics. pp 35-36.

Jiang, X. and Ogden, R.W. (2000). Some new solutions for the axial shear of a circular cylindrical tube of compressible elastic material. *International Journal of Non-Linear Mechanics*. 35: 361-369

Jindong, L. and Huosheng, H. (2003). Building a Simulation Environment for Optimising Control Parameters of an Autonomous Robotic Fish. *Proceedings of the 9th Chinese Automation & Computing Society Conference in the UK, Luton, England*, 20 September 2003. Pp 317 -322

Jindong, L. and Huosheng, H. (2004). Building a 3D Simulator for Autonomous Navigation of Robotic Fishes. *Proceedings of 2004 IEEE/RSJ International Conference on Intelligent Robots and Systems. September 28-October 2, 2004, Sendai, Japan*. pp 613 - 618

Jindong, L. and Huosheng, H. (2007). A Methodology of Modelling Fish-like Swim Patterns for Robotic Fish. *Proceedings of the 2007 IEEE International Conference on Mechatronics and Automation*, August 5 - 8, 2007, Harbin, China pp 1316 - 1321

Joachim, H. (2003). MAKRO & MAKROplus (Multi segment autonomous sewer robot). *Available online at: wwwais.fhg.de/projects/Makro/makro.html*

Joachim, H. and Frank, K. (1997). Landmark-Based Autonomous Navigation in Sewerage Pipes. *GMD– German National Research Center for Computer Science Schloß Birlinghoven, 53754 Sankt Augustin, Germany*. Pp 1-5

John, J.V. (1993). Fish Swimming. *Chapman and Hall, 2-6 Boundary Row, London SE1 8HN, UK*. pp 1-10.

Kalev, H.L. (2002).Cyc: An Expert Framework for Consensus Knowledge Quantification. *Available online at http://www.kalevleetaru.com/Publish /Cyc_Consensus_Knowledge_Quantification.pdf*

Kato, N. (2000). "Control performance in the horizontal plane of a fish robot with mechanical pectoral fins". *IEEE Journal of Oceanic Engineering*. pp 121-129.

Kazuyki, I., Zhixiao, Y., Kazuhiko, S., Kazuyki, H., Akio, G. and Fumitoshi, M. (2005). A rescue system for collecting information designed for ease of use – a proposal of a rescue systems concept. *Advanced Robotics*, 19(3): 249-272.

Katsuihiko, O. (2005). Modern Control Engineering, 4th edition. *Pearson Education Inc. (www.pearsoned.co.in)*. pp 69-70.

Kelly, B. (2011). Strength/Mechanics of Materials. *Available online at http://www.engineersedge.com/ strength_of_materials.htm*

Kelly, D.A. (2002). The functional morphology of penile erection: tissue Designs for increasing and maintaining stiffness. *Integrated and Comparative Biology*. 42: 216-221.

Kelly, D.A. (2007). Penises as Variable-Volume Hydrostatic Skeletons. *Ann N.Y. Academic. Science* 1101: 453-463.

Kevin, B. (2003). How snakebots work. *Available online at: http://electronics.howstuffworks.com /snakebot.htm.* Accessed 8.00pm 11, August 2007

Kevin, J. D. (1997). Limbless Locomotion: Learning to Crawl with a Snake Robot. *A PhD thesis at the Robotics Institute Carnegie Mellon University, 5000 Forbes Avenue, Pittsburg, PA 15213.*

Kier, W.M and Smith, K. K. (1985). Tongues, tentacle and trunks: the biomechanics of movement in muscular-hydrostat. *Zoological Journal of the Linnean Society.* 83: 307-324.

Kirkinis, E. and Ogden, R. W. (2002). On Extension and Torsion of a Compressible Elastic Circular Cylinder. *Mathematics and Mechanics of Solids* 7: 373

Koehl, M. A. R., Quillin, K. J. and Pell, C. A. (2000). Mechanical Design of Fiber-Wound Hydraulic Skeletons: The Stiffening and Straightening of Embryonic Notochords. America. *Zoologist.*, 40:28–41.

Kolecki, J. C. (2002). An Introduction to Tensors for Students of Physics and Engineering. *NASA/TM—2002-211716. National Aeronautics and Space Administration, Glenn Research Center. Available online at http://www.sti.nasa.gov*. pp 1-10.

Konukseven, I. and Choset, H. (1997). Mobile Robot Navigation: Implementing the GVG in the presence of Sharp Corners. *Proceedings of IROS 97*. pp 1-10.

Kristan, W.B., Stent, G.S. and Ort, C.A. (1974). Neuronal control of swimming in the medicinal leech: I. Dynamics of the swimming rhythm. *Journal of Comparative Physiology*. 94: 97-119.

Kumph, J. M. (1996). RoboPike. *Available online at: http://web.mit.edu/towtank/ www/Pike/pike.html*. Access in December 5, 2010

Lee, J. Y. and Choset, H. (2004). Motion Planning for a Rod-shaped Robot in R^3: Connecting the Rod-HGVG using the Point-HGVG. *Proceedings of the 2004 IEEE International Conference on Robotics & Automation New Orleans, LA*, April 2004. Pp 1-10

Lee, J. Y. and Choset, H. (2005a). Sensor-based Exploration for Convex Bodies: A new Roadmap for a Convex-Shaped Robot. *IEEE Transactions on Robotics*. 21(2), pp 1-10.

Lee, J. Y. and Choset, H. (2005b). Sensor-Based Planning for a Rod-shaped Robot in Three Dimensions: Piecewise Retract of R^3 x S^2. *The International Journal of Robotics Research*. 24(5): 343-383.

Lenat, D. B. (1995), "Cyc: A Large-Scale Investment in Knowledge Infrastructure, *Communications of the ACM* 38, no. 11.

Liang, J. (2002). "Researchful Development of Underwater Robofish II- Development of a Small Experimental Robofish". *Robot*. 24(3): 234-238.

Lighthill, M. J. (1960) "Note on the swimming of slender fish," *Journal of Fluid Mechanics*. 9:305–317. Abstract and introduction only.

Lighthill, M. J. (1971). Large-amplitude elongated-body motion theory. *Proceeding of Royal Society. London*. 179: 125-138. Abstract and introduction only.

Lilianes, P. (2000). Robotics. *ERCIM News No. 42.pdf*, July 2000, pg 8-9 (www.ercim.org)

Ma, S., Shigeo, H. and Hiroshi, Y. (1992). CT ARM-I: Coupled Tendon-Driven Manipulator Model I -Design and Basic Experiments. *Proceeding. IEEE International Conference on Robotics and Automation* pp.2094- 2100.

Ma, S. and Mitsuru, W. (2002). Time-optimal control of kinematically redundant manipulators with limit heat characteristics of actuators. *Advanced Robotics.* 16(8) : 735-749.

Mann, K.H. (1962). Leeches (Hirudinea). Their structure, physiology, ecology and embryology. *Pergamon Press*. pp 1-10

Marina, K. and Hermann, S. (2002). Visual Orientation and Motion Control of MAKRO – Adaptation to Sewer Environment. *Available online at: www.ais.fraunhofer.de/projects/Makro/makro-engl/makro-e.html*

Masayuki, A., Yoshinori, T. and Hirose, S. (2008). Development of "Souryu-VI" and "Souryu-V:" Serially Connected Crawler Vehicles for in-Rubble Searching Operations. *Journal of Field Robotics*, 25: 31–65. (DOI: 10.1002/rob.20229)

Matsuura, H., Mizutame, M., Moriyama, Y., Shimada, H., Hirose, S. and Umetani, Y. (1985); Measuring/Grinding System for Water Turbine Runner, *Proceeding 2nd International Conference on Advanced Research*. pp 199-206.

Merodio, J. and Ogden, R. W. (2003). Instabilities and loss of ellipticity in fiber-reinforced compressible non-linearly elastic solids under plane deformation. *International Journal of Solids Structures*. 40: 4707–4727. (doi:10.1016/S0020-7683(03)00309-3)

Merodio, J. and Ogden, R. W. (2005). Mechanical response of fiber-reinforced incompressible non-linearly elastic solids. *International Journal of Nonlinear. Mechanics*. 40: 213–227. (doi:10.1016/j.ijnonlinmec.2004.05.003)

Meyer, J, and Guillot, A. (2008). Biologically Inspired Robots. *Handbook of Robotics - Springer (Malestrom), Edts Bruno Siciliano, Oussama Khatib*. pp 1395-1422

Meyers, J.J., O'Reilly, J.C., Monroy, J.A. and Nishikawa, K.C. (2003). Mechanism of Tongue protraction in microhylid frogs. *Journal of Experimental Biology. 207: 21-31*.

Mezoff, S., Papastathis, N., Takesian, A. and Trimmer, B.A. (2004). The Biomechanical and Neural Control of Hydrostatic Limb movement in *Manduca Sexta*. *The Journal of Experimental Biology*. 207: 3043-3053.

Miller, G. (2010). Snakerobots. *http://www.snakerobots.com.* Accessed 6pm, 06/06/2006.

Miller, K. and Arbor, A. (2008) Experimental Loading Conditions used to implement Hyperelastic and Plastic Material Models. *Available online at www.axelproducts.com.* Accessed 8.00am 06/06/2008.

Moreland, R.B., Traisch, A., Mcmillin, M.A. (1995). PGE1 suppresses the induction of collagen synthesis by transforming growth factor-B1 in human corpus cavernosum smooth muscle. *Journal of Urology*. 153: 826–834.

Mori, M. and Hirose, S. (2006). Locomotion of 3D Snake-Like Robots; Shifting and Rolling Control of Active Cord Mechanism ACM-R3. *Journal of Robotics and Mechatronics*. 18(5): 521-528.

Muller, K.J., Nicholls, J.G. and Stent, G.S. (1981). Neurobiology of the leech. *Cold Spring Harbor Laboratory: New York*.pp 1-50

Nagatani, K., Hirayama, T., Gofuku, A. and Tanaka, Y. (2002). Motion planning for mobile manipulator with keeping manipulability. *Proceedings of the IEEE/RSJ International Conference on Intelligent Robots and Systems*. pp 1663–1668.

Nagrath, I.J. and Gopal, M. (2005). Control Systems Engineering, 4th edition. *Publisher New Age International Publishers (www.newagepublishers.com).* pp 194-197.

Neustadter, D. M., Herman, R. L., Drushel, R. F., Chestek, D. W., and Chiel, H. J. (2007). The kinematics of multifunctionality: comparisons of biting and swallowing in Aplysia californica, *Journal of Experimental Biology.* 210(2): 238 - 260.

Nobuto, M., Makoto, J., Toyomi, M., Takamitsu, S., Takehiro, H., Yasuhidemorikawa, T., Soji O., Masaki K. and Kazuo, N. (2003). Development of a functional model for a master–slave combined manipulator for laparoscopic surgery. *Advanced Robotics*. 17(6) : 523-539

O'Dunlaing, C. and Yap, C.K. (1985). A "Retraction" Method for Planning the Motion of a Disc, *Algorithmica*. 6:104-111.

Ogden, R.W. (1997). Non-Linear Elastic Deformations. *Publisher: Courier Dover* pp 169-229

Ogden, R.W. (2000). Stress Softening and residual strain in the aximuthal shear of a pseudo-elastic circular cylindrical tube. *International Journal of Non- linear mechanics*. 36(3):477-487

Ogden, R.W. (2004). Mechanics of Rubberlike Solids. Xxi ICTAM, 15-21 August 2004, Warsaw, Poland. pp 1-2.

Ogden, R.W. and Roxburgh, D.G. (1999). A pseudo-elastic model for the Mullins effect in filled rubber. Proceeding of Royal Society A. 455: 2861-2877

Ohno, H. and Hirose, S. (2000). Study on Slime Robot (Proposal of Slime Robot and Design of Slim Slime Robot), *Proceeding of IROS 00 Kagawa*, pp.2218-2223.

Ohno, H. and Hirose, S. (2001). Design of Slim Slime Robot and its Gait of Locomotion, *Proceeding of IROS 01 Hawaii*.pp 1-10

Osuka, K, and Kitajima, H. (2003). "Development of Mobile Inspection Robot for Rescue Activities: MOIRA", *Proceeding. of the 2003 IEEE/RSJ Int'l Conference on Intelligent Robots and Systems, Las Vegas, Nevada*. Pp 3373-3377.

Paap, K.L., Dehlwisch, M. and Klaassen, B. (1996). "GMD-Snake: A Semi-Autonomous Snake-like Robot," *3rd International Symposium on Distributed Autonomous Robot Systems (DARS 96), RIKEN, Saitama, Japan*. pp 1-10

Paap, K.L., Dehlwisch, M. and Klaassen, B. (1997). "GMD-snake: A semi-autonomous snake-like robot". *Available online at: http://set.gmd.de/rs/snake/* Accessed August 2007.

Park, S.J., Goodman, M.B. and Pruitt, B.L. (2007). Analysis of nematode mechanics by piezoresistive displacement clamp. *PNAS*. 104 (44):1-10

Paulina, V. and Jörg, C. (2003). WormBot – A Mobile Robotic Worm. Progress Report January 2003. *Available online at: http://www.iniunizh.ch /~conradt/projects/ WormBot/*. Accessed August 2007.

Peterson, D. R. and Bronzino, J. D. (2008). Biomechanic: Priciples and Applications. *CRC Press, New York* pp 1-10.

PFA, (1994). Joint Industry Foam Standards and Guidelines, SECTION 4.0. Published by Polyurethane Foam Association: July, 1994. *Available online at http://www.pfa.org*.

Quillin, K.J. (2000) Ontogenetic scaling of burrowing forces in the earthworm lumbricus terrestris. *Journal of Experimental Biology*. 203: 2757-2770.

Reznik, D. and Lumelsky, V. (1992). Motion Planning with Uncertainty for Highly Redundant Kinematic Structures I. 'Free Snake' Motion. *IEEE/RSJ International Conference on Intelligent Robots and Systems*. pp 1-10

Richard, L. L. and Thomas, J. B. (2008). Musculoskeletal Soft Tissue Mechanics. Biomechanics: Principles and Applications. *CRC Press*. Edt: Donald R.P and Joseph D. Bronzino pp 1-13.

Robinson, G. and Davies, J.B.C. (1999) "Continuum Robots - A State of the Art," *IEEE Conference on Robotics and Automation*, pp. 2849-2854.

Robotshop Incorporation (2008). History of Robotics: Timeline. *Available online at: http://www.robotshop.com/content/PDF/timeline.pdf* Accessed August 2011.

Rooney, F.J. and Carroll, M.M. (2007). Some exact solutions for a class of compressible non-linearly elastic materials. *International Journal of Non-Linear Mechanics*, 42 (2) : 321-329. (doi:10.1016/j.ijnonlinmec.2007.01.007)

Roy, B. (2010). The theory of adhesive bonding. *Available online at http://www.roymech.co.uk/Useful_Tables/Adhesives/Adhesive_Bond.html.* Accessed August 2011.

Ryder, G.H. (1990). Strength of Materials, 3rd Edition. *ELBS McGraw-Hill*. pp 1-129, 259-286.

Seibel, E.J., Carroll, R.E., Dominitz, J.A., Johnston, R.S., Melville, C.D., Lee, C.M., Seitz, S.M. and Kimmey, M.B. (2008). Tethered capsule endoscopy, a low-cost and high-performance alternative technology for the screening of esophageal cancer and Barrett's esophagus. *IEEE Transaction on Biomedical Engineering*. 55(3):1032-42.

Sfakiotakis, M. and Tsakiris, D.P. (2006). SIMUUN: A simulation environment for undulatory locomotion. *International Journal of Modelling and Simulation*, Vol. 26 (2006), pp. 350-358.

Shammas, E., Wolf, A., Brown, H. B., and Choset, H. (2003). New Joint Design for Three-dimensional Hyper Redundant Robots. *Proceedings of the 2005 IEEE International Conference on Robotics and Automation, Las Vegas, Nevada*, October 2003. pp 1-10.

Shigeo, H., Koji, I., Yoji, U. (1989). Development of Shape-Memory Alloy Actuators. Performance Assessment and Introduction of a New Composing Approach, *Advanced Robotics*. 3(1): 3-16.

Skierczynski, B.A., Wilson, R.J.A., Kristian, W.B. Jr and Skalak, R. (1996). A model of the Hydrostatic Skeleton of the Leech. *Journal of Theoretical Biology* 181: 329-342.

Sokoloff, A. J. (2004). Activity of tongue muscles during respiration: it takes a village? *Journal Applied Physiology* 96:438-439. doi:10.1152/japplphysiol.01079.2003

Srinivasan, M. V. (1992). Distance Perception in Insects. Centre for Visual Sciences, Research School of Biological Sciences, *Australian National University, Australia. Published by Cambridge University Press*. pp 1-10.

Srinivasan, M.V., Zhang, S.W., Chahl, J. S., Stange, G. and Garratt, M. (2004). An overview of insect-inspired guidance for application in ground and airborne platforms. Proc. Instn mech Engrs Vol 218 Part G: *Journal of Aerospace Engineering*, 375-388

Stern, T.W., Nusbaum, M.P., Perez, L.E. and Kristan, W.B. (1986). A kinematic study of crawling behavior in the leech, Hirudo medicinalis. *Journal of Comparative Physiolology*. A158: 593-603.

Stevenson, R.D. and Josephson, R.K. (1990). Effect of Operating Frequency and Temperature on Mechanical Power Output from Moth Flight-Muscle. *Journal of Experimental Biology*. 149: 61-78.

Streitlien, K., Triantafyllou, G. S., and Triantafyllou, M. S. (1996). "Efficient foil propulsion through vortex control," *AIAA Journal*. 34: 2315–2319.

Takanashi, N., Choset, H. and Burdick, J.W. (1993). Local Sensor based Planning for Hyper-Redundant Manipulator. *Proceeding of IEEE International Conference on Intelligent Robots and Systems*. July 1993. Pp 1-10

Thomas, H., John, W., Julian, V. (2005).Biologically inspired solutions to colonic endoscope propulsion *Available online at: http://biro-net.aber.ac.uk/Symposium_2005/BIRO%20Proceedings/posters/Poster_bioloch2005.pdf*

Trimmer, B.A., Takesian, A.E., Sweet, B.M., Rogers, C.B., Hake, D.C. and Rogers, D.J. (2006). Caterpillar Locomotion and Burrowing Robots. *7th International Symposium on Technology and Mine Problem, Monterey*, CA. pp 1-10

Wadepuhl, M. and Beyn, W.J. (1989). Computer simulation of the hydrostatic skeleton. The physical equivalent, mathematics and application to worm like forms. *Journal of Theoretical Biology* 136: 379-402.

Wadepuhl, M., Beyn, W.J. and Alscher, C. (1997). Stepwise adaptation of a computer model to the leech Hirudo medicinalis L. II. Effects of geometry, compartmentalization and nonlinear length tension curves. *Preprint, University of Bielefeld*. Pp 1-100

Wainwright, P.C. and Bennett, A.F. (1992). The Mechanism of tongue projection in Chameleons. *Journal of Experimental Biology* 168: 1-21.

Wilbur, C., Vorus, W., Cao, Y., and Currie, S. (2002) A Lamprey-Based Undulatory Vehicle. *Neurotechnology for Biomimetic Robots, Edts: J. Ayers, J. Davis and A. Rudolph. MIT Press*, pp 285-296.

William, C. (2006). Snake-Like Robot Can Crawl on Land or Swim. *Available online at http://www.gorobotics.net/The-News/Latest-News/Snake%11Like-Snake-Like-Robot-Can-Crawl-on-Land-or-Swim/*

Wilson, R.J.A., Skierczynski, B.A., Blackwood, S., Skalak, R. and Kristan, W.B. (1996). Mapping motor neuron activity to overt behaviour in the leech: Passive biomechanical properties of the body wall. *Journal of Comparative Physiolology*. 178:637-654.

Witbrock, M., Matuszek, C., Brusseau, A., Kahlert, R.C., Fraser, C.B., Lenat, D.B. (2005). Knowledge Begets Knowledge: Steps towards Assisted Knowledge Acquisition in Cyc in Papers. *2005 AAAI Spring Symposium on Knowledge Collection from Volunteer Contributors (KCVC), Stanford, California*, March 2005. pp. 99-105

Wolf, A., Brown, H.B., Casciola, R., Costa, A., Schwerin, M., Shamas, E. and Choset, H. (2003). *Proceedings of the 2003 IEEE/RSJ International Conference on Intelligent Robots and Systems, Las Vegas, Nevada*, October 2003. pp 1-10

Wolf, A., Choset, H. H., Brown, H. B., and Casciola, R. W. (2005). Design and control of a mobile hyper-redundant urban search and rescue robot. *Advanced Robotics*. 19(3): 221-248.

Woods, W.A. Jr, Fusillo, S.J. and Trimmer, B.A. (2008). Dynamic properties of a Locomotory muscle of the tobacco hornworm Manduca Sexta during strain cycling and Simulated natural crawling. *The Journal of Experimental Biology* 211:873-882.

Yamada, H., Chigisaki, S., Mori, M., Takita, K., Ogami, K. and Hirose, S. (2005). Development of Amphibious Snake-like Robot ACM-R5, *ISR2005, Proceeding ISR* 2005, pp. 133,2005.

Yamada, H. and Hirose, S. (2006). Development of Practical 3-Dimentinal Active Cord Mechanism ACM-R4. *Journal of Robotics and Mechatronics*, 18(3): 305-311.

Yekutieli, Y., Sagiv-Zohar, R., Hahner, B. and Flash, T. (2005a). Dynamic Model of the Octopus Arm II. Control of Reaching Movements. *Journal of Neurophysiology* 94: 1459 -1468.

Yekutieli, Y., Sagiv-Zohar, R., Aharonov, R., Engel, Y., Hochner, B. and Flash, T. (2005b). Dynamic Model of the Octopus Arm I. Biomechanics of the Octopus Reaching Movement. *Journal of Neurophysiology* 94:1443-1458.

Yekutieli, Y., Sagiv-Zohar, R., Hahner, B. and Flash, T. (2005c). Analyzing octopus movements using three-dimensional reconstruction. *Journal of Neurophysiology* 98: 1775-1790.

Yekutieli, Y., Sumbre, G., Flash, T. and Hochner, B. (2002). How to move with no rigid skeleton? The Octopus has the answers. *Biologist* 49(6): 1-10

Yim, M. (1994). Locomotion with a Unit Modular Reconfigurable Robot. *Department of Mechanical Engineering . Palo Alto: Stanford University*. Pp 1-20

Yu, J.Z., Chen, E.K., Wang, S. and Tan, M. (2002). "Research Evolution and Analysis of Biomimetic Robot Fish". *Control Theory and Application*. 20(4):1-10 (DOI:cnki:ISSN:1000-8152.0.2003-04-000)

Zhang, Y., Schervish, M. and Choset, H. (2002). Probabilistic Hierarchical Spatial Model for Mine Locations and its Application in Robotic Landmine Search. *Proceedings of the 2002 IEEE/RSJ Conference on Intelligent Robots and Systems. EPFL, Lausanne, Switzerland.* October 2002. Pp 1-10

Zufferey, J. and Floreano, D. (2005). Toward 30-gram Autonomous Indoor Aircraft: Vision-based Obstacle Avoidance and Altitude Control. *Proceedings of the 2005 IEEE International Conference on Robotics & Automation Barcelona, Spain* April pp 18-22.

APPENDIX A

HYDROSTATIC JOINTS

A1 OTHER RUBBER BASED HYDROSTATIC JOINTS DESIGNS

The following rubber based design can be exploited also for making artificial hydrostatic joints

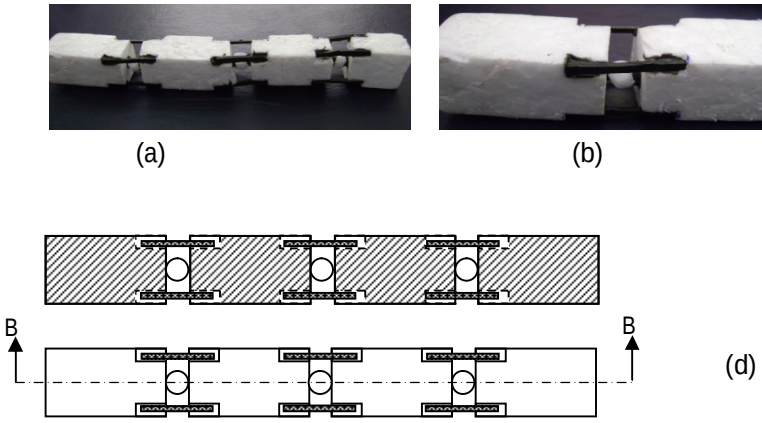


Figure A1 a) Ball-Socket-Tendon Design b) Closer View c) Another Closer view d) Cross-section of the model

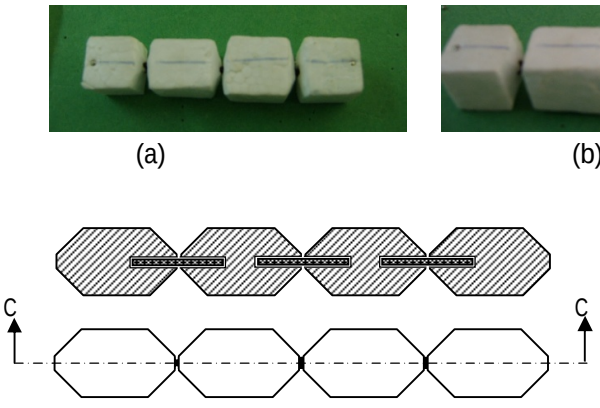
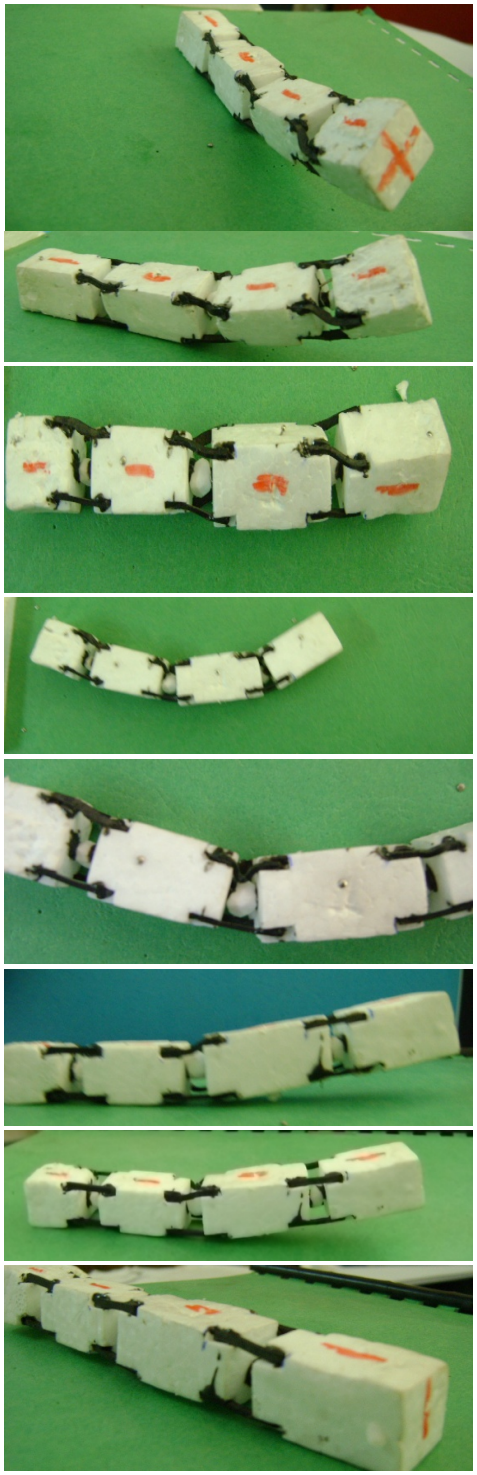


Figure A2 Spinal-Chord / Bead Model a) Top View b) Perspective view b) Cross-section of the model



The Ball-Socket-Tendon Design is even more rigid than the Diamond design. It excels it also at twisting, complexity and biomimicry. Hydrostatic bodies are known for their great flexibility and strong rigidity at load bearing.

Figure A3 Ball-Socket-Tendon Design Kinematics



Spinal-Chord/Bead Model has greater flexibility and rigidity in its implementation. As shown in the last diagram (on the right) twisting while remaining planar is even more easier.

Figure A4 Spinal-Chord/Bead Model Kinematics

A2 POSSIBLE APPLICATION AREAS OF ARTIFICIAL HYDROSTATIC JOINTS

There are several possible areas where the artificial hydrostatic joint designed can be used, they are;

1. Military – as tree climber or observation post
2. Under water robots - robotic fish
3. Snake / serpentine robot
4. Minimally invasive surgery
5. Space exploration
6. Stealth devices
7. Manufacturing arm over short distances

A2.1 Military – application as tree climber or observation post

Depicted in figure A5 is a possible use of the artificial hydrostatic joint as an observation post for military purposes. The artificial hydrostatic joint is flexible enough to be folded and carried about for deployment wherever needed and a rubber cover will enhance gripping of the structure being climbed. The artificial hydrostatic joint will have to support 3D motion to achieve this.

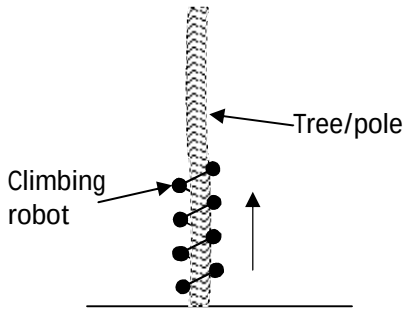


Figure A5 Tree climbing robot

A2.2 Under water robots

Rubber does not soak water and does not react with it, it can withstand saline environments also. Under water robots like a fish robot (figure A6) can use the artificial hydrostatic joint for its flexible tail without the need to ever worry about maintenance. Submarine and ship hauls are commonly coated with rubber, vehicles in salt laden environments like Lagos in Nigeria are commonly coated with rubber spray underneath.

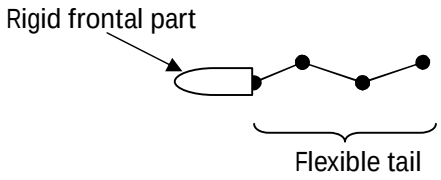


Figure A6 Underwater devices in form of fish

A2.3 Snake robot

The artificial hydrostatic joint can be used to build a 3D device that has a rod shape and is programmed to behave and move as a snake or serpentine robot – figure A7. Furthermore, covering the structure with rubber will give a firm grasp of different terrain.

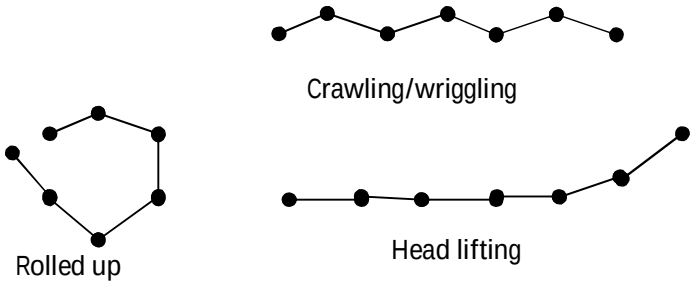


Figure A7 Snake/serpentine robot can be assembled from the artificial hydrostatic joint

A2.4 Minimally invasive surgery

Minimally invasive surgery (MIS) or band aid surgery or keyhole surgery is a modern surgical technique in which operations especially in the abdomen are performed through small incisions (usually 0.5-1.5cm) as compared to larger incisions needed in traditional surgical procedures. Minimally invasive surgery depends heavily on one or more form of endoscopy. Since its inception in design, it has gone in sophistication from rigid lens system and later fibre optic light guide to robotic guided flexible arms, to hyper-redundant robotic based arm currently. Precision in locating the diseased part (i.e. access port location) brings about true minimally invasive surgery in the form of tethered capsule endoscope and wireless capsule endoscope especially in the digestive tract- Degani et al, 2006; Seibel et al, 2008.

The fact that the artificial hydrostatic joint presented in this work can be miniaturized means that a rod shaped, cable controlled or active on board actuator as described by Afolayan and Madakson (2009) can make it very useful for this type of surgical operation. Also, a medical grade rubber or silicone will have less impact (bruising and laceration) on the internal organs. The model shown in figure A8 has onboard space to carry miniature loads like camera, battery, controller and drug to the operation site. It can be self propelling with actuators attached.

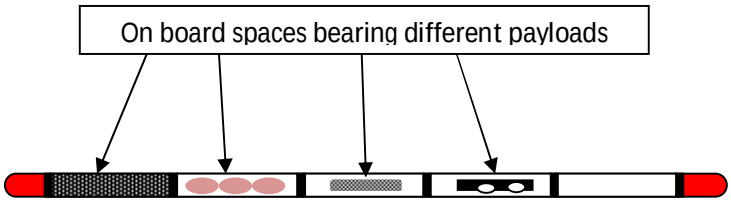


Figure A8 A rod-shaped endoscope with sections bearing different payloads (equipment). It can be self propelling if actuators are attached.

A2.5 Space exploration

Following the foot print of the NASA snakebot, the artificial hydrostatic joint can be used to make large numbers of crawling robots that can be deployed over large areas. Beside this, it can access crevices and terrains larger robots will not be able to access.

A2.6 Stealth devices

A stealth device can be made to look like a harmless rod that can move about on its own like a snake robot. It can also be deployed inside water and remain there while giving feedback of the information captured.

A2.7 Manufacturing arm over short distance

If one of its end is fixed, it can be made to follow a convoluted path to reach a component for repair or adjustment or for inspection – figure A9.

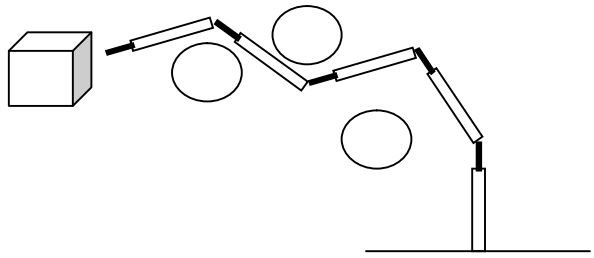


Figure A9 A short and sturdy design can be used as manufacturing arm

APPENDIX B

TRANSLATING THE LIFE MACKEREL MODEL TO A CAD MODEL

1. A lateral and dorsal picture of the live fish (figure B1) was taken using Sony Cyber-shot digital camera (model DSC-S730) at a resolution of 3 megapixels, F-stop of f/2.8, exposure time of 1/40sec, ISO speed of 100 and JPEG compression mode.

2. The 1:1 scale image (lateral and dorsal view) of the fish was projected on a cardboard, figure B2 (A,B,C) and manually traced.

3. This cardboard picture is then used to create the CAD geometry (figure B3).

4. Furthermore, all the dimensional constraints such as quarter pulley heights and width were taken from it. As an example the rings major and minor axes used for the haul and tail was taken as shown in figure B4.



Lateral view



Dorsal view

Figure B1 The Lateral and dorsal view of the life Mackerel used in the modeling

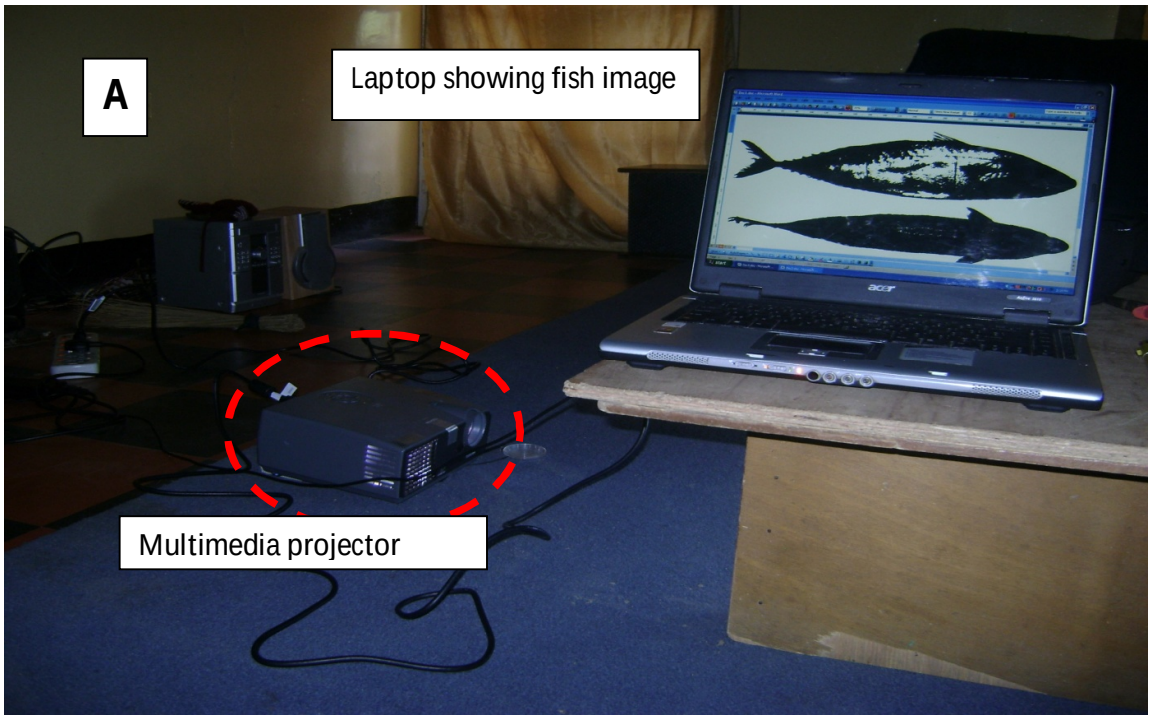


Figure B2a Projecting the mackerel image on a board and tracing it out (scale 1:1)

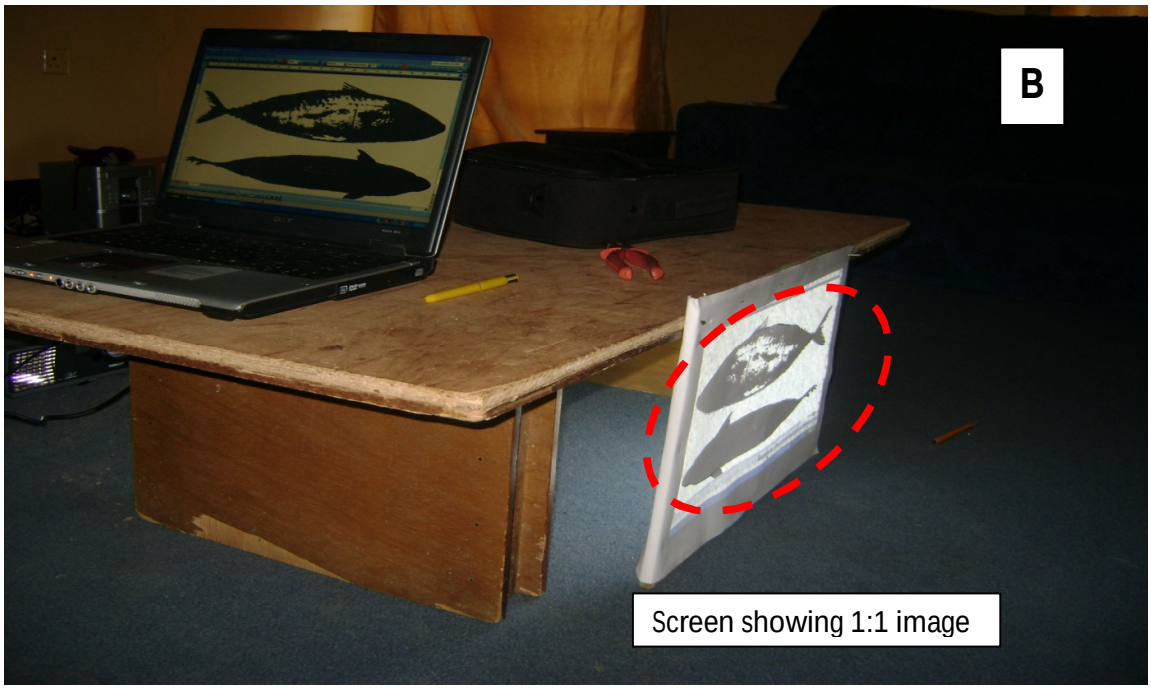


Figure B2b Projecting the mackerel image on a board and tracing it out (scale 1:1)

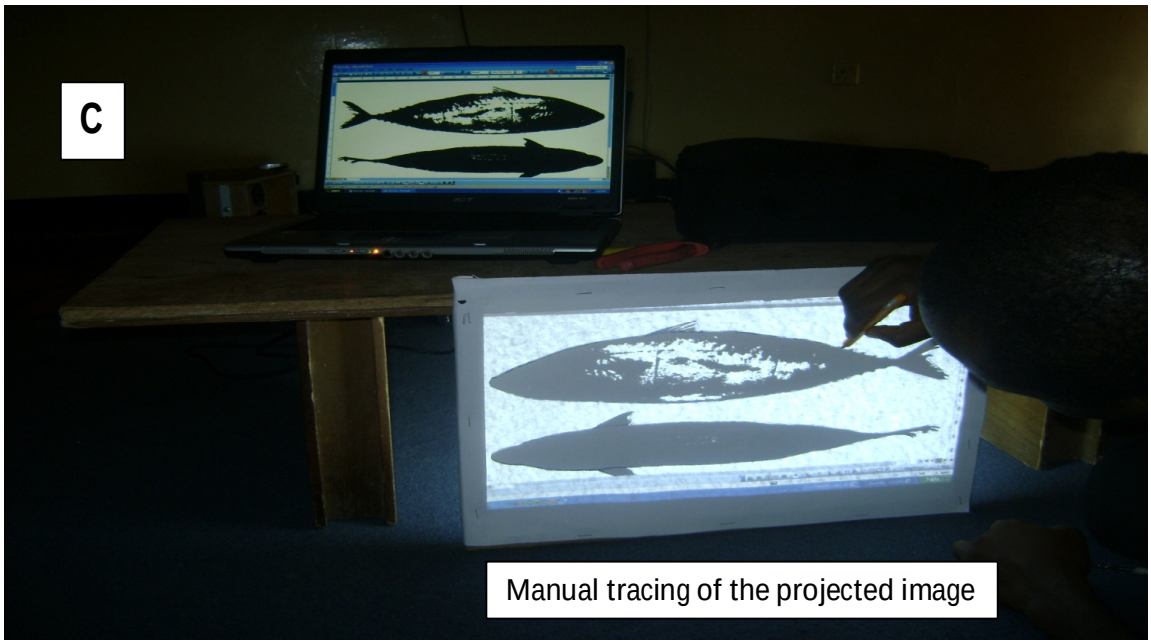


Figure B2c Projecting the mackerel image on a board and tracing it out at scale 1:1 - continuation

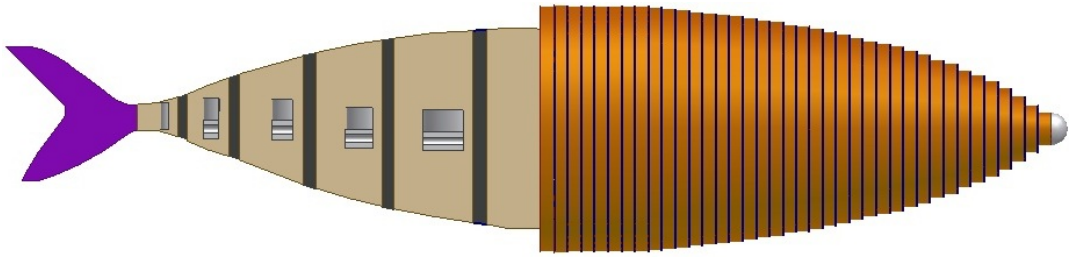


Figure B3 CAD model of the live fish after copying it – here the tail has not being covered. The life fish lateral view is displayed again as a show of the precision of the translation process

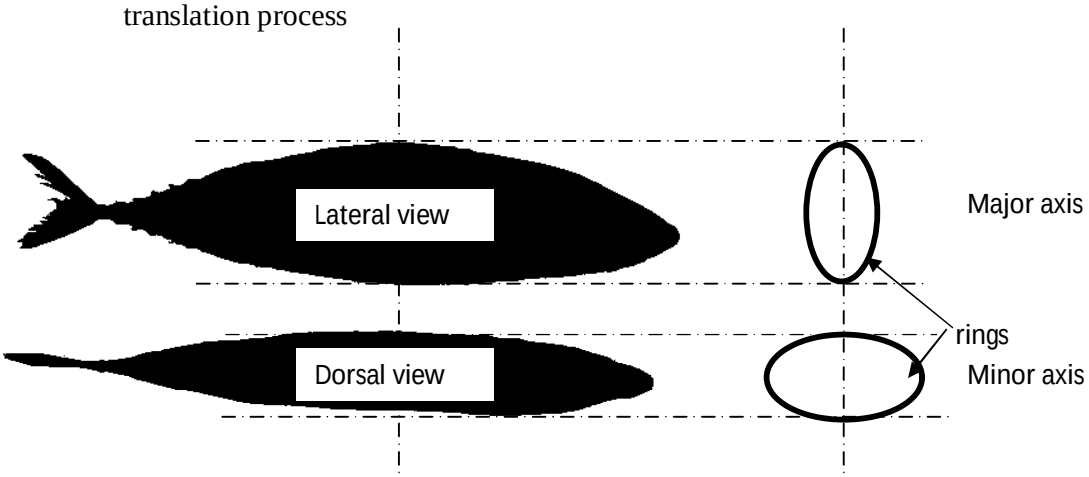


Figure B4 The dimensions of the rings used for the haul.

APPENDIX C

THE FREQUENCY LOSS PATTERN MACHINE

C1 DESCRIPTION

The test equipment was designed to test rubber in the cantilever mode. Figure C1 shows the equipment consisting of data logger, linear motor driver, test board and precision signal generator.

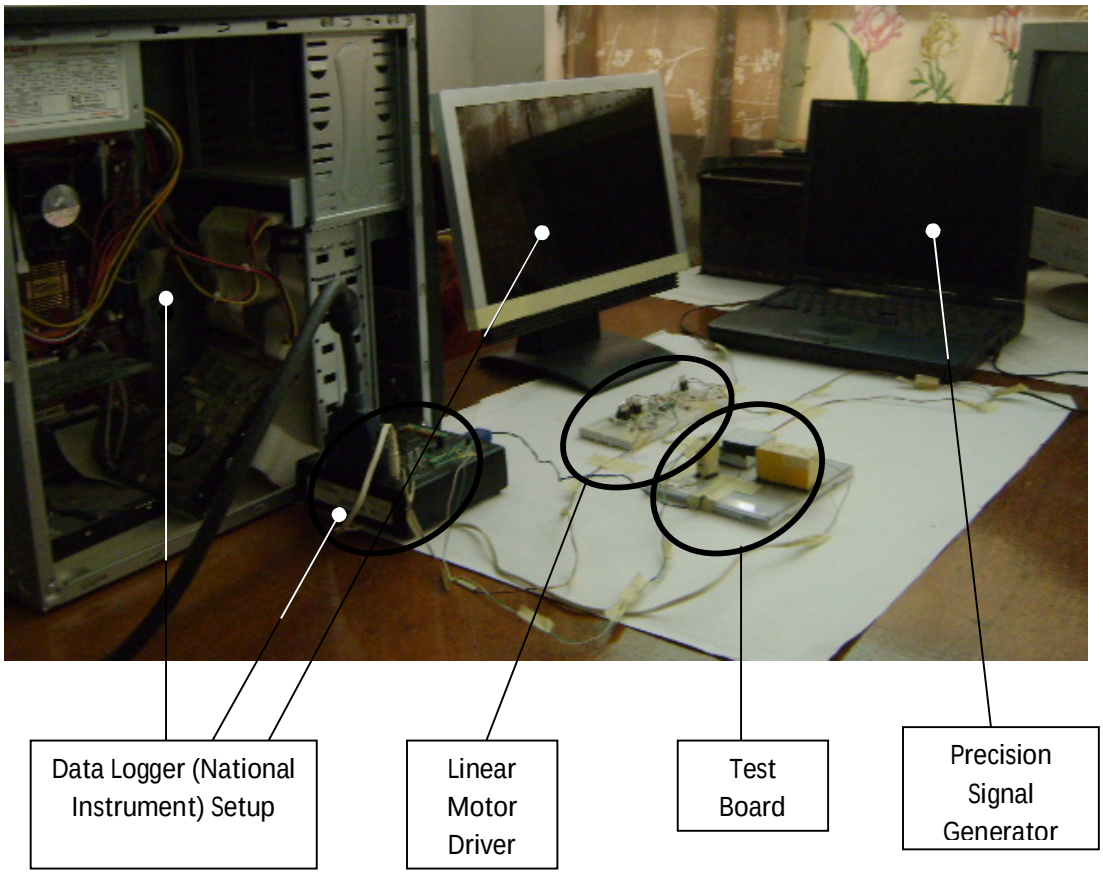


Figure C1 The Frequency Loss Determination Equipment

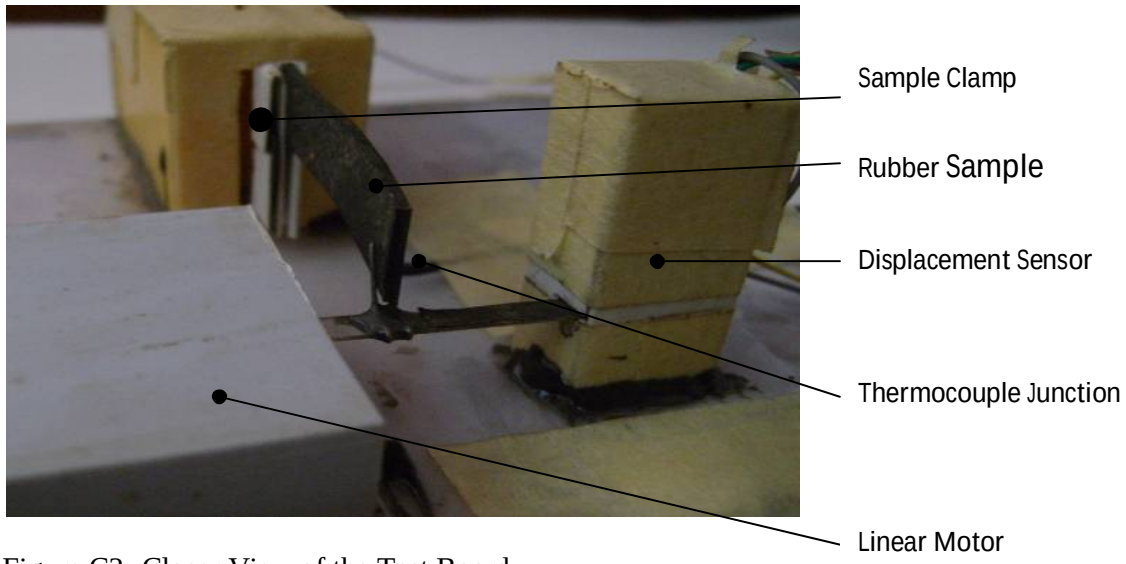


Figure C2- Closer View of the Test Board

The test board (figure C2) consists of a linear motor, displacement sensor, thermocouple junction, and load sensor. The motor driver electronics is on a separate board. The sample is held in place by the clamp while the linear motor oscillates at a frequency determined by the pulse rate from a power amplifier connected to the computerized signal generator. The plastic strip holding the rubber sample is not transparent in some part (about two thirds) so that when it moves in and out, it activates the photocell and makes it to generate an on-off signal. The signal accessory (figure C3) captures all the voltage levels from the signal generator, linear motor, photocell, thermocouple junction nearby and even the sample holder (that has built in piezo sensor). The really critical signal is outlined in figure C4. The delay in signal is a function of the property of the rubber and the frequency of the oscillation. The amplitude of the signals are not so relevant but the timing.

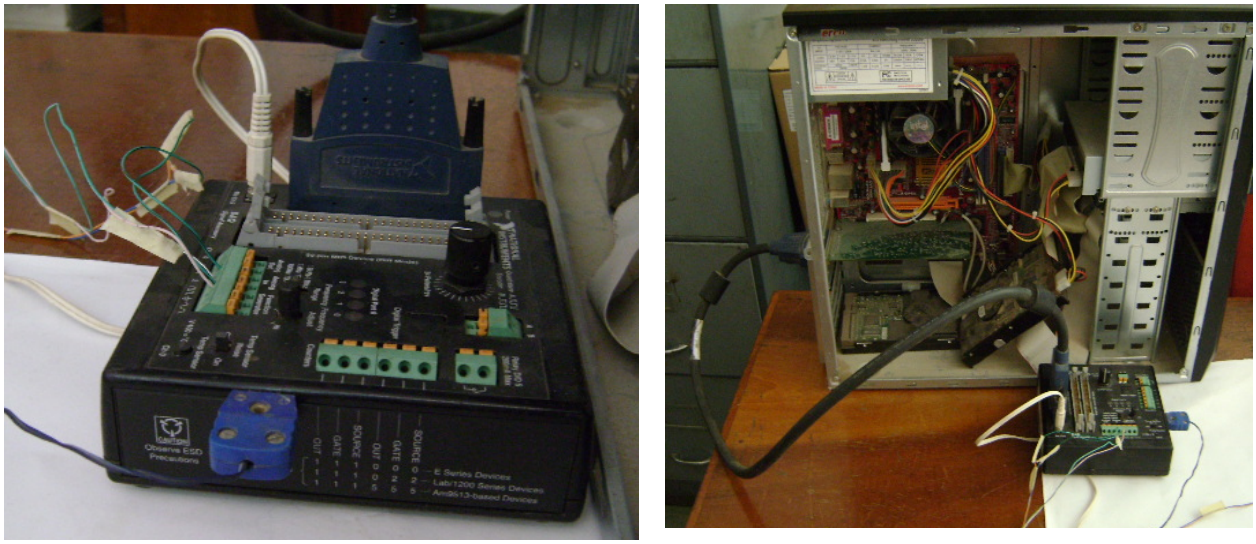


Figure C3 The DAQ Signal Accessories (Left) Showing its interfacing to a computer (Right)

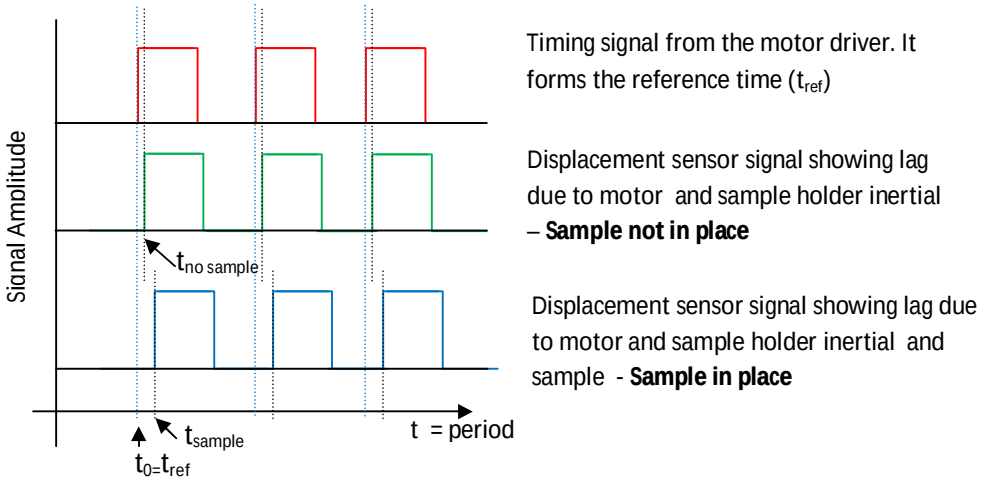


Figure C4 Signal pattern showing presence and absence of sample rubber. The delay is increased when sample is in place. The absolute value of this delay is obtained from $t_{sample} - t_{no\ sample} - t_{ref}$

C1.1 Design of the linear motor

The linear motor provides the motive force for the oscillatory motion. Figure C5 and C6 show the assembly drawing of the motor and the semi darkened polystyrene plastic stripe which it used for holding the sample and modulating the photocell.

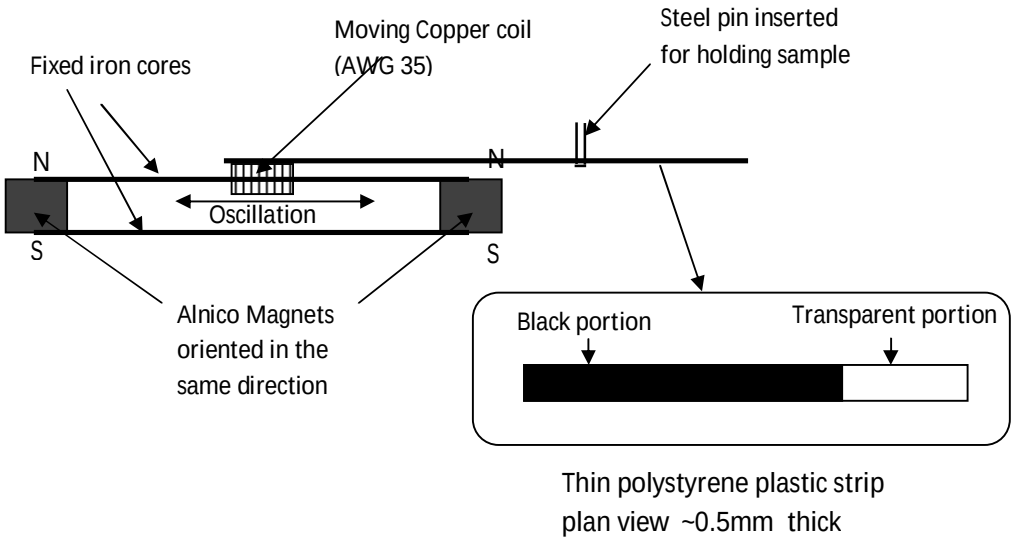


Figure C5 Linear motor design and its component

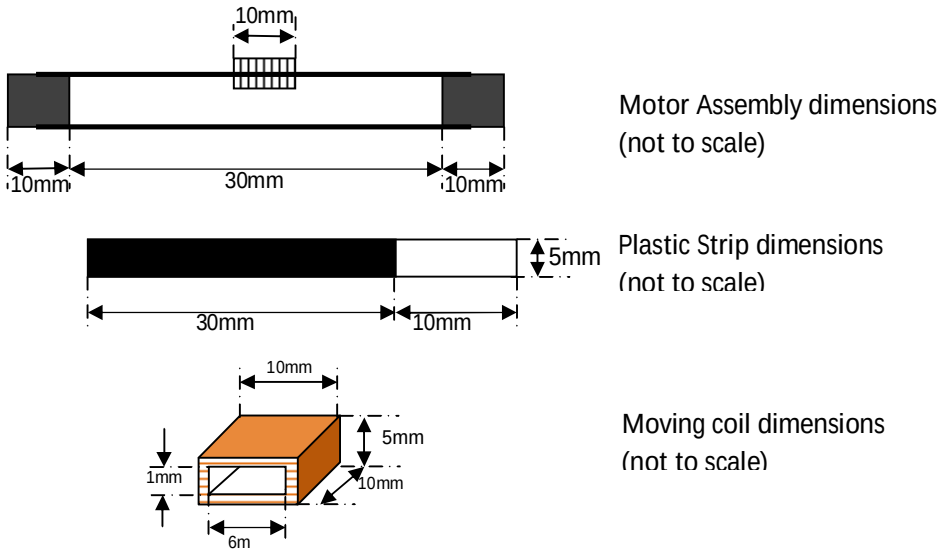


Figure C6 Linear motor components dimensions.

This design approach greatly reduces inertial by using light weight materials – copper coil without iron core (~43.0mg) and polystyrene plastic (~1.0mg). It was tested and found to be capable of oscillation greater than 50Hz – figures C7-C11 show the motor head inertia at frequencies 0.5,1.0, 10, 15 and 25Hz.

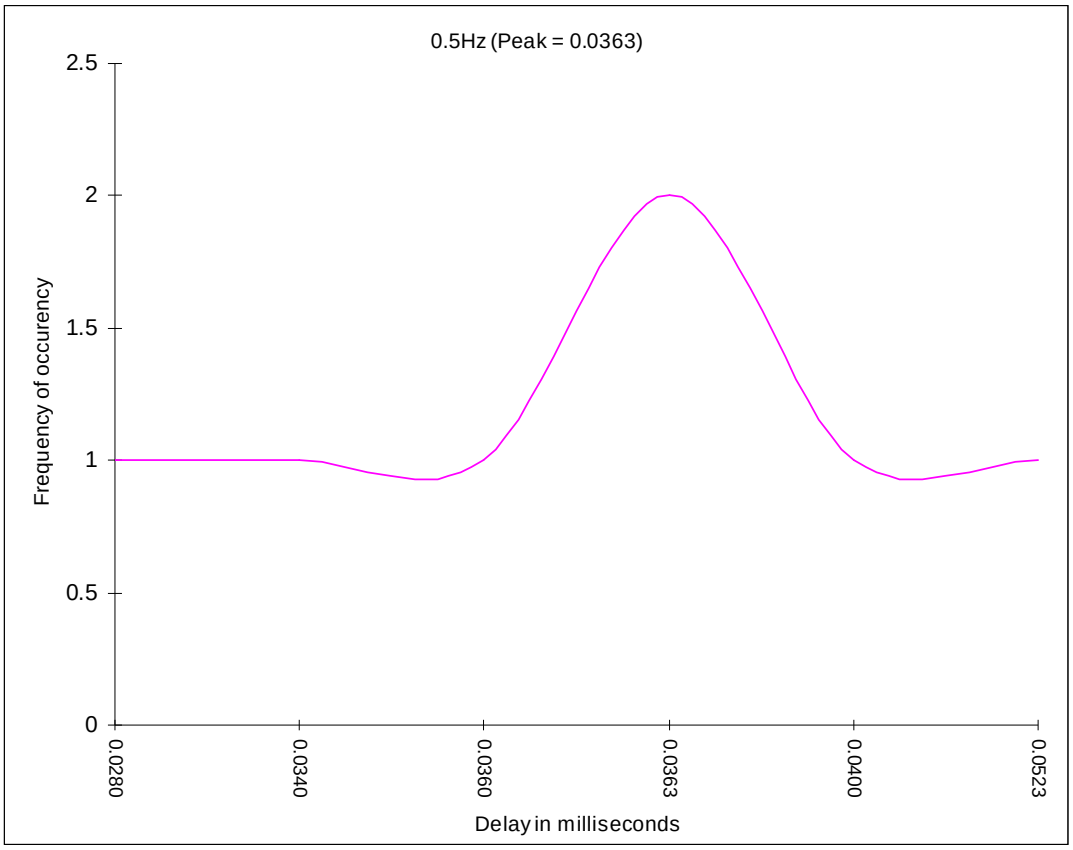


Figure C7 Expanded view for header inertia at 0.5Hz

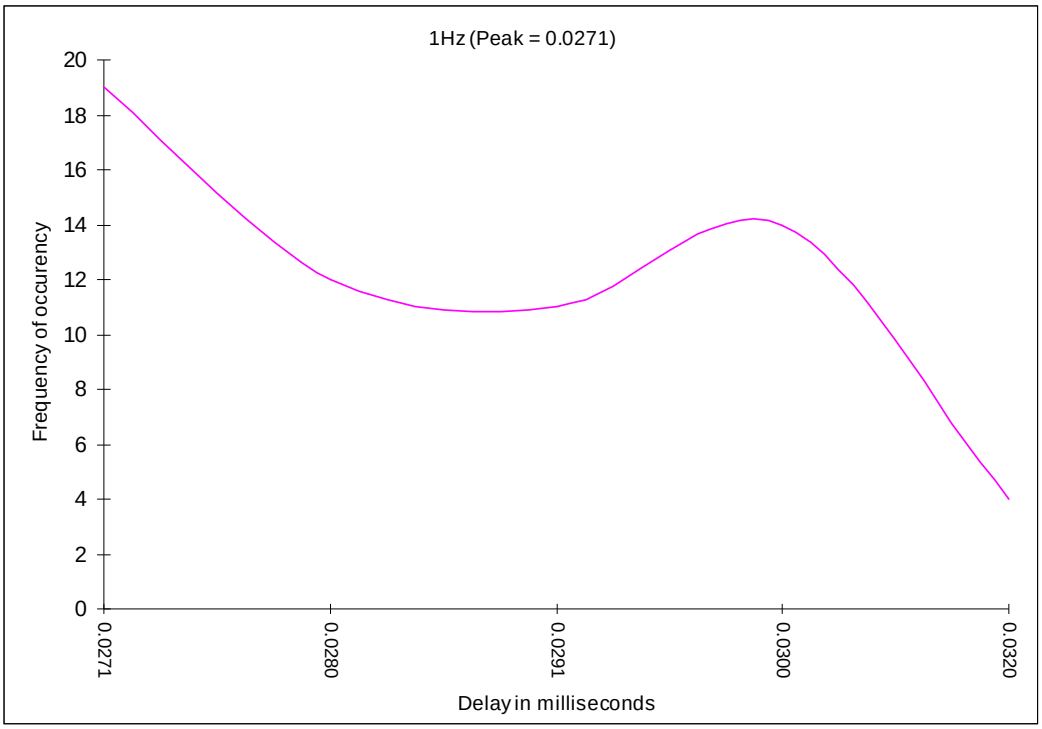


Figure C8 Expanded view for header inertia at 1Hz

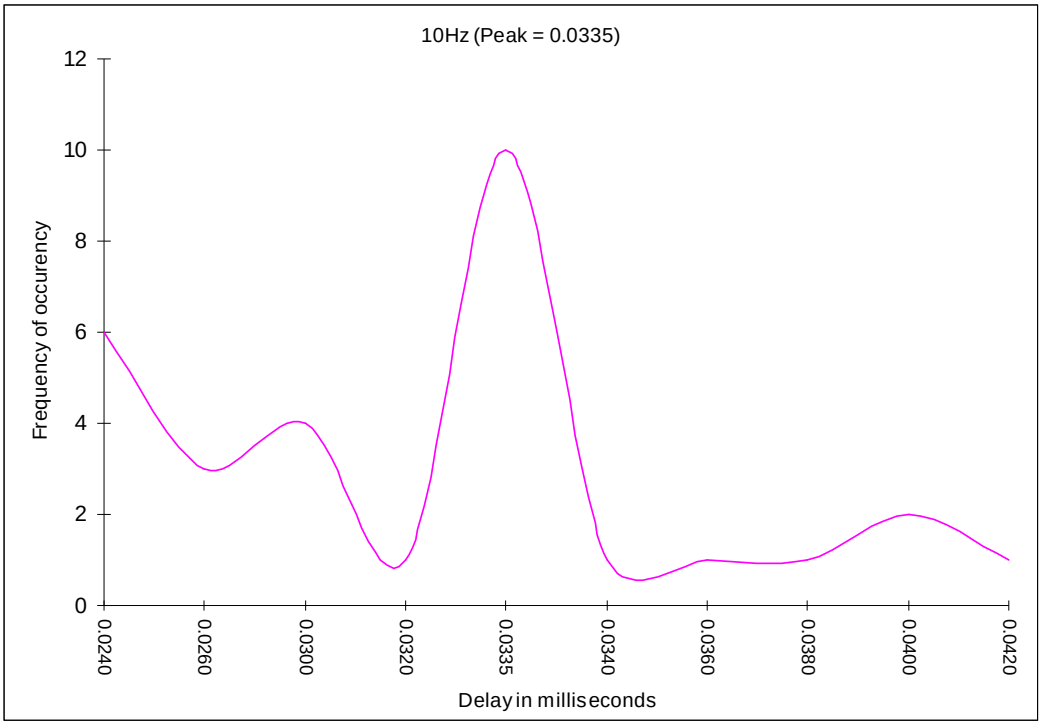


Figure C9 Expanded view for header inertia at 10Hz

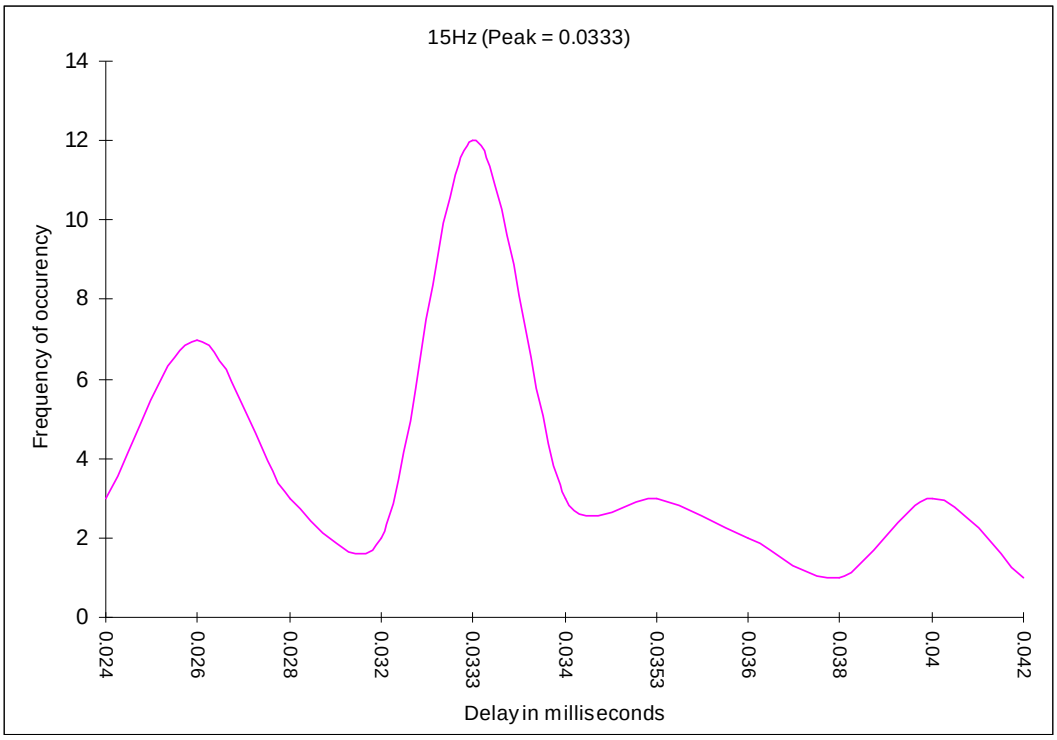


Figure C10 Expanded view for header inertia at 15Hz

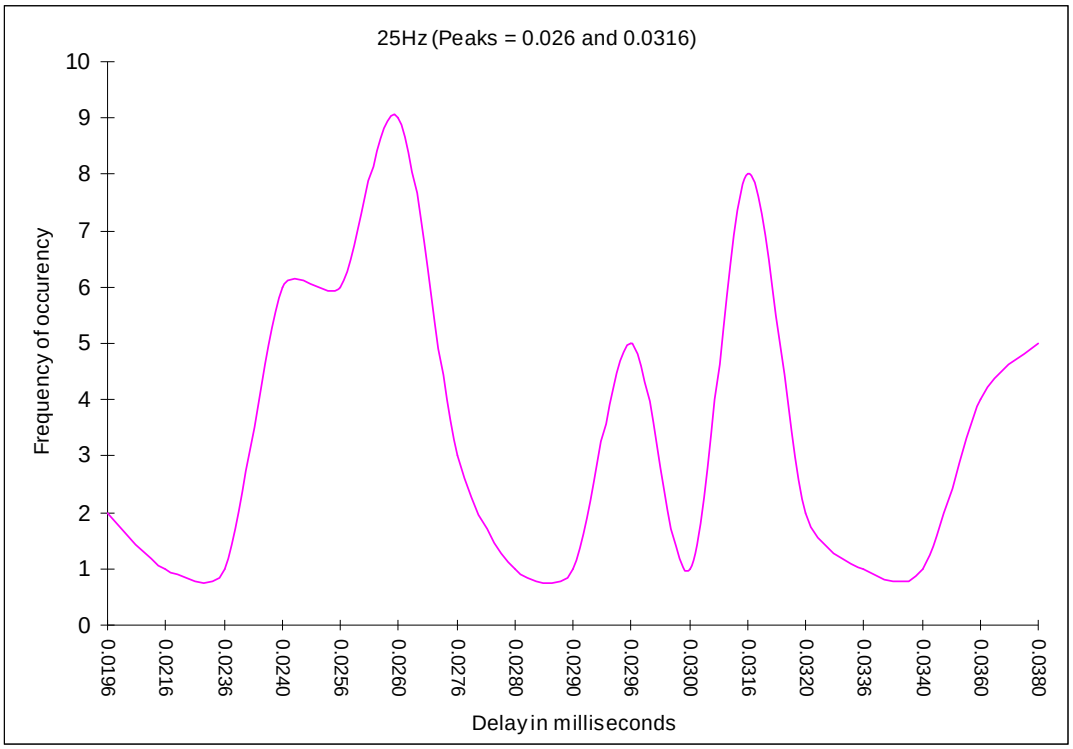


Figure C11 Expanded view for header inertia at 25Hz

Its speed is precisely controlled by the computerized motor driver. The motor driver interfaces with the Spectral Plus 5.0 software that generates the timing signal. The motor driver (figure C12) is controlled by pulses from the computer sound card line out port which it converts to an alternating square wave signal using 4027 J-K flip flop bistable multivibrator. The 4027 bistable multivibrator drives a power transistor bridge to which the motor coil is connected. The square wave signal has 50% duty cycle.

Although the signal input to the motor (and hence the rubber sample) is a square wave, the actual influence on the sample is rather like a shock load or technically an impulsive loading. This is more so for the fact that the rubber response is much slower than the slew rate of the motor <20ms and the period of measurement is also

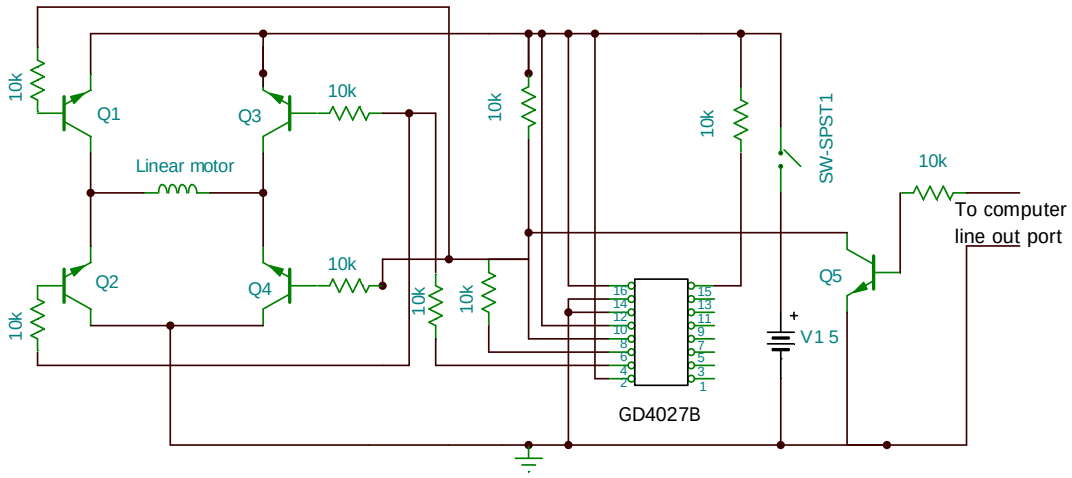


Figure C12 Circuit diagram of the motor driver

very short (the time it takes for the photocell to signal block its light path). Also if the rubber sample is approximated by a linearly damped-mass-spring body (voigt body), the impulsive input implies that its response will give its dynamic characteristic (Katsuihiko, 2005; Nagrath and Gopal, 2005). For linear-time-invariant system (for which it is an approximation in this scenario), the impulsive response is given by

$$C(s)=G(s)R(s)=G(s)$$

where $L\ \delta(t)=1=R(s)$ and transfer function = $C(s)/R(s)=G(s)$,

therefore $c(t) = L^{-1}G(s)=g(t)$

and using convolution integral;

$$c(t) = \int_0^t g(t-\tau)r(\tau)d\tau$$

the system's response can be found to any input (Katsuihiko, 2005; Nagrath and Gopal, 2005). Summarily, driving the sample with a square wave signal allows the rubber to give realistic response that is a function of its nature.

C1.2 Design of the displacement sensor

This uses a photocell (figure C13) to measure the reaction time of the sample, header and the motor. The reaction time measured is rather relative – that is, it sends signal to the data logger as soon as its light path is blocked without recourse to how long the motion was started. This design is used instead of absolute reaction time to reduce measurement error. The plastic strip has to travel the same distance for it to block the light. The time the signal generator sends its signal and the time the photocell sends its signal are functions of the sample (rubber) stiffness, the stiffer the rubber, the longer the lagging of the photocell signal behind the motor signal (t_{ref} of figure C4). The accuracy of the measurement is thus left to the National Instrument PCI data logger built in timing facilities (which is already factory calibrated).

C1.3 Temperature monitoring using thermocouple junction

A nichrome-constantan thermocouple junction is placed near the sample (within 1cm) so as

to measure the environmental temperature while the experiment is going on. The National Instrument Data Signal Accessories used in this experiment provides a built-in cold junction and all the necessary compensation required. The sample was temperature stabilized using fan before each experiment.

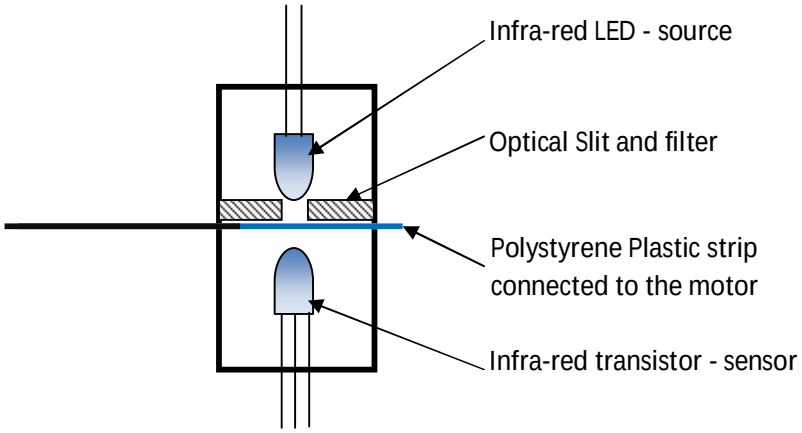


Figure C13 Internal design of the displacement sensor

C1.4 The sample clamp

This has a built in force sensor using a piezoelectric plate for its transducer. The clamp was not designed to measure the absolute force (as a function of the sample stiffness) and was not calibrated. Its function is to act as a double check on the photocell reaction response in case it misses any data point for whatever reason. It might be possible to deduce parameters like shear complex, phi or loss angle of the sample if calibrated.

C1.5 Computerized Signal Generator

The signal generator uses Spectral Plus 5.0 software (figure C14 is the interface) for its precision signal source. It is hosted on Dell Latitude CPt S500GT laptop with these specifications: BIOS – Phoenix ROM BIOS PLUS Version 1.10 A05, OS - Microsoft XP Professional Version 2002 with service pack 2, DirectX Version 9.0c, RAM – 192MB,

Microprocessor – Intel Celeron 498MHz, Display Resolution (used) – 1024 X 768 (32bit),Sound Card ESS Maestro 3PCI, Sound Driver es198x.sys

The signal generator output is via the line out port which is then amplified using a power amplifier to drive the linear motor. The signal pattern is pulsed with a fixed width of 0.2 ms (200μs) for all the frequencies used for the experiment.

C1.6 Data Logger and Signal Accessories

The National Instrument VI logger (figure C4 and C15) was hosted on Mercury Model P25G System with the following specification: BIOS – American Megatrends Inc 080012, 12/28/2005, OS - Microsoft XP Professional Version 2002 with service pack 2, DirectX Version 8.1, RAM – 256MB, Microprocessor – Intel Pentium 4 1.80GHz, Display Resolution (used) – 1280 X 1024 (32bit). The data logger has capability to export the data in different file format for further processing on different software. CSV format was used in this project and further data mining was done using MS Excel® 2003.

C2 HOW TO USE THE MACHINE

C2.1 Sample preparations and mounting on the machine

A rubber sample is cut into strips of 20mm x 10mm. The rubber samples are then preconditioned by bending them (+/-45^{o}) and extending to 200% and relaxing them 30 times. Furthermore, they are to be allowed to stabilize geometrically and thermally before proceeding with the test by leaving them in a temperature stabilized environment at which the test will be performed.

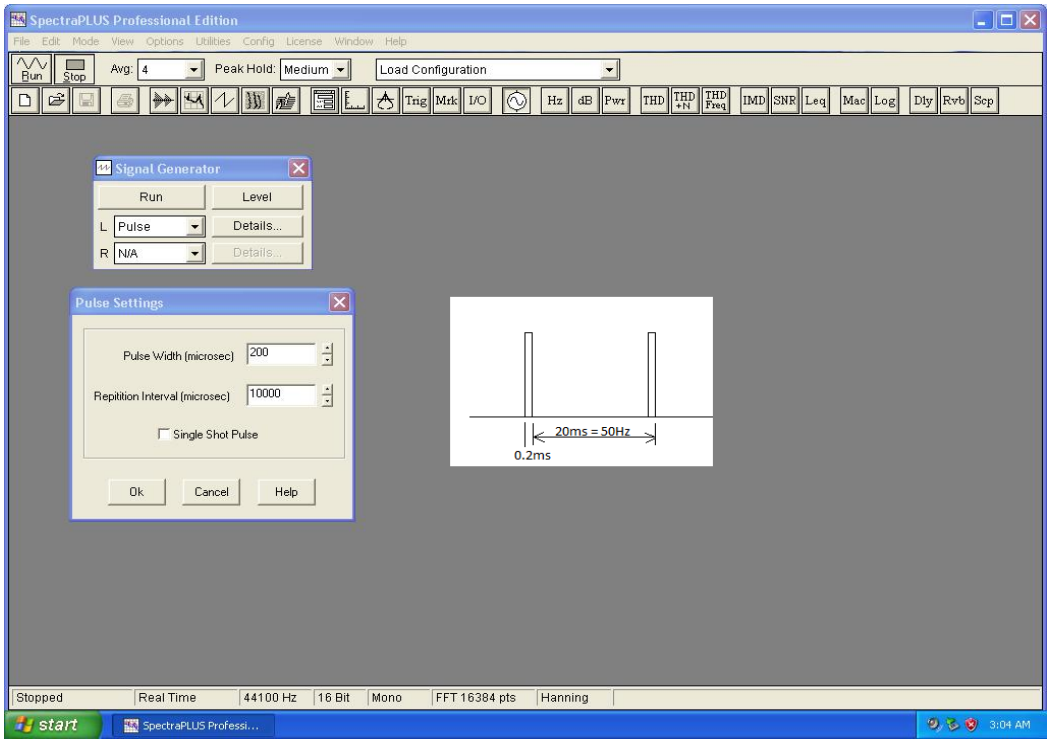


Figure C14 - The Spectral Plus 5.0 Signal Generator software interface showing the dialog boxes for the signal frequency and type setting. Inset is the timing for the selected setting.

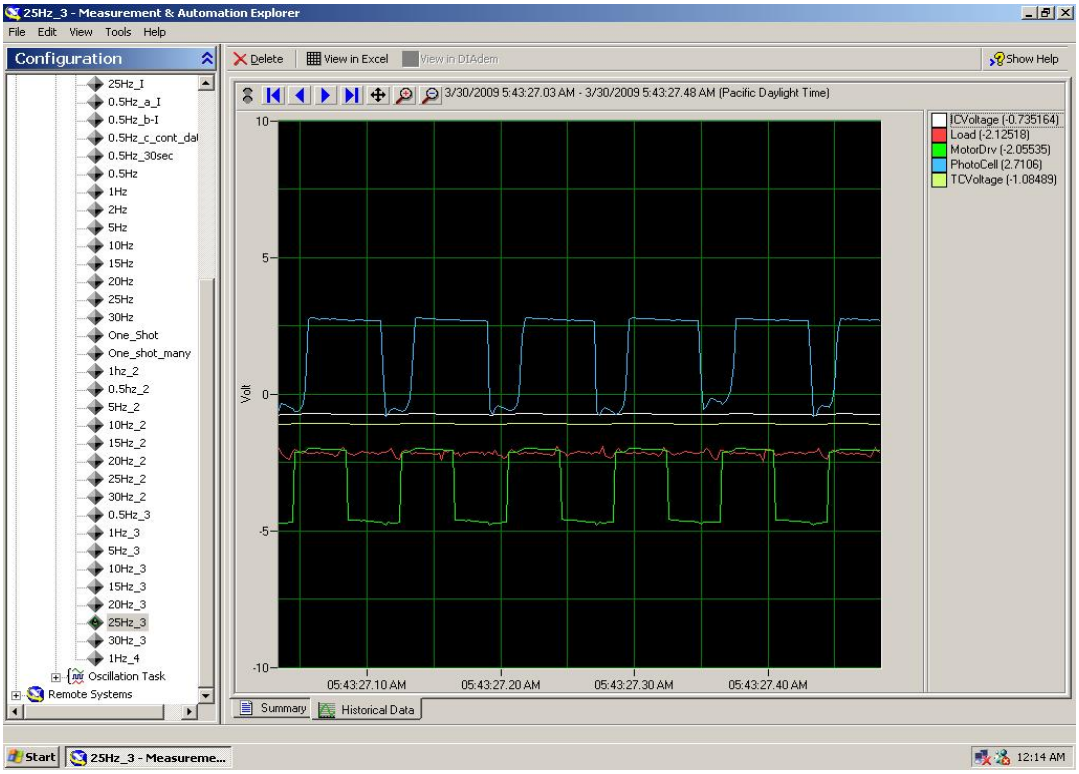


Figure C15 - National Instrument VI Logger interface – showing result at 25Hz input frequency

C2.2 Performing the test

1. The National Instrument VI Logger interface is started up and allowed to warm up for minimum of 30min as recommended by the manufacturer. This is to allow the data capture card to stabilize also thermally.
2. A sample is then mounted in the sample holder and the machine powered up.
3. The test frequency value is then entered into the Spectral Plus 5.0 Signal Generator software. The moment the OK button is clicked, the holder and sample begins to oscillate.
4. The National Instrument VI Logger interface is then commanded to start capturing data.
5. Data is captured for a 1min period.
6. The signal generator is stopped.
7. A new test frequency is then entered into Spectral Plus 5.0 Signal Generator software and step 4 and 5 repeated until the frequency range desired is covered
8. The data captured is then exported into MS Excel for data mining

C2.3 Possible sources of error in measurement and the precaution to take

C2.3.1 Timing errors caused by motor inertia

Absolute timing was not used but the relative time lag. It means motor lag will be constant as long as (1) the supply current to the windings is constant, and (2) the sample holder does not change weight i.e. the holder is not being eroded by the oscillatory motion. Pulsing the motor winding at very small interval removes the first problem. The use of plastic material for the parts the plastic strip glides over (only one, at the entrance into the photocell casing) ensures reduced erosion and thus weight loss.

Furthermore the use of very light weight material for this moving part ensures that it can follow the input signal in a timely manner. The motor was tested and found to be capable of oscillations greater than 50Hz (reaction time of $\leq$ 20ms) which is much greater than the maximum frequency range of 30Hz (Period T=33.33ms) used in this experiment.

C2.3.2 Analog-Digital conversion time

The NI PCI 1064 D/A conversion card to which the DAQ Signal accessories is connected to is a 16 channel device capable of 20Mhz conversion rate multiplexed between the channels. That is approximately 1.25Mhz per channel, this is more than adequate for this work that requires testing at maximum of 30Hz.

C2.3.3 Out of synchronization error due to signal generator and the recorded values by the data logger.

This is solved by recording the signal generator output (driving the motor) and using it as the reference (figure C16) for all other values. It was found that this lag is constant and can thus be treated as a bias.

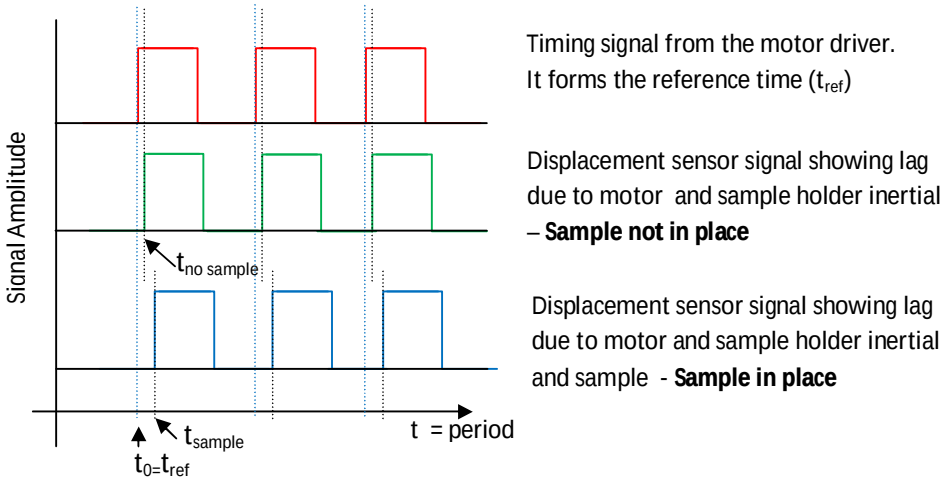


Figure C16 Signal pattern showing presence and absence of sample rubber. The delay is increased when sample is in place. The absolute value of this delay is obtained from t_{sample} - $t_{no\ sample}$ - t_{ref}. $t_{no\ sample}$ is fixed and is the lag due to the motor inertia. t_{ref} interval is controlled by the precision signal generator.

C2.3.4 Temperature

Temperature has very serious influence on the property of elastomers, even filled ones. Compounding, vulcanization and filling reduce this influence as much as possible. The environmental temperature was stabilized using fan and the experiments were performed quickly – each requiring about a minute to do. The maximum temperature variation between the experiments is 1.1^{o}C as captured by the data logger using the nichrome-constantan thermocouple junction.

APPENDIX D
CODE LIST (PSEUDO CODE) USED IN THE ROBOT FIRMWARE

```
---  C:\Tunde\PhD\3rd Presentation\BlueMac\BlueMac.asm  ------------------
 1:     ; start date 20th May 2010
 2:
 3:     ;the following routines are intended
 4:     ;    1 Oscillating PWM x3  -> for straight swimming
 5:     ;    2 Left enhanced Oscillating PWM x3  -> turn left
 6:     ;    3 Right enhanced Oscilating PWM x3  -> turn right
 7:     ;Other embelishments as follows
 8:     ;    4 Depth Control
 9:     ;    5 Obstacle detection and avoidance
 10:    ;    6 Object detection and tracking
 11:    ;    7 Human overide
 12:    ;    8 Another swimming mode -> derived from turning algorithm
 13:
 14:
 15:    ;------------------------PRELIMINARIES----------------------
 16:        list p=18F4520, n=48, t=ON, st=OFF
 17:        #include "p18F4520.inc"
 18:      ;Oscillator switch enabled, RC oscillator with OSC2 as I/O pin.
 19:       CONFIG  OSC=INTIO67
 20:       CONFIG  PBADEN=OFF
 21:       CONFIG  WDT=OFF


0000    D004     BRA 0xa
0008    D0A1     BRA 0x14c
000A    0EF0     MOVLW 0xf0
000C    6ED3     MOVWF 0xfd3, ACCESS
000E    8C9B     BSF 0xf9b, 0x6, ACCESS
0010    A6D3     BTFSS 0xfd3, 0x3, ACCESS
0012    EF08     GOTO 0x10
0014    F000     NOP
0016    6A13     CLRF 0x13, ACCESS
0018    6A14     CLRF 0x14, ACCESS
001A    6A2D     CLRF 0x2d, ACCESS
001C    6A31     CLRF 0x31, ACCESS
001E    0E05     MOVLW 0x5
0020    6E30     MOVWF 0x30, ACCESS
0022    6E2F     MOVWF 0x2f, ACCESS
0024    0EB7     MOVLW 0xb7
0026    6E35     MOVWF 0x35, ACCESS
0028    0E01     MOVLW 0x1
002A    6E03     MOVWF 0x3, ACCESS
002C    0E00     MOVLW 0
002E    6E04     MOVWF 0x4, ACCESS
0030    0E05     MOVLW 0x5
0032    6E05     MOVWF 0x5, ACCESS
0034    0E05     MOVLW 0x5
0036    6E0D     MOVWF 0xd, ACCESS
```

```
0038    0E40     MOVLW 0x40
003A    6E0E     MOVWF 0xe, ACCESS
003C    0E00     MOVLW 0
003E    6E0F     MOVWF 0xf, ACCESS
0040    0E8E     MOVLW 0x8e
0042    6E10     MOVWF 0x10, ACCESS
0044    0EE8     MOVLW 0xe8
0046    6E11     MOVWF 0x11, ACCESS
0048    0E0F     MOVLW 0xf
004A    6E29     MOVWF 0x29, ACCESS
004C    0E00     MOVLW 0
004E    6E28     MOVWF 0x28, ACCESS
0050    0E29     MOVLW 0x29
0052    6E2A     MOVWF 0x2a, ACCESS
0054    0E01     MOVLW 0x1
0056    6E2B     MOVWF 0x2b, ACCESS
0058    6A83     CLRF 0xf83, ACCESS
005A    0EC8     MOVLW 0xc8
005C    6E95     MOVWF 0xf95, ACCESS
005E    6A81     CLRF 0xf81, ACCESS
0060    0E0F     MOVLW 0xf
0062    6EC1     MOVWF 0xfc1, ACCESS
0064    0E07     MOVLW 0x7
0066    6E93     MOVWF 0xf93, ACCESS
0068    6A82     CLRF 0xf82, ACCESS
006A    6894     SETF 0xf94, ACCESS
006C    6A80     CLRF 0xf80, ACCESS
006E    8092     BSF 0xf92, 0, ACCESS
0070    8292     BSF 0xf92, 0x1, ACCESS
0072    6AD5     CLRF 0xfd5, ACCESS
0074    80D5     BSF 0xfd5, 0, ACCESS
0076    6AF2     CLRF 0xff2, ACCESS
0078    94F2     BCF 0xff2, 0x2, ACCESS
007A    B4F2     BTFSC 0xff2, 0x2, ACCESS
007C    D7FE     BRA 0x7a
007E    0EC0     MOVLW 0xc0
0080    6ED6     MOVWF 0xfd6, ACCESS
0082    0E63     MOVLW 0x63
0084    6ED7     MOVWF 0xfd7, ACCESS
0086    0E1E     MOVLW 0x1e
0088    6E0C     MOVWF 0xc, ACCESS
008A    0E1E     MOVLW 0x1e
008C    6E0B     MOVWF 0xb, ACCESS
008E    0E0A     MOVLW 0xa
0090    6E0A     MOVWF 0xa, ACCESS
0092    0E14     MOVLW 0x14
0094    6E09     MOVWF 0x9, ACCESS
0096    0E82     MOVLW 0x82
0098    6E17     MOVWF 0x17, ACCESS
009A    0EA2     MOVLW 0xa2
009C    6E1C     MOVWF 0x1c, ACCESS
009E    0EAC     MOVLW 0xac
00A0    6E21     MOVWF 0x21, ACCESS
```

```
00A2    0EEC     MOVLW 0xec
00A4    6E18     MOVWF 0x18, ACCESS
00A6    0ED2     MOVLW 0xd2
00A8    6E1D     MOVWF 0x1d, ACCESS
00AA    0EBF     MOVLW 0xbf
00AC    6E22     MOVWF 0x22, ACCESS
00AE    8013     BSF 0x13, 0, ACCESS
00B0    C021     MOVFF 0x21, 0x20
00B2    F020     NOP
00B4    C01D     MOVFF 0x1d, 0x1b
00B6    F01B     NOP
00B8    C018     MOVFF 0x18, 0x16
00BA    F016     NOP
00BC    9ED0     BCF 0xfd0, 0x7, ACCESS
00BE    0E70     MOVLW 0x70
00C0    6EF2     MOVWF 0xff2, ACCESS
00C2    0E00     MOVLW 0
00C4    6EF1     MOVWF 0xff1, ACCESS
00C6    6AF0     CLRF 0xff0, ACCESS
00C8    92F2     BCF 0xff2, 0x1, ACCESS
00CA    8EF2     BSF 0xff2, 0x7, ACCESS
00CC    8ED5     BSF 0xfd5, 0x7, ACCESS
00CE    0E03     MOVLW 0x3
00D0    6E32     MOVWF 0x32, ACCESS
00D2    8C14     BSF 0x14, 0x6, ACCESS
00D4    A013     BTFSS 0x13, 0, ACCESS
00D6    EC72     CALL 0xe4, 0
00D8    F000     NOP
00DA    B413     BTFSC 0x13, 0x2, ACCESS
00DC    ECD2     CALL 0x3a4, 0
00DE    F001     NOP
00E0    EF6A     GOTO 0xd4
00E2    F000     NOP
00E4    B614     BTFSC 0x14, 0x3, ACCESS
00E6    EF86     GOTO 0x10c
00E8    F000     NOP
00EA    C021     MOVFF 0x21, 0x20
00EC    F020     NOP
00EE    B813     BTFSC 0x13, 0x4, ACCESS
00F0    C022     MOVFF 0x22, 0x20
00F2    F020     NOP
00F4    C01C     MOVFF 0x1c, 0x1b
00F6    F01B     NOP
00F8    BA13     BTFSC 0x13, 0x5, ACCESS
00FA    C01D     MOVFF 0x1d, 0x1b
00FC    F01B     NOP
00FE    C017     MOVFF 0x17, 0x16
0100    F016     NOP
0102    BC13     BTFSC 0x13, 0x6, ACCESS
0104    C018     MOVFF 0x18, 0x16
0106    F016     NOP
0108    7013     BTG 0x13, 0, ACCESS
010A    0012     RETURN 0
```

```
010C    5035    MOVF 0x35, W, ACCESS
010E    B414    BTFSC 0x14, 0x2, ACCESS
0110    EF98    GOTO 0x130
0112    F000    NOP
0114    6E20    MOVWF 0x20, ACCESS
0116    B813    BTFSC 0x13, 0x4, ACCESS
0118    C022    MOVFF 0x22, 0x20
011A    F020    NOP
011C    6E1B    MOVWF 0x1b, ACCESS
011E    BA13    BTFSC 0x13, 0x5, ACCESS
0120    C01D    MOVFF 0x1d, 0x1b
0122    F01B    NOP
0124    6E16    MOVWF 0x16, ACCESS
0126    BC13    BTFSC 0x13, 0x6, ACCESS
0128    C018    MOVFF 0x18, 0x16
012A    F016    NOP
012C    7013    BTG 0x13, 0, ACCESS
012E    0012    RETURN 0
0130    C021    MOVFF 0x21, 0x20
0132    F020    NOP
0134    B813    BTFSC 0x13, 0x4, ACCESS
0136    6E20    MOVWF 0x20, ACCESS
0138    C01C    MOVFF 0x1c, 0x1b
013A    F01B    NOP
013C    BA13    BTFSC 0x13, 0x5, ACCESS
013E    6E1B    MOVWF 0x1b, ACCESS
0140    C017    MOVFF 0x17, 0x16
0142    F016    NOP
0144    BC13    BTFSC 0x13, 0x6, ACCESS
0146    6E16    MOVWF 0x16, ACCESS
0148    7013    BTG 0x13, 0, ACCESS
014A    0012    RETURN 0
014C    0000    NOP
014E    6E00    MOVWF 0, ACCESS
0150    CFD8    MOVFF 0xfd8, 0x1
0152    F001    NOP
0154    CFE0    MOVFF 0xfe0, 0x2
0156    F002    NOP
0158    B4F2    BTFSC 0xff2, 0x2, ACCESS
015A    D007    BRA 0x16a
015C    D040    BRA 0x1de
015E    C002    MOVFF 0x2, 0xfe0
0160    FFE0    NOP
0162    5000    MOVF 0, W, ACCESS
0164    C001    MOVFF 0x1, 0xfd8
0166    FFD8    NOP
0168    0011    RETFIE 0x1
016A    94F2    BCF 0xff2, 0x2, ACCESS
016C    0EC3    MOVLW 0xc3
016E    6ED6    MOVWF 0xfd6, ACCESS
0170    0E63    MOVLW 0x63
0172    6ED7    MOVWF 0xfd7, ACCESS
0174    B214    BTFSC 0x14, 0x1, ACCESS
```

```
0176    EFD3    GOTO 0x1a6
0178    F000    NOP
017A    A014    BTFSS 0x14, 0, ACCESS
017C    D7F0    BRA 0x15e
017E    B015    BTFSC 0x15, 0, ACCESS
0180    D0AB    BRA 0x2d8
0182    2E0B    DECFSZ 0xb, F, ACCESS
0184    D004    BRA 0x18e
0186    C00C    MOVFF 0xc, 0xb
0188    F00B    NOP
018A    7813    BTG 0x13, 0x4, ACCESS
018C    9013    BCF 0x13, 0, ACCESS
018E    2E0A    DECFSZ 0xa, F, ACCESS
0190    D004    BRA 0x19a
0192    C00C    MOVFF 0xc, 0xa
0194    F00A    NOP
0196    7A13    BTG 0x13, 0x5, ACCESS
0198    9013    BCF 0x13, 0, ACCESS
019A    2E09    DECFSZ 0x9, F, ACCESS
019C    D004    BRA 0x1a6
019E    C00C    MOVFF 0xc, 0x9
01A0    F009    NOP
01A2    7C13    BTG 0x13, 0x6, ACCESS
01A4    9013    BCF 0x13, 0, ACCESS
01A6    8483    BSF 0xf83, 0x2, ACCESS
01A8    8283    BSF 0xf83, 0x1, ACCESS
01AA    8083    BSF 0xf83, 0, ACCESS
01AC    6A06    CLRF 0x6, ACCESS
01AE    0E00    MOVLW 0
01B0    6416    CPFSGT 0x16, ACCESS
01B2    9483    BCF 0xf83, 0x2, ACCESS
01B4    641B    CPFSGT 0x1b, ACCESS
01B6    9083    BCF 0xf83, 0, ACCESS
01B8    6420    CPFSGT 0x20, ACCESS
01BA    9283    BCF 0xf83, 0x1, ACCESS
01BC    ECE9    CALL 0x1d2, 0
01BE    F000    NOP
01C0    2A06    INCF 0x6, F, ACCESS
01C2    0E07    MOVLW 0x7
01C4    1483    ANDWF 0xf83, W, ACCESS
01C6    6E33    MOVWF 0x33, ACCESS
01C8    5006    MOVF 0x6, W, ACCESS
01CA    6633    TSTFSZ 0x33, ACCESS
01CC    D7F1    BRA 0x1b0
01CE    8413    BSF 0x13, 0x2, ACCESS
01D0    D7C6    BRA 0x15e
01D2    0E0F    MOVLW 0xf
01D4    6E07    MOVWF 0x7, ACCESS
01D6    2E07    DECFSZ 0x7, F, ACCESS
01D8    EFEB    GOTO 0x1d6
01DA    F000    NOP
01DC    0012    RETURN 0
01DE    92F2    BCF 0xff2, 0x1, ACCESS
```

```
01E0    6A34     CLRF 0x34, ACCESS
01E2    A882     BTFSS 0xf82, 0x4, ACCESS
01E4    8834     BSF 0x34, 0x4, ACCESS
01E6    AA82     BTFSS 0xf82, 0x5, ACCESS
01E8    8A34     BSF 0x34, 0x5, ACCESS
01EA    AC82     BTFSS 0xf82, 0x6, ACCESS
01EC    8C34     BSF 0x34, 0x6, ACCESS
01EE    AE82     BTFSS 0xf82, 0x7, ACCESS
01F0    8E34     BSF 0x34, 0x7, ACCESS
01F2    0000     NOP
01F4    B834     BTFSC 0x34, 0x4, ACCESS
01F6    EF07     GOTO 0x20e
01F8    F001     NOP
01FA    BA34     BTFSC 0x34, 0x5, ACCESS
01FC    EF0F     GOTO 0x21e
01FE    F001     NOP
0200    BC34     BTFSC 0x34, 0x6, ACCESS
0202    EFBE     GOTO 0x37c
0204    F001     NOP
0206    BE34     BTFSC 0x34, 0x7, ACCESS
0208    EFA8     GOTO 0x350
020A    F001     NOP
020C    D7A8     BRA 0x15e
020E    BC34     BTFSC 0x34, 0x6, ACCESS
0210    EF23     GOTO 0x246
0212    F001     NOP
0214    BE34     BTFSC 0x34, 0x7, ACCESS
0216    EF98     GOTO 0x330
0218    F001     NOP
021A    EF4A     GOTO 0x294
021C    F001     NOP
021E    BC34     BTFSC 0x34, 0x6, ACCESS
0220    EF88     GOTO 0x310
0222    F001     NOP
0224    BE34     BTFSC 0x34, 0x7, ACCESS
0226    EF18     GOTO 0x230
0228    F001     NOP
022A    EF5E     GOTO 0x2bc
022C    F001     NOP
022E    0012     RETURN 0
0230    A014     BTFSS 0x14, 0, ACCESS
0232    D795     BRA 0x15e
0234    8A14     BSF 0x14, 0x5, ACCESS
0236    7C14     BTG 0x14, 0x6, ACCESS
0238    D792     BRA 0x15e
023A    9A14     BCF 0x14, 0x5, ACCESS
023C    8C14     BSF 0x14, 0x6, ACCESS
023E    0012     RETURN 0
0240    EC1D     CALL 0x23a, 0
0242    F001     NOP
0244    D78C     BRA 0x15e
0246    BA14     BTFSC 0x14, 0x5, ACCESS
0248    EF20     GOTO 0x240
```

```
024A    F001    NOP
024C    7014    BTG 0x14, 0, ACCESS
024E    A014    BTFSS 0x14, 0, ACCESS
0250    EF2E    GOTO 0x25c
0252    F001    NOP
0254    B214    BTFSC 0x14, 0x1, ACCESS
0256    EF3C    GOTO 0x278
0258    F001    NOP
025A    D781    BRA 0x15e
025C    9A14    BCF 0x14, 0x5, ACCESS
025E    8214    BSF 0x14, 0x1, ACCESS
0260    C016    MOVFF 0x16, 0x25
0262    F025    NOP
0264    C01B    MOVFF 0x1b, 0x26
0266    F026    NOP
0268    C020    MOVFF 0x20, 0x27
026A    F027    NOP
026C    5035    MOVF 0x35, W, ACCESS
026E    6E16    MOVWF 0x16, ACCESS
0270    6E1B    MOVWF 0x1b, ACCESS
0272    6E20    MOVWF 0x20, ACCESS
0274    EF43    GOTO 0x286
0276    F001    NOP
0278    9214    BCF 0x14, 0x1, ACCESS
027A    C025    MOVFF 0x25, 0x16
027C    F016    NOP
027E    C026    MOVFF 0x26, 0x1b
0280    F01B    NOP
0282    C027    MOVFF 0x27, 0x20
0284    F020    NOP
0286    D76B    BRA 0x15e
0288    BC14    BTFSC 0x14, 0x6, ACCESS
028A    EFA8    GOTO 0x350
028C    F001    NOP
028E    EC1D    CALL 0x23a, 0
0290    F001    NOP
0292    D038    BRA 0x304
0294    AA14    BTFSS 0x14, 0x5, ACCESS
0296    D036    BRA 0x304
0298    D000    BRA 0x29a
029A    9A14    BCF 0x14, 0x5, ACCESS
029C    EC51    CALL 0x2a2, 0
029E    F001    NOP
02A0    D75E    BRA 0x15e
02A2    0E01    MOVLW 0x1
02A4    6E15    MOVWF 0x15, ACCESS
02A6    C010    MOVFF 0x10, 0x16
02A8    F016    NOP
02AA    C00C    MOVFF 0xc, 0x12
02AC    F012    NOP
02AE    0012    RETURN 0
02B0    BC14    BTFSC 0x14, 0x6, ACCESS
02B2    EFBE    GOTO 0x37c
```

```
02B4    F001    NOP
02B6    EC1D    CALL 0x23a, 0
02B8    F001    NOP
02BA    D027    BRA 0x30a
02BC    AA14    BTFSS 0x14, 0x5, ACCESS
02BE    D025    BRA 0x30a
02C0    D000    BRA 0x2c2
02C2    9A14    BCF 0x14, 0x5, ACCESS
02C4    EC65    CALL 0x2ca, 0
02C6    F001    NOP
02C8    D74A    BRA 0x15e
02CA    0E03    MOVLW 0x3
02CC    6E15    MOVWF 0x15, ACCESS
02CE    C011    MOVFF 0x11, 0x16
02D0    F016    NOP
02D2    C00C    MOVFF 0xc, 0x12
02D4    F012    NOP
02D6    0012    RETURN 0
02D8    2E12    DECFSZ 0x12, F, ACCESS
02DA    D001    BRA 0x2de
02DC    D010    BRA 0x2fe
02DE    B215    BTFSC 0x15, 0x1, ACCESS
02E0    D007    BRA 0x2f0
02E2    C018    MOVFF 0x18, 0x16
02E4    F016    NOP
02E6    C01D    MOVFF 0x1d, 0x1b
02E8    F01B    NOP
02EA    C022    MOVFF 0x22, 0x20
02EC    F020    NOP
02EE    D75B    BRA 0x1a6
02F0    C017    MOVFF 0x17, 0x16
02F2    F016    NOP
02F4    C01C    MOVFF 0x1c, 0x1b
02F6    F01B    NOP
02F8    C021    MOVFF 0x21, 0x20
02FA    F020    NOP
02FC    D754    BRA 0x1a6
02FE    9013    BCF 0x13, 0, ACCESS
0300    6A15    CLRF 0x15, ACCESS
0302    D72D    BRA 0x15e
0304    7614    BTG 0x14, 0x3, ACCESS
0306    9414    BCF 0x14, 0x2, ACCESS
0308    D72A    BRA 0x15e
030A    7614    BTG 0x14, 0x3, ACCESS
030C    8414    BSF 0x14, 0x2, ACCESS
030E    D727    BRA 0x15e
0310    BA14    BTFSC 0x14, 0x5, ACCESS
0312    EF44    GOTO 0x288
0314    F001    NOP
0316    0EDC    MOVLW 0xdc
0318    6022    CPFSLT 0x22, ACCESS
031A    D721    BRA 0x15e
031C    0E01    MOVLW 0x1
```

```
031E    2618    ADDWF 0x18, F, ACCESS
0320    5E17    SUBWF 0x17, F, ACCESS
0322    0E03    MOVLW 0x3
0324    261D    ADDWF 0x1d, F, ACCESS
0326    5E1C    SUBWF 0x1c, F, ACCESS
0328    0E02    MOVLW 0x2
032A    2622    ADDWF 0x22, F, ACCESS
032C    5E21    SUBWF 0x21, F, ACCESS
032E    D717    BRA 0x15e
0330    BA14    BTFSC 0x14, 0x5, ACCESS
0332    EF58    GOTO 0x2b0
0334    F001    NOP
0336    0EB3    MOVLW 0xb3
0338    6422    CPFSGT 0x22, ACCESS
033A    D711    BRA 0x15e
033C    0E01    MOVLW 0x1
033E    2617    ADDWF 0x17, F, ACCESS
0340    5E18    SUBWF 0x18, F, ACCESS
0342    0E03    MOVLW 0x3
0344    261C    ADDWF 0x1c, F, ACCESS
0346    5E1D    SUBWF 0x1d, F, ACCESS
0348    0E02    MOVLW 0x2
034A    2621    ADDWF 0x21, F, ACCESS
034C    5E22    SUBWF 0x22, F, ACCESS
034E    D707    BRA 0x15e
0350    EC1D    CALL 0x23a, 0
0352    F001    NOP
0354    B014    BTFSC 0x14, 0, ACCESS
0356    D703    BRA 0x15e
0358    0E05    MOVLW 0x5
035A    640C    CPFSGT 0xc, ACCESS
035C    D700    BRA 0x15e
035E    060C    DECF 0xc, F, ACCESS
0360    0E00    MOVLW 0
0362    060B    DECF 0xb, F, ACCESS
0364    640B    CPFSGT 0xb, ACCESS
0366    C00C    MOVFF 0xc, 0xb
0368    F00B    NOP
036A    060A    DECF 0xa, F, ACCESS
036C    640A    CPFSGT 0xa, ACCESS
036E    C00C    MOVFF 0xc, 0xa
0370    F00A    NOP
0372    0609    DECF 0x9, F, ACCESS
0374    6409    CPFSGT 0x9, ACCESS
0376    C00C    MOVFF 0xc, 0x9
0378    F009    NOP
037A    D6F1    BRA 0x15e
037C    B014    BTFSC 0x14, 0, ACCESS
037E    D6EF    BRA 0x15e
0380    0E35    MOVLW 0x35
0382    600C    CPFSLT 0xc, ACCESS
0384    D6EC    BRA 0x15e
0386    2A0C    INCF 0xc, F, ACCESS
```

```
0388    520C    MOVF 0xc, F, ACCESS
038A    2A0B    INCF 0xb, F, ACCESS
038C    600B    CPFSLT 0xb, ACCESS
038E    C00C    MOVFF 0xc, 0xb
0390    F00B    NOP
0392    2A0A    INCF 0xa, F, ACCESS
0394    600A    CPFSLT 0xa, ACCESS
0396    C00C    MOVFF 0xc, 0xa
0398    F00A    NOP
039A    2A09    INCF 0x9, F, ACCESS
039C    6009    CPFSLT 0x9, ACCESS
039E    C00C    MOVFF 0xc, 0x9
03A0    F009    NOP
03A2    D6DD    BRA 0x15e
03A4    2A2D    INCF 0x2d, F, ACCESS
03A6    A080    BTFSS 0xf80, 0, ACCESS
03A8    2A30    INCF 0x30, F, ACCESS
03AA    B080    BTFSC 0xf80, 0, ACCESS
03AC    0630    DECF 0x30, F, ACCESS
03AE    A280    BTFSS 0xf80, 0x1, ACCESS
03B0    2A2F    INCF 0x2f, F, ACCESS
03B2    B280    BTFSC 0xf80, 0x1, ACCESS
03B4    062F    DECF 0x2f, F, ACCESS
03B6    9413    BCF 0x13, 0x2, ACCESS
03B8    0E05    MOVLW 0x5
03BA    602D    CPFSLT 0x2d, ACCESS
03BC    D001    BRA 0x3c0
03BE    0012    RETURN 0
03C0    C032    MOVFF 0x32, 0xffa
03C2    FFFA    NOP
03C4    6A2D    CLRF 0x2d, ACCESS
03C6    7613    BTG 0x13, 0x3, ACCESS
03C8    6A31    CLRF 0x31, ACCESS
03CA    0E08    MOVLW 0x8
03CC    602F    CPFSLT 0x2f, ACCESS
03CE    8231    BSF 0x31, 0x1, ACCESS
03D0    6030    CPFSLT 0x30, ACCESS
03D2    8431    BSF 0x31, 0x2, ACCESS
03D4    0E05    MOVLW 0x5
03D6    6E2F    MOVWF 0x2f, ACCESS
03D8    6E30    MOVWF 0x30, ACCESS
03DA    9080    BCF 0xf80, 0, ACCESS
03DC    9280    BCF 0xf80, 0x1, ACCESS
03DE    5031    MOVF 0x31, W, ACCESS
03E0    26F9    ADDWF 0xff9, F, ACCESS
03E2    0012    RETURN 0
03E4    D75E    BRA 0x2a2
03E6    D771    BRA 0x2ca
03E8    A613    BTFSS 0x13, 0x3, ACCESS
03EA    0000    NOP
03EC    0000    NOP
03EE    0012    RETURN 0
```

APPENDIX E

PIEZO CRYSTAL BASED ULTRASONIC SENSORS - POSSIBLE REASONS WHY IT IS NOT WORKING

Commercial piezo crystal devises comes standardized at 40kHz. The reason is because the frequency cannot be perceived by animals such as dogs and bats that have hearing capabilities in the ultrasonic ranges. Figure E1 is a typical example of a commercial piezo crystal transmitter and receiver pair.



Figure E1 Parallax ping))) exemplifies commercial piezo sensor.

They are made as matched pairs. The transmitter transmits at an optimum value that is fixed, but itself is not sensitive to that frequency. The receiver in the other hand is designed to be very sensitive to a frequency (which is the transmitter frequency) and reject all other frequencies (kind of a mechanical notch filter) - this behavior is shown in figure E2.

A piezo element's oscillations first approach the minimum impedance frequency (f_m) / resonance frequency (f_r), at which the element vibrates most readily, and most efficiently converts electrical energy into mechanical energy. As cycling frequency is further increased, impedance increases to the maximum impedance frequency (f_n) / anti-resonance frequency (f_a), thus the piezo crystal will naturally reject frequency about f_m (or f_r) but will respond very well to frequencies at f_n (or f_a).

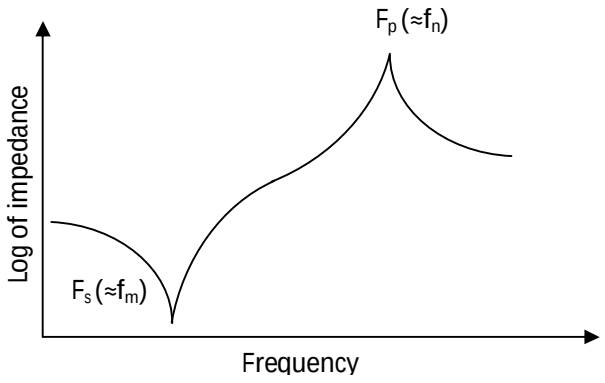


Figure E2 The signal response of matched piezo crystal transmitter and receiver.

The piezo crystal plates for the sensors are 5mm in diameter. When electricity is applied, the crystal bends and reverses its bending direction when the polarity is changed. This can be done at rates up to million times per second for some materials, the one used in this project is optimized for 40kHz. The recommended voltage is less or equal to 20V to avoid crystal breakdown due to excessive bending stress. The higher voltage generate more signal strength.

The piezo crystal plates drive the medium forward and backward at the designed or applied frequency. This action is not a problem when the fluid its interacting with is air, with average density of 1.184kg/m^3 (if mean temperature is equals 25.9 ºC). If the fluid is water, the density becomes **approximately** 1000 kg/m^3 , that is 847 fold increment of mass of fluid to move. This seems to be an overload for the sensor used by the fish robot.

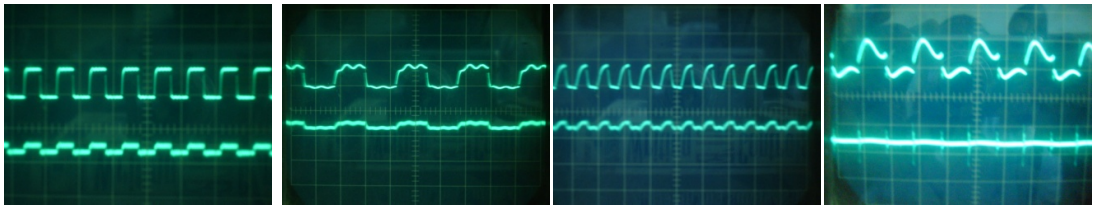
An **alternative** proposition was to use common buzzer plates, figure E3 (10mm to 20mm sizes) also made up of piezo crystal material by Afolayan (2010).

Unfortunately, a rigorous experimentation and calculation shows that this idea will not work for the robot as follows;

1. An experiment on this crystal response (figure E4) shows that these buzzers are made for audible ranges. The response is perfect for the 10kHz and distorted at 20kHz range. At 60kHz, it becomes triangular wave and discontinue at 100khz. The input is a square wave and with constant 5V peak values. The microcontroller inputs are logic gates and run at 8MIP (125ns per instruction), any discontinuity or drop from 5V could be interpreted as separate data input.



Figure E3 Watch Buzzer crystal plates



10kHz 20kHz 60kHz 100kHz

Figure E4 The response of watch buzzer plates to various input frequencies. The top chart is the transmitter output and the bottom plot is the receiver response to the transmitted signal

2. Back plane transmission. The buzzers are designed to transmit sound in all direction – figure E5. It means if used for this work, there will not be any localization of any

detectable objects. Compared to the commercial one of figure E6, the beam is concentrated and narrow.

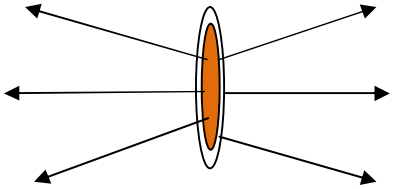


Figure E5 Watch buzzer plate radiation is in all direction

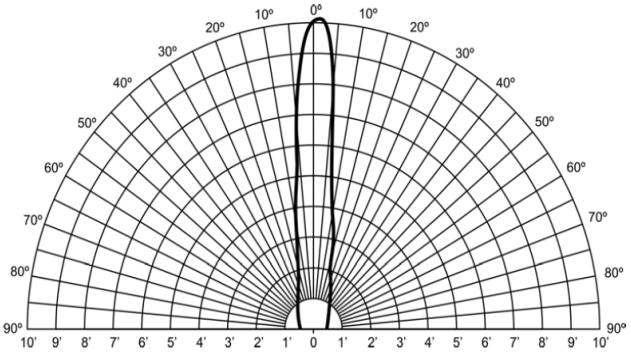


Figure E6 Radiation pattern of Parallax ping)))

3. Tuning and matching – since they don't come in pairs, optimum transmission cannot be achieved as shown in figure E2. A dedicated notch filter will be needed to remove unwanted signals. If no filter is built in, it means every sound and vibration will be picked up rendering it useless for any pure sensing purposes.

4. Audible frequencies will not work

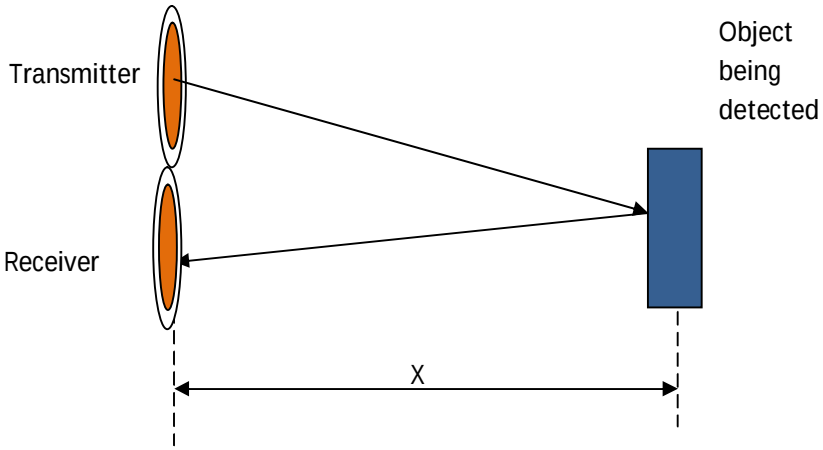


Figure E7 Transmitter-receiver pair using buzzer plate piezo crystals

If the object is located at distance X

And the speed of sound in water is ≈1500m/s.

Time of flight = T_f = 2X / (1500m/s) time to go and come back

If X= 30cm = 0.3m - a value selected being less that the robot length of 394.01cm

T_f = 0.0002s

= 0.2ms

- If transmitter frequency were 4.5kHz as recommended by Afolayan (2010), the period T of oscillation =

T = 1/ 4.5kHz = 0.222ms

Since T > T_f then there will be no single complete oscillation before the signal is expected back.

- If transmitter frequency were 10kHz, using the information from figure E4 the period T of oscillation =

  T = 1 / 10 kHz = 0.1ms

  T : T_f = 0.2 /0.1 = 2

  there will be two complete oscillations before the signal is expected back but will not be enough to saturate the plate acting as sensor.

- If transmitter frequency were 20kHz - that is the edge of human audible range the crystal were designed for as evidence in figure E4 where the response start to deteriorate, the period T of oscillation will be =

  T = 1 / 20 kHz = 0.05ms

  T : T_f = 0.2 /0.05 = 4

there will be 4 complete oscillations before the signal is expected back but may just be enough to saturate the plate acting as sensor. Another problem that arises automatically is called ringing, that is the dying off of the vibration with time since they are mechanical objects. The sensor will continue to send signals even after the driver has stopped supplying voltage to it.

APPENDIX F

INDENTATION FORCE DEFLECTION (IFD) UNIT

Indentation Force Deflection (IFD) is defined as the amount of force, in pounds, required to indent a fifty square inch, round indentor foot into a predefined foam specimen a certain percentage of the specimen's total thickness according to the Polyurethane Foam Association (http://www.pfa.org). The value 6 is assumed for a collapsed and very succulent polyurethane foam as used in this project – the foam used is from an old cushion chair. Table F1 list the Polyurethane foam association IFD table.

Table F1 Polyurethane foam association IFD table

IFD value	**Common usage**
6-12	Bed pillows, thick back pillows
12-18	back pillows, upholstery padding, wraps
18-24	thin back pillows, tufting matrix, very thick seat cushions,wraps
24-30	average seat cushions, upholstery padding, tight seats, certain mattress types, quilting
30-36	firmer seat cushions, mattresses
36-45	thin seat cushioning and firm mattresses
45 and upward	shock absorbing foams, packaging foams, carpet pads, and other uses requiring ultra-firm foams

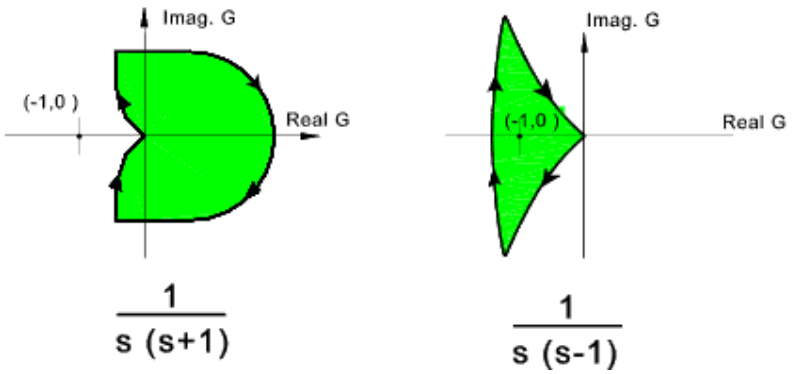
(Source: http://www.pfa.org)

APPENDIX G

INTERPRETING THE NYQUIST DIAGRAM

Source: http://www.roymech.co.uk/Related/Control/Nyquist.html

In the Nyquist plots below the area covered to the right of the locus(shaded) is the Right Hand Plane (RHP)



A closed loop control system is absolutely stable if the roots of the characteristic equation have negative real parts. This means the poles of the closed loop transfer function, or the zeros of the denominator (1 + GH(s)) of the closed loop transfer function, must lie in the (LHP). The Nyquist stability criterion establishes the number of zeros of (1 + GH(s) in the RHP directly from the Nyquist stability plot of GH(s) as indicated below.

The closed loop control system whose open loop transfer function is GH(s) is stable only if..

$$N = -P_o \leq 0$$

where

1) P_o = the number of G(s) poles in the RHP ³ 0

2) N = total number of CW encirclements of the (-1,0) in the G(s) plane.

If N > 0 the number of zeros (Z_o) in the RHP is determined by $Z_o = N + P_o$

If N ≤ 0 the (-1,0) point is not enclosed by the Nyquist plot.

If N ≤ and P_0 then the system is absolutely stable only if N = 0. That is if and only if the (-1,0) point does not lie in the shaded region..

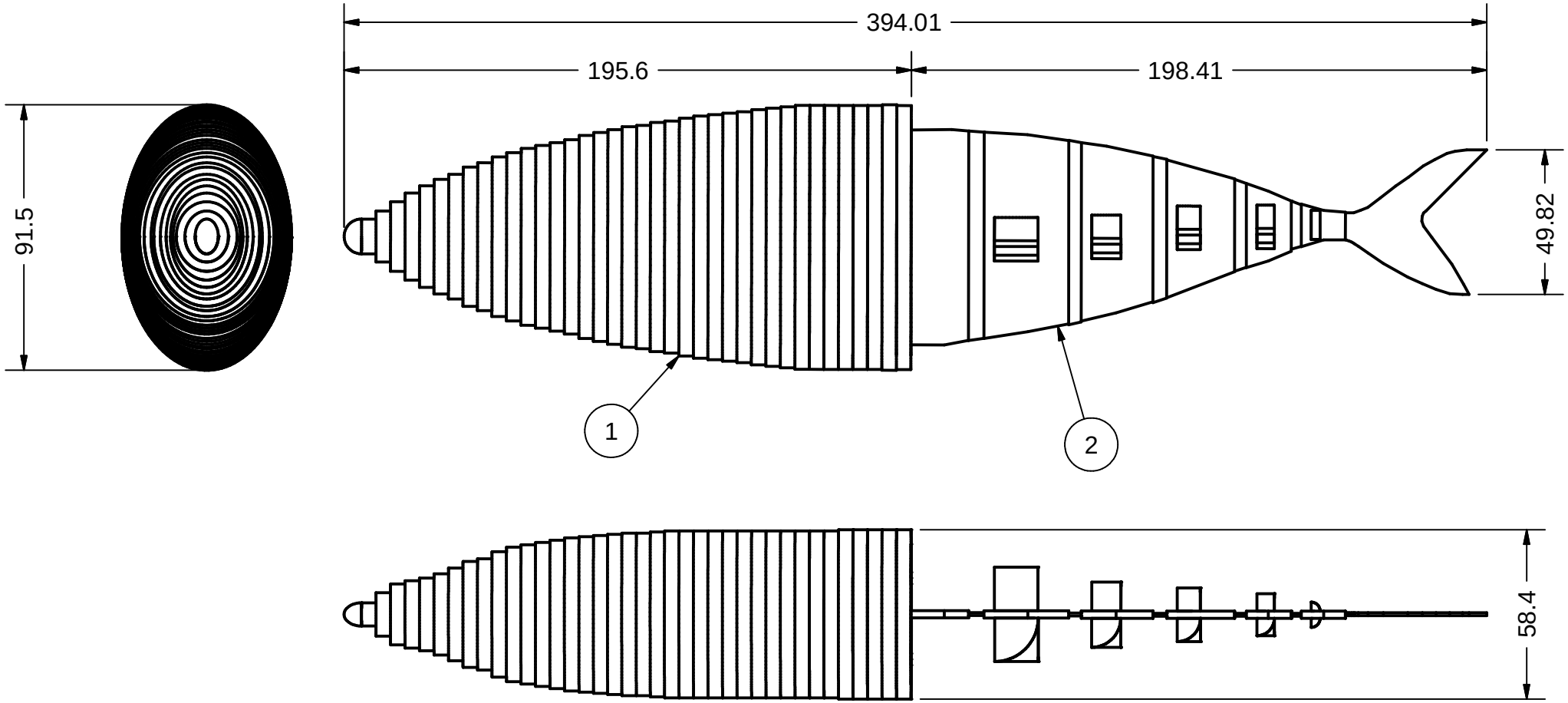
Considering the LH plot above of 1/s(s+1). The (-1,0) point is not in the RHP therefore N<= 0. The poles are at s =0, and s=-1, both outside of the RHP and therefore $P_o = 0$.

Thus $N = -P_o = 0$ and the system is therefore stable.

Considering the RH plot above of 1/s(s-1). The (-1,0) point is enclosed in the RHP and therefore N > 0 (N= 1). The poles of GH are at s= 0 and s = +1 . S= +1 is in the RHP and therefore $P_o = 1$.

N ¹ - P_o Indicating that this system is unstable..

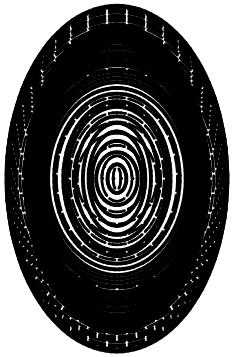
There are $Z_o = N + P_o$ zeros of 1+GH in the RHP.



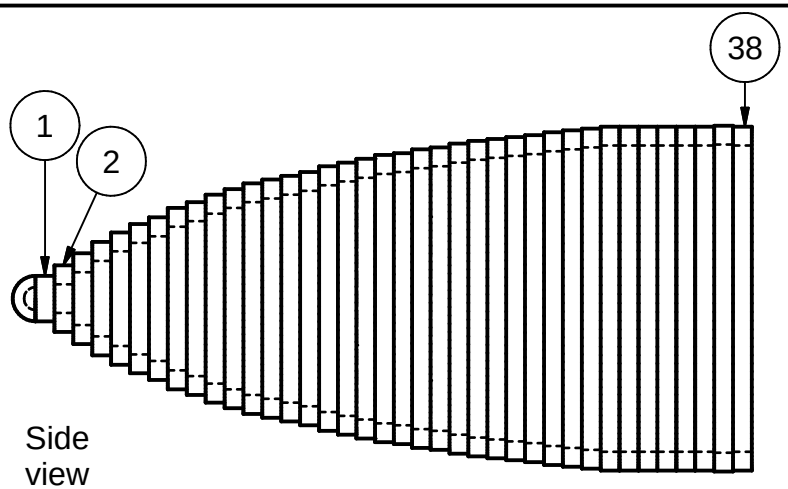
1 Haul Assembly (Drawing no 2)

2 Tail Assembly (Drawing no 3)

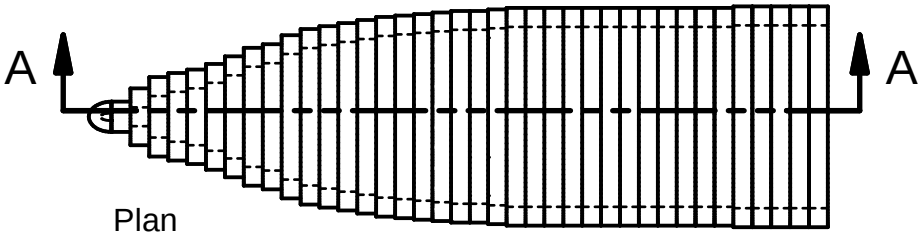
MECHANICAL ENGINEERING DEPARTMENT AHMADU BELLO UNIVERSITY		
Part name:	Fish robot assembly	Drawing No 1
Drawn by:	AFOLAYAN M.O.	Material:
Approved by:	Dr. D.S. Yawas	
Software:	Autodesk Inventor 7	Scale 2:1
Date:		Unit: mm



Front elevation

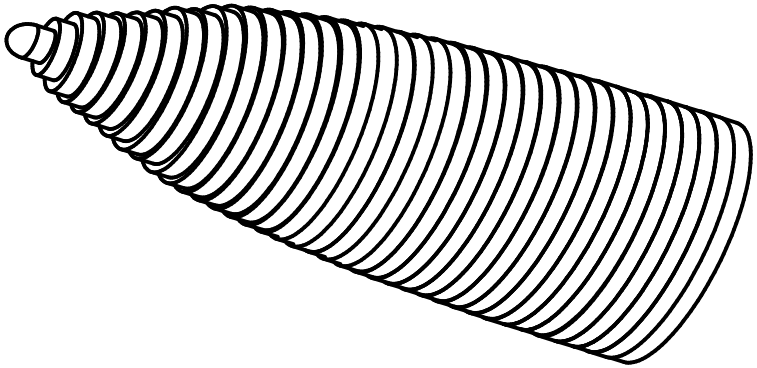


Side view

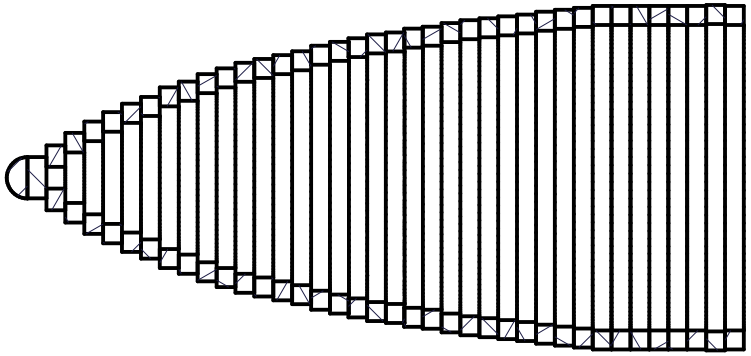


Plan

The balloons (1,2.....38) refers to the rings position in drawing number 4.

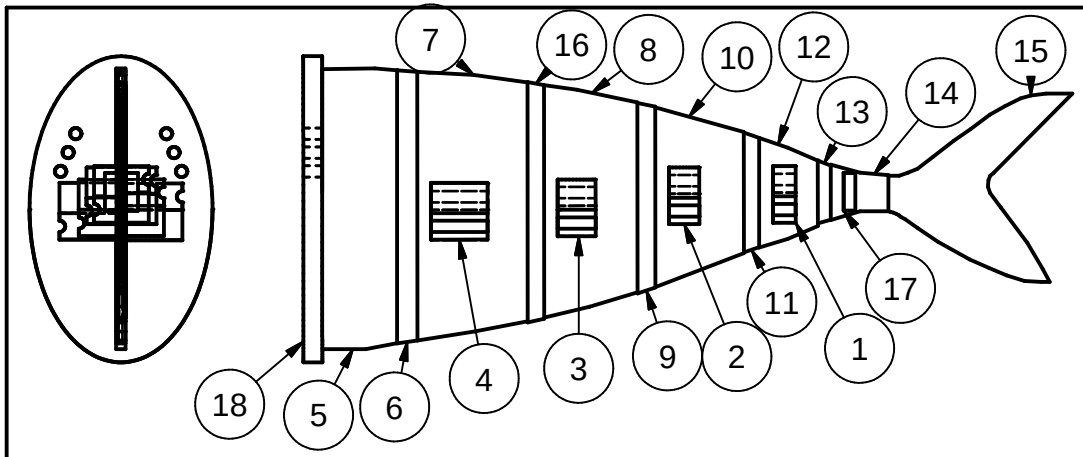


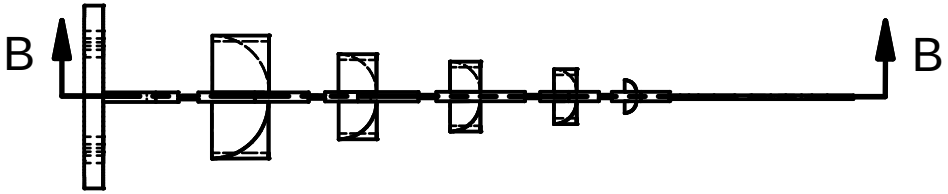
Isometric view

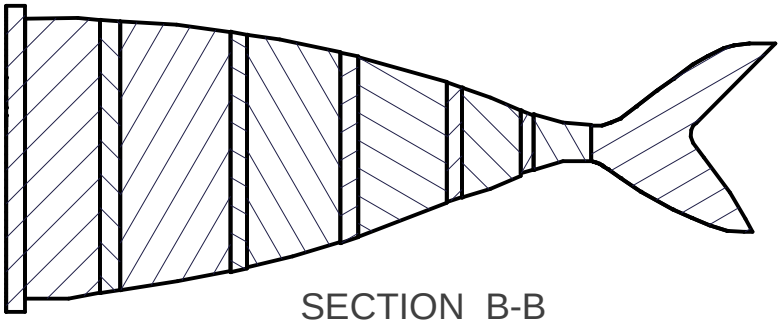


SECTION A-A
SCALE 1 / 2

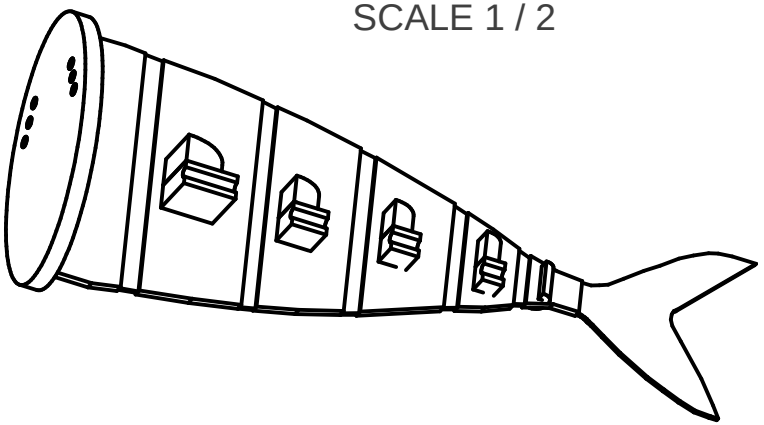
MECHANICAL ENGINEERING DEPARTMENT AHMADU BELLO UNIVERSITY			
Part name:	Haul Assembly		Drawing No 2
Drawn by:	AFOLAYAN M.O.		Material: Plywood
Approved by:	Dr. D.S. Yawas		
Software:	Autodesk Inventor 7		Scale 1:2
Date:			Unit: mm







SECTION B-B
SCALE 1 / 2

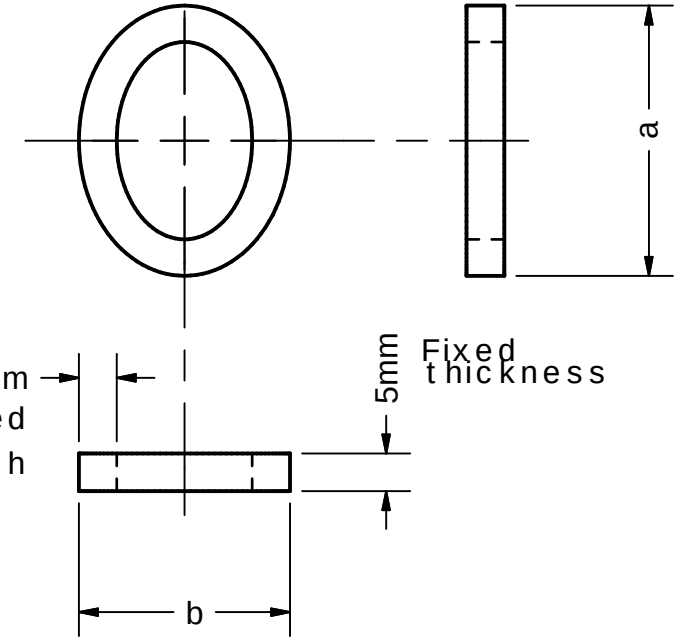


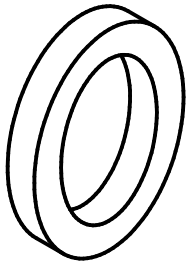
Parts List			
ITEM	QTY	PART NUMBE	DESCRIPTION
18	1	Base	Base
17	2	QTR_1	Quarter pulley 1
4	2	QTR_2	Quarter pulley 2
3	2	QTR_3	Quarter pulley 3
2	2	QTR_4	Quarter pulley 4
1	2	QTR_5	Quarter pulley 5
5	1	6b	
6	1	r4	
7	1	5	
8	1	4	
9	1	r2	
10	1	3	
11	1	r1	
12	1	2	
13	1	r0	
14	1	1	
15	1	0	
16	1	r3_	

MECHANICAL ENGINEERING DEPARTMENT AHMADU BELLO UNIVERSITY			
Part name:	Tail assembly		Drawing No 3
Drawn by:	AFOLAYAN M.O.		Material:
Approved by:	Dr. D.S. Yawas		
Software:	Autodesk Inventor 7		Scale 1:2
Date:			Unit: mm

Ring Position	1	2	3	4	5	6	7	8	9	10	11	12	13	14	15	16	17	18	19	20
a	8	15	21	23.2	25	28	32	36.5	38.4	43.2	46.4	48	49.6	51.2	52.8	53.6	54.4	55.2	56	56
b	12	17.6	24	30	35	39.5	43	48	51	55	58	61	63	65	67	70	72	74	76	77

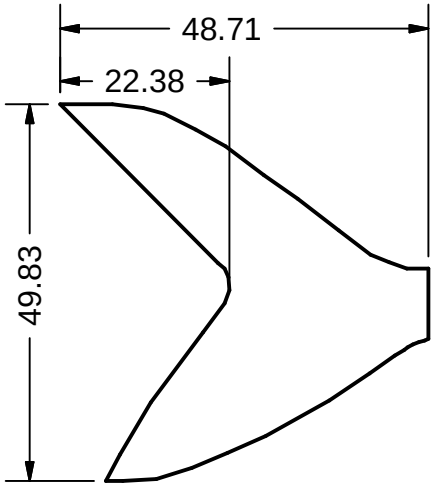
Ring Position	21	22	23	24	25	26	27	28	29	30	31	32	33	34	35	36	37	38
a	56.8	57.6	57.6	57.6	57.6	57.6	57.6	57.6	57.6	57.6	57.6	57.6	57.6	58.4	58.4	58.4	58.4	58.4
b	79	80	82	83.5	84.5	85.5	86.5	88	89	90	91	91	91	91	91	91	91.5	91

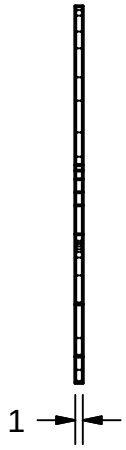


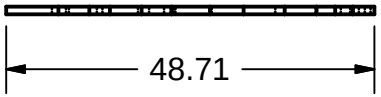


Isometric view of ring

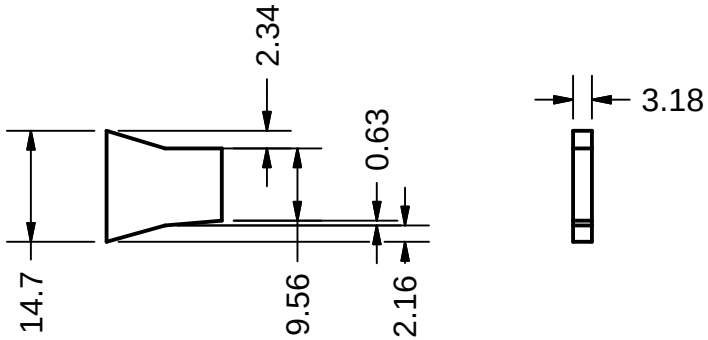
MECHANICAL ENGINEERING DEPARTMENT AHMADU BELLO UNIVERSITY			
Part name:	Rings (for the haul)		Drawing No 4
Drawn by:	AFOLAYAN M.O.		Material: Plywood
Approved by:	Dr. D.S. Yawas		
Software:	Autodesk Inventor 7		Scale 1:1
Date:			

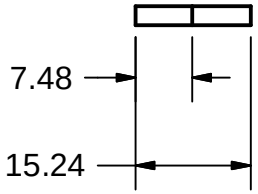




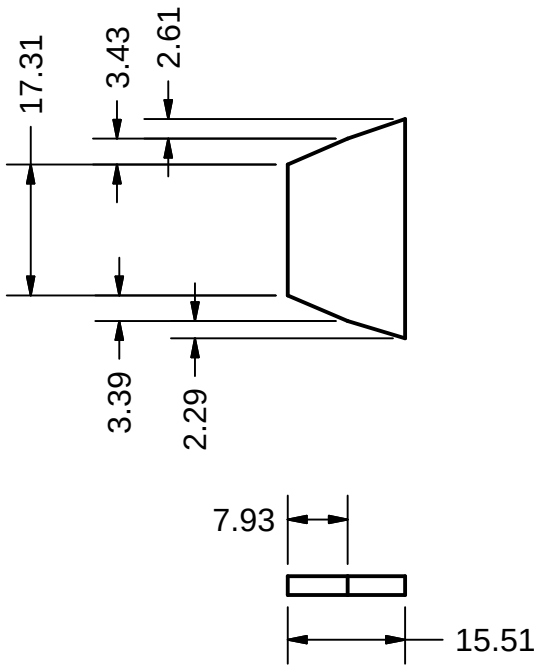


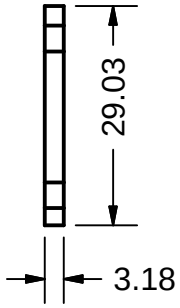
MECHANICAL ENGINEERING DEPARTMENT AHMADU BELLO UNIVERSITY			
Part name:	Tail Fin		Drawing No 5
Drawn by:	AFOLAYAN M.O.		Material: Plywood
Approved by:	Dr. D.S. Yawas		
Software:	Autodesk Inventor 7		Scale: 1:1
Date:			Units: mm



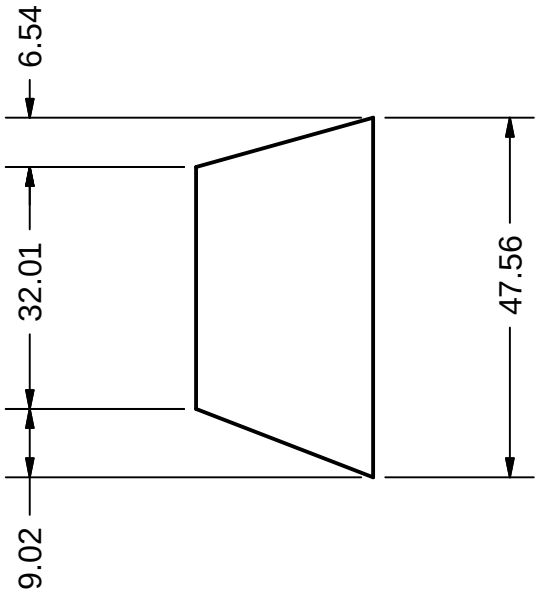


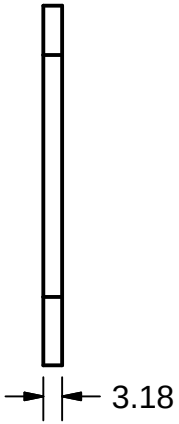
MECHANICAL ENGINEERING DEPARTMENT AHMADU BELLO UNIVERSITY			
Part name:	Tail support structure - segment 1		Drawing No 6
Drawn by:	AFOLAYAN M.O.		Material: Plywood
Approved by:	Dr. D.S. Yawas		
Software:	Autodesk Inventor 7		Scale: 1:1
Date:			Units: mm

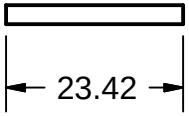




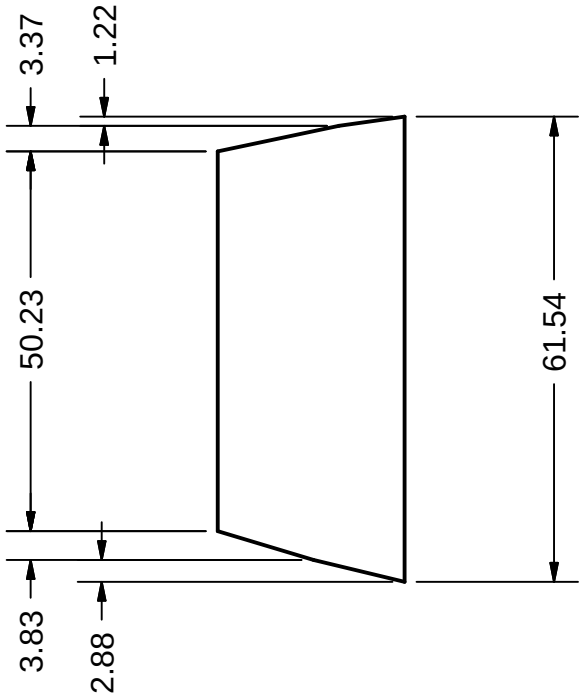
MECHANICAL ENGINEERING DEPARTMENT AHMADU BELLO UNIVERSITY			
Part name:	Tail support structure - segment 2		Drawing No 7
Drawn by:	AFOLAYAN M.O.		Material: Plywood
Approved by:	Dr. D.S. Yawas		
Software:	Autodesk Inventor 7		Scale: 1:1
Date:			Units: mm

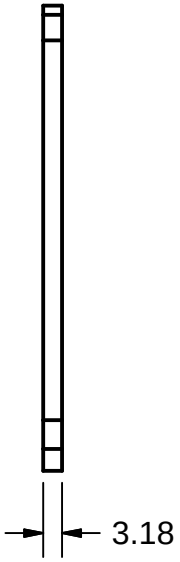


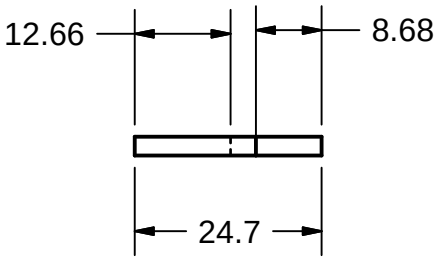




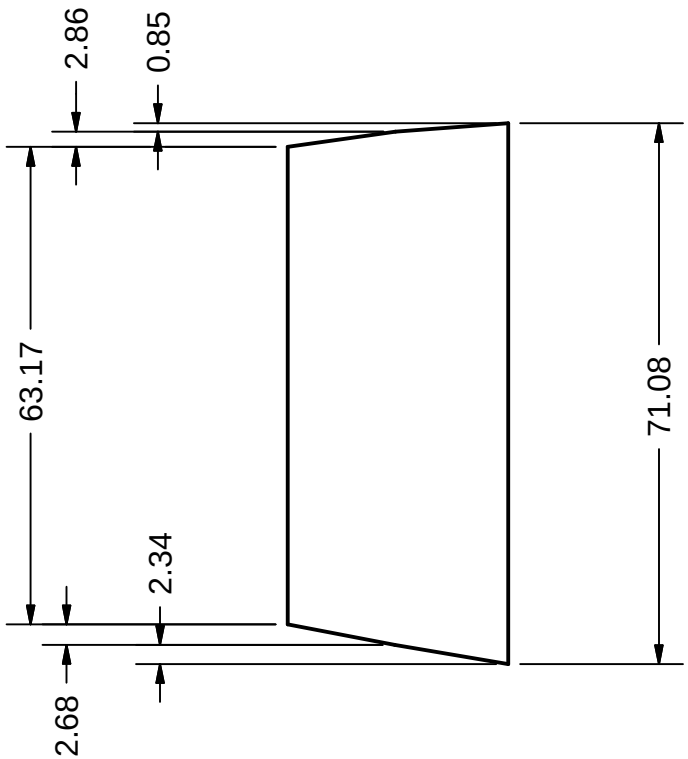
MECHANICAL ENGINEERING DEPARTMENT AHMADU BELLO UNIVERSITY			
Part name:	Tail support structure - segement 3		Drawing No 8
Drawn by:	AFOLAYAN M.O.		Material: Plywood
Approved by:	Dr. D.S. Yawas		
Software:	Autodesk Inventor 7		Scale: 1:1
Date:			Units: mm

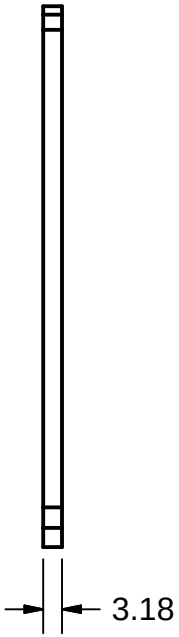


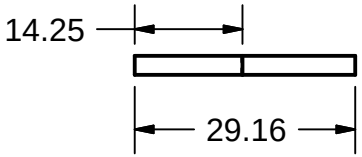




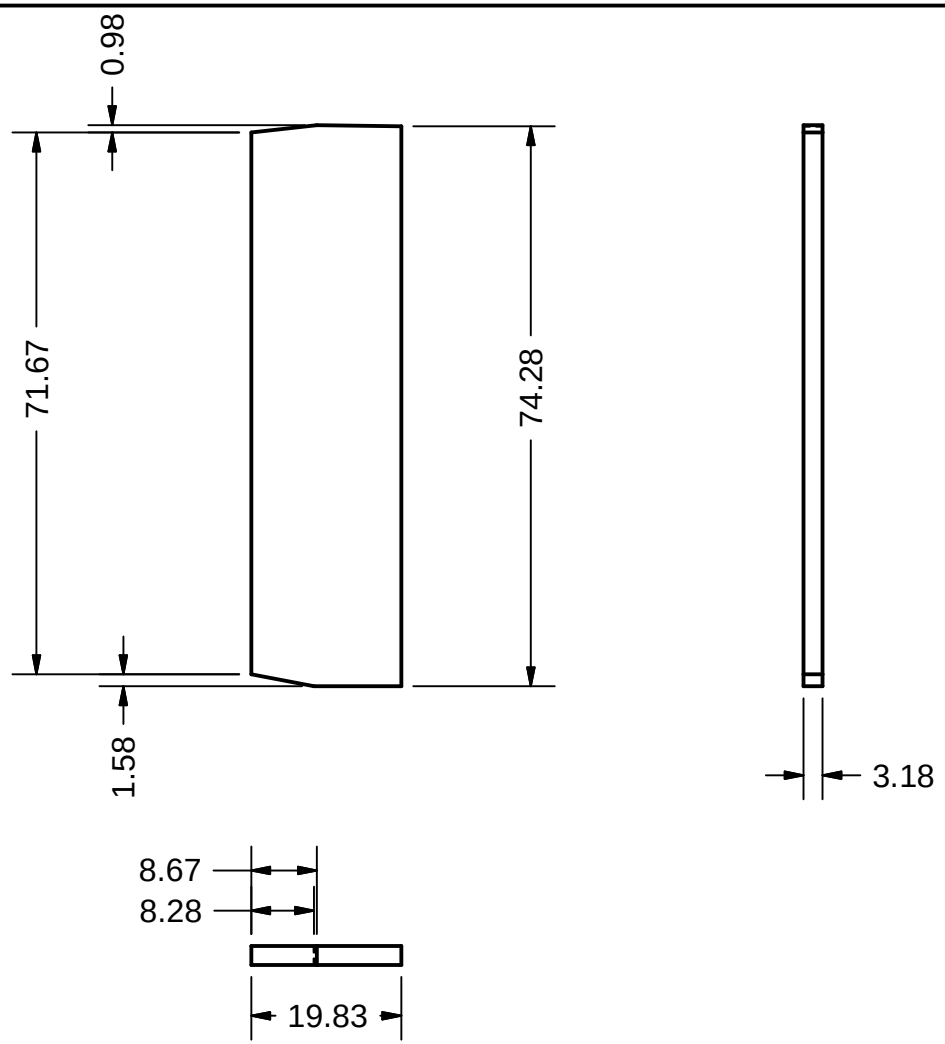
MECHANICAL ENGINEERING DEPARTMENT AHMADU BELLO UNIVERSITY			
Part name:	Tail support structure - segment 4		Drawing No 9
Drawn by:	AFOLAYAN M.O.		Material: Plywood
Approved by:	Dr. D.S. Yawas		
Software:	Autodesk Inventor 7		Scale: 1:1
Date:			Units: mm



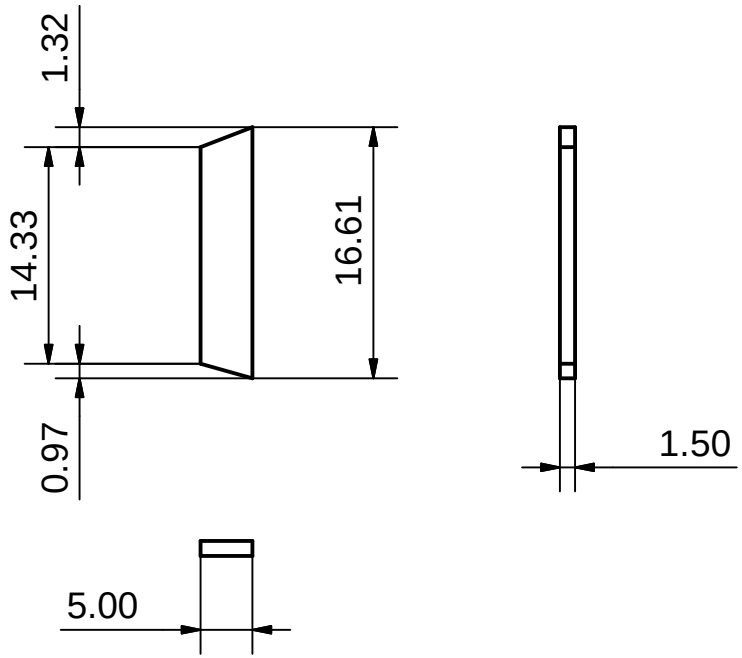




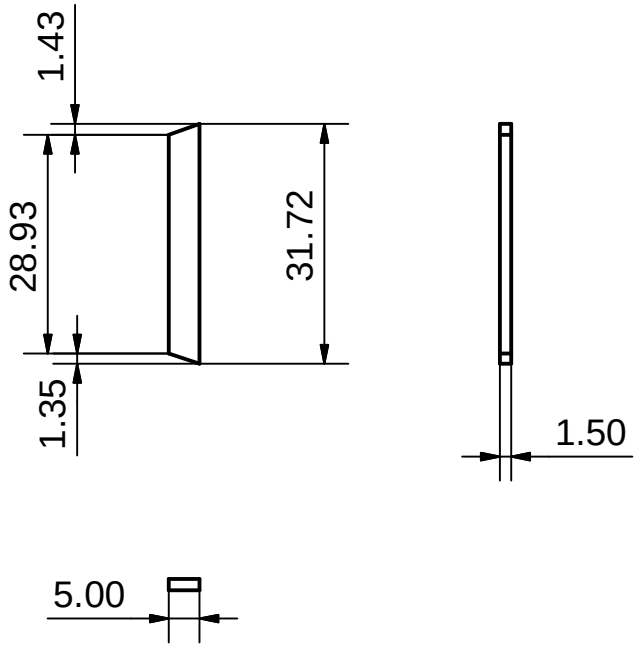
MECHANICAL ENGINEERING DEPARTMENT AHMADU BELLO UNIVERSITY			
Part name:	Tail support structure - segment 5		Drawing No 10
Drawn by:	AFOLAYAN M.O.		Material: Plywood
Approved by:	Dr. D.S. Yawas		
Software:	Autodesk Inventor 7		Scale: 1:1
Date:			Units: mm



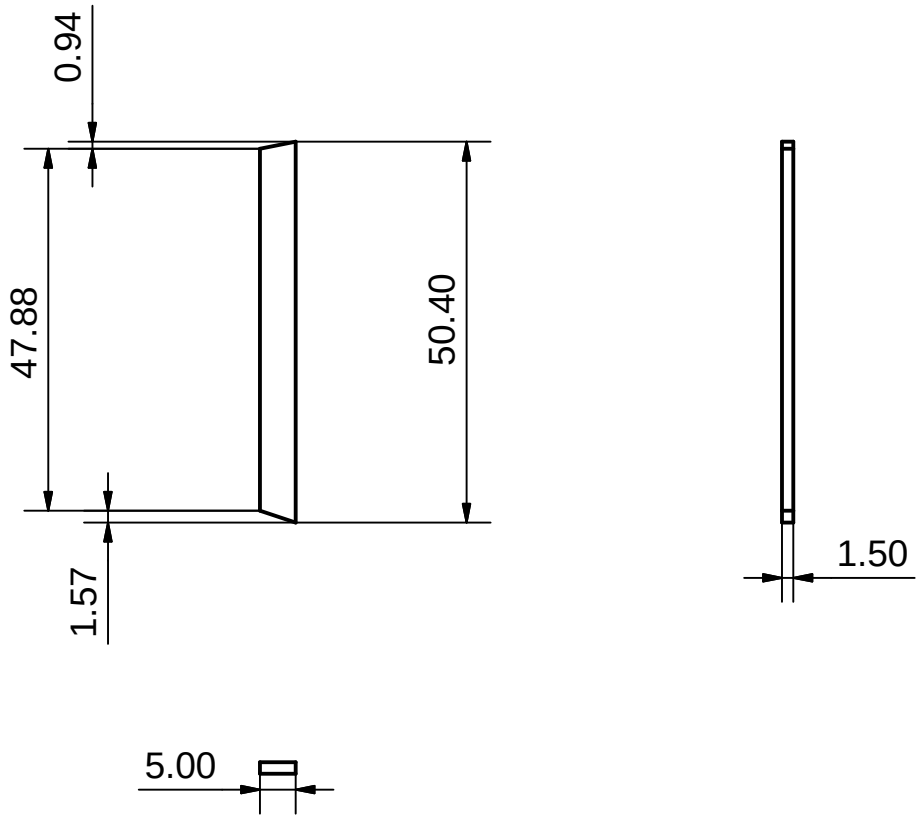
MECHANICAL ENGINEERING DEPARTMENT AHMADU BELLO UNIVERSITY			
Part name:	Tail support structure - segment 6		Drawing No 11
Drawn by:	AFOLAYAN M.O.		Material: Plywood
Approved by:	Dr. D.S. Yawas		
Software:	Autodesk Inventor 7		Scale: 1:1
Date:			Units: mm



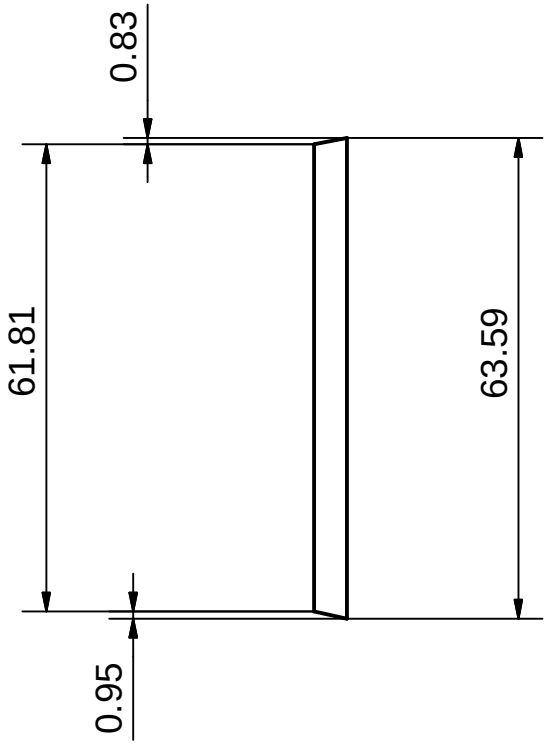
MECHANICAL ENGINEERING DEPARTMENT AHMADU BELLO UNIVERSITY			
Part name:	Rubber stripe - 1		Drawing No 12
Drawn by:	AFOLAYAN M.O.		Material: Vulcanized Rubber (tire inner tube)
Approved by:	Dr. D.S. Yawas		
Software:	Autodesk Inventor 7		Scale 2:1
Date:			Unit: mm

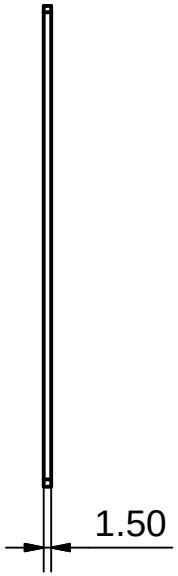


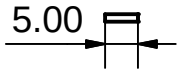
MECHANICAL ENGINEERING DEPARTMENT AHMADU BELLO UNIVERSITY			
Part name:	Rubber stripe - 2		Drawing No 13
Drawn by:	AFOLAYAN M.O.		Material: Vulcanized Rubber (tire inner tube)
Approved by:	Dr. D.S. Yawas		
Software:	Autodesk Inventor 7		Scale 1:1
Date:			Unit: mm



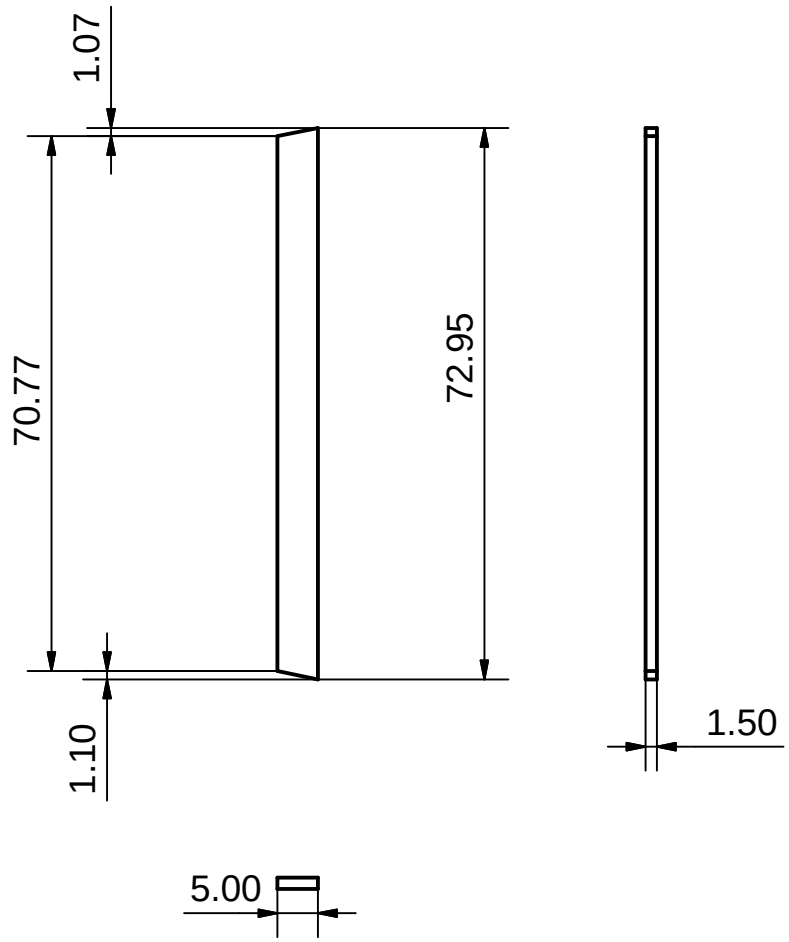
MECHANICAL ENGINEERING DEPARTMENT AHMADU BELLO UNIVERSITY			
Part name:	Rubber stripe - 3		Drawing No 14
Drawn by:	AFOLAYAN M.O.		Material: Vulcanized Rubber (tire inner tube)
Approved by:	Dr. D.S. Yawas		
Software:	Autodesk Inventor 7		Scale 1:1
Date:			Unit: mm



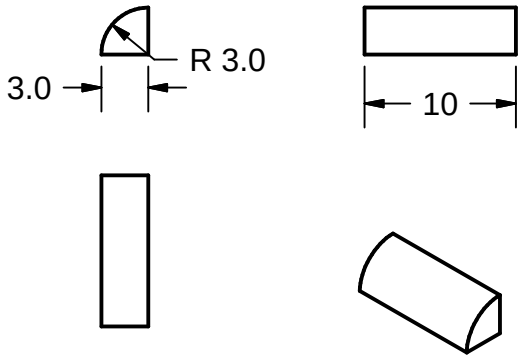




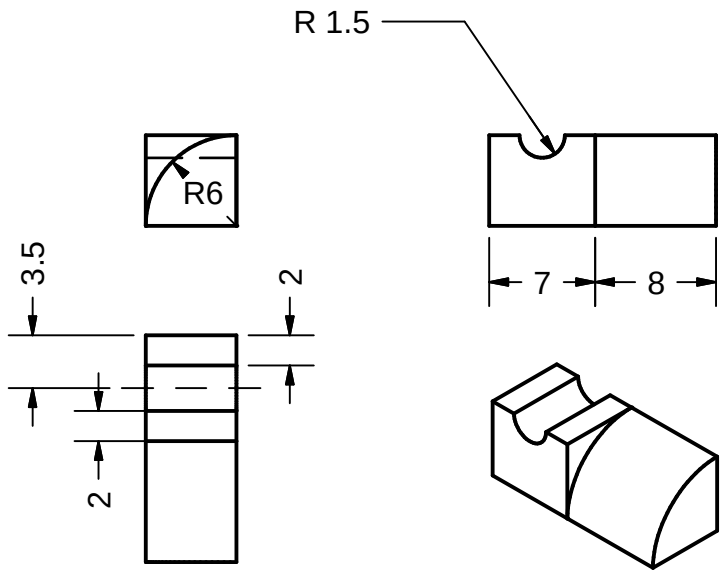
MECHANICAL ENGINEERING DEPARTMENT AHMADU BELLO UNIVERSITY			
Part name:	Rubber stripe - 4		Drawing No 15
Drawn by:	AFOLAYAN M.O.		Material: Vulcanized Rubber (tire inner tube)
Approved by:	Dr. D.S. Yawas		
Software:	Autodesk Inventor 7		Scale 1:1
Date:			Unit: mm



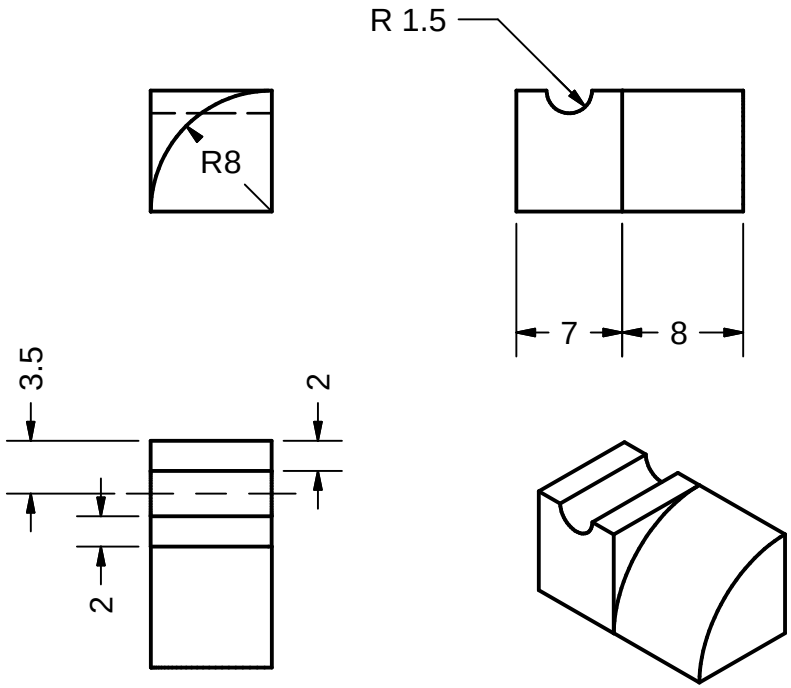
MECHANICAL ENGINEERING DEPARTMENT AHMADU BELLO UNIVERSITY			
Part name:	Rubber stripe - 5		Drawing No 16
Drawn by:	AFOLAYAN M.O.		Material: Vulcanized Rubber (tire inner tube)
Approved by:	Dr. D.S. Yawas		
Software:	Autodesk Inventor 7		Scale 1:1
Date:			Unit: mm



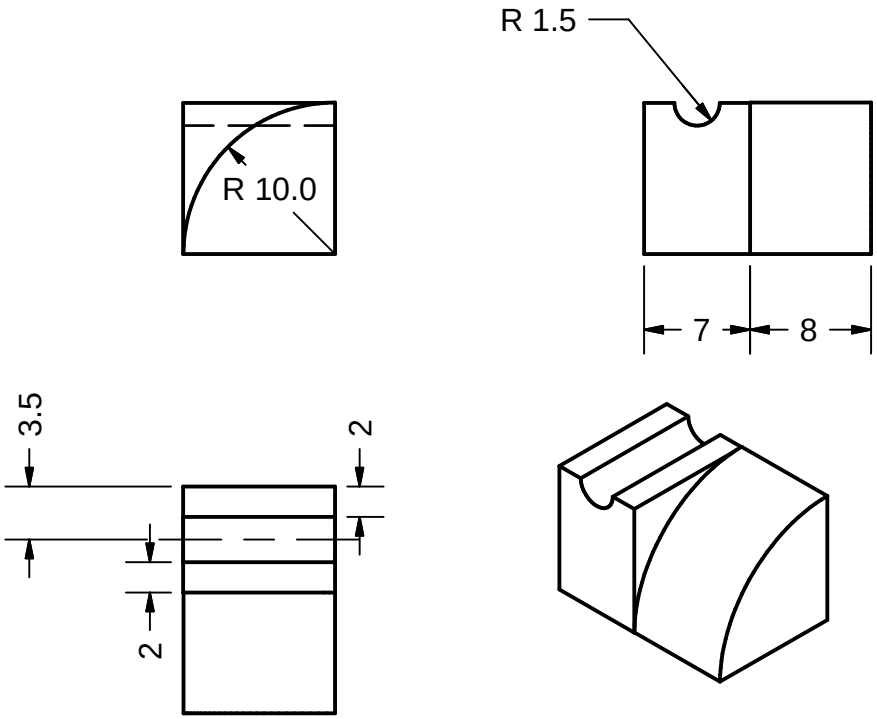
MECHANICAL ENGINEERING DEPARTMENT AHMADU BELLO UNIVERSITY			
Part name:	Quarter Pulley 1		Drawing No 17
Drawn by:	AFOLAYAN M.O.		Material: Plywood
Approved by:	Dr. D.S. Yawas		
Software:	Autodesk Inventor 7		Scale 2:1
Date:			Units: mm



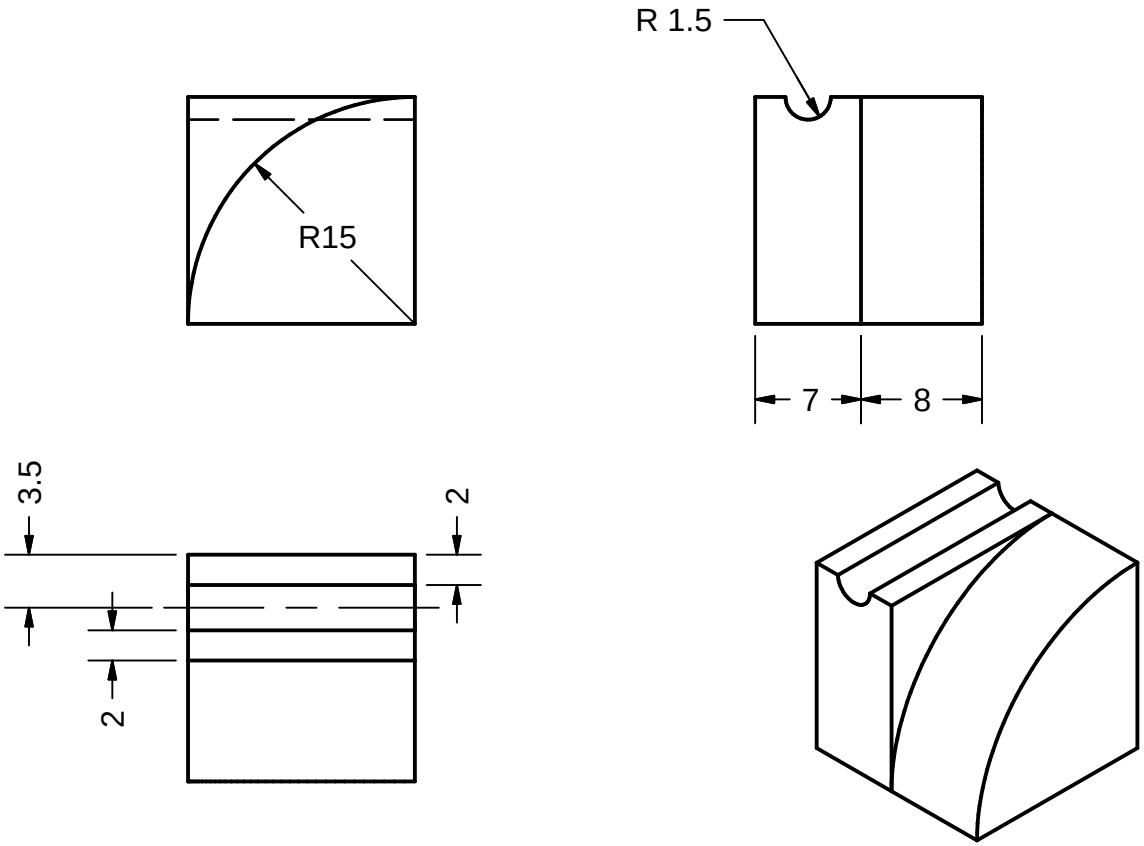
MECHANICAL ENGINEERING DEPARTMENT AHMADU BELLO UNIVERSITY			
Part name:	Quarter Pulley 2		Drawing No 18
Drawn by:	AFOLAYAN M.O.		Material: Plywood
Approved by:	Dr. D.S. Yawas		
Software:	Autodesk Inventor 7		Scale 2:1
Date:			Units: mm



MECHANICAL ENGINEERING DEPARTMENT AHMADU BELLO UNIVERSITY			
Part name:	Quarter Pulley 3		Drawing No 19
Drawn by:	AFOLAYAN M.O.		Material: Plywood
Approved by:	Dr. D.S. Yawas		
Software:	Autodesk Inventor 7		Scale 2:1
Date:			Units: mm



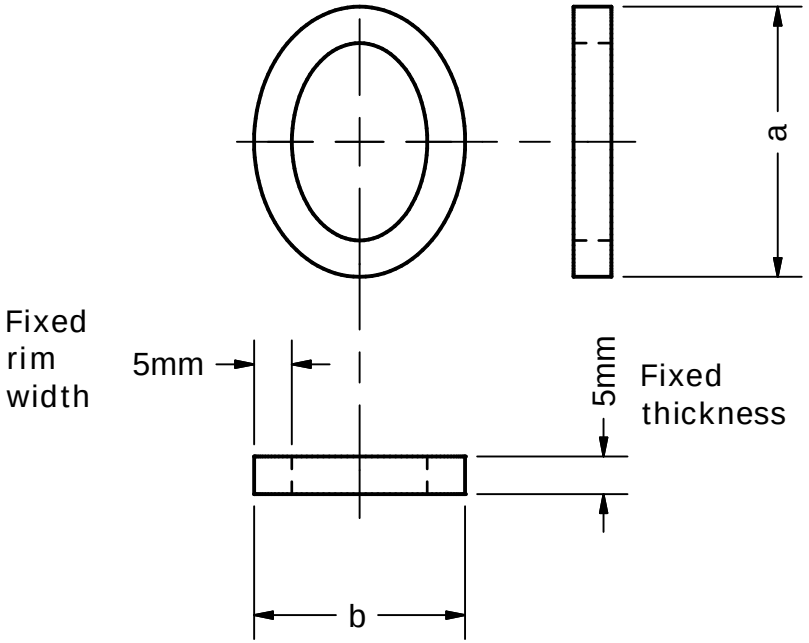
MECHANICAL ENGINEERING DEPARTMENT AHMADU BELLO UNIVERSITY			
Part name:	Quarter Pulley 4		Drawing No 20
Drawn by:	AFOLAYAN M.O.		Material: Plywood
Approved by:	Dr. D.S. Yawas		
Software:	Autodesk Inventor 7		Scale 2:1
Date:			Units: mm

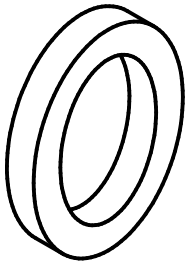


MECHANICAL ENGINEERING DEPARTMENT AHMADU BELLO UNIVERSITY			
Part name:	Quarter Pulley 5		Drawing No 21
Drawn by:	AFOLAYAN M.O.		Material: Plywood
Approved by:	Dr. D.S. Yawas		
Software:	Autodesk Inventor 7		Scale 2:1
Date:			Units: mm

Ring Position	1	2	3	4	5	6	7	8	9	10	11	12	13	14	15	16	17	18	19	20
a	57.6	57.6	56.8	56.8	56.8	56	56	54.4	54.4	54.4	52.8	51.2	51.2	49.6	48	48	46.4	44.8	43.2	41.6
b	91	90.5	90	89	89	88	86	85.5	83	81	79.5	78	76	74	73	71	69	67	65	62
Material	U	U	P	U	U	P	U	U	P	U	U	P	U	U	P	U	U	P	U	U

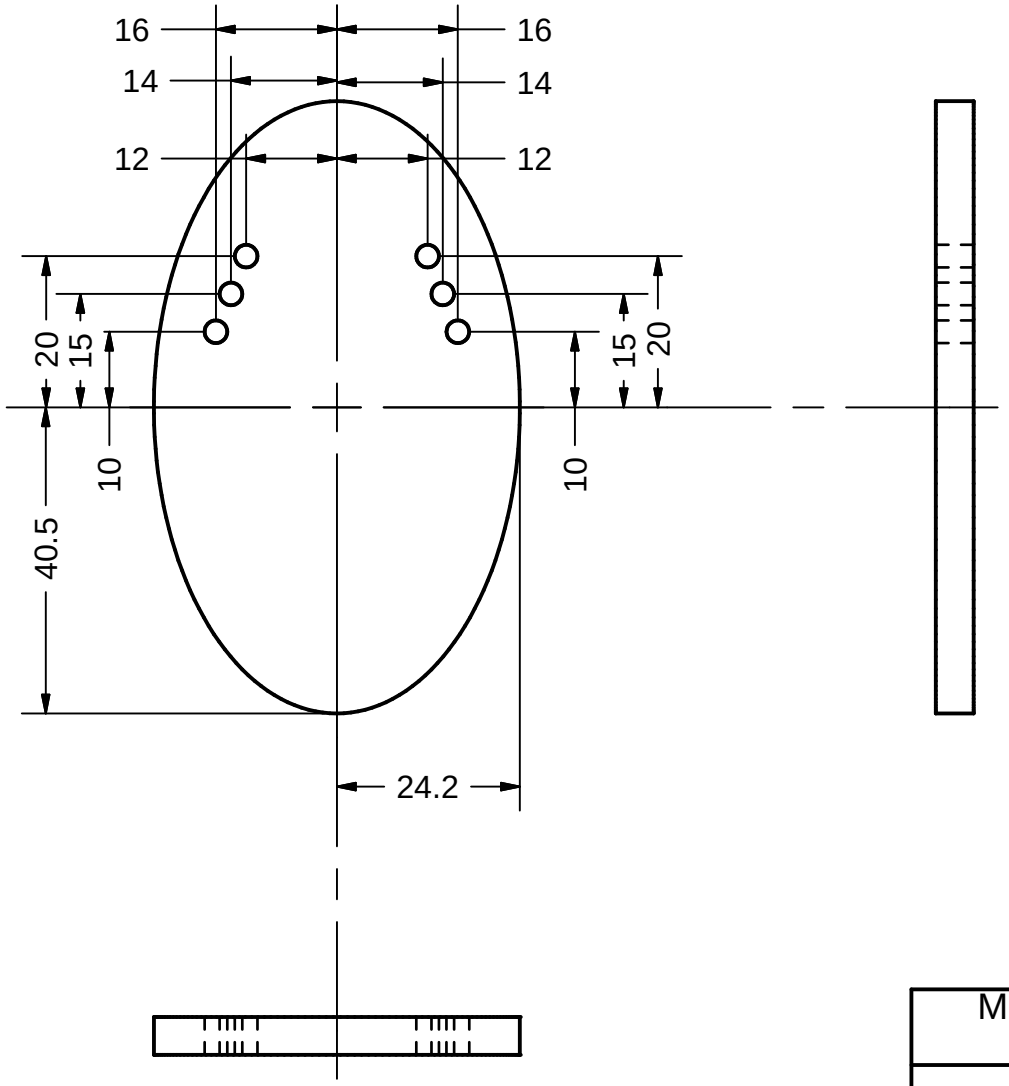
Ring Position	21	22	23	24	25	26	27	28	29	30	31	32	33	34	35	36
a	40	38.4	35.2	33.6	32	30.4	28.8	25.6	23.2	20.8	17.6	14.4	11.2	9.6	8	8
b	60	56	53	49.5	46	43	39.5	36	32	28	24	20	18	15	13	12
Material	P	U	U	P	U	U	P	U	U	P	U	U	P	U	U	P



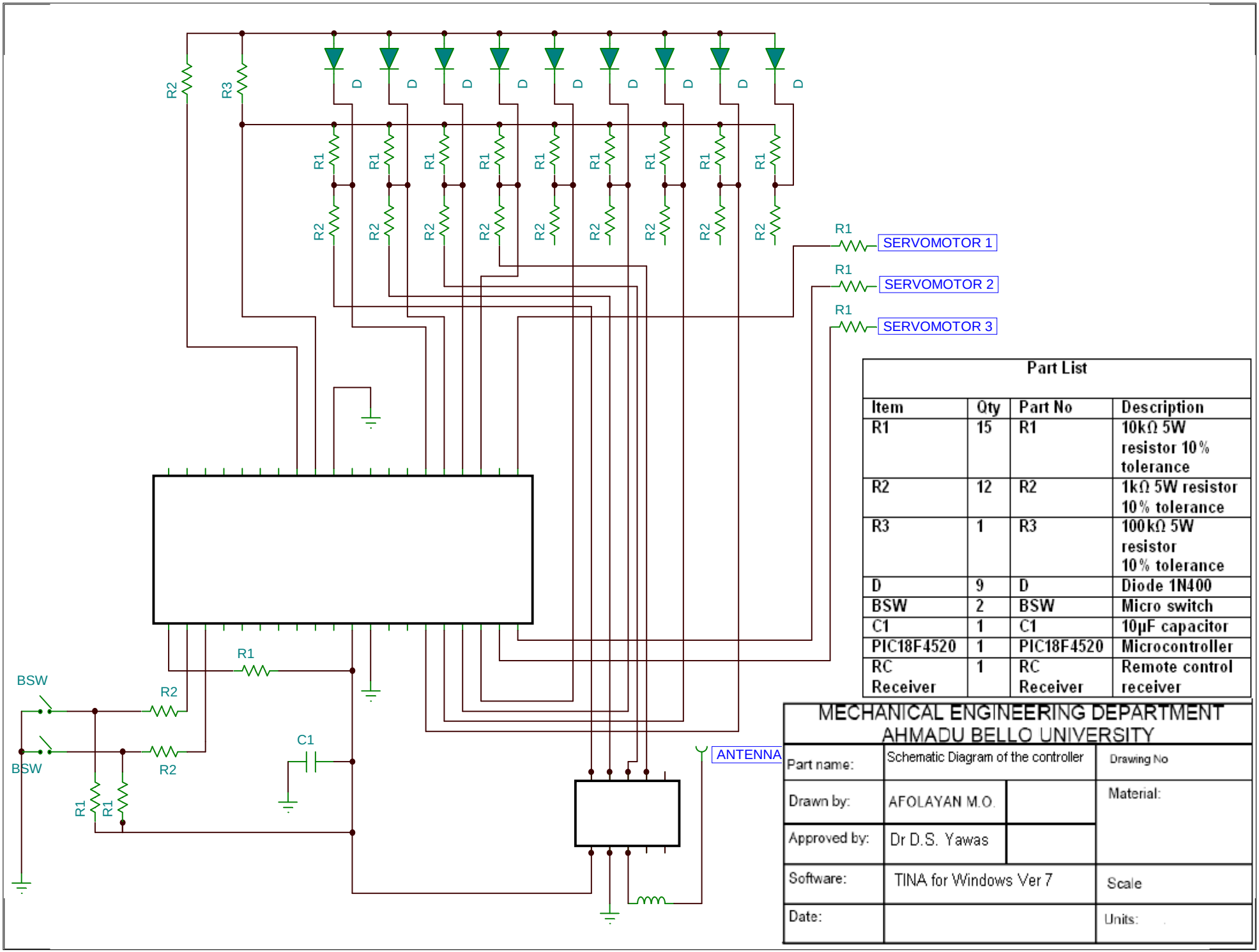


Isometric view

MECHANICAL ENGINEERING DEPARTMENT AHMADU BELLO UNIVERSITY			
Part name:	Rings (for the tail)		Drawing No 22
Drawn by:	AFOLAYAN M.O.		Material: P= Plywood U= Collapsed Polyurethane foam
Approved by:	Dr. D.S. Yawas		
Software:	Autodesk Inventor 7		Scale
Date:			



MECHANICAL ENGINEERING DEPARTMENT AHMADU BELLO UNIVERSITY			
Part name:	Head board		Drawing No 23
Drawn by:	AFOLAYAN M.O.		Material: Plywood
Approved by:	Dr. D.S. Yawas		
Software:	Autodesk Inventor 7		Scale 1:1
Date:			Units: mm



Part List

Item	Qty	Part No	Description
R1	15	R1	10kΩ 5W resistor 10% tolerance
R2	12	R2	1kΩ 5W resistor 10% tolerance
R3	1	R3	100kΩ 5W resistor 10% tolerance
D	9	D	Diode 1N400
BSW	2	BSW	Micro switch
C1	1	C1	10μF capacitor
PIC18F4520	1	PIC18F4520	Microcontroller
RC Receiver	1	RC Receiver	Remote control receiver

MECHANICAL ENGINEERING DEPARTMENT AHMADU BELLO UNIVERSITY			
Part name:	Schematic Diagram of the controller		Drawing No
Drawn by:	AFOLAYAN M.O.		Material:
Approved by:	Dr D.S. Yawas		
Software:	TINA for Windows Ver 7		Scale
Date:			Units: